Journal of Turbomachinery

Published Quarterly by ASME

VOLUME 127 • NUMBER 4 • OCTOBER 2005

TECHNICAL PAPERS

This journal is printed on acid-free paper, which exceeds the ANSI Z39.48-1992 specification for permanence of paper and library materials. ⊗™
♲ 85% recycled content, including 10% post-consumer fibers.

ERRATUM

The ASME Journal of Turbomachinery is abstracted and indexed in the following:

Aluminum Industry Abstracts, Aquatic Science and Fisheries Abstracts, Ceramics Abstracts, Chemical Abstracts, Civil Engineering Abstracts, Compendex (The electronic equivalent of Engineering Index), Corrosion Abstracts, Current Contents, Ei EncompassLit, Electronics & Communications Abstracts, Energy Information Abstracts, Engineered Materials Abstracts, Engineering Index, Environmental Science and Pollution Management, Excerpta Medica, Fluidex, Fuel and Energy Abstracts, INSPEC, Index to Scientific Reviews, Materials Science Citation Index, Mechanical & Transportation Engineering Abstracts, Mechanical Engineering Abstracts, METADEX (The electronic equivalent of Metals Abstracts and Alloys Index), Metals Abstracts, Oceanic Abstracts, Pollution Abstracts, Referativnyi Zhurnal, Shock & Vibration Digest, Steels Alert

Interaction of Shroud Leakage Flow and Main Flow in a Three-Stage LP Turbine

Jochen Gier

Bertram Stubert

Bernard Brouillet

Laurent de Vito

MTU Aero Engines,
Dachauer Str. 665,
Muenchen 80995, Germany

Endwall losses significantly contribute to the overall losses in modern turbomachinery, especially when aerodynamic airfoil load and pressure ratios are increased. In turbines with shrouded airfoils a large portion of these losses are generated by the leakage flow across the shroud clearance. Generally the related losses can be grouped into losses of the leakage flow itself and losses caused by the interaction with the main flow in subsequent airfoil rows. In order to reduce the impact of the leakage flow and shroud design related losses a thorough understanding of the leakage losses and especially of the losses connected to enhancing secondary flows and other main flow interactions has to be understood. Therefore, a three stage LP turbine typical for jet engines is being investigated. For the three-stage test turbine 3D Navier-Stokes computations are performed simulating the turbine including the entire shroud cavity geometry in comparison with computations in the ideal flow path. Numerical results compare favorably against measurements carried out at the high altitude test facility at Stuttgart University. The differences of the simulations with and without shroud cavities are analyzed for several points of operation and a very detailed quantitative loss breakdown is presented.
[DOI: 10.1115/1.2006667]

Introduction

Shrouded airfoils are widely used in many turbines of different applications. In aero engines the low pressure turbine is generally build with shrouded airfoils. Although clearances of modern turbines are generally quite small, leakage flow related losses still contribute significantly to the overall losses of a turbine.

Much research has been undertaken in the past focussing on the flow inside the labyrinth seals aimed at understanding and optimizing the labyrinth discharge coefficients (Egli [1], Rhode et al. [2,3], Takenaga et al. [4]). Millward and Edwards [5] investigated windage heating in labyrinth seals.

Denton and Johnson [6] presented two-dimensional experimental data for the flow over a shrouded steam turbine. Recently a number of investigations addressed the connection between the cavity leakage flow and the main flow in turbines. Pfau et al. [7] performed detailed experimental investigations on the flow structure at the exit of an annular cascade. They found changes in the main flow exit angle compared to a configuration without leakage flow and pitchwise variation in the reentering flow.

Peters et al. [8] performed experimental investigations in a $1\frac{1}{2}$ stage low-speed axial turbine with a tip cavity above the rotor. They also reported indications of circumferentially nonuniform cavity exit flow and a significant negative incidence to the following stator. Similar effects on the subsequent stator were described by Anker and Mayer [9] for the same configuration. Kortschunov and Döhler [10] investigated the effect of artificial jets in a linear cascade.

Hunter and Manwaring [11,12] performed an extensive experimental and numerical investigation on the flow in the cavity–main flow connection for a hub cavity in a two-stage low-speed test rig. They found significant changes in the flow fields of the two rows downstream of the first vane and its inner air seal. The low momentum of the cavity flow reentering into the main flow path and

mixing with the main flow was entrained into the first rotor secondary flow and transported radially up to 7.5% span of this high aspect ratio airfoil.

A more general discussion of cavity related effects including losses can be found in Traupel [13] and Denton [14]. The descriptions of the losses given in these publications concentrate on losses caused by the leakage and the mixing of the cavity flow with the main flow. Denton provides a number of relations for the leakage flow fraction as well as the related mixing losses based on the assumption of constant circumferential velocity in the cavity flow.

Wallis et al. [15] performed investigations on a tip cavity configuration in a four-stage axial turbine. They report four different losses connected with the cavity flow: The cavity entry, the clearance gaps, the mixing with the main flow and the incidence on the following row. They aimed at reducing losses by reducing the mixing losses with the main flow. Therefore, different turning devices were designed and tested, which reduced the flow angle difference of the cavity flow and the main flow. However, all of the turning devices resulted in an efficiency drop compared to the reference configuration.

There is also quite a number of papers focussing on the effects of coolant flows on the main flow especially for high pressure turbines, e.g., McLean et al. [16,17], Girgis et al. [18]. A common result of these investigations is the significance of interaction effects of the injection flow with the main flow and the related losses, which can amount up to 1% or 2% in efficiency. There are also a number of compressor cavity studies indicating a comparable significance and complexity of shroud leakage flows, e.g., [19–21].

Most of the previous studies discussed above focuses either on some of the interaction phenomena between leakage flow of shrouded turbines or on estimates of losses. This paper builds upon this background to construct a more complete picture of the interaction between leakage and main flow and the resulting losses in shrouded turbines. This is done for a test turbine, which is typical for low pressure turbines in aeroengines. For this investigation numerical simulation is employed and compared to experimental measurements carried out in the main flow.

Since in a real aeroengine this turbine would follow a two-stage high pressure turbine the airfoil numbering starts with Vane 3 (V3).

Numerical Method

The simulations are performed with the TRACE_S 3D compressible Navier-Stokes code, which is based on a block-structured finite volume scheme. The code computes the multiple rows fully coupled. Time integration for this investigation is done using an implicit procedure to reach steady state conditions. The convective fluxes are computed with a higher order MUSCL scheme combined with the flux differencing method of Roe. Convective fluxes are limited with a special version of the Van Albada Limiter. For the diffusive fluxes a central scheme is employed.

The stage coupling is based on the mixing plane technique with flux averaging and nonreflecting boundary interfaces and full mass conservation. The code is vectorized and parallelized. More numerical details can be found in Fritsch et al. [22].

Turbulence Modeling. The investigated turbine operates at Reynolds numbers typical for jet engine conditions. Thus a reliable representation of turbulence in the boundary layers is important. Therefore, the Wilcox k-ω [23] two-equation model in low-Reynolds version was employed with extensions for compressibility and system rotation. Since the model does not need wall distances it appears relatively well suited also for complex cavity geometries.

The equations are time-discretized by 2×2 block-implicit time stepping. The resulting system of equations is solved with a Gauss-Seidel algorithm. For more details, please refer to Gier et al. [24].

Transition Modeling. Since the flow in a low pressure turbine is significantly governed by laminar-to-turbulent transition, a transition model is employed in combination with the k-ω turbulence model for this investigation. It is based on the correlations of Abu-Ghannam and Shaw [25] with modifications of Drela [26]. It was selected from the variety of different models, because it takes the boundary layer shape and thus the pressure gradients into account. It is also dependent on the free-stream turbulence level, which is taken from the local turbulence level at the boundary layer edge provided by the turbulence model. Further details with additional references are given in [24] and [27].

Mesh Generation. The mesh covering both the main flow channel and the cavities is made of structured grids exclusively. This allows the use of the same CFD solver as for the current design applications at MTU. The grid is generated in a rather automatic way in three steps:

1. Cavities. Thanks to the axisymmetry of the present cavities, the grids are first defined in the 2D plane (x, r) and then they are extended in the pitchwise direction to form a 3D volume. The 2D definition is done in a semiautomatic mode directly in the CAD environment. The (x, r) contours of the intersections with the main flow channel and of the main flow mixing planes are exported from the CAD tool and transmitted to the grid generator for the main flow channel (red and green lines in Fig. 1. A view of the complete geometry can be seen in Fig. 2.

2. Main Flow Channel. The computational mesh for the main flow channel consists of 12 blocks. Each vane or blade is gridded with one O-type grid around the airfoil and a H-type grid for the major part of the channel. At hub and tip, the grid is limited by contour from the CAD tool.

3. Merging Process and Definition of Intersections. While merging the different grid blocks, the connectivity of the different parts is inherited and put together automatically. Thus, only the interfaces between the associated parts have to be defined. When joining grids (main flow and cavity) rotate alike and have the same
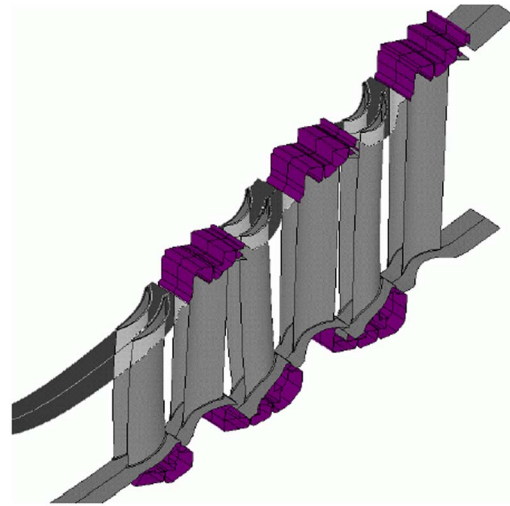
Fig. 1 View of test turbine with modeled cavities

pitch, an abutting interface is defined and the solver is told to interpolate the aerodynamic data on both sides. When joining grids do not rotate alike but exhibit an axisymmetric structure at the common surface, the identical mixing plane technique as between two adjacent rows is used to exchange aerodynamic data.

4. Grid Resolution. For resolving small flow features and to assure a dimensionless wall distance y^+ towards the blade profiles of about 1 the boundary layer grid is heavily clustered close to the surface. The resulting number of grid nodes in a row passage is approximately 600,000 with 65 nodes in radial and 69 nodes in circumferential direction. The total number of grid nodes for the main flow channel is about 3.6 million, for the configuration with cavities 4.2 million (220 blocks).

Boundary Conditions. Nonreflecting boundary conditions are applied at inlet and outlet. Measured total pressure, total temperature and flow angle distributions are prescribed at the inlet and static pressure at the outlet. The inlet turbulence intensity is below 1% which is lower than in a real engine because of the specific test rig configuration.

At solid walls velocities are set to zero except for rotating walls. All walls are assumed to be adiabatic. Turbulent kinetic energy is set to zero and the specific dissipation rate is determined according to

$$\omega_w = \frac{6\mu_w}{(C_{\varepsilon 2} - 1) \cdot C_\mu \rho y_w^2} \tag{1}$$
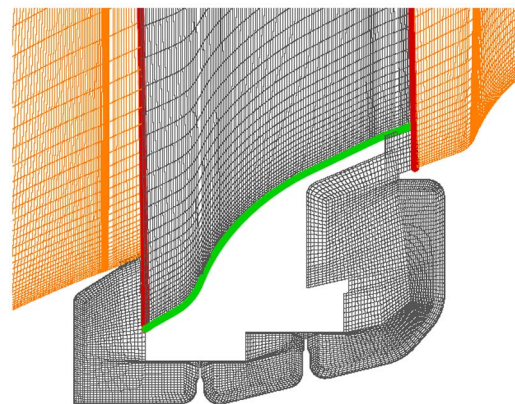
Fig. 2 Mesh in third vane inner air seal (IAS2)
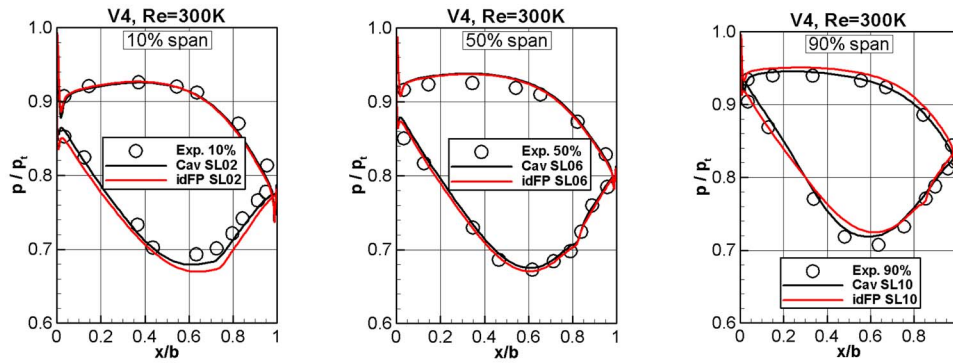
Fig. 3 Static pressure in second vane (V4) for cavity and ideal flow path computations

At the endwalls a fully turbulent flow regime is to be expected. Therefore, a wall function formulation according to Spalding is employed here as well as within the cavities, enabling the use of a somewhat coarser endwall grid resolution without a significant loss in accuracy and thus reducing the computational effort noticeably.

All results were accepted as converged, when massflow and efficiency of the component and the individual stages remained constant within very sharp limits and with residuals down by at least two orders of magnitude. For the cavity computations this leads to significant convergence time increases due to the slow convergence of the energy equation in the slowly moving and strongly recirculating flows inside the cavities.

Impact of Cavity Modelling

Comparison With Experimental Data. To assess the quality of the numerical simulation as well as to judge the differences between computations geometrically modeling the cavities and computations in the ideal flow path, some comparison examples are discussed in this section. In Fig. 3 the static pressures on the middle guide vane (V4) are plotted at the 3 radial locations that were instrumented.

At midspan the difference between the two computations is marginal with a slightly smaller load for the cavity computation. This is caused by the by-pass of mass through the inner air seal of this vane. Both distributions correspond quite well to the experimental data. In the tip region the cavity computation exhibits a stronger negative incidence, which results in a larger peak Mach number, which is in accordance with the data. Also the separation bubble, appearing in the ideal flow path computation at 80% axial chord is suppressed in the cavity computation. At the hub section at 10% span the aerodynamic load of the cavity computation is smaller than for the ideal flow path. This gives a better agreement with the experiment. The reason is the by-pass of flow through the inner air seal.

In the third vane, shown in Fig. 4, the same trends can be observed at the three radial locations. In total the pressure distributions in this vane seem to be a little bit unloaded, which besides computation accuracy might be also due to hardware deviations. Still the simulation and experiment correspond reasonably well for this vane.

In Fig. 5 radial distributions of the isentropic efficiency are plotted for the three Re numbers investigated. For the intermediate Re number of 300,000 a computation of a configuration with half the clearances is added. For all Re numbers it becomes evident that the efficiency in the core flow is hardly affected by the presence of the cavity leakage flow. However, it is strongly affected up to 25% span from the endwalls. General agreement is considerably better for the cavity computations, although especially at the hub the efficiency drop is somewhat overpredicted. Also the computed efficiency is too high between 60% and 70% span. The reason for this is not yet understood. Possibly radial mixing is stronger than computed or turbulence is not adequately modeled in this region. The main flow radial gradient of the total pressure is also reasonably well captured by all computations (Fig. 5). The cavity computations exhibit a little bit thicker boundary layer.

The difference between the ideal flow path and the cavity computations is limited in terms of airfoil flow structure in the core flow as can be seen in Fig. 6. Here the computed flow streamtraces in the vicinity of the airfoil are compared to flow visualization in the test rig for different airfoils of the vane 4 row (pos. 1 and pos. 2). In the computation the separation bubble is quite well captured in terms of the streamwise extent as well as the radial extent. Taking a detailed look it appears that the ideal flow path computation tends to form a small bubble at about 80%
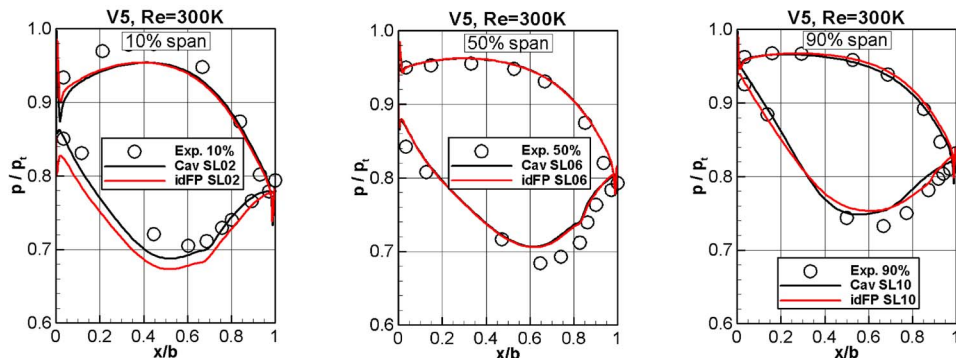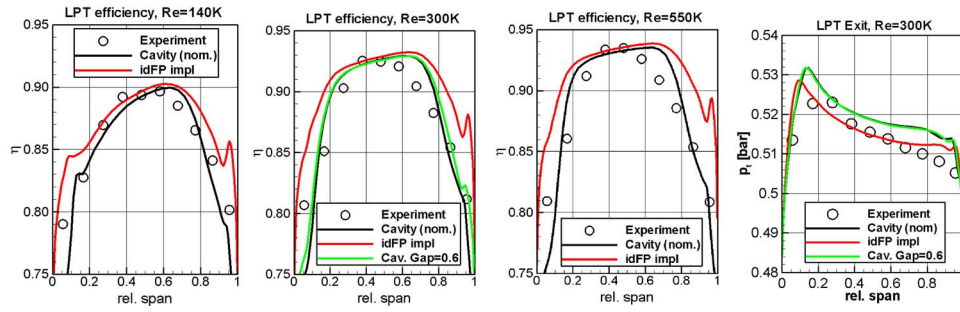

Fig. 4 Static pressure in third vane (V5) for cavity and ideal flow path computations

Fig. 5 Isentropic efficiency distribution and exit total pressure for cavity and ideal flow path in comparison to experimental data

span (location A) while the cavity computation does not. The reason seems to be that in the cavity computation the secondary flow is stronger and is radially extending further into the main flow. This is indicated by the stronger radial slope of the streamtraces in area B in Fig. 6.

The reduction of the efficiency in the endwall regions between ideal flow path and cavity computation for this turbine is fairly large (Fig. 7). At design Reynolds number (300 K) this difference is about 2.6%, somewhat reducing to about 2.2% at the low Reynolds number. This effect is discussed further below. The overall efficiency level of the cavity computation is close to the experimental data, however the efficiency lapse is overpredicted. This effect is likely to be ascribed to the transition modeling, which produces too large suction side separation bubbles at the lowest Reynolds numbers.

Plausibility and General Features of Leakage Flow. Inside the inner and outer air seals a complex flow structure, driven by the leakage flow, develops. The flow structure developing inside the hub cavity is displayed in Fig. 8 for both clearances. In this figure a meridional slice is displayed. Since circumferential variations are relatively small inside the cavities, this distribution is representative for the entire circumference. The flow enters the cavity upstream of the second vane through a large vortex. There are several vortices formed inside the cavity by the complex geometry and clearance fins. Finally the leakage flow reenters the main flow through the gap between second vane and blade. Here an additional vortex is formed, which like the entrance vortex turns clockwise. These two vortices fill the gap between the adjacent airfoil rows.

Reducing the clearance by half from 1.2 mm to 0.6 mm reduces the leakage flow through the cavity also approximately by half. By inspection of Fig. 8 it can be seen that this does not change the flow structure. However, the entrance vortex and the exit vortex grow a little bit. At the exit the vortex grows especially axially forwards, which squeezes the exiting leakage flow and reduces its axial flow component. Also the entropy level in the rear part of the cavity rises. This makes sense, because in the case of the smaller gap less lower entropy fluid coming from the main flow flushes the cavity while the windage losses generation inside the cavity basically remains constant.

At the outer air seal a similarly complex flow structure develops (Fig. 9). The leakage flow is entering the outer air seal through the downstream side of the large entrance vortex upstream of the second rotor leading edge. The flow is then turned and driven through the clearance seals, forming additional vortices. It eventually leaves the cavity relatively smoothly by forming two smaller exit vortices. The smaller clearance case is very similar, hardly exhibiting any change in the extent of the vortices.

In Fig. 10 the hub contour of the second vane is shown. On the left side a photograph with colour traces from experiment and on the right side the equivalent simulation result are displayed. Besides the nice agreement of the passage vortex driven hub streamlines in the rear part of the passage special focus should be put onto the front part. Here the same stagnation line in circumferential direction is present in experiment as well as in the computation. Both the position and the structure with a stagnation point about two thirds of the pitch towards the airfoil pressure side are well captured. The presence of the airfoil passage causes some circumferential inhomogeneity of the recirculating flow in the en-
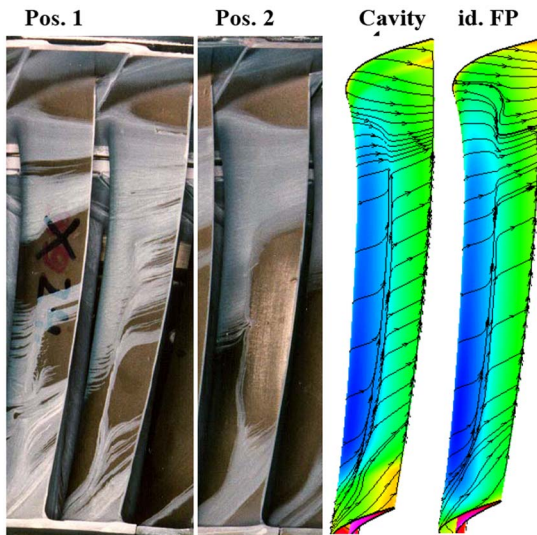
Fig. 6 Stream traces on vale 4 (V4)
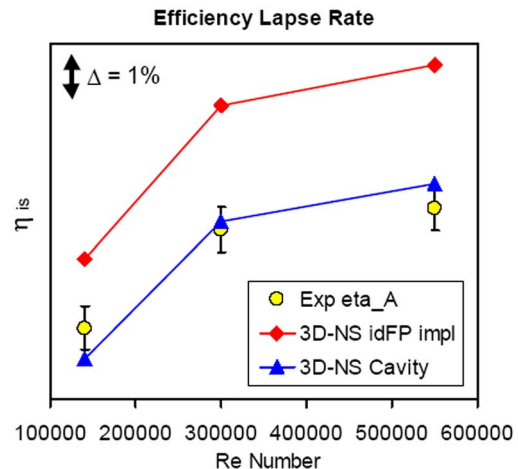
Fig. 7 Turbine efficiency Reynolds number lapse rate

clearance = 1.2 mm

clearance = 0.6 mm

(a)

(b)
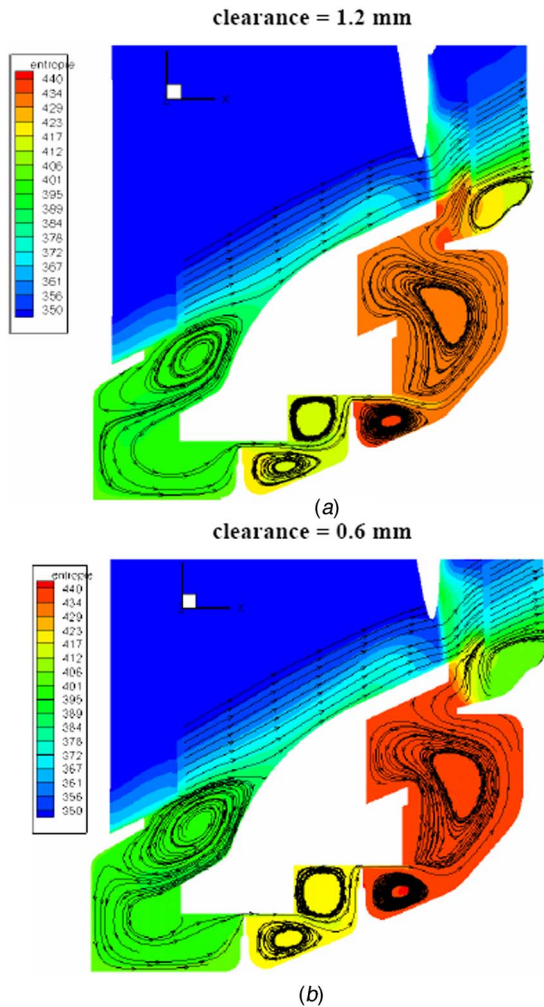
Fig. 8   Flow structure and entropy in inner air seal IAS2 for two clearances, Re=300,000 (projection into meridional plane)

trance vortex upstream of the stagnation line.

Another important plausibility check is the evaluation of the leakage flow rates. These are shown in Fig. 11. Except for the first inner air seal (IAS1) below the first vane, which was closed in experiment and simulation, all seals have leakage flow fractions between 0.4% and 0.75% of total flow. The clearances are basi-
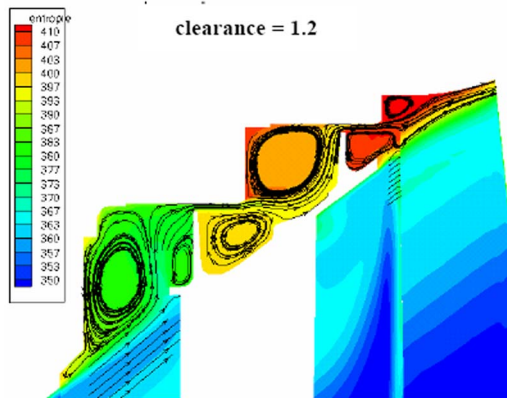
Fig. 9   Flow structure and entropy in outer air seal OAS2 for 1.2 mm clearances, Re=300,000 (projection into meridional plane)
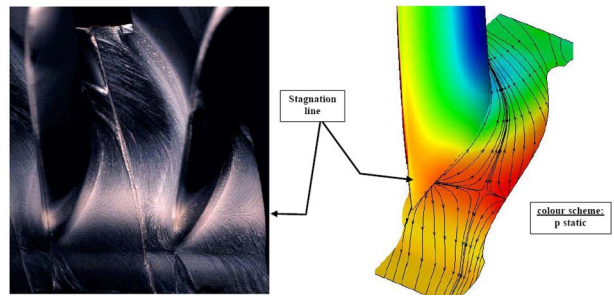
Fig. 10   Flow visualization on the hub of the second vane, Re =300 K

cally identically 1.2 mm and thus the relative gaps (clearance/airfoil span) through the turbine are slightly decreasing. However, the leakage flow through the inner air seals is significantly smaller. The obvious reason is the smaller relative area of the inner air seal gaps compared to the outer air seals. In addition the higher pressure ratio of the second inner air seal (vane 4 =row 3) compared to the third IAS (vane 5=row 5) is seen to be responsible for the somewhat larger leakage flow in the second IAS despite its smaller relative gap area.

Denton [12] reports an estimate of leakage losses in shrouded turbines based on simple analysis. Assuming constant axial velocity, which is also a fairly good approximation for this test turbine, the relative leakage flow is

$$\frac{\dot{m}_L}{\dot{m}_m} = \frac{g}{h} C_c \sqrt{\sec^2 \alpha_2 - \tan^2 \alpha_1} \qquad (2)$$

Using a typical contraction coefficient C_c of 0.6 this formula gives the relative leakages shown in Table 1. Comparing these with the cavity computation (Fig. 11, Table 1 right column) shows a reasonable agreement, when the value coming out of Eq. (2) is divided by $\sqrt{2}$ for taking two clearances per cavity into account (two gaps). Except for the first blade (B3), where the value out of Eq. (2) is somewhat higher the leakage levels are quite similar and the difference between hub and casing seals is captured. However, this is only the case when the relative gap *areas* are taken for g/h and not the relative gaps themselves. Also the trends are not cap-
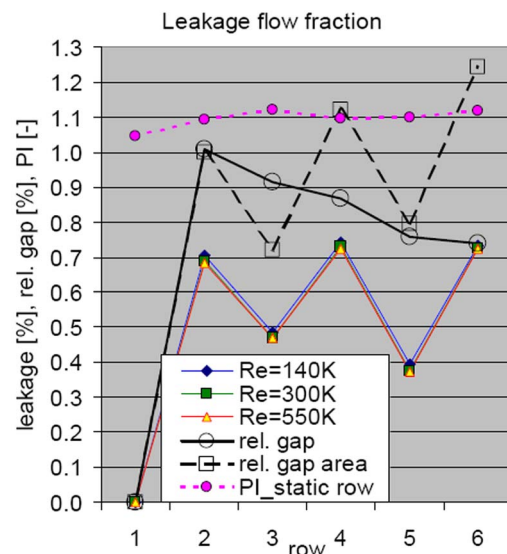
Fig. 11   Leakage flow fraction, relative gap, relative gap area, and static pressure ratio for all airfoil seals

Table 1 Relative leakage flow based on Eq. (2)

	1 gap m_L/m_m [%]	2 gaps m_L/m_m [%]	CFD (Re=300 K) m_L/m_m [%]
B3	1.37	**0.97**	0.69
B4	1.01	**0.71**	0.73
B5	0.94	**0.66**	0.73
V4	0.69	**0.49**	0.47
V5	0.81	**0.57**	0.38

tured well.

Finally one interesting detail should be addressed. In Fig. 12 the relative leakage flows through the outer air seals are shown in a closeup. At the lower Reynolds numbers the losses occurring in the main flow increase by increased friction and enlarged suction side boundary layer growth including separation bubbles. The flow structure in the cavities however is hardly affected by the Reynolds number and thus the flow blockage also hardly changes. The increased blockage in the main flow and the basically constant blockage in the leakage flow must result in an increase of leakage flow fraction with decreasing Reynolds number. This turns out to be the case as can be seen in Fig. 12.

To conclude this chapter, the authors feel that the current numerical simulation not only exhibits a good agreement with the experimental data but also the computed flow features in the not instrumented cavity regions correspond to engineering experience.

Effects of Interaction Between Cavity and Main Flow

Cavity flows and the main flow interact in the region where the flow enters and leaves the cavity (Figs. 8–10). Also the pressure distributions of the vanes in Figs. 3 and 4 show an increased negative incidence. This negative incidence can also be seen in Fig. 13. Close to the endwalls this amounts up to 5 deg. Depending on the airfoil design and general flow conditions this can lead to pressure side flow separation and increased suction side peak Mach numbers.

Furthermore, the fluid leaving the cavity has gathered a higher entropy. At the vane tip sections the upstream outer air seal releases a thickened boundary layer caused by the leakage and the related mixing losses. This thicker vane inlet boundary layer intensifies the formation of the passage vortex system in the tip region of the vanes (except of course for the first vane). This effect can already be obtained from Fig. 6 but becomes more obvious from Fig. 14.

It is important to note that at the tip the passage vortex related pressure minimum is not only more pronounced but that it moved quite a way radially into the main flow. This means that the passage vortex in this vane not only collects less energetic fluid but

Fig. 13 Comparison of radial distribution of yaw angle at vane 4 inlet for ideal flow path and cavity computation

really gains strength. This can be expected to cause additional losses inside the vane and the subsequent rows. At the hub this effect is much smaller. Here, a part of the inlet boundary layer is sucked into the hub cavity upstream of the vane significantly reducing the effect of a disturbed vane inlet boundary layer.

In the case of the reduced clearance gaps (0.6 mm) the secondary flow pattern looks very much like the reference gap case (1.2 mm). The intensity of the passage vortex is somewhat reduced and also the distance the vortex core has moved into the flow channel. However, qualitatively it is not half way between the full gap and the ideal flow path. It is concluded thereupon, that there is a loss mechanism involved, which is not primarily dependent on the leakage flow rate governed by the clearance.

Evaluation of Cavity Related Loss Mechanisms

Leakage flow through the inner and outer air seals introduces several loss mechanisms, which reduce turbine performance. As discussed in the introduction several authors addressed cavity flow related losses. While Traupel [11] reports more integral loss in-

Fig. 12 Leakage flow in OAS for different Reynolds numbers
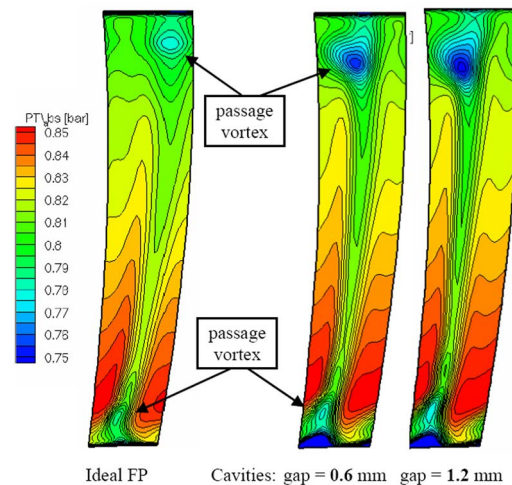
Fig. 14 Total pressure distribution in axial plane downstream of vane 4 (V4)

crease, Denton [12] puts a special focus on the mixing losses of the reentering leakage flow without mentioning flow field changes and losses in subsequent rows. Wallis et al. [13] mention four losses, which are losses at cavity entry, sealing fins, mixing losses of reentering flow and incidence related losses in subsequent rows.

Based on the observations of this study combined with the findings in literature five groups of cavity related losses are identified. First effect is the "by-pass" effect of the leakage flow. The leakage flow does not reduce its enthalpy level like the main flow although it is subject to approximately the same pressure drop. In terms of the enthalpy-entropy diagram the flow through the labyrinth seals equals a horizontal line from row inlet to exit pressure, resulting in an entropy rise depending on the pressure difference.

For stator vanes this results in a reduction in exit velocity for a fixed mass flow. In rotor blades the work extraction is reduced. This results in a reduced isentropic efficiency, because due to the pressure drop across the clearances the overall pressure ratio and thus the isentropic power is not equally reduced as the real power output. Hence, this "by-pass" effect can be viewed either as reduced work output by reduced enthalpy reduction or as increased losses through a flow fraction, which changes pressure only by loss generation across clearance fins. Since losses occurring in the entry region of a cavity contribute to the overall cavity through-flow, they can be combined with the clearance losses.

Another loss mechanism, which is considered to be very significant in literature is the mixing losses connected to the velocity differences between the reentering cavity flow and the main flow. For these Denton [12] provides a simple estimate for the momentum losses due to mixing.

A third loss generation process is surely the windage by differently rotating walls inside the cavities. A fourth loss source appear to be the steps in the flow path, which will be discussed further below. Finally the presence of cavity leakage flows changes the inflow to the subsequent airfoil rows as seen in the last section. These "subsequent row losses" are mainly incidence and secondary flow losses, which including their interdependence not only depend on the cavity exit flow but also on the airfoil and turbine design parameters.

Relative Magnitude of Cavity Related Loss Mechanisms. In this chapter the attempt is being made to get an estimate of the relative magnitude of the five above mentioned loss mechanisms for the investigated turbine. These considerations are based on the numerical simulation combined with analysis. Although such a simulation definitely does not capture all complex physical effects, based on the verification step, it is claimed that it captures the main flow characteristics necessary for this analysis to be reasonably valid. The division between ideal conditions and real conditions will be made by comparing the ideal flow path and the cavity computations for the intermediate Reynolds number case.

The losses attributed to cavity induced effects are related to the losses generated by the main flow in the ideal flow path computation, which can be computed by the following approach.

According to Denton [12] the enthalpy loss coefficient ζ is quantitatively equivalent to the entropy loss coefficient ζ_s

$$\zeta_S \approx \zeta = \frac{h_2 - h_{2is}}{h_{t2} - h_2} \quad \text{with} \quad h_{t2} - h_2 = 1/2 \cdot v_2^2 \quad (3)$$

For the ideal flow path computation and this point of operation the average loss coefficient for the airfoils was

$$\bar{\zeta} \approx 0.05$$

With this a total enthalpy loss for the three-stage turbine can be computed:

$$\Delta h_{\text{loss,row}} = \zeta \cdot \frac{\bar{v}_2^2}{2} = 1 \frac{\text{kJ}}{\text{kg}} \left(\text{with} \quad v_2 \approx 200 \frac{m}{s} \right)$$

Table 2 Enthalpy loss of "bypass" mechanism (5)

row	Δh row [kJ/kg]	m_L/m_m row	Δh_{loss} row [kJ/kg]
B3	8	0.0070	0.056
V4	10.5	0.0047	0.049
B4	10.5	0.0073	0.077
V5	11	0.0038	0.042
B5	11	0.0074	0.081
LPT		–	**0.305**

$$\Delta h_{\text{loss,LPT}} = 6 \cdot \Delta h_{\text{loss,row}} = 6 \frac{kJ}{kg} \quad (4)$$

This number is quite close to the equivalent number based on the individual airfoil losses. In order to quantify the loss associated with the "by-pass" effect it is assumed that the pressure drop is hardly changed by the by-pass, which means that a horizontal line can be drawn in the h-s diagram for the leakage flow. This means that the overall enthalpy drop in the airfoil row is reduced by this amount of leakage flow. Hence a simple formula can be set up:

$$\Delta h_{\text{loss,row,bypass}} = \frac{\dot{m}_L}{\dot{m}_m} \cdot \Delta h_{\text{row}} \quad (5)$$

In the test turbine reaction was close to 50% except for the first stage. Using the simulation data the "by-pass" loss can be estimated as in Table 2.

Relating this result to the total loss generated by the airfoils in the ideal flow path this loss amounts to 5% of the main flow loss for the current configuration.

To estimate the mixing losses of the reentering flow the momentum loss formula of Denton [12] is used. It is given by

$$\zeta_{\text{mix}} = \frac{T\Delta s}{0.5 \cdot v_2^2} = \frac{2}{v_2^2} \cdot \frac{\dot{m}_L}{\dot{m}_m} \left[v_{\Theta 2}^2 \left(1 - \frac{v_{\Theta L}}{v_{\Theta 2}} \right) + v_{x2}^2 \left(1 - \frac{v_{xL}}{v_{x2}} \right) \right] \quad (6)$$

In Figs. 15 and 16 the axial and absolute circumferential velocities are shown for OAS1 and IAS2. Plugging in these velocities according to Eq. (6) the loss coefficients in Table 3 are evaluated.

Interestingly both loss coefficients are very similar, although the relative leakage fraction of the outer air seal is about 50% higher. The reason is that for the same leakage flow the mixing is more intensive at the hub due to the larger velocity differences between cavity exit and main flow.

Using the ζ values evaluated in the first blade and second vane cavity combined with the same average exit velocity as in Eq. (4) for all vanes and rotors, respectively, the overall mixing loss of the reentering flow can be estimated to

$$\Delta h_{\text{loss,mix}} = \sum_{\text{rows}} \zeta_{\text{loss,mix,row}} \cdot 1/2 \cdot \bar{v}_2^2 = 0.76 \frac{\text{kJ}}{\text{kg}} \quad (7)$$

This number corresponds to approximately 12.5% of the losses in the ideal flow path.

The windage losses can be estimated through the total temperature change between inlet and exit of the cavities. In the outer air seals this temperature drops by approximately 0.3 K, while the temperature rises in the inner air seal by approximately 3 K. The difference between inner and outer air seals is actually not surprising. In the outer air seals the absolute circumferential velocity is

Table 3 Loss coefficient based on Eq. (6)

row	seal	ζ mix row
B3	OAS1	0.008
V4	IAS2	0.007
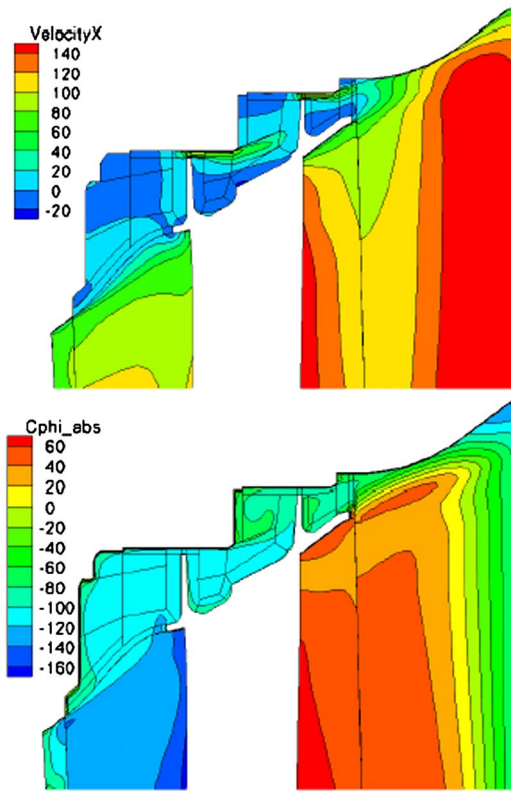
Fig. 15 Axial and absolute circumferential velocity in OAS1 (blade 3) in (m/s)

Fig. 16 Axial and absolute circumferential velocity in IAS2 (vane 4) in (m/s)

slightly larger than the rotation velocity of the outer shroud (approximately 100 m/s), actually leading to a small amount of work extraction. At the hub, however, the rotation and the absolute velocity of the flow leaving the rotor in the main stream is of opposite sign. Thus the velocity difference is about 120 m/s. Using the temperature differences the loss generation due to windage in the hub cavities can be estimated:

$$\Delta h_{\text{windage,vane}} = \frac{m_L}{m_m} \cdot c_p \Delta T_t = 0.004 \cdot 1.0045 \cdot 3 \approx 0.012 \frac{\text{kJ}}{\text{kg}} \quad (8)$$

For two inner air seals (Vane 4 and 5) this is equivalent to 0.4% of the loss in the ideal flow path. Hence, although the windage losses quantification is quite heavily depending on the accuracy of the numerical solution, which cannot be expected to be very precise for the loss-related flow details inside the cavities, the windage losses can be expected to be approximately one order of magnitude smaller than "by-pass" losses and mixing losses.

Originally the working hypothesis in this investigation was that there are only four loss mechanisms and the fourth mechanism is the "subsequent row losses," which could be approximated by subtracting the first three loss types from the whole difference between ideal flow path and cavity computation. However, when the result of the simulation with the reduced gap came out at some point in the investigation, this result mismatched the original expectation.

Actually the total loss increase between ideal flow path and cavity computation turned out to be $\Delta h = 1.6$ kJ/kg. Reducing the gap by half only recovered approximately $\Delta h = 0.45$ kJ/kg instead of 0.8 kJ/kg, which would be exactly in the middle (Fig. 17). In terms of efficiency this means that even if the clearances were zero there would still be a significant efficiency difference between ideal and cavity geometry (dashed line extension).

The "by-pass" and the mixing loss according to Eqs. (5) and (6) depend linearly on the leakage flow fraction. Since the leakage
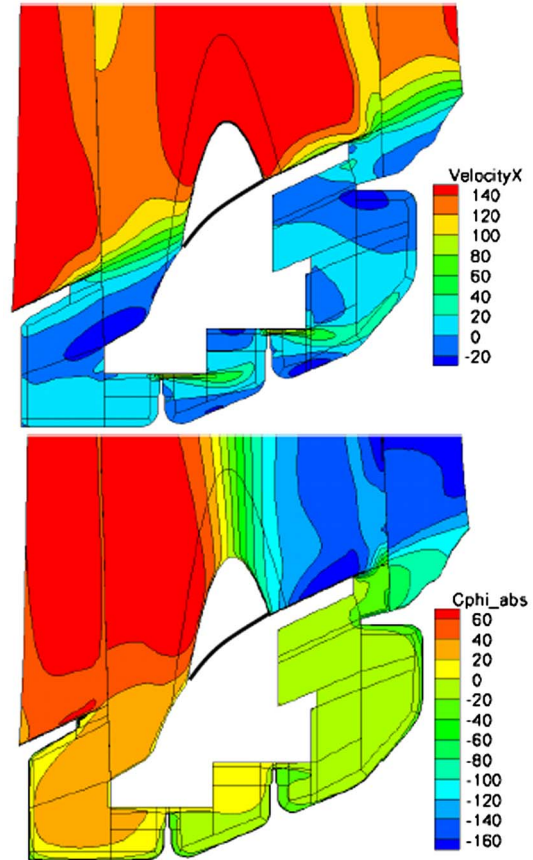
flow is reduced by 50% in the reduced gap case, these loss components in first order are also reduced by half, i.e., from together $\Delta h = 1.06$ kJ/kg to $\Delta h = 0.53$ kJ/kg (red triangle in Fig. 17). This is slightly more than the $\Delta h = 0.45$ kJ/kg computed by the numerical simulation. At least partially this could be explained by the further reduction of the axial velocity component of the reentering leakage flow and its influence on the mixing loss. Reducing the clearance gaps to zero should reduce these two loss components to zero, thus leaving about $\Delta h = 0.6$ kJ/kg unexplained, since no obvious mechanism could be identified, which explains an equivalent increase of secondary flow losses (according to Fig. 14 the passage vortex seems even to be reduced for the 0.6 mm gap
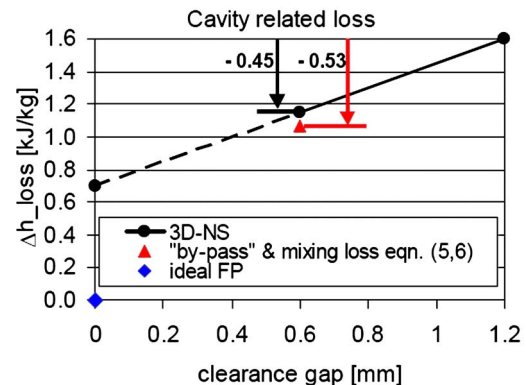
Fig. 17 Cavity related losses for turbine

Table 4 Relative fraction of cavity related losses

	Δh [kJ/kg]	$\Delta h/\Delta h_{\text{total}}$ [%]
total Δ(ideal FP–cavity)	1.6	100.0
"by-pass" losses	0.3	18.8
mixing losses @ reentry	0.76	47.5
windage	0.04	2.5
"step losses"	0.3	18.8
"subsequent row losses"	0.2	12.5

Table 5 Stackup of cavity related losses for different clearance gap configurations

	gap=1.2 mm Δh [kJ/kg]	gap=0.6 mm Δh [kJ/kg]	gap=0 mm Δh [kJ/kg]
total Δ(ideal FP–cavity)[a]	1.6	1.15	0.7
"by-pass" losses	0.3	0.15	0
mixing losses @ reentry	0.76	0.38	0
windage	0.04	0.04	0.04
"step losses"	0.3	0.35	0.5
"subsequent row losses"	0.2	0.23	0.16

[a]Result of numerical simulation, gap=0 extrapolated

case).

The only cause for this additional loss appear to be the steps in the real flow path. For example downstream of the first rotor (B3) the flow duct features a backward facing step at the hub, in which the entry vortex of the inner air seal is located. Such steps are present at all cavity inlets and exits. In a first order approximation these steps can be viewed as causing a Carnot loss depending on the area ratio:

$$\zeta_C = \frac{\Delta p}{\rho/2 v_1^2} = \left(1 - \frac{A_1}{A_2}\right)^2 \qquad (9)$$

Actually Eq. (9) describes a pressure loss and not an enthalpy or entropy loss, but the difference for these flows is surely much smaller than the approximation quality of simple one-dimensional estimates. Furthermore this loss cannot be used for the reentering cavity flows, since these are captured in Eq. (6) characterizing the mixing losses.

Hence, only the 5 cavity entries and the first vane inner air seal exit (no leakage) can be taken for this loss estimate in the cases with flow through the seals. With an approximate average area ratio of 1.07 for each step, based on the geometrical difference between upstream and downstream area of the steps, it can be estimated:

$$\Delta h_{\text{loss,steps}} = \zeta_C \cdot v_x^2 \approx 0.07^2 \cdot \left(100 \frac{m}{s}\right)^2 \approx 0.05 \frac{\text{kJ}}{\text{kg}}$$

$$\Delta h_{\text{loss,steps,total}} = \sum_{\text{steps}} \Delta h_{\text{loss,steps}} = 6 \cdot 0.05 \frac{\text{kJ}}{\text{kg}} = 0.3 \frac{\text{kJ}}{\text{kg}} \qquad (10)$$

With this result the loss breakdown in Table 4 is obtained. For the "subsequent row losses," for which no direct evaluation seems feasible, the losses of the first four effects are subtracted from the overall loss change between ideal flow path and cavity computation.

This means that at nominal clearances the mixing losses make up about 50% of the cavity related losses and thus the largest part. The "by-pass" losses and the "step losses" turn out to be of the same magnitude for the given clearance gap. The "subsequent row losses," which mainly include incidence and secondary flow losses are somewhat smaller.

For the extreme (theoretical) case of vanishing clearance gaps the "by-pass" losses and the mixing losses have to approach zero. On the other hand the "step losses" will increase, since now also the cavity exits form flow path steps without throughflow.

For the vanishing gaps the "step losses" increase is estimated to $\Delta h = 0.2$ kJ/kg, because only 5 additional steps have to be taken into account and the step height is somewhat smaller for the re-entry steps. It would be alternatively possible to split the mixing losses into the circumferential mixing losses and the axial mixing losses and to integrate the "step losses" into the axial mixing.

The resulting stackup for the three gap cases is reported in Table 5. The "step-loss" value for the reduced gap is slightly modified, modeling that the mixing in the re-entry is already increased by the reduced seal throughflow. The "subsequent row losses" remain fairly constant, but this is of course depending on the estimate of the other loss components.

The essence of this loss evaluation is that the pure presence of the real cavities and their platforms introduces losses, referred to as "step losses," which also induce additional secondary flow losses. Their presence is also responsible for the fact, that the passage vortex in the second vane does not change that much between the two gap cases. They also cause the large difference between the two cavity computations on one side and the ideal flow path computation on the other side in terms of radial efficiency distribution (Fig. 5). The magnitude of these losses will heavily depend on the platform design and steepness of the flow duct and thus will be different for different turbine designs. It should also be mentioned that losses due to circumferential inflow and outflow in the cavity–main flow path connection occur, which are difficult to accurately assess in a steady-state computation. To assess this a fully coupled unsteady simulation would be needed. The influence of these circumferential non-uniformities will have to be included in one of the discussed loss mechanisms or assessed separately.

To conclude this loss evaluation it should be noted that it is based on a numerical simulation and is performed for a given test turbine. Changing the design parameters of the turbine will surely affect this loss breakdown to a certain extent, it being a change in the relative magnitudes between the different loss components or between total cavity losses and ideal flow path losses.

Conclusions

In this paper the interaction between the main flow and the leakage flow in a shrouded turbine has been investigated for an aeroengine low pressure turbine rig. To assess the quality of the numerical simulation on which the analysis is based, the measured data gathered in the main flow was compared to the computation. In addition, plausibility checks were performed to judge the cavity computation details in absence of very fine experimental cavity data. Both checks revealed a pretty reasonable computation quality.

The investigation showed that there are significant interaction effects between main and cavity flow. As frequently described in literature, the leakage flow resulted in an incidence change for the subsequent airfoil row. Furthermore it became obvious that the increased thickness of the inlet boundary layer to the subsequent row caused an intensification of the passage vortex system in this subsequent row. These mechanisms also cause a radial shift in the mass flow distribution.

An attempt was made to separate different loss mechanisms in this investigation. These mechanisms are referred to as "by-pass" loss, mixing loss of the reentering flow, windage losses, "step losses" and "subsequent row losses," the latter combining losses due to incidence and increased secondary flows.

The main result of this analysis was that the mixing losses amounted to about 50% of the total cavity related losses, while the "by-pass" and "step losses" made up approximately 20% of the cavity losses. Losses due to incidence and secondary flows were estimated to have a smaller fraction. The windage losses came out fairly negligable.

The "step losses" become stronger in cases with reduced leakage flow and are strongly dependent on the main turbine design features.

Further work in this area can focus on further improving simulation quality based on more detailed measurements and investigation of other typical turbines. Also it could be worthwhile looking into effects of unsteadiness.

Acknowledgment

Nomenclature

A = area (m^2)
C_{e2}, C_μ = constants
C_c = Contraction coefficient
g = clearance gap (m)
h = airfoil height (m)
$\dot{m}$ = mass flow rate (kg/s)
p = pressure (Pa)
r = radius (m)
s = entropy (kJ/(kg K))
T = temperature (K)
y = wall distance (m)
v = velocity (m/s)
α = flow angle (from axis) (deg)
μ = dynamic viscosity (Pa s)
η = efficiency
ρ = density (kg/m^3)
ω = specific turbulence dissipation (1/s)
ζ = enthalpy loss coefficient
ζ_s = entropy loss coefficient=$(T_2\Delta s)/(h_{t2}-h_2)$

Subscripts

C = Carnot
L = leakage
m = main flow
is = isentropic
t = total
w = wall
x = axial
Θ = circumferential
1 = inlet
2 = exit

References

[1] Egli, A., 1935, "The Leakage of Steam Through Labyrinth Seals," Trans. ASME, **57**, pp. 115–122.
[2] Rhode, D. L., Johnson, J. W., and Broussard, D. H., 1996, "Flow Visualization and Leakage Measurements of Steped Labyrinth Seals; Part I: Annular Groove," ASME Paper No. 96-GT-136.
[3] Rhode, D. L., Younger, J. S., and Wernig, M. D., 1996, "Flow Visualization and Leakage Measurements of Stepped Labyrinth Seals; Part II: Sloping Surfaces," ASME Paper No. 96-GT-137.
[4] Takenaga, H., Matsuda, T., and Yokota, H., 1998, "An Experimental Study on Labyrinth Seals for Steam Turbines," *Proceedings, 8th International Symposium on Flow Visualization*, Sorrento, Italy.
[5] Millward, J. A., and Edwards, M. F., 1994, "The Windage Heating of Air Passing through Labyrinth Seals," ASME Paper No. 94-GT-56.
[6] Denton, J. D., and Johnson, C. G., 1976, "An Experimental Study of the Tip Leakage Flow Around Shrouded Turbine Blades," CEGB Research Report CEGB-R/M/N848.
[7] Pfau, A., Treiber, M., Sell, M., and Gyarmathy, G., 2000, "Flow Interaction From the Exit Cavity of an Axial Turbine Blade Row Labyrinth Seal," ASME Paper No. 2000-GT-481.
[8] Peters, P., Breisig, V., Giboni, A., Lerner, Ch., and Pfost, H., 2000, "The Influence of the Clearance of Shrouded Rotor Blades on the Development of the Flowfield and Losses in the Subsequent Stator," ASME Paper No. 2000-GT-478.
[9] Anker, J. E., and Mayer, J. F., 2002, "Simulation of the Interaction of Labyrinth Seal Leakage Flow and Main Flow in an Axial Turbine," ASME Paper No. GT-2002-30348.
[10] Korschunov, B. A., and Döhler, S. W., 1996, "Einfluß von Leckageströmungen an der Laufradspitze auf die Aerodynamischen Charakteristiken des Folgenden Leitgitters," BWK Bd. 48, pp. 49–55.
[11] Hunter, S. D., and Manwaring, S. R., 2000, "Endwall Cavity Flow Effects on Gaspath Aerodynamics in an Axial Flow Turbine: Part I—Experimental and Numerical Investigation," ASME Paper No. 2000-GT-651.
[12] Hunter, S. D., and Manwaring, S. R., 2000, "Endwall Cavity Flow Effects on Gaspath Aerodynamics in an Axial Flow Turbine: Part II—Source Term Model Development," ASME Paper No. 2000-GT-513.
[13] Traupel, W., 1966, *Thermische Strömungsmaschinen*, Springer-Verlag, Berlin.
[14] Denton, J. D., 1993, "Loss Mechanisms in Turbomachines," ASME Paper No. 93-GT-435.
[15] Wallis, A. M., Denton, J. D., and Demargne, A. A. J., 2000, "The Control of Shroud Leakage Flows to Reduce Aerodynamic Losses in a Low Aspect Ratio, Shrouded Axial Flow Turbine," ASME Paper No. 2000-GT-475.
[16] McLean, Ch., Camci, C., and Glezer, B., 2001, "Mainstream Aerodynamic Effects Due to Wheelspace Coolant Injection in a High-Pressure Turbine Stage: Part I: Aerodynamic Measurements in the Stationary Frame," J. Turbomach., **123**, pp. 687–696.
[17] McLean, Ch., Camci, C., and Glezer, B., 2001, "Mainstream Aerodynamic Effects Due to Wheelspace Coolant Injection in a High-Pressure Turbine Stage: Part II: Aerodynamic Measurements in the Rotational Frame," J. Turbomach., **123**, pp. 697–703.
[18] Girgis, S., Vlasic, E., Lavole, J.-P., and Moustapha, S. H., 2002, "The Effect of Secondary Air Injection on the Performance of a Transonic Turbine Stage," ASME Paper No. GT-2002-30340.
[19] Wellborn, S. R., and Okiishi, T. H., 1999, "The Influence of Shrouded Stator Cavity Flows on Multistage Compressor Performance," J. Turbomach., **122**, pp. 486–498.
[20] Demargne, A. A. J., and Longley, J. P., 2000, "The Aerodynamic Interaction of Stator Shroud Leakage and Mainstream Flows in Compressors," ASME Paper No. 2000-GT-570.
[21] Wellborn, S. R., 2001, "Details of Axial-Compressor Shrouded Stator Cavity Flows," ASME Paper No. 2001-GT-495.
[22] Fritsch, G., Hoeger, M., Blaha, C., and Bauer, D., 1997, "Viscous 3D Compressor Simulations on Parallel Architectures," AIAA Paper No. 97-2876.
[23] Wilcox, D. C., 1988, "Reassessment of the Scale Determining Equation for Advanced Turbulence Models," AIAA J., **25**, No. 11, pp. 1299–1310.
[24] Gier, J., Ardey, S., and Heisler, A., 2000, "Analysis of Complex Three-Dimensional Flow in a Three-Stage LP Turbine by Means of Transitional Navier-Stokes Simulation," ASME Paper No. 2000-GT-645.
[25] Abu-Ghannam, B. J., and Shaw, R., 1980, "Natural Transition of Boundary Layers—The Effects of Turbulence, Pressure Gradient and Flow History," J. Mech. Eng. Sci., **22**, No. 5, pp. 213–228.
[26] Drela, M., 1995, *Implementation of Modified Abu-Ghannam/Shaw Transition Criterion*, MIT Aero-Astro, Cambridge, MA.
[27] Gier, J., and Ardey, S., 2001, "On the Impact of Blade Count Reduction on Aerodynamic Performance and Loss Generation in a Three-Stage LP Turbine," ASME Paper No. 2001-GT-197.

Fluid Flow and Heat Transfer in Rotating Curved Duct at High Rotation and Density Ratios

A. K. Sleiti
e-mail: asleiti@ucf.edu

J. S. Kapat

Mechanical, Materials and Aerospace
Department,
University of Central Florida,
Orlando, FL 32816

*Prediction of flow field and heat transfer of high rotation numbers and density ratio flow in a square internal cooling channels of turbine blades with U-turn as tested by Wagner et al. (ASME J. Turbomach., **113**, pp. 42–51, 1991) is the main focus of this study. Rotation, buoyancy, and strong curvature affect the flow within these channels. Due to the fact that RSM turbulence model can respond to the effects of rotation, streamline curvature and anisotropy without the need for explicit modeling, it is employed for this study as it showed improved prediction compared to isotropic two-equation models. The near wall region was modeled using enhanced wall treatment approach. The Reynolds Stress Model (RSM) was validated against available experimental data (which are primarily at low rotation and buoyancy numbers). The model was then used for cases with high rotation numbers (as much as 1.29) and high-density ratios (up to 0.4). Particular attention is given to how secondary flow, velocity and temperature profiles, turbulence intensity, and Nusselt number area affected by Coriolis and buoyancy/centrifugal forces caused by high levels of rotation and buoyancy in the immediate vicinity of the bend. The results showed that four-side-average Nu, similar to low Ro cases, increases linearly by increasing rotation number and, unlike low Ro cases, decreases slightly by increasing density ratio.* [DOI: 10.1115/1.2019276]

Introduction

In engineering applications such as gas turbines and electric generators, characteristics of the flow field, and heat transfer in internal cooling rotating ducts with strong curvature are very important to understand, as the curvature can completely alter these characteristics. The turbine blades are cooled using pressurized air from compressor. The blades, in addition to the temperature loads are however stressed by the rotational forces, (i.e. the Coriolis and the centrifugal forces). These rotational induced forces complicate the flow structure within the ducts. When performing experiments, it is very difficult to achieve conditions with high rotational speeds and density ratios and hence numerical simulations are needed.

The internal cooling channels of gas turbine blades usually consist of two or more straight passages connected with 180 deg bends. As the fluid reaches the bend in channels with zero rotation number, a centripetal acceleration is generated, which is balanced by an opposing pressure gradient. For low curvature bends, the pressure gradient varies almost linearly from the convex to the concave surfaces. The high momentum fluid in the duct center favors the outer surface. Continuity requires that the outward motion in the center of the duct be balanced by a reverse flow along the walls, where the Coriolis force due to the streamwise velocity component is zero. This flow behavior will generate a circular motion in the cross-stream plane. At the exit of the bend two opposing rotating cells appear, with vorticity in the streamwise direction. The Dean [1] number (De) is the parameter that measures the curvature effect relative to viscous effect [De $=\text{Re}(D_h/r)^{1/2}$]. The Dean number gives a measure of the degree of stability. The flow is considered unstable when exceeding the critical Dean number according to Rayleighs criteria. For the flow in a bend the convex side (inner) is stable, while the concave side (outer) is unstable. The fluid viscosity affects the stability of the flow through bend and hence it is important for turbulence modeling.

Experimental investigations on rotating U channels have been performed by few researchers compared to The stationary case. Wagner et al. [2] and Wagner et al. [3] performed heat transfer measurements in smooth wall channels with U bend with rotation numbers of up to 0.475 and a density ratio of up to 0.22. There results showed that near the inlet of the second pass, the thermal boundary layers are thin because of the U-turn effect. With increasing axial distance from the turn, the turn dominated secondary flows, and turbulence decay and the rotational effects on heat transfer become more prominent Johnson et al. [4] continued with 45 deg skewed ribs. Mochizuki et al. [5] and Shih et al. [6] performed heat transfer measurements. Cheah et al. [7] performed laser Doppler anemometry measurements. Hwang and Kuo [8] derived heat transfer correlations. Iacovides et al. [9] performed experiments on local heat transfer in rotating square ended U bend. Liou and Chen [10] performed laser Doppler velocimetry study on smooth duct with 180 deg straight corner turn. Including in-line ribs in recent study, Liou et al. [11] performed flow and heat transfer measurements. The Taslim group of Taslim, [12] Taslim et al., [13] Taslim and Korotky, [14] and Taslim and Lengkong [15] performed heat transfer coefficient measurements on 45-degree round corner staggered ribs. The effect of a variety of rib configuration on heat transfer could be found in Taslim [16].

On the prediction efforts, many researchers proposed turbulence modeling modifications due to curvature effect. Prandtl [17] proposed to add correction to the mixing length, based on a local dimensionless curvature parameter. To modify the turbulent length scale, Bradshaw [18] used the Richardson number, which is not possible in the standard two-equation models because the turbulent length scale is not given explicitly. Launder et al.[19] introduced a Richardson number modification in the *e* equation. Since streamline curvature makes redistribution among the Reynolds stresses, Wilcox and Chambers [20] applied modification to the turbulent kinetic energy. Launder [21] showed that the isotropic EVMs have a limited capability to accurately predict the complex secondary flows in a bend. This is clear from the fact that under

unstable conditions (concave side) the wall normal component is amplified and the streamwise component is reduced and for the convex side the opposite happens.

Bredberg [22] questioned the strategy of Wilcox and Chambers for [20] achieving improved predictions, through only redistribution among the stress components because the level of turbulence energy is different on the concave and convex sides. Instead he used a Richardson number modified e-equation and achieved more realistic profiles for the turbulent kinetic energy. Hellsten, [23] Shih et al. [6] and Lin et al. [24] have focused on the e equation. Luo and Lakshminarayana [25] studied a nonrotating (two-dimensional) case using k-ε, k-ε (algebraic stress model), and Reynolds stress model (RSM) turbulence models, with RSM providing the best predictions for major features including strong enhancement of turbulence near the concave wall, large reduction of turbulence near the convex wall, and separation down stream of the convex wall. The simulation with RSM showed that the mean flow inside the bend is nearly insensitive to the upstream inflow conditions. Variation of δ/R has more influence on the turbulence amplification near the concave wall than on turbulence damping near the convex wall. In Luo and Lakshminarayana [26] they concluded that for RSM to capture the large amplification of turbulence in concave boundary layers, the generation term in the e equation should not keep pace with that in the k equation. Studying nonrotating channels, Rumsey et al. [27] concluded that the RSM turbulence model was able to capture the full extent of suppressed turbulence near the convex wall, while the one and two-equation models and the explicit algebraic stress model (EASM) were not.

The flow inside turbine blades ducts is complicated (bends, ribs, rotation, and buoyancy) and needs a three-dimensional simulation. Zhang et al. [28] studied numerically the flow structure and friction factor for fully developed flow in parallel rotating rectangular ducts. They concluded that possibly four kinds of secondary vortices exists: due to centrifugal force, due to Coriolis force, Dean vortices due to the centrifugal instability, and Coriolis vortices due to the Coriolis instability. Besserman and Tanrikut [29] and Choi et al. [30] pointed out the importance of resolving the near wall region in curved ducts. Iacovides et al. [31] used a differential stress model (DSM), with and without modification to the ε equation. The results were improved slightly compared to results using ASM. Iacovides et al. [32] compared between using different wall treatments with an ASM. The separated region inaccurately predicted, with only a slight improvement using the full LRN version of the model. In the study by Nikas and Iacovides [33] it was concluded that for heat transfer predictions a low Reynolds number turbulent model is preferable to a zonal model in the near wall region. From numerical simulations in the Cheah et al. [7] U bend, Bredberg [22] used unmodified LRN two-equation models and showed that length-scale corrections were needed, especially when predicting heat transfer within the bend region. Using a LRN k-ω model to simulate U bend, Rigby et al. [34] achieved reasonable accuracy. Bonhoff et al. [35] employed the RSM model using FLUENT code with standard wall functions. The average heat transfer predictions were close to the Wagner et al. [3] results except a slight overestimation in the second pass. Chen et al. [36] simulated the same case using near wall second-moment closure model and compared to a two-layer k-ε model, which performed the worst. The comparison with experimental data clearly demonstrated that the secondary flows in rotating two-pass channels have been strongly influenced by the Reynolds stress anisotropy resulting from the Coriolis and centrifugal buoyancy forces as well as the U-turn wall curvature. The exact formulation of rotational body forces in Reynolds stress turbulence model is a big advantage over two-equation models, which are also based on isotropic flow assumption. In a recent paper by the authors using RSM (see Sleiti and Kapat [37]), the anisotropy in such flow conditions was clearly shown.

The objective of this study is to perform a 3D numerical simu-lation of the flow field and heat transfer in the immediate vicinity of the U bend of internal cooling channel for high rotation numbers (up to Ro=1.29) and high density ratio (up to 0.4) as the literature review in the subject revealed that no studies have been performed to cover that range. This choice of Ro and DR range is based on the argument that if high heat transfer rates, with reasonable changes in pressure drops, can be achieved by increasing Ro and DR then the need for ribs that complicate internal cooling channels can be limited. Particular attention would be given to how secondary flows, velocity and temperature profiles, and turbulence intensities and consequently, heat transfer rate are affected by Coriolis, buoyancy and centrifugal forces caused by high-speed rotation and high-density ratios. Reynolds stress turbulence model and enhanced near wall treatment will be employed. FLUENT computational fluid dynamics (CFD) Code will be used for this simulation. While this study is concerned with the immediate vicinity of the U-bend region, the reader is referred to Sleiti and Kapat, [37] where the authors studied the first and second passes for the same Ro and DR ranges.

Governing Equations

The continuity, momentum and energy equations for a Newtonian incompressible fluid are given as

$$\frac{\partial \rho}{\partial t} + \frac{\partial \rho U_i}{\partial x_i} = 0 \tag{1}$$

$$\frac{\partial \rho U_i}{\partial t} + \frac{\partial \rho U_i U_j}{\partial x_i} = \rho g_i + F_i - \frac{\partial P}{\partial x_i} + \frac{\partial}{\partial x_i}(2\mu S_{ij}) \tag{2}$$

$$\frac{\partial \rho E_0}{\partial t} + \frac{\partial \rho U_i E_0}{\partial x_i} = \rho U_i F_i - \frac{\partial q_i}{\partial x_i} + \frac{\partial}{\partial x_j}(U_i T_{ij}) \tag{3}$$

where F_i are the additional body forces that can affect the fluid motion such as rotation, magnetic, or electric field, etc and s_{ij} is the strain rate tensor, T_{ij} are the surface forces similar to the viscous and pressure terms in the momentum equations, and E_0 is the total internal. Assuming constant rotation velocity the extra terms due to rotation (body-force modification to the Navier-Stokes equations) are

$$a_i^{ce} = \varepsilon_{ijk}\varepsilon_{klm}\Omega_j\Omega_l x_m \text{ and } a_i^{co} = 2\varepsilon_{ijk}\Omega_j U_k \tag{4}$$

Computational Approach

Reynolds stress model (RSM) Gibson and Launder [38], Launder [21], and Launder [39] solves the Reynolds stresses $\tau_{ij} = \overline{u_i' u_j'}$, using individual transport equations. The exact transport equations for the transport of the Reynolds stresses, may be written as follows:

$$\frac{D\tau_{ij}}{Dt} = \frac{\partial D_{T,ij}}{\partial x_k} + \frac{\partial D_{L,ij}}{\partial x_k} + P_{ij} + G_{ij} + \phi_{ij} - \varepsilon_{ij} + F_{ij} + S \tag{5}$$

where $D\tau_{ij}/Dt = \partial/\partial t(\rho \overline{u_i' u_j'}) + C_{ij}$ and $\partial/\partial t(\rho \overline{u_i' u_j'})$ is the local time derivative, C_{ij} the convection term, $D_{T,ij}$ the turbulent diffusion term, $D_{L,ij}$ the molecular (viscous) diffusion term, P_{ij} the stress production term, G_{ij} the buoyancy production term, ϕ_{ij} the pressure strain term, ε_{ij} the dissipation term, F_{ij} the production term by system rotation, and S the source term. Of the various terms in these exact equations, $C_{ij}, D_{L,ij}, P_{ij}$, and F_{ij} do not require any modeling. However, turbulent diffusion ($D_{T,Ij}$), buoyancy production (G_{ij}), pressure strain (ϕ_{ij}), and dissipation (ε_{ij}) need to be modeled to close the equations. These terms are given as

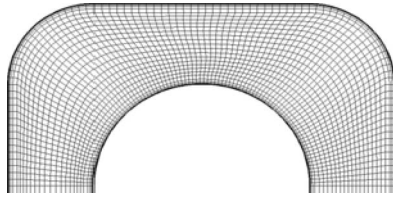$$C_{ij} = \frac{\partial}{\partial x_k}(\rho u_k \overline{u_i' u_j'})$$

Fig. 1   Numerical grid

$$D_{T,ij} = -\frac{\partial}{\partial x_k}\left[\rho\overline{u_i' u_j' u_k'} + \overline{p(\delta_{kj}u_i' + \delta_{ik}u_j')}\right]$$

$$D_{L,ij} = \frac{\partial}{\partial x_k}\left[\mu\frac{\partial}{\partial x_k}(\overline{u_i' u_j'})\right]$$

$$P_{ij} = -\rho\left(\overline{u_i' u_k'}\frac{\partial u_j}{\partial x_k} + \overline{u_j' u_k'}\frac{\partial u_i}{\partial x_k}\right)$$

$$G_{ij} = -\rho\beta(g_i\overline{u_j'\theta} + g_j\overline{u_i'\theta})$$

$$\phi_{ij} = \overline{p\left(\frac{\partial u_i'}{\partial x_x} + \frac{\partial u_j'}{\partial x_i}\right)}$$

$$F_{ij} = -2\rho\Omega_k(\overline{u_j' u_m'}\varepsilon_{ikm} + \overline{u_i' u_m'}\varepsilon_{jkm})$$

$$\varepsilon_{ij} = \frac{2}{3}\delta_{ij}(\rho\varepsilon + Y_M) \qquad (6)$$

The pressure-strain term ϕ_{ij} is modeled according to the proposals by Gibson and Launder [38], Fu et al. (see [40]), and Launder [21]. Turbulent diffusive transport term $D_{T,i,j}$ is modeled by the gradient diffusion model of Daly and Harlow (see [40]). The FLUENT manual THE FLUENT USER'S GUIDE [40] provides more details on modeling other terms.

The results for the four-leg square channel with smooth walls and the U turn tested by Wagner et al. [3] and Wagner et al. [2] was used in this study for comparison with the use of two of the four legs with one U turn. Enhanced wall treatment is used for the near wall treatment of the flow and heat transfer. For the pressure interpolation at the faces, the PRESTO scheme was chosen, which showed better results for cases where the pressure profile has a high gradient at the cell face. A uniform velocity profile is assumed at the entrance of the channel with 3% turbulence level and 70% hydraulic diameter as the length scale. At the exit, a zero normal gradient exit boundary condition is set. The density of the fluid is approximated by $\rho = \rho_o T_o / T$ to account for density variations, while piecewise linear functions were used to account for the viscosity, thermal conductivity, and specific heat properties variations.

Figure 1 shows the numerical grid generated using GAMBIT grid generator for this study. For RSM with enhanced near wall treatment y^+ for the first cell next to a wall must be of order unity. To resolve the near wall viscous region ten grid points were placed in the boundary layer near all walls. The convergence criterion for all quantities error was 10E-5 and 10E-6 for the energy equation. A grid-refinement study was performed using three different grid distributions of $40 \times 40 \times 320$, $40 \times 40 \times 420$, and $52 \times 52 \times 320$ grid points. The grid refinement in the axial direction of the bend region showed 3% maximum enhancement to the solution. A comparison between calculated and measured values of Nusselt number on the trailing surface (for Re=25,000, R_o=0.24, $\Delta\rho/\rho$ =0.13) showed a maximum of 4% enhancement in Nusselt number between $40 \times 40 \times 320$ and $52 \times 52 \times 320$ grid distribution in the U turn region. Table 1 gives the grid refinement study on the leading surface for Re=25,000, R_o=0.238, and DR=0.13. A maximum of 3% enhancement could be achieved by increasing

Table 1   Nu/Nuo on the leading surface using different grids

Grid	S/Dh 12	Diff %	S/Dh 16	Diff %	S/Dh 24	%
$40 \times 40 \times 320$	0.86	7.5	3.4	9.5	1.45	7.4
$52 \times 52 \times 320$	0.84	5.8	3.32	7	1.42	5
$40 \times 40 \times 420$	.85	6.2	3.35	8	1.43	6
Exp., Wagner et al.[a] Wagner et al.[b]	0.8	0.0	3.1	0	1.35	0

[a]Reference [2].
[b]Reference [3].

the grid points in either direction. Thus all results presented here are based on $40 \times 40 \times 320$ grid points. As a comparison, Chen et al. [36] performed a grid independent study for the same case using second moment closure. They concluded that $41 \times 41 \times 111$ grid points are adequate to resolve the whole channel.

Results and Discussion

The geometry of the two-pass channel is shown in Fig. 2. The four walls of the square duct are denoted as the leading, trailing, inner, and outer sides. All walls are heated to a constant temperature. In this study, the range of rotation numbers considered was 0.0, 0.215, 0.43, 0.86, and 1.29. Density ratios of 0.13, 0.229, and 0.4, which correspond to wall temperatures of 344, 389, and 500 K, respectively, were studied with the Reynolds number fixed to 25,000. Comparison between the calculations and measurements was performed for rotation numbers of 0.0 and 0.24 and for a coolant-to-wall density ratio ($\Delta\rho/\rho$) of 0.13. Nusselt numbers were calculated based on the average bulk temperature and normalized with a smooth tube correlation (Kays and Crawford [41]) for fully developed, nonrotating, turbulent flow

$$Nu_o = 0.0176\ Re^{0.8} \qquad (7)$$

The bulk temperature for every element was taken as the average of mass weighted average of the element inlet and outlet tempera-
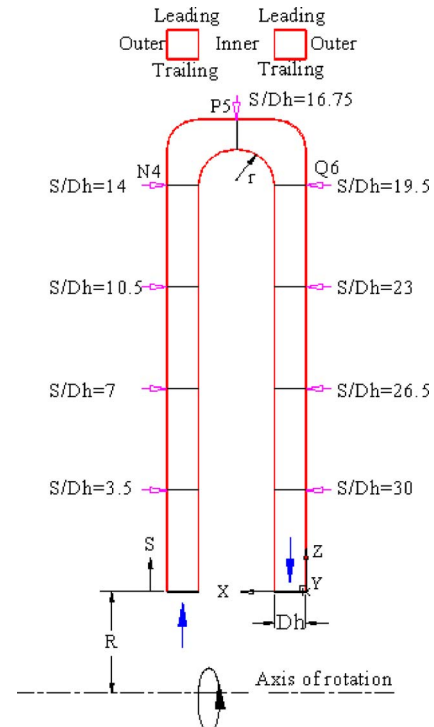

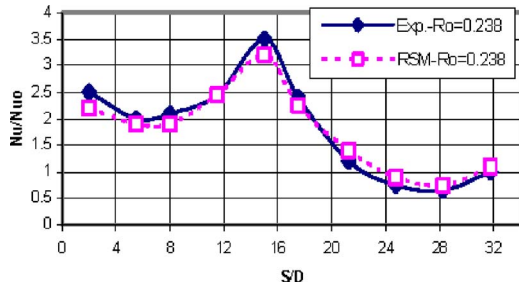**Fig. 2   Geometry for two pass square channel**

Fig. 3 Predicted and measured, Wagner et al. [3], Nusselt number ratios on the trailing surface for DR=0.13

tures. The coolant temperature is T_0 [i.e., $\theta = (T-T_0)/T_w-T_0)=0$] at the duct entrance and the wall temperature was kept constant at $T=T_w(\theta=1)$ for all sidewalls. The predicted and measured Nusselt number ratios on the trailing surface are shown in Fig. 3. They are in good agreement to within the experimental uncertainty except at the channel inlet. This is due to the difference between the experimental and assumed boundary conditions.

It is worth stating that in an unpublished study by the authors a thorough validation of predictions using RSM and enhanced near wall treatment was performed on stationary and rotating channels. The results using RSM were also compared to two-equation model predictions, where RSM coefficients were tuned to enhance

Leading side

Plane P5   Plane Q6

Fig. 4 Secondary flow vectors
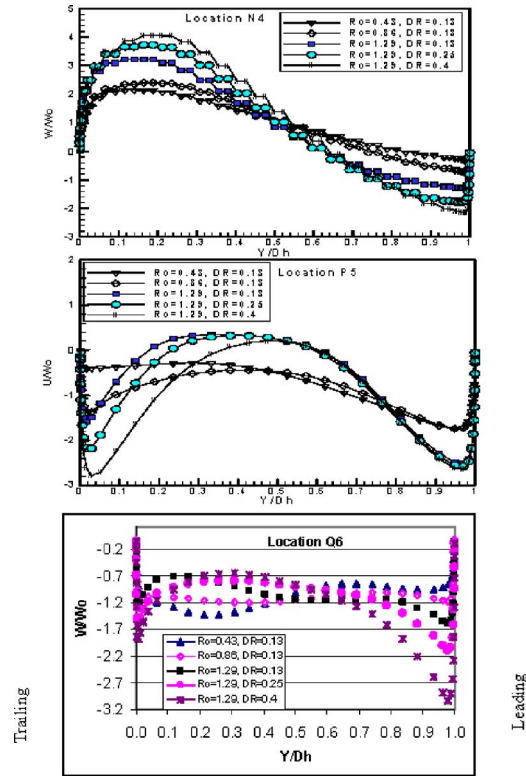
Fig. 5 Streamwise velocity profile in vertical direction

predictions. The results for Nu/Nuo presented in Fig. 3 are in better agreement with experimental measurements than the predictions by Bonhoff et al. [42] where they also used RSM in FLUENT CFD code but with wall functions. The better agreement in this study is mainly due to the enhanced near wall treatment and to the tuned coefficients in RSM. In the following discussion for all figures, note that $Y/Dh=0$ corresponds to trailing surface, $Y/Dh=1$ corresponds to leading surface, $X/Dh=0$ corresponds to outer surface at location Q6, $X/Dh=1$ corresponds to inner surface at location Q6, $X/Dh=3.5$ corresponds to inner surface at location N4, $X/Dh=4.5$ corresponds to outer surface at location N4, $Z/Dh=0$ corresponds to inner surface at location P5, and $Z/Dh=1$ corresponds to outer surface at location P5.

Secondary Flow. Figure 4 shows the secondary flow for different rotation numbers and density ratios at the center (location P5) and exit (location Q6) of the U turn. At the center of the U turn, Prandtl's secondary flow of the first kind (generated by inviscid effects) due to rotational Coriolis force is rapidly reduced because the streamwise velocity component (u) is now parallel to the angular velocity Ω. But the Coriolis force still can be produced by crossstream component (w), which results in a small vortex near the trailing-outer surface. As the fluid enters the U turn, the colder heavier fluid near the trailing surface is accelerated first then the lighter hotter fluid next, which causes the fluid to be thrown toward the outer side resulting in clockwise vortex (also predicted by Chen et al. [36] for Ro=0.24).

Prandtl's secondary flow of the second type (stress induced) due to the anisotropy of the turbulent Reynolds stresses also appeared in the leading-outer corner for Ro=0.43. Increasing rotation number, the corner vortices are suppressed and the crossstream secondary motion is govern by the Coriolis force and pressure gradient where a third small vortex appeared near the trailing-outer surfaces at Ro=1.29 due to the increase in Coriolis force. Increasing DR did not affect the structure of the vortices much. At the U-turn exit (plan Q6) three effects are interacting:

Fig. 6 Streamwise velocity profile in horizontal direction

Fig. 7 Temperature distribution

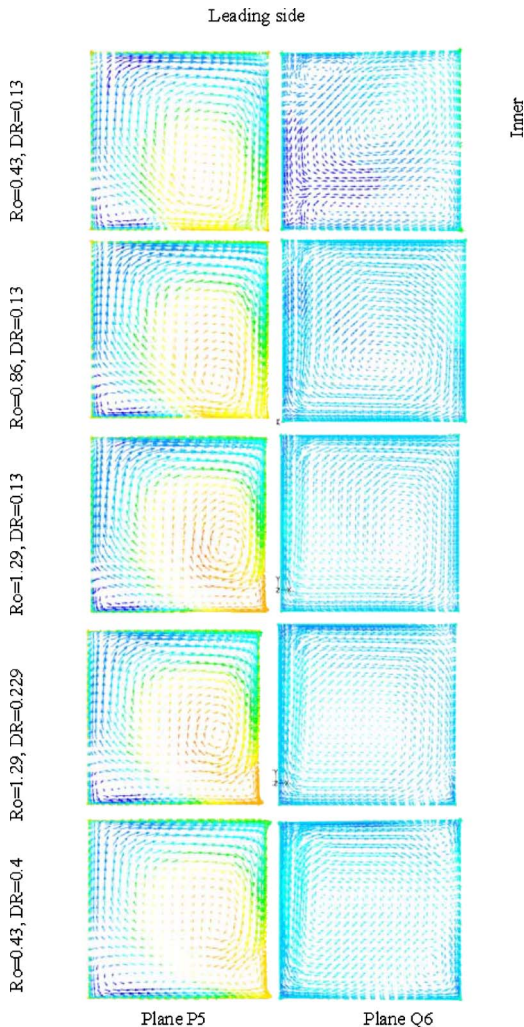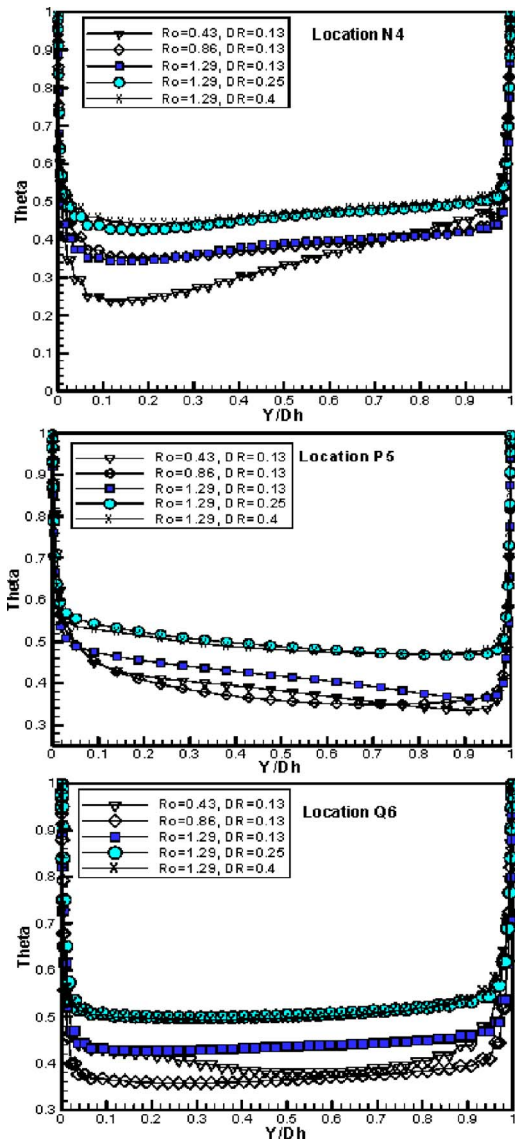the Coriolis force that pushes the cold fluid toward the leading surface, the effect of the circulation in the center of the U bend, and the buoyancy force aligned with meanstream flow. The combined effect of curvature, Coriolis, and centrifugal buoyancy forces resulted in three vortices appearance (at Ro=0.43): a large vortex near the leading, a vortex near the trailing, and a small vortex near the leading-outer sides. Increasing Ro up to 1.29, the Coriolis induced large vortex dominates, which is shifted downward, and the two small vortices are suppressed. Increasing DR to 0.229, a small vortex appears at the trailing-inner corner and a second vortex appears at the leading-inner surface as DR increased to 0.4 as a result of increasing buoyancy.

Velocity and Temperature Profiles. Figure 5 and 6 show the streamwise velocity and Fig. 7 gives the temperature distribution. At the entrance of the U turn, high Ro increases the rapid acceleration of the colder fluid near the trailing surface (increase in Nu) and the separation of the hotter fluid near the leading surface (increase in Nu), and then increasing the DR enhanced this behavior but tended to decrease Nu because the temperature difference (Tw-Tb) increases. In the horizontal direction between inner and outer surfaces the gradients in temperatures and velocities are so small. The mixing of the fluid is better than for low rotation num-

bers. At the center of the U turn, station P5, increasing Ro from 0.43 to 0.86 increases the velocity of the hotter fluid near the trailing surface rapidly, while the heavier colder fluid velocity ratio near the leading surface remained the same. Increasing Ro to 1.29 causes further increase of the velocity near both trailing and leading surfaces.

Increasing DR to 0.25 and 0.4 caused more increase in the streamwise velocity ratio near the trailing surface because the fluid is lighter, while the velocity ratio near the leading remained unchanged because the fluid is heavier and the flow separates at Ro=1.29 and DR up to 0.4. In the horizontal direction the centrifugal force and the Coriolis force due to +V velocity component are acting toward the outer surface. As a result the flow is heated uniformly having higher velocity magnitudes near the outer surface (slightly higher Nu) and separates at Dh/3 from the inner surface (slightly lower Nu) for high Ro and DR, which cause high-pressure gradients. At the exit of the U turn, where the Coriolis force is acting toward the leading surface, high Ro and DR increase the velocity of the slightly hotter fluid near the leading surface (increase in Nu), and also slightly increase the velocity (increase in Nu) near the trailing surface, and then increasing the DR enhanced this behavior but tended to decrease Nu because the temperature difference (Tw-Tb) increases. In the horizontal direction between inner and outer surfaces the variations in temperatures and velocities are so small. The mixing of the fluid is better than for low rotation numbers.
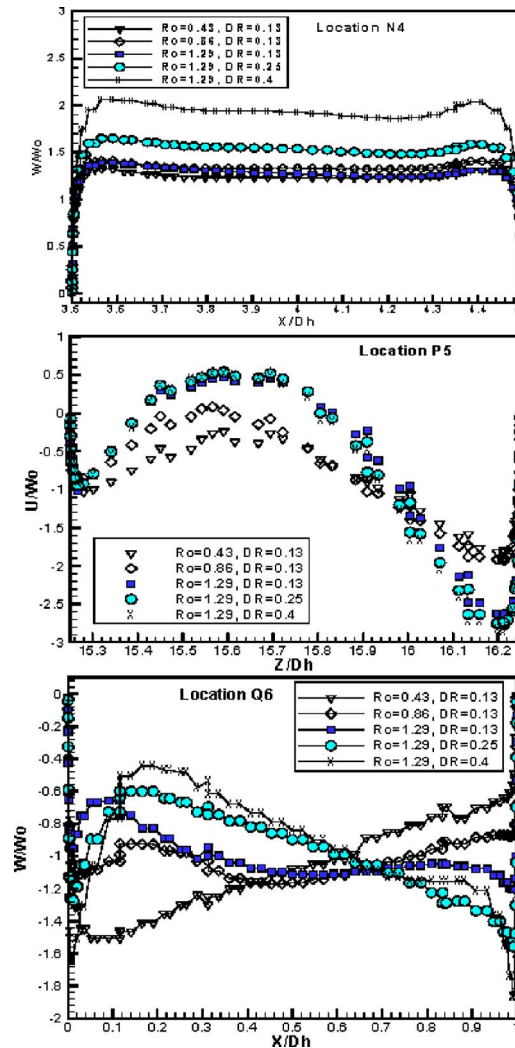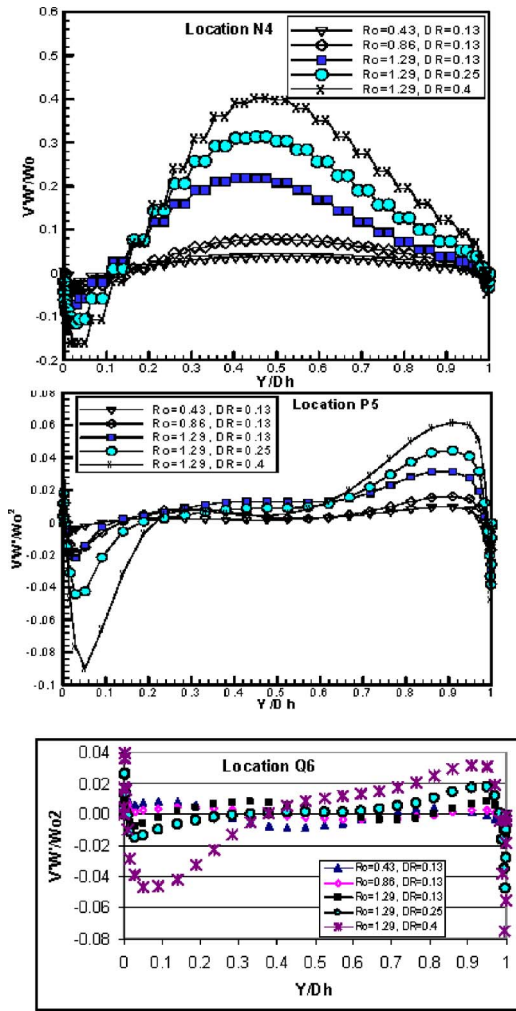
Fig. 8 Re shear stress components in vertical direction

Fig. 9 Reynolds shear stress components in horizontal direction

Reynolds Shear Stress Components. The shear stresses, $\overline{v'w'}$, are depicted in Figs. 8 and 9. At the entrance of the U turn, high rotation (strong Coriolis) and buoyancy numbers cause the increase of shear stresses near the trailing side, where an increase by a factor of 4 of that for low rotation numbers was observed at the entrance of the U turn. At the center of the U turn the curvature effect strongly attenuates the shear stress at low rotation numbers (close to zero at the center of the channel). Increasing Ro and DR caused a sharp increase in shear stress near the trailing and convex (inner) surfaces. At the U-turn exit the turbulence has been greatly damped over a large region and the higher shear stress is found near the trailing outer and with change in sign near the leading surfaces and it is increasing by increasing both DR and Ro.

Normal Reynolds Stress Components. An important measure of any turbulent flow is how intense are the turbulent fluctuations. This can be quantified in terms of the specific Reynolds stress components, $\overline{u'^2}, \overline{v'^2}$, and $\overline{w'^2}$. These three normal stresses can also be regarded as the kinetic energy per unit mass of fluctuating velocity field in the three coordinate directions. These Reynolds stresses are often normalized relative to the freestream mean-flow velocity to give the relative turbulence intensity. The normal stresses $\overline{w'^2}$ are depicted in Figs. 10 and 11. It has been observed that at the U-turn entrance, normal stresses $\overline{w'^2}$ increase by increasing Ro and density ratio by a factor of 8 at the center of the duct. The increase in turbulent intensities has a favorable effect on the heat transfer. At the center of the U turn (P5) the normal stresses $\overline{u'^2}$ are still high but less than at the entrance and the
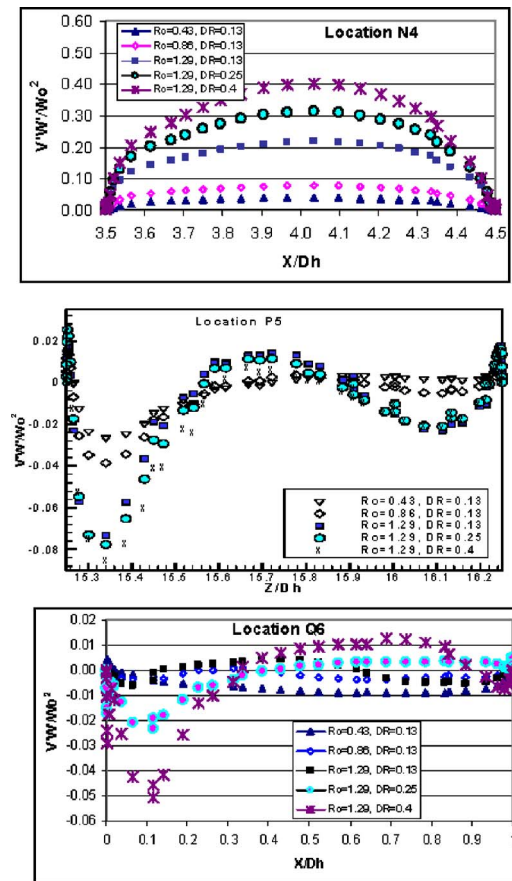
increase in normal stress favors the concave (outer) and leading surfaces. At the U-turn exit the normal stresses $\overline{w'^2}$ are much less in magnitude (turbulence decay) and higher intensities were found near the outer surface. The well-known anisotropy in the normal stresses was observed in all planes and it was shown in previous work by the authors Sleiti and Kapat [37].

Local Nusselt Number. In order to study the affect of increasing rotation number and density ratio on heat transfer distribution, the Nusselt number is calculated at nine locations on the leading and trailing, for Ro of up to 1.29 and DR of up to 0.4. Note that this approach gives a comparison between different levels of Ro and DR. Calculation of the Nusselt number is based on the mass weighted average bulk temperature at every section of the nine locations. The results are shown in Fig. 12. On the leading and trailing surfaces of the first and second passes, Nu increases with Ro and slightly increases then decreases as DR increases.

Table 2 gives the calculated Nusselt number at three locations: inlet, center, and exit of the U turn for different Ro and DRs. The results are summarized as follows:

- Leading surface: At the inlet of the U-turn location N4, the Nusselt number increases by a factor of 2 by increasing Ro from 0.43 to 1.29, then decreases slightly by increasing DR from 0.13 to 0.4. At the center (Location P5) and the exit (Location Q6) of the U turn the Nusselt number increases slightly and by a factor of 1.7, respectively, by increasing Ro, then decreases slightly by increasing DR.

- Trailing surface: At the inlet of the U-turn location N4, the Nusselt number increases by increasing Ro, then decreases slightly by increasing DR. At the center (Location P5) the Nusselt number increases by a factor of 2.4 by increasing
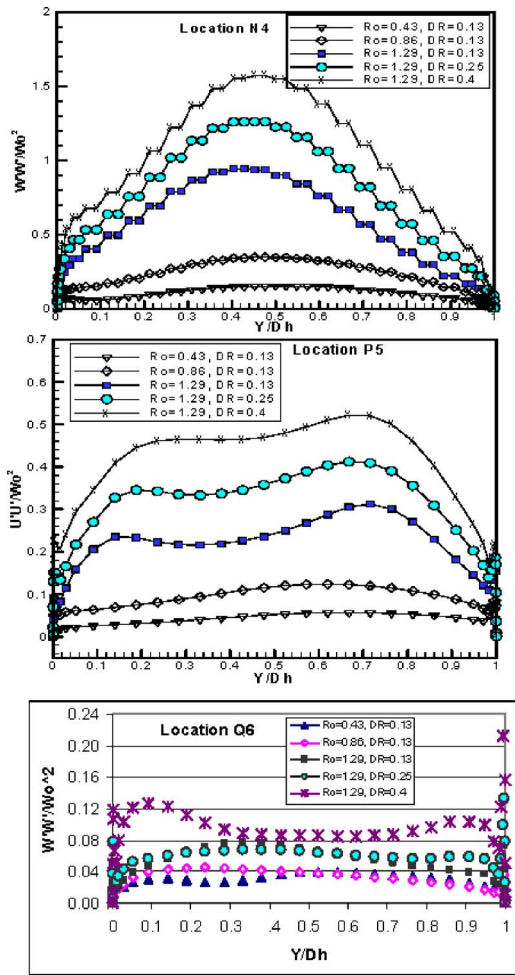
Fig. 10 Stream wise normal stress components in vertical direction

Ro, while increasing density ratio decreases the Nusselt number. At the exit (Location Q6) of the U turn, the Nusselt number increases slightly by increasing Ro and DR.

- Inner surface: At the inlet of the U turn (location N4), the Nusselt number increases by a factor of 1.6 by increasing Ro, then decreases slightly by increasing DR. At the center (Location P5) and the exit (Location Q6) of the U turn, the Nusselt number increases slightly by increasing Ro, then decreases slightly by increasing DR. This behavior is the same as on the leading surface.
- Outer surface: At the inlet of the U turn (location N4), at the center (Location P5), the Nusselt number increases by increasing Ro, then decreases slightly by increasing DR. At the exit (Location Q6) of the U turn, the Nusselt number decreases by increasing Ro, then increases slightly by increasing DR.

Average Nusselt Number. The average Nusselt number versus Ro for four surfaces (leading, trailing, outer, and inner) was calculated for the three locations and given in Fig. 13. The four-side-average Nu was calculated based on the bulk temperature at every location. It is clearly shown that Nu correlate with Ro and a linear correlation for Nu as a function of Ro is possible to derive. The increase in the average Nusselt number is more in the center than at the entrance and the exit of the U turn.

Total Pressure Drop. Figure 14 shows the mass weighted average pressure drop across the channel. In the first pass the total pressure increases as Ro increases to reach the maximum value in

the U turn, then starts to decrease in the second pass. Increasing DR decreases the total pressure as the density of the fluid is decreasing.

Conclusions

The results of a 3D numerical simulation of the flow field and heat transfer in the U bend of internal cooling channel for high rotation numbers (up to Ro=1.29) and high-density ratio (up to 0.4) show the following:
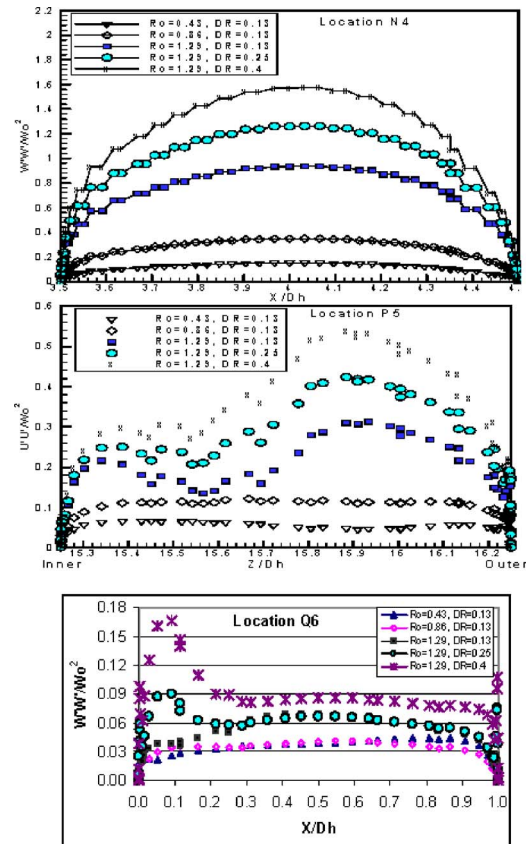
Fig. 11 W′ W′ normal stress components
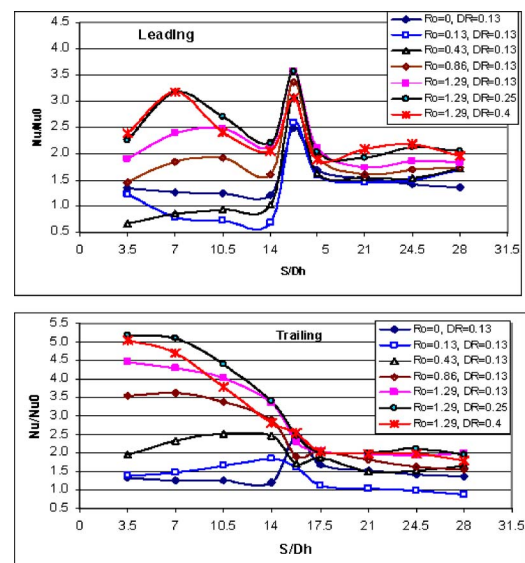
Fig. 12 Local Nusselt number ratio

Table 2 Nusselt number enhancement (Nu/No)

Location	Surface		Ro=0.43 DR=0.13	Ro=0.86 DR=0.13	Ro=1.29 DR=0.13	Ro=1.29 DR=0.25	Ro=1.29 DR=0.4
N4	Leading	$Y/Dh=1$	1.133	1.684	2.310	2.338	2.147
	Trailing	$Y/Dh=0$	2.702	2.566	3.698	3.386	2.823
	Inner	$X/Dh=3.5$	2.170	2.557	3.555	3.251	2.817
	Outer	$X/Dh=4.5$	2.153	2.507	3.423	3.102	2.716
P5	Leading	$Y/Dh=1$	3.118	3.217	3.911	3.606	3.061
	Trailing	$Y/Dh=0$	1.129	2.064	2.663	2.768	2.691
	Inner	$Z/Dh=15.25$	2.937	3.131	3.699	3.105	2.447
	Outer	$Z/Dh=16.25$	3.037	3.158	3.895	3.543	2.978
Q6	Leading	$Y/Dh=1$	1.349	1.818	2.289	2.082	1.901
	Trailing	$Y/Dh=0$	1.890	2.103	1.983	2.095	2.129
	Inner	$X/Dh=1$	2.215	2.275	2.831	2.532	2.167
	Outer	$X/Dh=0$	2.342	1.854	1.763	2.118	2.163

At the center of the U bend, increasing the rotation number, the corner vortices are suppressed and the cross-stream secondary motion is govern by the weak cross stream Coriolis force and pressure gradient where a third small vortex appeared near the trailing-outer surfaces. At the U-turn exit, the combined effect of curvature, Coriolis, and centrifugal buoyancy forces resulted in the appearance of three vortices (at Ro=0.43). Increasing Ro, the large and small vortices are suppressed, while increasing DR to 0.4, two small vortices appear at the trailing-inner and leading–inner surfaces.

High Ro increases the rapid acceleration of the colder fluid near the trailing surface (increase in Nu) and the separation of the hotter fluid near the leading surface (increase in Nu). Increasing DR causes an increase and then decrease in Nu in the first and second passages, a decrease in Nu in all surfaces of the U turn except in the trailing surface. At the center of the channel the flow separates and a severe pressure gradient is encountered.

Increasing Ro and DR caused rapid increase in shear stress and turbulence intensities mainly caused by increasing both Ro and DR. It is possible to derive linear correlation for the increase in Nu as a function of Ro.

Nomenclature

De = Dean number
DR = density ratio
D_h = hydraulicdiameter
h = heat transfer coefficient
k = thermal conductivity of coolant
Nu = local Nusselt number, hD_h/K
Nu_o = Nusselt number in fully developed turbulent nonrotating duct flow
Pr = Prandtl number
R = radius from axis of rotation
S = distance in streamwise direction
T = local coolant temperature
Re = Reynolds number, $W_o D_h/$
r = inner radius of bend
Ro = rotation number, $\Omega D_h/W_o$
T_b = coolant bulk temperature
T_o = coolant temperature at inlet
T_w = wall temperature
W_o = inlet velocity
ρ = density of air
$\Delta\rho/\rho$ = density ratio, $(T_w-T_o)/T_w$
Ω = rotational speed
θ = dimensionless temperature, $(T-T_o)/(T_w-T_o)$
μ = dynamic viscosity of coolant
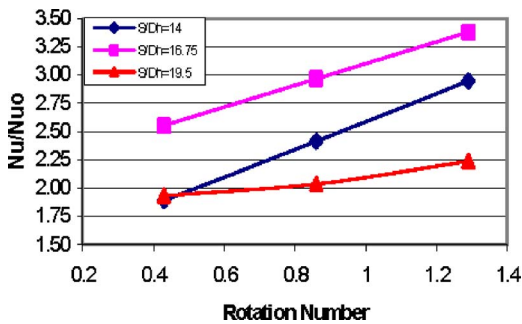
Fig. 13 Average Nusselt number for DR=0.13
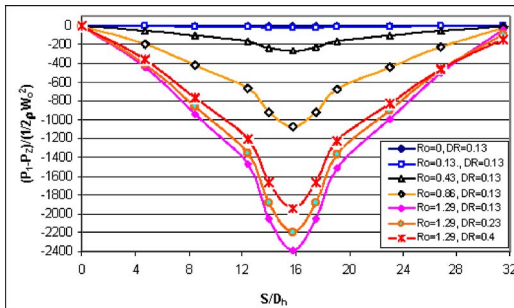
Fig. 14 Total pressure drop

References

[1] Dean, W. R., 1927, "Note on the Motion of Fluid in a Curved Pipe," Philos. Mag., **4**, pp. 4208–4223.
[2] Wagner, J. H., Johnson, B. V., and Hajek, T. 1991, "Heat Transfer in Rotating Passages With Smooth Walls and Radial Outward Flow," ASME J. Turbomach., **113**, pp. 42–51.
[3] Wagner, J. H., Johnson, B. V., and Kopper, F. C., 1991, "Heat Transfer in Rotating Serpentine Passages With Smooth Walls," ASME J. Turbomach., **113**, pp. 321–330.
[4] Johnson, B. V., Wagner, J. H., Stuber, G. D., and Yeh, F. C., 1994, "Heat Transfer in Rotating Serpentine Passages With Trips Skewed to the Flow," ASME J. Turbomach., **116**, pp. 113–123.
[5] Mochizuki, S., Takamura, J., Yamawaki, S., and Yang, W.-J., 1994, "Heat Transfer in Serpentine Flow Passages With Rotation," ASME J. Turbomach., **116**, pp. 133–140.
[6] Shih, T.-S., Liou, W. W., Shabbir, A., Yang, Z., and Zhu, J., 1995, "A New k-ε Eddy Viscosity Model for High Reynolds Number Turbulent Flows," Comput. Fluids, **24**, pp. 227–238.
[7] Cheah, S. C., Iacovides, H., Jackson, D. C., Ji, H., and Launder, B. E., 1996, "LDA Investigation of the Flow Development Through Rotating U-Duct,"

ASME J. Turbomach., **118**, pp. 590–596.

[8] Hwang, G. J., and Kuo, C. R., 1997, "Experimental Studies and Correlations of Convective Heat Transfer in a Radially Rotating Serpentine Passage," ASME J. Heat Transfer, **119**, pp. 460–466.

[9] Iacovides, H., Jackson, D. C., Kelemenis, G., Launder, B. E., and Yuan, Y. M., 1999, "Experiments on Local Heat Transfer in Rotating Square-Ended U-Bend," Int. J. Heat Fluid Flow, **20**, pp. 302–310.

[10] Liou, T. M., and Chen, C.-C., 1999, "LDV Study of Developing Flows Through a Smooth Duct With a 180 deg Straight-Corner Turn," ASME J. Turbomach., **121**, pp. 167–174.

[11] Liou, T. M., Cheng, M.-Y., and Tsai, M.-H., 2002, "Fluid Flow and Heat Transfer in a Rotating Two-Pass Square Duct With In-Line 90-deg Ribs," ASME J. Turbomach., **124**, pp. 260–268.

[12] Taslim, M. E., 1999, "45-Degree Round-Corner Rib Heat Transfer Coefficient Measurements in a Square Channel," ASME J. Turbomach., **121**, pp. 1–9.

[13] Taslim, M. E., Li, T., and Spring, S. D., 1998, "Measurements of Heat Transfer Coefficients and Friction Factors in Passages Rib-Roughened in All Walls," ASME J. Turbomach., **120**, pp. 256–570.

[14] Taslim, M. E., and Korotky, G. J., 1998, "Low-Aspect Ratio Rib Heat Transfer Coefficient Measurements in Square Channel," ASME J. Turbomach., **120**, pp. 831–838.

[15] Taslim, M. E., and Lengkong, A., 1998, "45 deg Staggered Rib Heat Transfer Coefficient Measurements in a Square Channel," ASME J. Turbomach., **120**, pp. 571–580.

[16] Taslim, M. E., 2000, "Aero-Thermal Performance of Internal Cooling Systems in Turbomachines," *VKI Lecture Series 2000-03*, von Karman Institute for Fluid Mechanics, Rhode Saint Genese, Belgium.

[17] Prandtl, L., 1929, Report NACA TM-625.

[18] Bradshaw, P., 1969, "The Analogy Between Streamline Curvature and Buoyancy in Turbulent Shear Flow," J. Fluid Mech., **36**, pp. 177–191.

[19] Launder, B. E., Priddin, C. H., and Sarma, B. I., 1977, "The Calculation of Turbulent Boundary Layers on Spinning and Curved Surfaces," ASME J. Fluids Eng., **99**, pp. 231–239.

[20] Wilcox, D. C., and Chambers, T. L., 1993, "Streamline Curvature Effects on Turbulent Boundary Layers," AIAA J., **15**, pp. 574–580.

[21] Launder, B. E., 1989, "Second-Moment Closure: Present … and Future?", Int. J. Heat Fluid Flow, **10**, pp. 282–300.

[22] Bredberg, J., 2002, "Turbulence Modelling for Internal Cooling of Gas-Turbine Blades," PhD thesis, Dept. of Thermo and Fluid Dynamics, Chalmers University of Technology, Göteborg.

[23] Hellsten, A., 1998, "Some Improvements in Menters *k*-Omega SST Turblence Model," 29th AIAA Fluid Dynamics Conference, Paper No. AIAA 98-2554.

[24] Lin, Y.-L., Shih, T. I.-P., Stephens, M. A., and Chyu, M. K., 2001, "A Numerical Study of Flow and Heat Transfer in a Smooth and a Ribbed U-Duct With and Without Rotation," ASME J. Heat Transfer, pp. 219–232.

[25] Luo, J., and Lakshminarayana, B., 1997, "Analysis of Streamline Curvature Effects on Wall-Bounded Turbulent Flows," AIAA J., **35**, pp. 1273–1279.

[26] Luo, J., and Lakshminarayana, B., 1997, "Prediction of Strongly Curved Turbulent Duct Flows With Reynolds Stress Model," AIAA J., **35**, pp. 91–98.

[27] Rumsey, C. L., Gatski, T. B., and Morrison, J. H., 2000, "Turbulence Model Predictions of Strongly Curved Flow in a U-Duct," AIAA J., **38** (8), pp. 1394–1402.

[28] Zhang, J., Zhang, B., and Ju, J., 2001, "Fluid Flow in a Rotating Curved Rectangular Duct," Int. J. Heat Fluid Flow, **22**, pp. 583–592.

[29] Besserman, D. L., and Tanrikut, S., 1991, "Comparison of Heat Transfer Measurements With Computations for Turbulent Flow Around a 180 Degree Bend," ASME Paper no.91-GT-2.

[30] Choi, Y. D., Iacovides, H., and Launder, B. E. 1989, "Numerical Computation of Turbulent Flow in a Square-Sectioned 180 deg Bend," ASME J. Fluids Eng. **111**, pp. 59–68.

[31] Iacovides, H., Launder, B. E., and Li, H.-Y., 1996, "Application of a Reflection-Free DSM to Turbulent Flow and Heat Transfer in Square-Sectioned U-Bend," Exp. Therm. Fluid Sci., **13**, pp. 419–429.

[32] Iacovides, H., Launder, B. E., and Li, H.-Y., 1996, "The Computation of Flow Development Through Stationary and Rotating U-duct of Strong Curvature," Int. J. Heat Fluid Flow, **17**, pp. 22–33.

[33] Nikas, K.-S., and Iacovides, H., 2001, "The Computation of Flow and Heat Transfer Through Square-Ended U-Bends, using Low-Reynolds Number Models," *2nd Int. Symp. on Turbulent Shear Flows Phenomena*, Stockholm, pp. 229–234.

[34] Rigby, D. L., Steinthorsson, E., and Ameri, A., 1996, "Internal Passage Heat Transfer Prediction Using Multiblock Grids and k-o Turbulence Model," ASME paper No. 97-GT-431.

[35] Bonhoff, B., Tomm, U., Johnson, B. V., and Jennions, I., 1997, "Heat Transfer Predictions for Rotating U-Shaped Coolant Channels With Skewed Ribs and With Smooth Walls," ASME paper no.97-GT-162.

[36] Chen, H. C., Jang, Y. J., and Han, J. C., 2000, "Computation of Heat Transfer in Rotating Two-Pass Square Channels by a Second-Moment Closure Model," Int. J. Heat Mass Transfer, **43**, pp. 1603–1616.

[37] Sleiti, A. K., and Kapat, J. S., 2004, "Effect of Coriolis and Centrifugal Forces on Turbulence and Transport at High Rotation and Buoyancy Numbers in Smooth Internal Cooling Channels," 42nd AIAA Aerospace Sciences Meeting and Exhibit, Reno, NV, AIAA, Reston, VA.

[38] Gibson, M. M., and Launder, B. E., 1978, "Ground Effects on Pressure Fluctuations in the Atmospheric Boundary Layer," J. Fluid Mech. **86**, pp. 491–511.

[39] Launder, B. E., Reece, G. J. and Rodi, W., 1975, "Progress in the Development of a Reynolds-Stress Turbulence Closure," J. Fluid Mech., **68** (3), pp. 537–566.

[40] *The FLUENT User's Guide, Version 6.2*, FLUENT Inc., Lebanon, NH.

[41] Kays, W. M., and Crawford, M. E., 1993, *Convective Heat and Mass Transfer*, McGraw-Hill.

[42] Bonhoff, B., Schneider, T., Johnson, B., and Jennions, I., 1997, "Prediction for Turbulent Flow in Rotating and Nonrotating Coolant Channels," *2nd Int. Symp. On Turbulence, Heat and Mass Transfer*, Delft, The Netherlands, pp. 883–892.

Fluid Dynamics and Performance of Partially and Fully Shrouded Axial Turbines

L. Porreca
e-mail: luca.porreca@ethz.ch

T. Behr

J. Schlienger

A. I. Kalfas

R. S. Abhari

Turbomachinery Laboratory,
Swiss Federal Institute of Technology,
8092 Zurich, Switzerland

J. Ehrhard
ALSTOM Switzerland Ltd.

E. Janke
Rolls Royce Deutschland

A unique comparative experimental and numerical investigation carried out on two test cases with shroud configurations, differing only in the labyrinth seal path, is presented in this paper. The blade geometry and tip clearance are identical in the two test cases. The geometries under investigation are representative of an axial turbine with a full and partial shroud, respectively. Global performance and flow field data were acquired and analyzed. Computational simulations were carried out to complement the investigation and to facilitate the analysis of the steady and unsteady flow measurements. A detailed comparison between the two test cases is presented in terms of flow field analysis and performance evaluation. The analysis focuses on the flow effects reflected on the overall performance in a multi-stage environment. Strong interaction between the cavity flow and the blade tip region of the rotor blades is observed up to the blade midspan. A marked effect of this interaction can be seen in the downstream second stator where different vortex structures are observed. Moreover, in the partial shroud test case, a strong tip leakage vortex is developed from the first rotor and transported through the downstream blade row. A measurable change in the second stage efficiency was observed between the two test cases. In low aspect ratio blades within a multi-stage environment, small changes in the cavity geometry can have a significant effect on the mainstream flow. The present analysis has shown that an integrated and matched blade-shroud aerodynamic design has to be adopted to reach optimal performances. The additional losses resulting from small variations of the sealing geometry could result in a gain of up to one point in the overall stage efficiency. [DOI: 10.1115/1.2008972]

Introduction

Modern turbomachinery designs aim to increase blade loading and pressure ratio while maintaining the same high efficiency level. This results in a higher power density and lower part count and therefore lower cost. In this perspective, secondary flows and the interactions between leakage and mainstream flow contribute considerably to the overall turbine losses. Particularly, for low aspect ratio blading, it has been shown [1,2] that the flow is highly three dimensional and the secondary effects are often dominant in the overall loss mechanism.

Leakage flows between rotating and stationary parts are commonly reduced with sealing devices such as shrouds and labyrinth seal paths. By lowering the mass flow through the labyrinth seal, a greater proportion of the total flow remains available for work extraction within the blade rows. Labyrinth leakages may account for up to 30% of the total aerodynamic losses in a turbine stage.

Wallis et al. [3] identified four entropy generation mechanisms in the leakage process: fluid entering into the shroud cavity, mixing in the clearance downstream of the fin, mixing with the mainstream flow and non-ideal incidence in the downstream stator row. In their investigation, the aim was to reduce the mixing losses by inserting turning devices into the labyrinth cavity to match the yaw angle of the main stream. However, the experiments showed that the overall efficiency dropped with respect to the reference configuration due to the poor performance of the turning devices.

Peters et al. [4] and Anker and Mayer [5] performed experimental and numerical investigations in a 1 and a half stage low speed axial turbine. They observed a significant incidence variation in the second stator acted by the leakage flow increasing with the clearance height. Morphis and Bindon [6] reported on an investigation of a one and a half stage axial turbine with unshrouded rotor blades. A reduction of the secondary flows in the second stator was observed due to the tip leakage flow.

Hunter and Manwaring [7] reported a detailed investigation on the effect of the hub leakage in the secondary flow structures of the downstream rotor and stator rows. An upward radial migration of the secondary flow at the hub of the first rotor was detected. Significant changes were observed in the flow field even in this high aspect ratio blading. Some studies focused also on axial compressor leakage influence in the main stream [8,9].

An emerging goal for modern designs is the accurate matching between the cavity flow and the main stream. Integrated blade-cavity-shroud design is instrumental in optimizing aerodynamic performances.

In this work, an analytical study is carried out attempting to isolate the effect of geometrical variations to the flow field and the aerodynamic performance using two test cases, where only the labyrinth seal geometry was changed while the blade geometry and the tip clearance were kept unchanged.

The first test case (PS) is representative of a partial shroud configuration. The second test case (FS) has a classical full shroud arrangement. Global performance is discussed in combination with the associated flow field including an unsteady data analysis for the partial shroud test case (PS). In fact, full shrouds increase the weight at the highest radius leading to increased stresses which rapidly approach the structural limits of the blades and disks. In some cases, mechanical integrity considerations call for a reduction of the shroud weight. Partial shroud designs are therefore used in an attempt to benefit from the advantages of shrouded configurations as well as enjoying reduced weight.

Copyright © 2005 by ASME
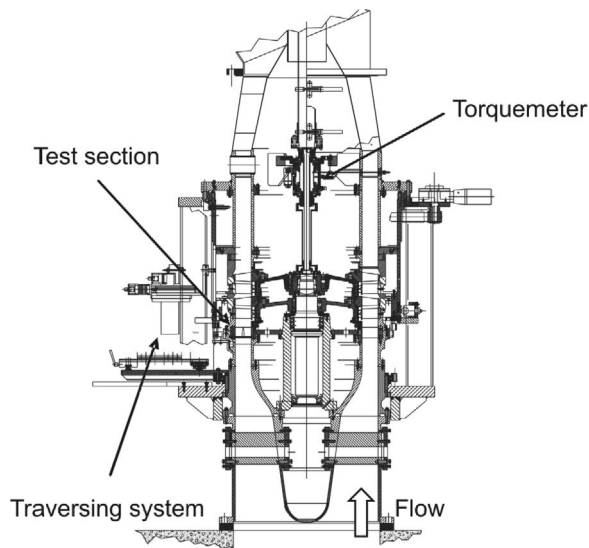
Fig. 1 "LISA" Two stages axial turbine facility

Fig. 2 Schematic of the shroud configuration: (a) partial shroud, (b) full shroud

Experimental Method

Research Facility. The experimental investigation was performed in the research turbine "LISA" at the Turbomachinery Laboratory of the Swiss Federal Institute of Technology Zurich (ETH Zurich). The facility can accommodate a maximum of two stages of an axial turbine. The air loop is of a closed type and includes a radial compressor, a two-stage water to air heat exchanger and a calibrated venturi nozzle for accurate mass flow measurements. A dc generator absorbs the turbine power and controls the rotational speed of the turbine shaft. The first and the second rotor are mechanically decoupled by a twin spool shaft design. The second stage torque is measured by a calibrated torquemeter. In order to achieve the same rotational speed, both shafts are coupled again before the dc generator. A cross section of the turbine is shown in Fig. 1.

The turbine design allows quick and precise assembly and an easy access to the measurement planes. A number of different intrusive and non-intrusive measurement techniques can be applied. The facility is equipped with a four-axis numerically controlled positioning system with ultrahigh precision in every direction. The turbine is normally operated at constant pressure difference across the stages. The turbine entry temperature is controlled to an accuracy of 0.3% and the rpm is kept constant by the dc generator with a range of ±0.02% (±0.5 rpm). In a typical measurement day, the pressure drop is stable within 0.3%. More details regarding the research facility are available in Schlienger [10]. The main operational parameters of the facility are listed in Table 1.

The variation of the labyrinth seal path has been applied to both stages of the two test cases. The partial shroud test case (PS) has two vertical fins and a shroud platform with cutbacks at leading and trailing edges. Conversely, the FS test case adopts an axisym-

metric shroud representative of a modern full-shroud design adapted to the geometrical constraints of the parallel annulus of the facility. The blade geometry as well as the tip clearance of 1% of the blade span is equal for both test cases. A schematic of the shroud configurations is shown in Fig. 2.

Main features of engine-like leakage flows are accounted for, including smooth geometry downstream of the shroud for simulating the reentry and mixing between the leakage and the mainflow streams.

Measurement Technology. Flow parameters including total and static pressure, flow angles velocity components and Mach number are measured at frequencies up to 40 kHz. The steady flow field is measured with miniature five hole probe with a tip diameter as small as 0.9 mm (Treiber et al. [11]). The mainstream flow field is measured using a 1.8 mm tip diameter single sensor fast response aerodynamic probe (FRAP) in virtual multi-sensor mode providing time resolved information (Kupferschmied et al. [12]). FRAP probe technology also provides unsteady temperature measurements at very low frequency (up to 10 Hz). The absolute uncertainties of the used probe techniques are listed in Table 2 (Schlienger et al. [13]).

The FRAP probe used in the investigation misses the third component (pitch) of the flow due to the virtual three-sensor mode. For large pitch angle (±4 deg), an increased error of static, total pressure and Mach number occurs. Temperature measurements obtained with FRAP are affected by an absolute uncertainty of the order of ±0.3 K.

The steady and unsteady turbine flow field has been measured in three planes at the exit of the first rotor, second stator and second rotor, namely A1, A2 and A3 (Fig. 3). The measurement mesh comprises a total of 690 points distributed uniformly in the circumferential direction every 5% pitch (23 points in 1.1 pitches) and 30 points in the radial direction, clustered towards the end walls. Additionally, the second stator steady static pressure distribution was acquired at different blade span as well as the static pressure distribution on both rotor outer casings.

Numerical Method

The simulations were performed using the commercial flow solver FLUENT 6.1, which is based on an unstructured finite volume scheme. Stage coupling is based on the mixing plane tech-

Table 1 Main parameter of "LISA" two-stages axial turbine research facility

Rotor speed [rpm]	2625
Overall pressure ratio	1.38
Mass flow [kg/s]	10.65
Blade count (stator/rotor)	42/42
Aspect ratio	1.8
Outer tip diameter [m]	0.8
Mach number (stator/rotor)	0.35/0.1
Reynolds number (Rotor)	$2*10^5$

Table 2 Uncertainty bandwidth of the used probes

Probe type	ϕ	β	Pt	Ps	Ma
5HP	0.3°	0.3°	60 Pa	130 Pa	0.4%
2D FRAP	0.3°	⋯	100 Pa*	150 Pa*	0.4%*

(* for flow pitch angle $<\pm4°$)

Fig. 3 Turbine traversing probe planes

Fig. 5 Mass averaged yaw angles at the exit of the first rotor–plane A1–(*a*) absolute, (*b*) relative
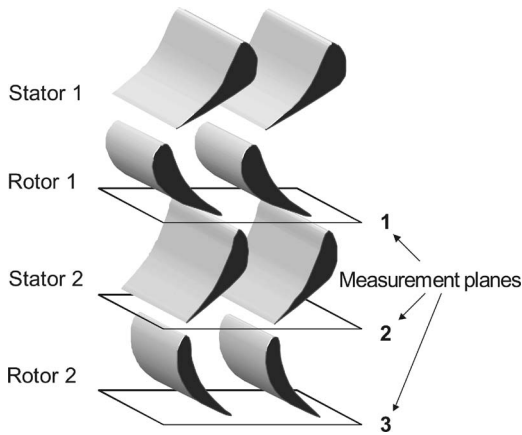
nique, i.e., each fluid zone is solved as a steady-state problem and at prescribed iteration intervals; the flow data at the mixing plane interface are averaged in circumferential direction on both interface boundaries.

The flow was assumed to be fully turbulent and turbulence closure was achieved using the Spalart-Allmaras turbulence model [14], which solves a transport equation for a quantity that is a modified form of the turbulent kinematic viscosity.

To facilitate efficient meshing of the non-axisymmetric partial shroud geometry and to reduce the turn-around time for grid generation, unstructured meshes covering both the main flow path and the tip leakage paths were chosen for both geometries. Following the hybrid meshing strategy of the commercial grid generator CENTAUR, prismatic elements were applied in regions of high solution gradients, and tetrahedra were used elsewhere with pyramids used in some locations to allow for a transition between the prisms and the tetrahedra. The total number of elements for both geometries is about 2.7 million, resulting in an average non-dimensional wall distance $y+$ of 13 and a maximum $y+$ of 49. Figure 4 shows a meridional view of the mesh around to the first rotor shroud for the partial and the full shroud test cases.

Each tip gap was resolved by 25–30 elements in radial direction. Measured total pressure, total temperature and flow angle distributions were prescribed at the inlet to the computational domain. The inlet turbulence intensity of 2% and a turbulent length scale of 0.1 m was chosen to reflect the flow conditions of the test
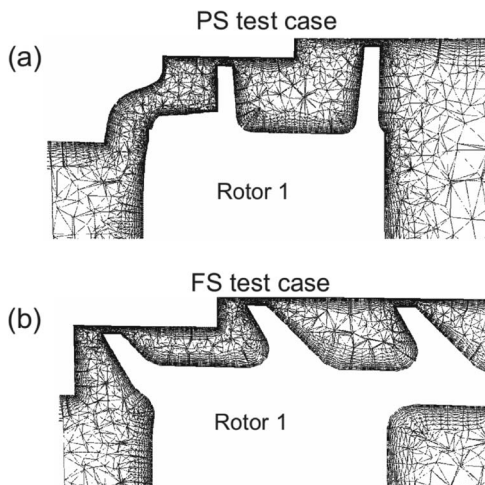

Fig. 4 Spatial discretization in the labyrinth path (*a*) partial shroud, (*b*) full shroud
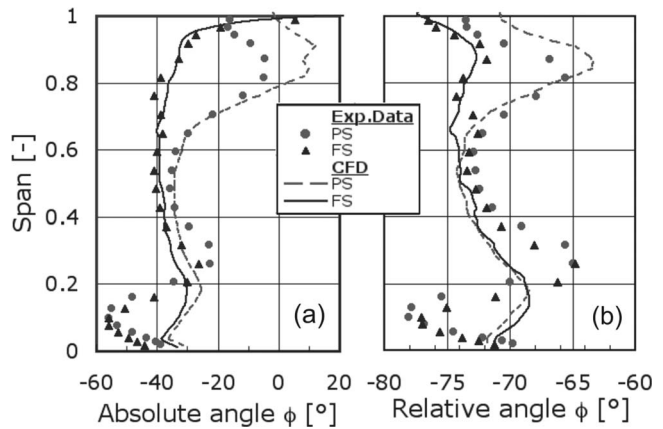
facility. A reference static pressure at hub exit and the radial equilibrium condition were prescribed at the outlet. All walls were assumed to be adiabatic.

Results and Discussion

The experiments were performed keeping the facility at constant pressure drop across the turbine and constant rotational speed. During a preliminary performance analysis, differences in the turbine operational point were observed between the two test cases. A 3% higher mass flow was experienced in the PS. The torque and power measured on the second stage were larger as much as 2%. This result can be explained taking into account reduced end wall coverage of the partial shroud platform in addition to the smaller number of sealing fins. As a consequence, the area available to the fluid is relatively larger at the tip region leading to a variation of the throttling characteristics of the turbine stage. This may have consequences reflected on the work extraction rate and hence to the overall turbine pressure drop at constant mass flow.

The work is presented with the following structure: Steady flow analysis is presented on both test cases comparing measured and predicted data. Additionally, experimental unsteady analysis is performed on the partial shroud (PS) case. Finally a performance comparison and a discussion of the results complete the investigation.

Steady Flow Field Analysis

First Rotor Exit-Plane A1. Leakage flow downstream of the first rotor still retains a large amount of the momentum of the upstream stator as shown in previous investigations (e.g., [3,7]). Therefore, a common design intention is to align this undeflected flow with the main stream in order to reduce the production of entropy in the mixing process. Figure 4 shows the mass averaged absolute and relative yaw angle downstream the first rotor of the two test cases. The flow has the same features until midspan. Closer to the tip in the PS test case, the measured data show that the fluid is underturned from approximately 60% span to the tip.

In this case, a vortex of considerable strength develops due to the trailing edge cut back of the shroud. The principal characteristics of this feature are similar to a tip leakage vortex. This behavior is detected by the overturning-underturning behavior (of the order 10 deg) from the tip to 80% span. In the absence of the shroud platform, the resulting tip gap at the end of the blade channel is of the order of the 10% of the blade span. Hence, the flow is easily moving over the blade tip from the pressure side to the suction side and generating the tip vortex. This feature results in a marked underloading of the rotor blade from approximately 60% to 100% span (Fig. 5).
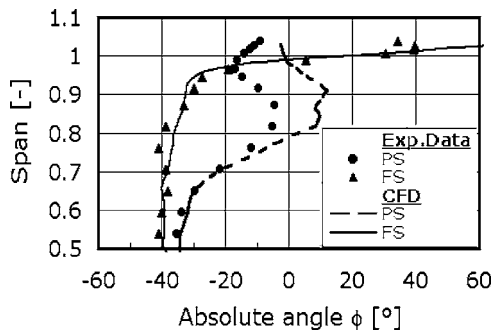
Fig. 6 Absolute mass averaged yaw angles from midspan up to the cavity at the exit of the first rotor–plane A1

Fig. 8 Measured static pressure distribution on the second stator: (*a*) 75%, (*b*) 90% span

Remaining swirl is observed at the tip region of the partial shroud test case (PS), therefore the design intention to align the cavity flow with the main stream is only partly achieved in this case. In the full shroud case (FS), the absolute flow angle remains almost constant past 90% span. The flow is appropriately turned and the blading is fully loaded until this point. Closer to the tip region (from 90% to 100% span), the flow is underturned aiming to align to the cavity flow as indicated in Fig. 6.

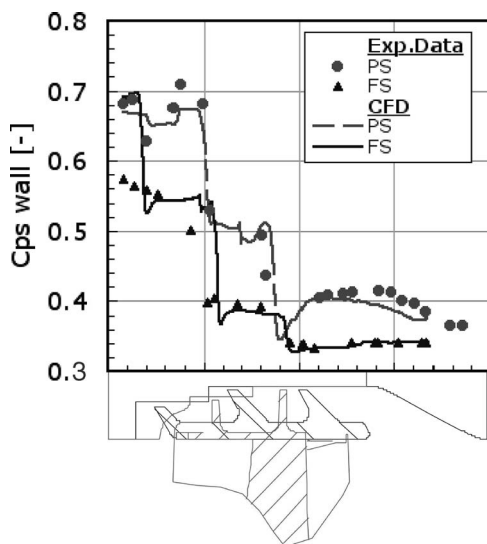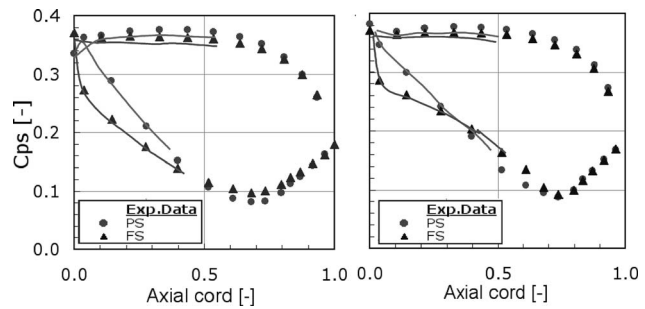In both cases a secondary flow structure is detected in the hub region. Previous investigations complementary to the present work [13,15], have shown that the development of the hub passage vortex is greatly affected by the reentry of the labyrinth leakage flow of the upstream stator hub shroud.

Computational fluid dynamics (CFD) calculations show a good agreement with the measured data at midspan. The difference between computed and measured yaw angle in this region is limited in the range of ±0.5° both in the absolute and in the relative frame. At the tip, calculations can correctly predict the yaw angle variation up to the cavity for the FS test case. In the PS geometry, the tip underloading is overestimated by approximately 10°. The underturning-overturning behavior at the hub region is not predicted. This is expected due to the fact that the stator hub leakage flow is not modeled in the CFD calculations. The vortical structures in this location are resulting from the interaction between leakage from the stator cavity and hub rotor passage vortex.

The larger cavity of the PS test case at the exit of the first rotor produces a strong leakage flow interaction with the main stream. Figure 7 shows the static pressure distribution which has been

measured on the outer casing over the rotor. In the PS case, the leakage flow is first expanded in the cavity (slight deceleration in region A) and then accelerated back into the main flow further downstream showing a decreased pressure (region B). The pressure distribution in the end wall outer casing of the second rotor (not shown here) reveals the similar flow features. The leakage flow experiences over both rotor casings the same expansion and re-acceleration together with the mainstream fluid. In the full shroud case (FS), having a smaller cavity, static pressure remains almost constant. Deceleration and acceleration of the leakage jet are not detected other than a low expansion to the downstream static conditions signifying relatively low local mixing. The CFD results confirm this tendency and they agree well with the measurements. The resultant flow is entrained back into the main stream impinging on the downstream leading edge of the stator leading edge. This process affects the incidence angle on the downstream stator leading edge and thereby the loading and the associate stator losses, being reflected on the overall stage performance. These effects are further discussed in the following sections of the present study.

Profile static pressure distribution (Fig. 8) across the stator blades shows a typical negative incidence behavior in the PS test case. This is the effect of the underloading of the PS tip rotor blade region and the incoming of the jet leakage. The incidence variation for the PS case with respect to the design blade angle is of the order of 22 deg and 14 deg at 75% and 90% span, respectively. Therefore, the stagnation point is shifted on the suction side causing a localized pressure increase. This leads to a greater radial pressure gradient from the tip to the hub of the passage with respect to the FS case. The same incidence variation and radial pressure gradient increase was also detected in previous experimental and numerical investigation in a multi-stage environment (Peters et al. [4], Anker and Mayer [5], Gier et al. [16]). However, in those studies this behavior was observed with increased tip clearances while keeping the labyrinth path unchanged.

Mach number and flow angles derived from five-hole-probe (5HP) data combined with static temperature measured by FRAP allow to compute the mass flow. The radial distribution at the exit of the first rotor is presented in Fig. 9(*a*). Both test cases show very similar profile up to 70% span. Further upstream in the radial direction, the PS case shows increased values between 0.7 and 0.9 span. The leakage mass flow (above 100% span) is, as well, slightly larger. The integrated flow profile shows a difference between the test cases of 4%, consistent with the mass flow measured by the more accurate venturi (3.1%) for the same pressure drop across the turbine.

From the five-hole-probe (5HP) measurements, pitch angle is derived (Fig. 9(*b*)). In the PS case, the tip leakage penetration into the main flow is clearly shown. From 80% span to the blade tip, negative pitch angles up to −25 deg are measured. In the FS case, pitch angle is almost constant until the blade tip. Negative angle is only detected in the cavity.

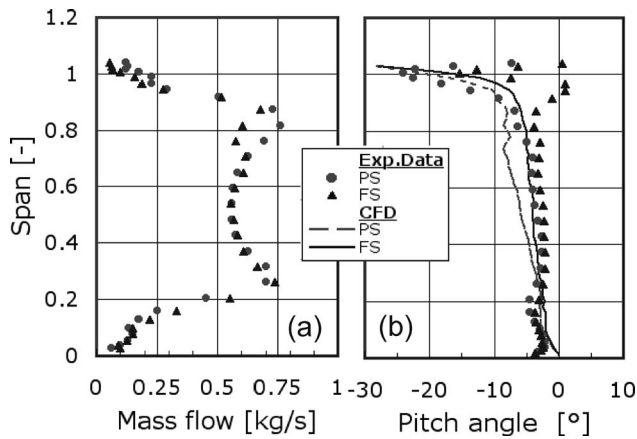Total and relative pressure measurements at the exit of the first

Fig. 7 End wall static pressure coefficient over the first rotor outer casing

Fig. 9 (*a*) **Mass flow distribution,** (*b*) **mass averaged pitch angle at exit of the first rotor–Plane A1**

Fig. 11 Mass averaged (*a*) **total pressure coefficient** (*b*) **yaw angle at the exit of the second stator—Plane A2**

rotor are presented in Fig. 10. Marked differences between PS and FS are detected from 60% span to the tip. In the relative frame of reference, the flow in the PS case shows higher total pressure reduction. This is associated with the strong leakage vortex over the tip at the trailing edge cutback and the larger relative clearance. In the FS case, the reduction of *Cpt* in both absolute and relative frame at 90%–100% span is most likely due to the wake generated by the shroud platform trailing edge rim. CFD calculations predict appropriately the total pressure coefficient in the relative frame and qualitatively in the absolute frame. At midspan, the difference between calculation and measurements are of the order of 2%. However, larger departures are noted at the hub because the hub leakage is not modeled in the computations.

Although at first sight, aerodynamic considerations tend to favor the choice of a full shroud arrangement, the ultimate designers choice is based on the overall performance as well as other competing mechanical integrity issues. In the present analysis, the aerodynamic effects on each individual blade row are assessed, before building the overall performance picture.

Second Stator Exit–Plane A2. The flow detected at the exit of the first rotor is significantly affecting the aerodynamic performance at the exit of the second stator. The flow is similar for both test cases from hub up to midspan. At the hub, the passage vortex is established with typical overturnig-underturning behavior. Further up in the radial direction, a marked underturning-overturning behavior is observed at 70% of the span in the full shroud test case (FS). This feature is caused by the cavity flow from the first rotor
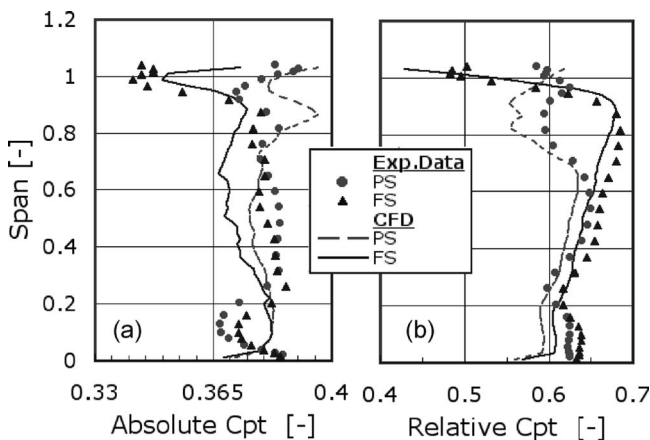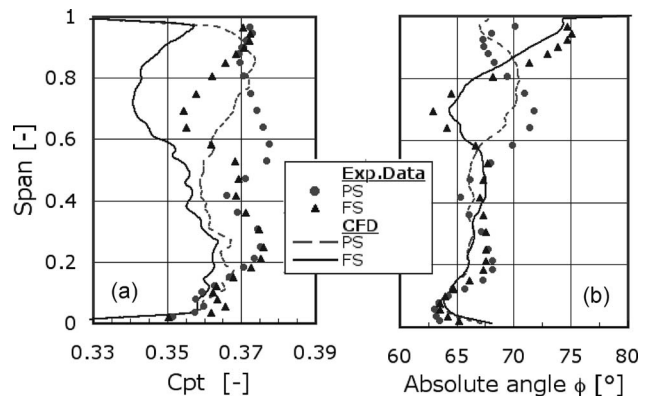
that is accelerated by the reentry channel in the main stream and rolled up with the tip passage vortex (Fig. 11). This vortical structure (named D+E) can be observed in the vector plot in Fig. 12(*b*). In the PS case, the turning acted by the stator row at the tip is reduced as much as 25% with respect to the FS case, having the inlet stator angle a negative incidence. Consequently the overturning-underturning of the tip passage vortex is decreased and observed at 90% span. In the FS case, the variation between underturning and the overturning occurring from 60% up to 100% span is of the order of 25 deg. On the other hand, the same variation in the PS case (observed between 70% and 100% span) is of the order of 10 deg. Moreover, a substantial overall *Cpt* reduction in the PS case appears in the pitch-wise profile in Fig. 11 between mid and 85% span. It can therefore be concluded that the losses associated with this vortex structure are reduced in the PS case.

The strong leakage vortex over the tip at the trailing edge cutback of the rotor tip (PS case) is convected downstream through the second stator. Due to the stronger radial pressure gradient compared to the FS case generated by the negative incidence, the vortex migrates radially towards the hub and detected at midspan at the stator exit, showing the overturning-underturning in Fig. 11(*b*) and the feature named D in Fig. 12(*b*).

The CFD prediction agrees well with the measurements of the yaw angle at midspan (Fig. 11). The prediction is in the range of ±1 deg from 30% to 50% span. Overturning-underturning is also captured at the hub as well as at the tip in both test cases within ±2 deg. The total pressure profile is underestimated except from the hub region. At midspan, the computed *Cpt* is 4% lower compared to the measured data. The higher overall *Cpt* of the PS is predicted but only qualitatively.

Figure 12 shows the steady total pressure coefficient downstream of the second stator together with the secondary flow vectors. Vortex structures are very similar for both test cases up to 40% span. The trailing edge wake is identified in both cases at approximately −20% blade pitch. Structure A is the hub passage vortex that contributes to the total pressure reduction in this region. Structures B and C are related to the blade row and leakage interactions as well as convected secondary flow features and vorticity shedding. In the PS test case, a strong vortex is identified at midspan (C). This structure is thought to be the leakage vortex originating from the first rotor. In the full shroud test case (FS), the moderate leakage vortex is rolled up in the passage vortex and identified in the structure E. The total pressure drop associated with this structure is larger with respect to the PS as previously discussed. This information may be insufficient to draw concrete conclusions about the blading loss generation in this multistage environment. Therefore, unsteady measurements of temperature and pressure derived from the FRAP probe are used. High frequency pressure and low frequency temperature signal are time averaged and combined providing steady entropy information.
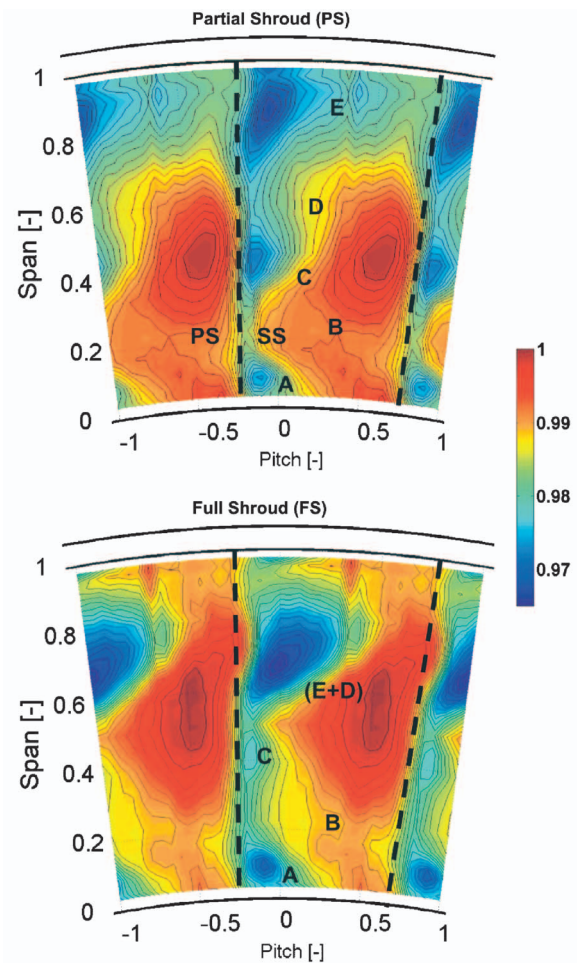

Fig. 10 Mass averaged total pressure coefficient at exit of the first rotor–Plane A1–(*a*) **absolute,** (*b*) **relative**
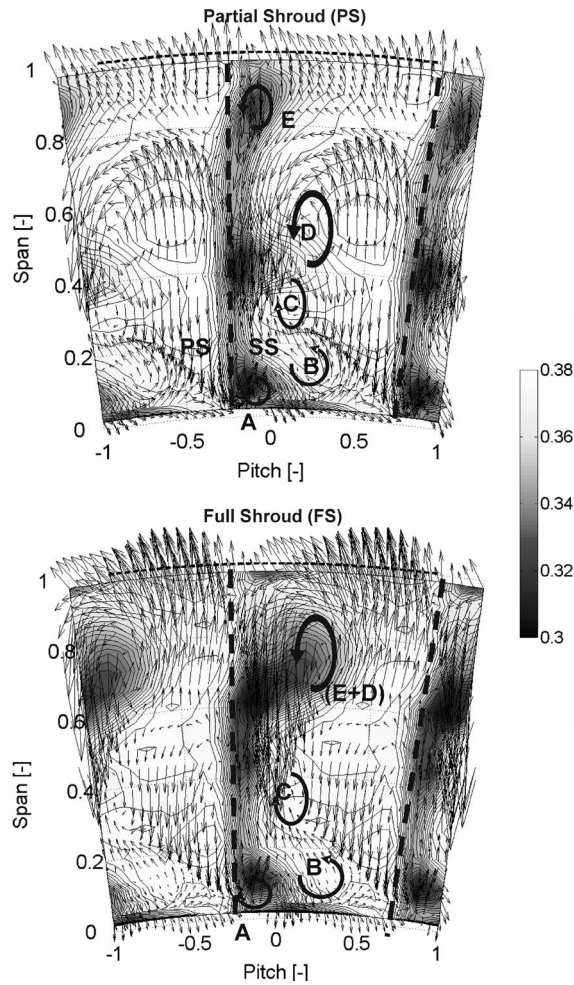
Fig. 12 Measured total pressure coefficient and secondary flow vector plot downstream of the second stator–Plane A2–(*a*) PS test case, (*b*) FS test case

Fig. 13 Measured entropy function downstream of the second stator—Plane A2—(*a*) PS test case (*b*) FS test case

Entropy evaluation is presented in Fig. 13. The entropy function is defined as $\exp(-\Delta s/R)$, where Δs is derived by the total pressure and total temperature measurements [17].

The reference values are taken in the same plane and selected in order to achieve $e=1$ (no losses), in the minimum entropy value. The various loss cores discussed earlier through the total pressure coefficient plots can be observed in these plots. They can be associated with the vortex structures detected in Fig. 12. As previously discussed, the magnitude of this loss in the passage vortex cores is increased in the FS due to the higher turning. In the PS test case, the strong vortex associate with the trailing edge cut back of the first rotor is creating relatively large losses at a lower radial position. In the partial shroud test case, the entropy function at midspan appears intensified. It is also interesting to notice that the area affected by the high entropy at the tip is quite extended compared to the full shroud case. This behavior cannot be fully appreciated by the total pressure coefficient and may be explained taking into account that the total pressure coefficient does not include any information about the temperature of the fluid.

Close inspection of Figs. 12 and 13 reveals that three of the vortical structures (A, C and E) are associated with intense and localized increased loss generation. The loss levels associated with the other two features (B and D) are relatively lower and diffused raising the background level of entropy.

At lower half of the span including the hub, both test cases show the same picture in terms of both loss and vortically moving fluid. However, in the top part of the plot, it can be noticed that there is a radial migration of lossy fluid induced by the strong interactions between the vortices and the radial pressure gradient variation. This affects the way that vorticity is shed from the trailing edge in the two cases. The intensity of loss generation in the midspan is therefore affected by the process of tip vortex formation.

In the FS test case, the tip vortex is strong and dominant covering the area between 60% and 80% span. In the PS test case, a combination of effects, as described earlier, pushes the initially generated vortex inward with two consequences. First, the midspan region is dominated by a double formation of counter rotating vortices that invokes compressing forces on the wake fluid, resulting in increased localized loss production. Second, the radial migration of the initial tip vortex gives space for the development of the loss core due to the indigenous passage vortex of the second stator (E in Fig. 12(*a*)). The latter vortical structure has strong similarities to a tip leakage vortex with the associate consequence to additional loss generation.

Unsteady Flow Field Analysis of the PS Test Case.

Unsteady Analysis—First Rotor Exit—Plane A1. Figure 14 shows the measured pitchwise mass-averaged variation of the yaw angle as a function of the blade span and the blade passing period. The maxima and the minima of the flow angle together with the relative angle change are also displayed.

The steady measurements derived from the 5HP data are presented superimposed to the angle variation, In the entire span, the steady value is in between the minima and the maxima of the
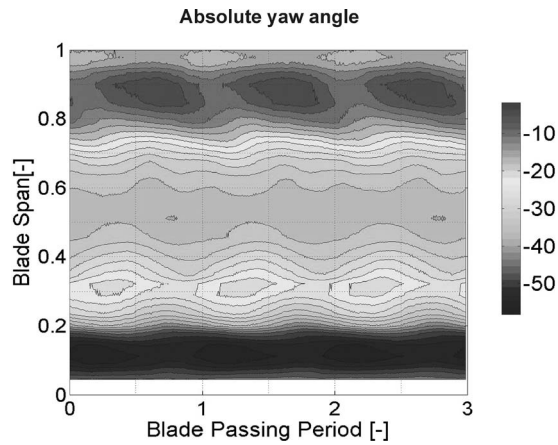
Fig. 14 Experimental time-distance diagram of the mass-averaged absolute yaw angle at the exit of the first rotor in three blade passing period (PS test case)—Plane A1

unsteady measurements, highlighting the accuracy and consistency of the data set derived from the two independent measurement techniques. The overturning-underturning is clearly observed from 10% to 30% span. At the tip region, yaw angles up to -10 deg underline the rotor underloading. The variation of the angle has the same period of the blade passing. This is the result of the variable position of the rotor relative to the downstream stator row. This blade phase results in a sinusoidal variation of the throttling rate of the turbine. From Fig. 14 can be observed that the angle variation is of the order of 8 deg from 20% to 35% span. This is the mark of the passage vortex detected at hub. The large yaw angle variation at 90% span (up to 7 deg) in Fig. 15 and the relative Cpt reduction at the same span (Fig. 16) is consistent with the behavior of the tip leakage vortex. At midspan, where secondary flows are less evident, the angle variation is significantly reduced being of the order of 2 deg.

The development of a double vortex structure is observed at the hub in Fig. 16. As shown in parallel clocking investigation (Behr et al. [18]) this behavior might be related to structures originated in the first stator row and transported through the rotor blade channel. The study also reveals that these features are dependent from the first stator index position with respect to the second stator. The wake seen at $T/T_0=0$ in Fig. 16 is significantly reduced due to the effect of the relative position of the downstream stator. From time $T/T_0=0.5$ to $T/T_0=0.833$, the total pressure reduction due to the wake is overtaken by the pressure rise due to
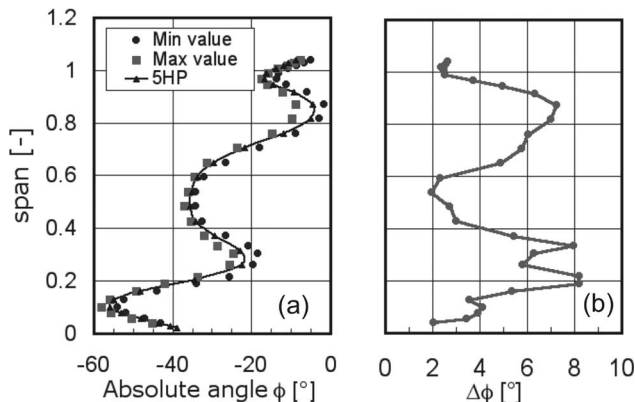
Fig. 15 Experimental mass-averaged yaw angle variation in three blade passing period at the exit of the first rotor. (PS test case)–Plane A1—(a) minimum and maximum values and 5HP measurements (b) variation range.
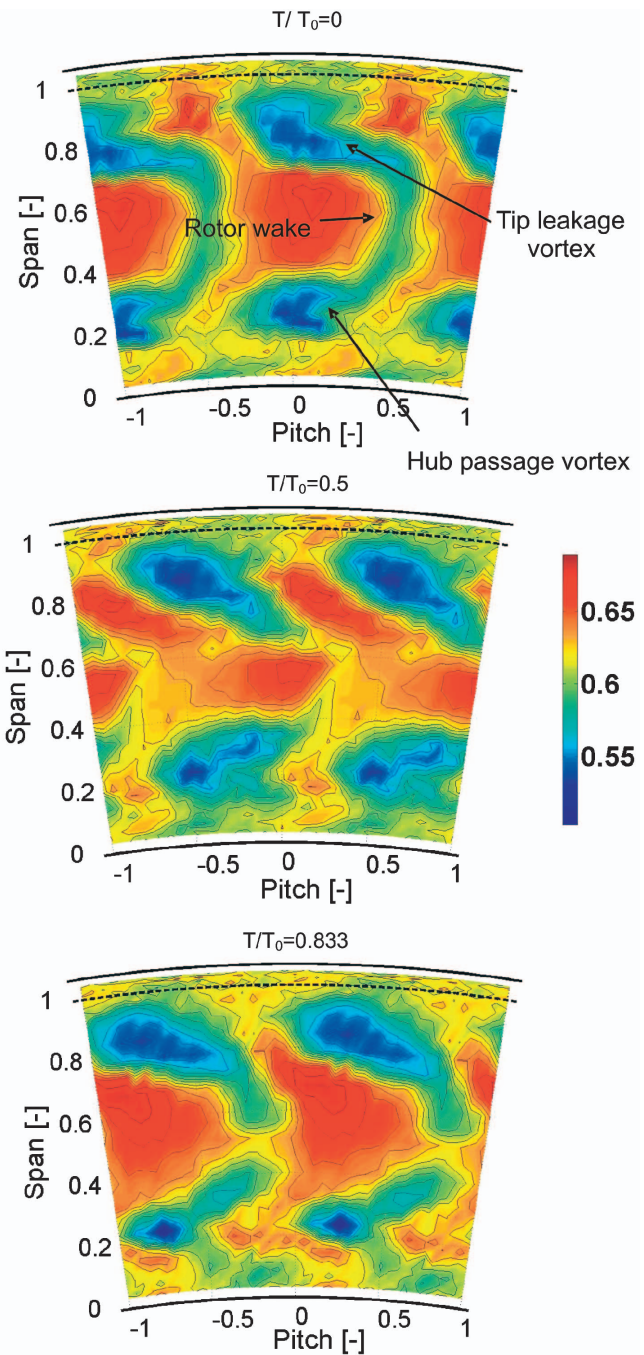
Fig. 16 Experimental time dependent relative total pressure coefficient in one blade passing period at the exit of the first rotor (PS test case)—Plane A1

the stator leading edge. However, the vortex of the leakage flow is continuously produced and is not influenced by the potential field. The large core at 70% span corresponding to the tip leakage vortex is present during all the blade passing period. This indicates that the secondary flows are resistant to the potential pressure field and the associated losses are higher than the losses associated with the blade wake.

Unsteady Analysis—Second Stator Exit—Plane A2. The unsteady measurements show the time dependent behavior of the flow structures identified by the steady analysis. Due to the presence of the first turbine stage, the inlet to the second stage is characterized by a highly three-dimensional pattern that affects the flow field
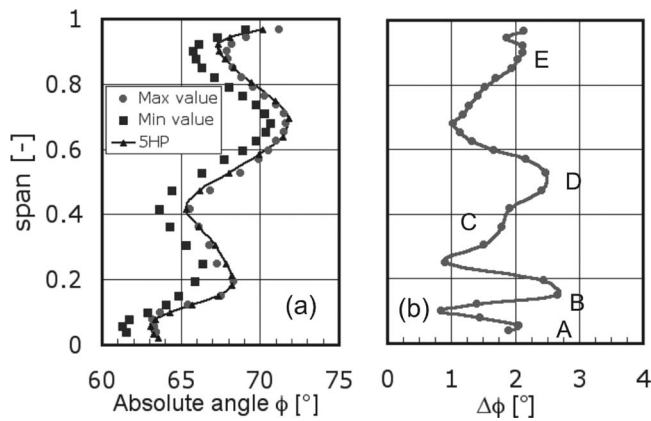
Fig. 17 Experimental mass averaged yaw angle variation in three blade passing period at the exit of the second stator (PS test case)—Plane A2—(a) minimum and maximum values and 5HP measurements, (b) variation range

Fig. 18 Frequency of occurrence of the measured unsteady absolute yaw angle at 5.5%, 15%, 36%, 52% and 90% span at the exit of the second stator (PS test case)—Plane A2. Symbols show the 5HP measurements.
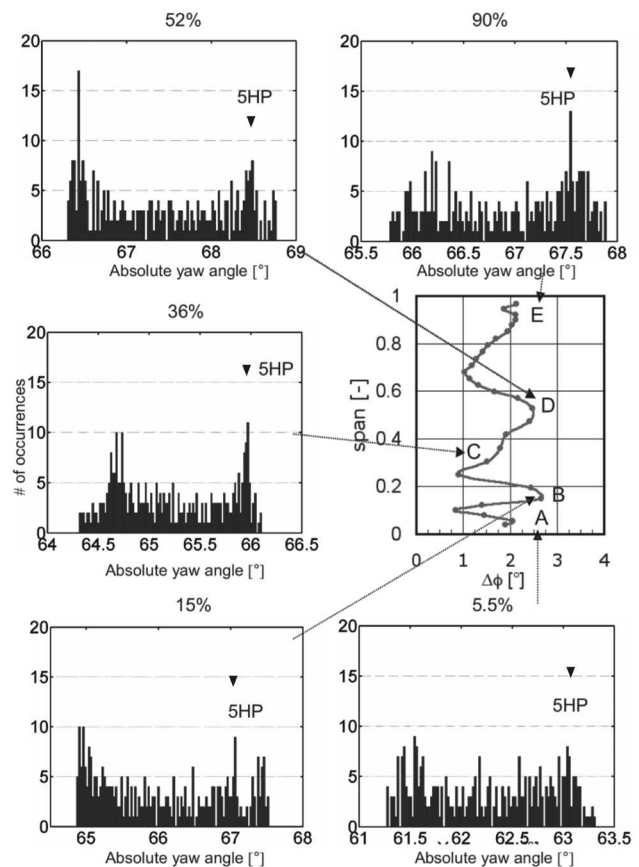
downstream this blade row. Secondary flow structures are predominant and they interact significantly with the main flow. Figure 16 shows the maximum and the minimum values of the yaw angle downstream the second stator. Steady data (from 5HP measurements) and relative variation are presented, in the same fashion as for the first rotor exit. In the entire span, the steady values are in between the variation.

The secondary flow structures observed in Fig. 12 from the steady measurements are also identified in the pitchwise average plots. In addition, the range of unsteady variation can be appreciated. The envelop of angle variation is shown in Fig. 17 between the maximum and the minimum angles. The flow angle variation is plotted as a difference $\Delta\phi$ showing that the maximum variation is limited to 2.7 deg. However, at the stator exit, this variation involves a significant momentum difference, owing to the high swirl. The flow features marked (A to E) in Fig. 17 correspond to the equivalent lettered regions of Fig. 12.

A marked result that can be appreciated from Fig. 17 is that the pneumatically averaged data (5HP) follow closely the trend of the unsteady data. Moreover, the agreement is very close to the maximum value of flow deflection.

The outcome of the foregoing discussion led to the statistical analysis of the unsteady variation of the flow angle in order to establish the relation between the pneumatically averaged data and the variations detected by the unsteady technique. The frequency of occurrence distribution of the unsteady flow angle results was constructed at each and every blade span position. The results are shown in Fig. 18. Five span locations are selected corresponding to the yaw angle variations maxima as described earlier in this section. In the mathematical sense, the distribution of the five-hole probe (5HP) data should asymptotically tend to a Dirac delta function. The pneumatically averaged data were therefore marked on the plot with a single point symbol. The physical characteristics of the measured distributions are discussed in view of their consequences to the designer's choices. The first interesting observation is that the distributions are bi-modal. In simple terms, this means that they show two peaks that have high probability of occurrence. The immediate consequence of the bi-modal distributions is that the most frequent values do not correspond to the average value. From the designer's perspective, this means that for most of the time the flow direction deviates from the mean. In the test case under consideration, this is of the order of 2 deg and 8 deg at the stator and rotor exit, respectively. At the rotor exit, the flow angle variations are higher but the tangential momentum difference is of the same order owing to the lower absolute swirl, compared to the stator exit.

As seen in Fig. 17, the 5HP measurements indicate the angle with the highest flow deflection. Cross comparison with Fig. 18 reveals that this coincides with the highest of the two most frequent angle values in the selected regions. It is therefore concluded that the 5HP measurements in regions of high vorticity tend to underestimate the deviation angle. Moreover, the leading edge design of the downstream rows should take into account a periodical incidence variation (with a frequency of 1.8 kHz) of 2 deg–3 deg at the stator exit and up to 8 deg at the rotor exit. This angle variation affects the local span loading as discussed in the performance analysis.

Performance Analysis

Efficiency. Mechanical method is used to evaluate second stage efficiency. Second rotor torque is measured by a torquemeter at five samples/s during the entire time of the data acquisition while the mass flow is continuously acquired during the measurements. The pressure ratio P_{03}/P_{01} is calculated by mass averaging the inlet total pressure in the area at exit of first and the second rotor. By referring the measured shaft power to the isentropic power provided by the fluid, the efficiency can be evaluated. In the current arrangement, mechanical dissipation and heat transfer terms are negligible. The torquemeter is in fact directly connected with the second stage shaft (power dissipation in the bearing is negligible) and the turbine reaches a constant thermal state over the running time. The following equation is used to calculate the aerodynamic efficiency:

$$\eta_{\text{second\_stage}} = \frac{M\omega/\dot{m}}{\bar{\bar{T}}_{01} C_p \left(1 - \frac{\overline{\overline{P_{03}}}^{\gamma-1/\gamma}}{\overline{\overline{P_{01}}}} \right)}.$$

The facility is open to the atmospheric pressure at the turbine exit. The turbine pressure drop oscillates with a variation of ±0.3% during a typical 10 h of operation. The measured pressures are corrected with a standard day condition.

The error analysis (Pfau, [19]) shows that the absolute overall uncertainty range on the efficiency (for a given geometry) is equal to 0.6%, while the relative uncertainty range between two test cases is equal to 0.3%.

The loss coefficient within the second stator passage is estimated for both test cases by the following equation:

$$Y = \frac{(\overline{\overline{P_{01}}} - \overline{\overline{P_{02}}})}{(\overline{\overline{P_{02}}} - \overline{\overline{p_2}})},$$

where $\overline{\overline{P_{01}}}$ and $\overline{\overline{P_{02}}}$ represent the mass averaged second stator inlet and outlet total pressure, $\overline{\overline{p_2}}$ is the stator static outlet pressure.

It was observed that the losses in the second stator are increased by almost 1% in the full shroud test case when compared to the partial shroud geometry. In the latter case, two opposing effects are occurring. On one hand, a strong negative incidence is detected from 60% to 100% span in the stator blade. This incidence mismatch is obviously increasing the profile losses at those locations. On the other hand, the flow turning in this region is decreased by around 25% when compared to the full shroud case. Therefore, the losses associated with the tip passage vortex are reduced. The extent of these two effects shows that the secondary flow losses reduction is larger than the increase of the profile losses. This result again illustrates that for a low aspect ratio high turning blade row, the vortical structure effects are predominant compared to other loss generation mechanisms.

Despite the second stator losses increased in the FS case, the second stage efficiency improves compared to the partial shroud case of 1%. This improvement can be attributed mainly to the increased loading of the tip of the rotor blades. The strong tip leakage vortex is not occurring anymore in the full shroud geometry due to the covering of the blade channel. Additionally, flow at the blade tip shows an improved matching with the leakage jet reducing mixing loss generation.

In order to have a qualitative picture of the aerodynamic performances and to relate them to the flow field, the spanwise efficiency variation is calculated with classical thermodynamic method

$$\eta(r) = \left(1 - \frac{\overline{T_{03}}}{\overline{T_{01}}}\right) \Bigg/ \left(1 - \frac{\overline{P_{03}}}{\overline{P_{01}}}\right)^{\gamma-1/\gamma}.$$

The relative uncertainty in the efficiency is directly related to the temperature drop relative uncertainty. With a total temperature drop of the order of 10°C, the relative uncertainty in the efficiency is higher than in the mechanical method and of the order of ±1%. However, this procedure allows detecting the performance increase/decrease at different span locations. Figure 18 shows the efficiency change between the partial shroud test case (as a reference value) and the full shroud case. The calculations are derived by interpolating the measured and spanwise averaged pressure, temperature and mass flow distribution. Radial efficiency distribution is then evaluated along streamtubes between the second stage inlet and outlet and then compared.

The variation is minimal up to midspan, underlining that the flow field and the aerodynamic performances are unchanged. The effect of the different shroud configuration is detected starting from 60% span. Closer to the tip, the full shroud case (FS) shows a significant improvement.

The difference between the mass averaged efficiency values is of the order of 2%, consistent with the value derived by the more accurate mechanical method.

Power. The local loading coefficient is derived from the unsteady data as follows. First, the time dependent yaw angle is derived from the unsteady measurements downstream of the first
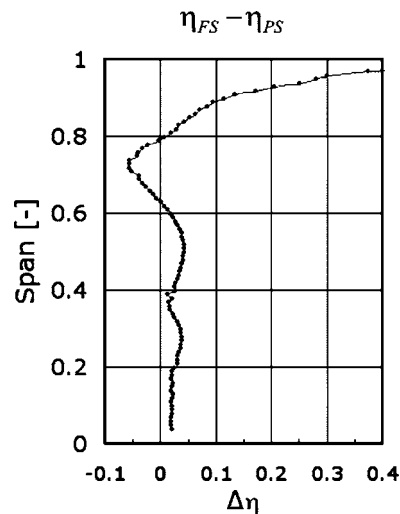
Fig. 19 Measured spanwise efficiency change between FS and PS test case

and the second rotor. Second, the minimum and the maximum values of this angle are derived from the pitchwise mass averaged data at each span position ($\bar{\phi}_{max}, \bar{\phi}_{min}$). Then velocity is derived from the local Mach number and the static temperature (V_{max}, V_{min}). The loading coefficient is then obtained as follows:

$$\bar{\psi}_{max,min} = \frac{\Delta\bar{V}_{\phi max,min}}{u}$$

Figure 19 shows the loading variation. In Fig. 20(a), the local minimum and the maximum loading coefficient is normalized by the mean value at midspan. The variation is almost negligible close to midspan where the flow is relatively not affected by the secondary structures. However, a variation up to 15% with respect to the averaged value is detected in the hub region. This unsteady aerodynamic loading enhances vibrations and blade stresses at each blade-passing period (1.8 kHz).

From the time dependent signal, the isentropic enthalpy drop has been also calculated as a function of the blade passing period (Fig. 21). This variation of work extraction implies that the blades experience a sinusoidal force along the span with a variation up to
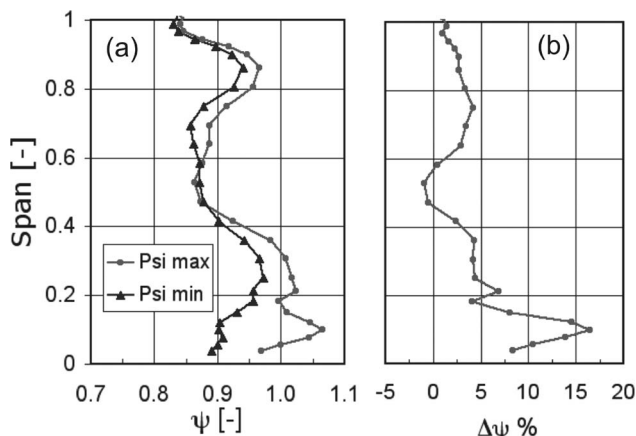
Fig. 20 Measured loading coefficient variation across the second rotor in three blade passing periods—PS test case—(*a*) minimum and maximum values, (*b*) variation range
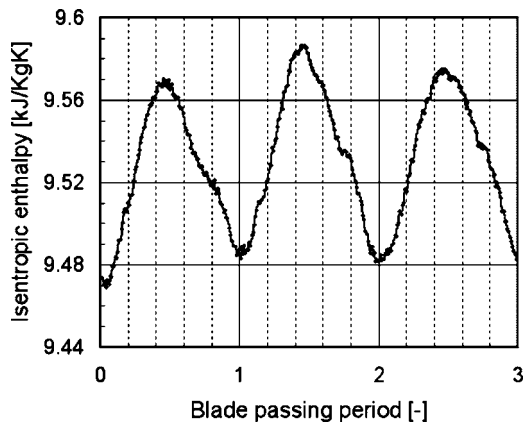
Fig. 21 Measured isentropic enthalpy drop across the second stage—PS test case

0.5%.

The mechanical design of the blade could take advantage of this analysis in order to evaluate correctly the vibration modes and improve the rotordynamics of the bladed disks.

Summary and Discussion

Typical pressure ratio and temperature ranges of this experimental facility are far from the actual engine conditions. However, the experiments and the simulations indicate that the shroud and labyrinth path may have a significant impact on the overall performance and, consequently, these issues need particular attention during the design process. Design tools and methodology can then be validated. The subsequent transfer from the test bench (where the present accurate and reliable measurements were performed) to engine conditions is commonly done by means of CFD.

In a multi-stage environment, the flow field within and after low aspect ratio blading is highly three-dimensional and unsteady. The classical understanding of the secondary flow behind a cascade based on uniform inlet flow may not be fully representative of such flow regimes. The second stage is subjected to unsteady inlet boundary conditions imposed by the nonuniformity of the first stage flow structures. Vortex-wake interactions, potential field of downstream rows and leakage flows have a primary effect on the performance of the downstream rows.

From the present analysis it follows that an optimal aerodynamic design has to involve different parameters that take into account the nonuniformity of the second stage inlet. Several aspects have to be considered, including shroud design, blade loading, second stator leading edge geometry, efficiency.

Despite the fact that the blade geometry and the tip clearance remained unchanged, in the PS case, large deviation between the blade angle and the measured flow in the tip region has been detected. Although aerodynamically superior, the use of full shrouds is not always feasible due to mechanical constrains. In such situations, partial shrouds may be employed. In all these cases, and particularly for the partial shrouds, an integrated blade-shroud design should be adopted. In the PS case, a different blade profile could be designed at the tip in order to increase the loading on the front part. With this approach, the localized tip leakage at the trailing edge cut back may be reduced driven by a reduced pressure difference across the tip, while loading at other span-1 would be increased.

Conclusions

A comprehensive investigation on two test cases with identical turbine blade geometries with a partial and a full shroud arrangement has been conducted. A unique comparative study was performed in order to address the effect of the leakage flow in the flow field and in the overall performance. Owing to the application of consistent experimental techniques supported by numerical methods, fluid dynamics and performance of partially and fully shrouded turbines have been studied.

Unsteady measurements show that in the partial shroud test case a tip leakage vortex is continuously produced in the first rotor tip region while the rotor wake intensity is modulated (and even cancelled) by the potential effect of the downstream stator. Statistical analysis showed that in the yaw angle distribution the mean value is not always the most frequent in the vortex region. The angle distribution is bi-modal with two individual peaks in the range of ±1.5 deg at the second stator exit and ±4 deg at the first rotor exit. The 5HP measurements fall closer to the high probability peak corresponding to the maximum flow deflection. Unsteady aerodynamic loading is derived for the second rotor showing a variation of the work coefficient up to 15% at the hub.

The CFD simulation shows a good agreement with the measured data at midspan in all aerodynamic parameters for the first stage. The discrepancy with the experimental data is of the order ±1 deg in the yaw angle and ±1% in total pressure. At the hub endwall, vortex structures are not captured because the hub leakage flow is not taken into account in the calculation.

Accurate performance measurements show an improvement of the overall second stage efficiency for the full shroud test case (FS) of the order of 1%. The improved control on the blade loading on the rotor and the matching of the cavity flow with the main stream is at the root of this result. However, the second stator experiences a lowered performance compared with the partial shroud test case (PS) of about 1%. The reason for this behavior is the increase of the tip passage vortex loss due to the increase of the turning in the region between 60% and 100% span. Despite the decrease of the profile losses due to the reduction of the negative incidence at the tip, the overall second stator losses are increased with respect to the partial shroud test case. Hence, tip leakage flow can have a significant effect on the secondary flow development in the subsequent blade rows. Leakage jets can thus be used in order to tune the secondary flows and eventually reduce their intensity.

The present study suggests that turbine designers need to perform an integrated time-dependent analysis of the shroud-tip area in order to maximize performance. Particular attention needs to be paid to the matching between the shroud and the blade geometry design. Reentry and mixing of the jet leakage into the main stream can have a critical impact on the flow field and, consequently, on the stage performance. As shown in this work, an improvement up to 1% in the overall stage efficiency can be achieved.

Nomenclature

Cp = specific heat at constant pressure
Cpt = total pressure coefficient
$\quad (P_{0meas} - P_{SExit})/(P_{0Inlet} - P_{SExit})$
Cps = static pressure coefficient
$\quad (P_{Smeas} - P_{SExit})/(P_{0Inlet} - P_{SExit})$
$\dot{m}$ = mass flow

M = second stage torque
P = pressure
R = perfect gas constant
Δs = entropy
T = temperature
T/T_0 = blade passing period fraction
V = flow velocity
PS = partial shroud test case
FS = full shroud test case
5HP = five-hole probe
FRAP = fast response aerodynamic probe

Greek

β = pitch angle
γ = isentropic exponent
η = turbine second stage efficiency
ϕ = yaw angle
ψ = loading coefficient
ω = rotational speed

Subscripts/Superscripts

0 = total conditions
S = static conditions
1,2,3 = measurement plane $A1$, $A2$ and $A3$
$\bar{\bar{P}}, \bar{\bar{T}}$ = mass and area averaged data
$\bar{P}, \bar{T}$ = mass pitchwise averaged data
min,max = minimum and maximum value
ref = reference value

References

[1] Langston, L. S., 2001, "Secondary Flows in Axial Turbines—A Review," *Heat Transfer in Gas Turbine Systems*, pp. 11–26.
[2] Chaluvadi, V. S. P., Kalfas, A. I., Banieghbal, M. R., Hodson, H. P., and Denton, J. D., 2001, "Blade Row Interaction in a High Pressure Turbine," AIAA J., **174**, pp. 892–901.
[3] Wallis, A. M., Denton, J. D., and Demargne, A. A. J., 2001, "The Control of Shroud Leakage Flows to Reduce Aerodynamic Losses in a Low Aspect Ratio, Shrouded Axial Flow Turbine," ASME J. Turbomach., **119**, pp. 1–8.
[4] Peters, P., Breisig, V., Giboni, A., Lerner, C., and Pfost, H., 2000, "The Influence of the Clearance of Shrouded Rotor Blades on the Development of the Flow Field and Losses in the Subsequent Stator," ASME Paper No. 2000-GT-478.
[5] Anker, J. E., and Mayer, J. F., 2002, "Simulation of the Interaction of Labyrinth Seal Leakage Flow and Main Flow in an Axial Turbine," ASME Paper No. GT-30348.
[6] Morphis, G., and Bindon, J. P., 1995, "The Flow in a Second Stage Nozzle of a Low Speed Axial Turbine and its Effect on Tip Clearance Loss Development," ASME J. Turbomach., **117**, pp. 571–577.
[7] Hunter, S., and Manwaring, S., 2000, "Endwall Cavity Flow Effects on Gaspath Aerodynamics in an Axial Flow Turbine: Part I—Experimental and Numerical Investigation," ASME Paper No. 2000-GT-651.
[8] Wellborn, S. R., 2001, "Details of Axial-Compressor Shrouded Stator Cavity Flows," ASME Paper No. 2001-GT-495.
[9] Demarge, A. A. J., and Longley, J. P., 2000, "The Aerodynamic Interaction of Stator Shroud Leakage and Mainstream Flows in Compressors," ASME Paper No. 2000-GT-570.
[10] Schlienger, J., 2003, "Evolution of Unsteady Secondary Flows in a Multistage Shrouded Axial Turbine," Ph.D. thesis No. 15230, ETH, Zurich, Switzerland.
[11] Treiber, M., Kupferschmied, P., and Gyarmathy, G., 1998, "Analysis of the Error Propagation Arising From the Measurements With a Miniature Pneumatic 5-Hole Probe," XIVth Symposium on Measuring Techniques for Transonic and Supersonic Flows in Cascades and Turbomachines.
[12] Kupferschmied, P., Köppel, O., Gizzi, W. P., and Gyarmathy, G., "Time Resolved Flow Measurements With Fast Aerodynamic Probes in Turbomachinery," Meas. Sci. Technol., **11**, pp. 1036,1054.
[13] Schlienger, J., Pfau, A., Kalfas, A. I., and Abhari, R. S., 2003, "Effect of Labyrinth Seal Variation on Multistage Axial Turbine Flow." ASME Paper No. GT-2003-38270.
[14] Spalart, P., and Allmaras, S., 1992, "A One-Equation Turbulence Model for Aerodynamic Flows," Technical Report No. AIAA-92-0439, American Institute of Aeronautics and Astronautics.
[15] Schlienger, J., Kalfas, A. I., and R. S. Abhari, 2004, "Vortex-Wake-Blade Interaction in a Shrouded Axial Turbine," ASME Paper No. GT-2004-53915.
[16] Gier, J., Stubert, B., Broulliet, B., and De Vito, L., 2003, "Interaction of Shrouded Leakage Flow and Main Flow in a Three-Stage LP Turbine," ASME Paper No. 2003-GT-38025.
[17] Denton, J. D., 1993, "Loss Mechanisms in Turbomachines," ASME J. Turbomach., **115**, pp. 621–658.
[18] Behr, T., Porreca, L., Kalfas, A. I., and Abhari, R. S., 2004, "Multistage Aspects and Unsteady Effects of Stator and Rotor Clocking in an Axial Turbine With Low Aspect Ratio Blading," ASME Paper No. GT2004-53612.
[19] Pfau, A., 2004. "Loss Mechanisms in Labyrinth Seals of Shrouded Axial Turbines," ETH Ph.D. dissertation No. 15226.

Unsteady Flow Interactions Within the Inlet Cavity of a Turbine Rotor Tip Labyrinth Seal

A. Pfau
e-mail: a.pfau@freesurf.ch

J. Schlienger

D. Rusch

A. I. Kalfas

R. S. Abhari

Turbomachinery Laboratory,
Swiss Federal Institute of Technology,
8092 Zurich, Switzerland

This paper focuses on the flow within the inlet cavity of a turbine rotor tip labyrinth seal of a two stage axial research turbine. Highly resolved, steady and unsteady three-dimensional flow data are presented. The probes used here are a miniature five-hole probe of 0.9 mm head diameter and the novel virtual four sensor fast response aerodynamic probe (FRAP) with a head diameter of 0.84 mm. The cavity flow itself is not only a loss producing area due to mixing and vortex stretching, it also adversely affects the following rotor passage through the fluid that is spilled into the main flow. The associated fluctuating mass flow has a relatively low total pressure and results in a negative incidence to the rotor tip blade profile section. The dominating kinematic flow feature in the region between cavity and main flow is a toroidal vortex, which is swirling at high circumferential velocity. It is fed by strong shear and end wall fluid from the pressure side of the stator passage. The static pressure field interaction between the moving rotor leading edges and the stator trailing edges is one driving force of the cavity flow. It forces the toroidal vortex to be stretched in space and time. A comprehensive flow model including the drivers of this toroidal vortex is proposed. This labyrinth seal configuration results in about 1.6% turbine efficiency reduction. This is the first in a series of papers focusing on turbine loss mechanisms in shrouded axial turbines. Additional measurements have been made with variations in seal clearance gap. Initial indications show that variation in the gap has a major effect on flow structures and turbine loss.
[DOI: 10.1115/1.2008973]

Introduction

The development of turbo machinery blade design is currently focusing on the characteristics of highly loaded stages. These are advantageous because the use of fewer blades that produce the same power at the same efficiency results in a substantially lower cost and a higher power density. Concerning low aspect ratio blades, as they are used in intermediate and high pressure turbines, the inherent strong secondary flows are enhanced by the design of higher turning airfoils. Consequently, the aerodynamic secondary flow losses increase.

In order to decrease secondary flows and reduce the migration of the low kinetic energy fluid into the main flow, the design of end wall regions has been increasingly addressed. Gregory-Smith et al. [1] successfully introduced the use of end wall profiling procedures to modify the secondary flow. Sauer et al. [2] proposed the use of leading edge modifications at the tip region to decrease secondary losses. These studies have shown effectiveness in controlling the secondary flow under controlled inflow conditions.

In shrouded turbines however, the inlet flow condition to a blade row is disturbed at the end wall by flow interactions with open cavities. Those open cavities are present at the inlet and exit of the labyrinth seals. The size of these cavities is determined by the axial thrust variation or the mechanical and thermal growth of the rotor assembly. As such the aerodynamic design has to allow for large inlet and exit cavities, particularly for steam turbine applications. Prior observations seem to suggest that secondary flow structures and losses are influenced by the steady and unsteady interactions with the cavity flow field.

The subject of cavity interactions in turbines was addressed the first time by Denton and Johnson [3]. However, it is only in recent years that this subject has been the focus of much research. Peters et al. [4] examined the effect of gap size on the steady interaction between the leakage flow and the secondary flow field of a subsequent stator in a 1.5 stage, shrouded axial turbine. Hunter and Manwaring [5] reported about two extra vortices generated in a downstream stator blade row. Wallis et al. [6] observed that strong interactions are present in open cavities of shrouded turbine blades. The following blade rows were found to receive the tip flow at a negative incidence. Anker and Mayer [7] numerically investigated the leakage interaction with the main flow and found that the tip leakage flow is not uniform in the pitch wise direction. Schlienger et al. [8] changed the geometry of the labyrinth exit cavities and compared the effects on the main flow as well as on the efficiency. These studies have focused mainly on the interaction happening in the main flow and following blade passages.

However, as the origins of these interactions are open cavities, an increased emphasis must be placed on the associated unsteady flow interactions within these cavities. The unsteady fluctuations may create large amplitude deviations to the time-averaged structure of the cavity flow. Thus, the actual cavity flow may be quite different than the steady model as proposed by Pfau et al. [9].

In the present work the inlet cavity to the second rotor tip labyrinth seal of a two stage axial turbine is investigated. This flow may be expected to have features similar to the unsteady wake flow avenues described by Binder [10] and unsteady vortex interactions observed by Chaluvadi et al. [11]. As the cavity region is small these flow features can only be experimentally measured with miniature probes of minimized blockage. Thus, a unique element of this work is the application of the new fast response aerodynamic probe (FRAP), which is described in a companion paper by Pfau et al. [12]. This probe provides spatially and temporally highly resolved measurements of the three-dimensional flow field.

Table 1   Main characteristics of the test turbine

Pressure ratio	1.32	Mass flow	9.86 kg/s
Max. power	400 kW	Turbine speed	2700 rpm
T_{inlet}	40 °C	P_{exit}	Ambient
Mach	0.1…0.4	Re_{Cax}	10^5
n (rotor/stator)	42	Tip diameter	800 mm
Seal gap	0.35 mm	Blade aspect ratio	1.8

a) 5 Hole Probe
(Z=0.17, 0.28, 0.41, 0.5, 0.67, 0.83)

b) Virtual 4 Sensor Probe
(Z=0.28, 0.41, 0.5, 0.67, 0.83)

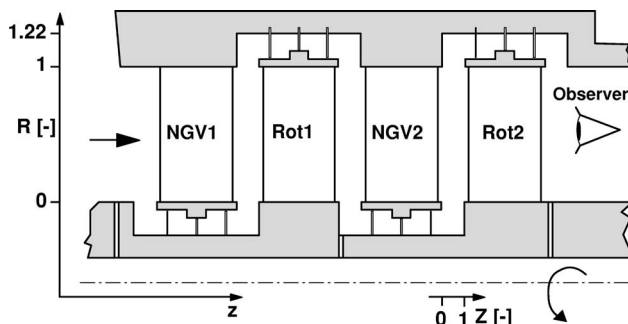**Fig. 2   Locations of measurement**

Methodology

Test Case and Measurement Technology. The cavity interaction flow was investigated in the two-stage low speed axial turbine "LISA." The test rig is described in detail in Sell et al. [13] The main characteristics of the turbine are summarized in Table 1.

The constant annulus and the four blade rows are depicted in Fig. 1. The stepped shrouds on the blades together with three sealing fins form the labyrinth seal. The geometry under investigation is similar to steam turbine applications, where large inlet and exit cavities allow for axial movement of the rotor blades. Consequently, the blade profiles are of a medium loaded type with leaned stator blades.

The tip gap was set to 0.36% of the blade height. In comparison to real applications this value is small, as gaps of 0.7%–1% blade height are commonly employed. The small gap was, however, chosen in order to increase the pure cavity to main flow interaction by sucking less leakage mass flow out of the inlet cavity. The experiments were performed at a rotational speed of 2700 rpm and a mass flow of 9.86 kg/s. In real steam turbine the fluid dynamic conditions are $Re=3*10^6$ and $M=0.3$ with a suction peak velocity of around $M=0.8$. Therefore, compressibility as well as viscous effects are not exactly modeled in this turbine. However, as the velocity triangles and reduced frequencies match to a real stage, unsteady effects, like vortex or potential field interactions, are comparable.

The coordinate system used to display the results is cylindrical. The radial direction r is made dimensionless with the blade height, such that $R=0$ denotes the hub and $R=1$ the tip radius of the blades. The cavity floor of the labyrinth is at $R=1.22$. The direction of the turbine axis is denoted with z, where a local non-dimensional coordinate Z is introduced (see also Fig. 2). It starts at the cavity entry lip and is made dimensionless with the axial width of the cavity ($z_{cav}=15$ mm). The circumferential direction is counted positive with the sense of rotation. The chosen view in the diagrams is upstream as the observer in Fig. 1 indicates. Therefore, the circumferential axis in the diagrams is reversed pointing into anti-rotational direction.

The data sets presented here comprise 2640 steady and 1725 time resolved measurement points. The 2640 steady data points are distributed onto six axial measurement planes as indicated in Fig. 2(a). Each plane is resolved by 23×19 points covering 1.1

Fig. 1   Cross section of the test geometry
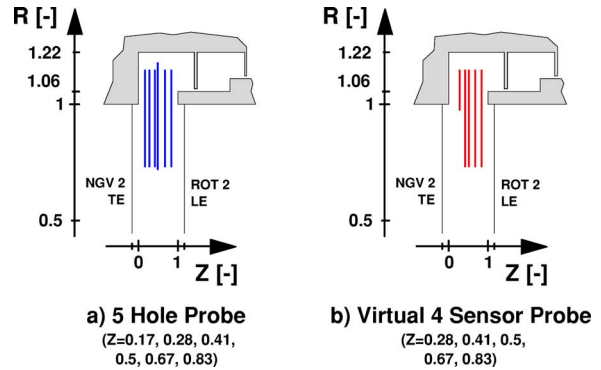
pitches. A miniature five hole pneumatic probe of 0.9 mm head diameter was applied. The calibration range of the aerodynamic model was ±10° in yaw and ±30° in pitch direction. The error band width in flow angle is ±0.3° and ±60 Pa and ±120 Pa total and static pressure, respectively [14]. In terms of non-dimensional pressures C_p this equals ±0.0019 and ±0.0038 for total and static pressure. Downstream of a stator, flow velocities of $M=0.3$ are present, which is measured accurate to within ±1.3%. The accuracy of the velocity components depend on the flow angles. The worst case of error band width of the non-dimensional velocities was found to be ±0.007 in axial (v_z), ±0.016 in tangential (v_Θ) and ±0.005 in radial (v_r) direction.

The unsteady data points cover the same downstream five axial positions as the pneumatic data grid but with an average resolution of 23×15 points per plane [see Fig. 2(b)]. Due to geometric constraints the measurement plane at $Z=0.28$ ranges from the cavity floor to $R=0.95$ only. The virtual four sensor fast response aerodynamic probe, that was used, is characterized by low blockage with a head diameter of 0.84 mm and the capability of measuring three-dimensional flow up to a frequency of 25 kHz. The probe's calibration limits the range to ±30° for yaw and −30° to +21° for the pitch angle. The probe concept is described in detail in Pfau et al. [12]. Flow angles are measured to ±0.4° for yaw and ±0.8° for pitch angle. The accuracies of total and static pressure are ±120 Pa and ±85 Pa which result in a typical error of 1.2% for Mach number. These numbers do not include unsteady aerodynamic effects on the probe tip.

Unsteady Data Postprocessing. Each position of the measurement grid is measured for 3 s at 200 kHz. The data sets are processed to yield the basic flow quantities, i.e., flow angles, total and static pressure by applying a phase lock average of 100 events. One event covers three consecutive rotor blade passages. Each rotor passage is resolved by 106 samples. In comparison to the highest frequency measured in the spectrum this temporal resolution results in an over sampled data set. However, for applying fast response measurement technology in a virtual three or four sensor mode this is a necessity, so that the measured relative position to the rotor of each probe is accurately known. A detailed description of the data postprocessing is given in Pfau et al.[12]

The basic flow quantities are reduced to Mach number and velocity components. The instantaneous velocity field is further processed to calculate the instantaneous vorticity. This is possible, because the data are highly resolved in both space and time and thus, a quasi-steady analysis at each instant of time can be correctly performed. Partial time derivatives of the vorticity are calculated by applying a time marching differential scheme on the control volume data sets. Therefore, all terms of the unsteady vorticity equation can be calculated, which allows for further description of the loss production mechanisms.

The data are measured in the absolute coordinate system. The transformation into the rotating coordinate system is done by

shifting the location of data points in the rotational direction. At each time step the rotor moves 0.08°. The rotational speed is subtracted from the circumferential velocity component. Then the relative norm of the velocity as well as the relative flow angles are calculated. Adding the relative dynamic head to the static pressure field results in the relative total pressure. Time averaging within the relative frame allows the separate rotor influences on the flow field to be evaluated.

Experimental Results

Absolute Frame of Reference.

Pitch Wise Averaged Data. Measurements taken with the pneumatic five hole probe are assumed to be time averaged data and show the flow structure in the absolute frame of reference. Figure 3 presents the pitch wise averaged data at the first, middle, and last axial positions given in Fig. 2. The error band is given for each quantity.

The non-dimensional total pressure in Fig. 3(a) shows a strong radial gradient between $R=0.93$ and 0.99. It decays with increasing Z. At $Z=0.17$, a total pressure wake at $R=1$ and a jet at $R=0.97$ are present. The wake jet character gets mixed out at the next axial position. The cavity flow shows a lower total pressure than the main flow. Close to the rotor inlet at $Z=0.83$ the total pressure profile has a more uniform distribution at radii lower than 0.93. Note the kink in the profile at $R=1.08$ and the associated higher level of total pressure at around $R=1.03$. The effect stems from the rotating shroud leading edge entraining kinetic energy into the fluid via shear.

The static pressure distribution in Fig. 3(b) is showing a radial pressure gradient. It is in radial equilibrium with the centrifugal forces to keep the fluid in a swirling motion. Coming from lower span the gradient increases in the vicinity of $R=1$. Here the first and last axial positions $Z=0.17$ and 0.83 show a local maximum in contrast to the midcavity position. All axial positions encounter a local minimum of static pressure around $R=1.06$. A strong radial pressure gradient connects the local minimum to the cavity floor wall. Note that the wall pressures of $Z=0.5$ and 0.83 at $R=1.22$ are results of pitch wise averaged wall pressure tap measurements.

The axial velocity component made nondimensional with the blade tip speed is given in Fig. 3(c). The over and under turning effect of the flow due to the stator passage vortex is seen in the velocity profile. The local maximum at $R=0.8$ is caused by under turning and coincides with the radial position of the loss core, see also Fig. 4(a). The over turning leads to a kink in the axial velocity profile at $R=0.93$. Zero through flow is found around $R=1.06$. The back flow component within the cavity reaches values up to 10% of the blade tip speed. The position of the local minima shift radially downwards with increasing Z.

The radial velocity in Fig. 3(d) indicates a vortical flow within the cavity having negative components at $Z=0.17$ and positive components at $Z=0.83$. Note, that the absolute value at $Z=0.83$ is about 0.07 higher than at $Z=0.17$. The sense of rotation is counterclockwise resulting in positive vorticity, see also Fig. 6. The center of the vortex is characterized by a local minimum in static pressure. The local minimum in Fig. 3(b) at $R=1.06$ is an indication of the vortex core. This is a first evidence of a toroidal vortex within the cavity. In Fig. 3(e) the over and under turning behavior results in a local maximum and minimum of tangential velocity at $R=0.8$ and $R=0.93$, respectively. At $Z=0.17$ a shear layer with a strong gradient in tangential velocity connects the over turning region to a wake of low tangential momentum. It has a velocity deficit of 0.08 compared to the swirling velocity of the cavity flow and 0.2 compared to the region of over turning at $R=0.93$. Moving downstream to $Z=0.5$ the wake is filled up as tangential momentum is transferred from the main flow and the cavity flow into the wake. Close to the shroud leading edge at $Z=0.83$ the wake is filled up and has gained additional momentum. There are two
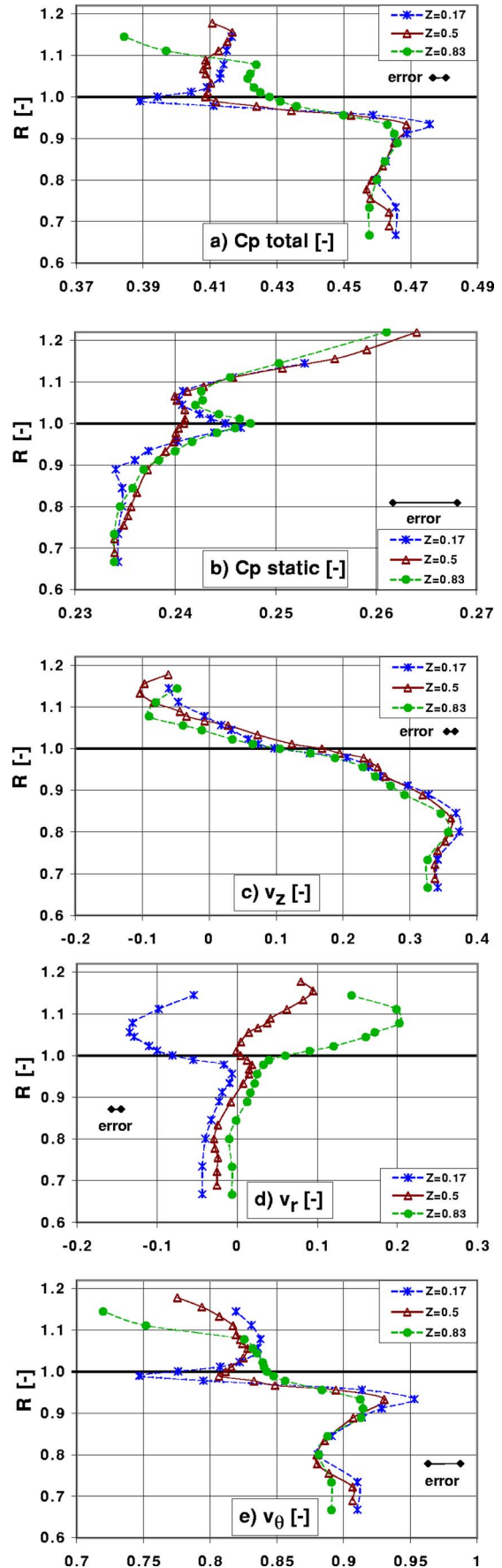

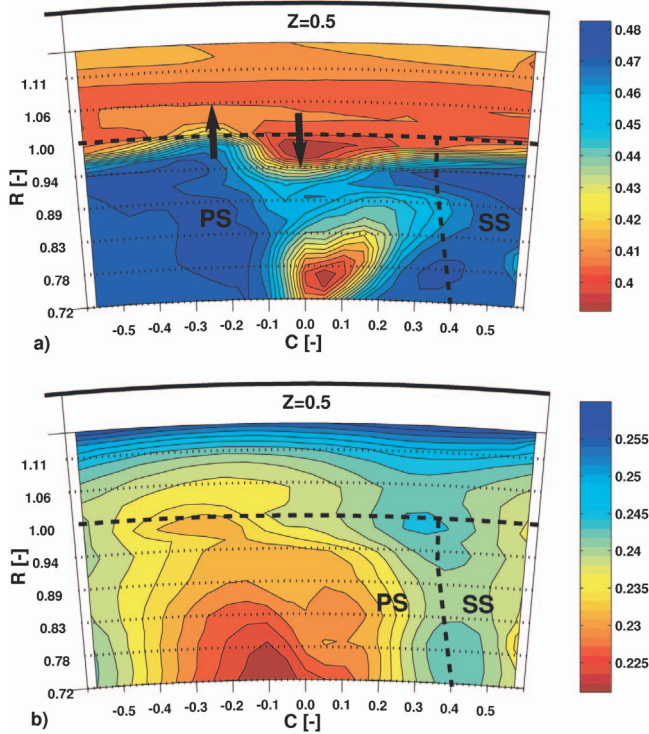
Fig. 3   Pitch wise averaged results

Fig. 4 *a*) Total pressure $C_{po}[-]$, *b*) Static pressure $C_p[-]$

Fig. 6 Vorticity components at $C=0.25$

trailing edge around $C=0.35$ a high static pressure is induced. At $C=-0.1$ the distance to the suction side surface is larger and therefore the static pressure is lower. This circumferential distribution propagates into the cavity volume and varies over one pitch by ±0.003 at $R=1.06$.

Comparing Figs. 4(*a*) and 4(*b*) the blade wake has convected $\Delta C=-0.4$ from the trailing edge position. The local minimum in

sources of tangential momentum entrainment in this flow region: the rotating shroud and the higher swirl component of the main flow. The shroud outer diameter at $R=1.06$ coincides with the kink in the tangential velocity profile.

Pressure and Velocity Field. The total pressure distribution at mid-cavity position $Z=0.5$ is displayed in Fig. 4(*a*). The cavity floor is depicted with a thick line. The tip radius and the trailing edge position of the stator are indicated with dashed lines. The distribution shows similar features as described in Pfau et al. [9]. The cavity flow has a lower level of total pressure. The main flow exhibits the secondary flow structure of a blade passage showing a loss core at $R=0.76$. On the pressure side of the stator wake the high total pressure gradient reaches the tip radius $R=1$. Here the thin boundary layer created on the passage tip end wall meets the cavity flow. The fluid has positive radial velocity and is moving into the cavity as the arrow indicates. Above the loss core, i.e., on the suction side of the blade wake, a low total pressure region has formed at $R=0.97$ showing the same order of magnitude as the loss core. This region is part of a wake in tangential momentum, as described in Fig. 3(*e*). It originates from the backward facing surface of the cavity at a radial position slightly higher than 1. The arrow illustrates the negative radial velocity and the flow out of the cavity.

The static pressure field in Fig. 4(*b*) is circumferential nonuniform due to the stator trailing edge. Close to the position of the
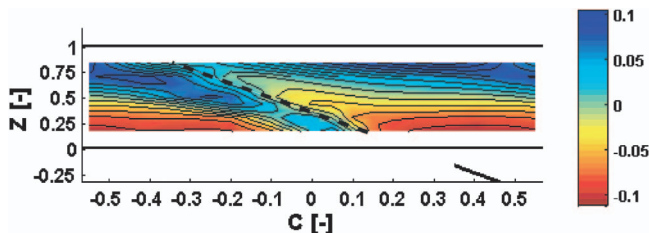

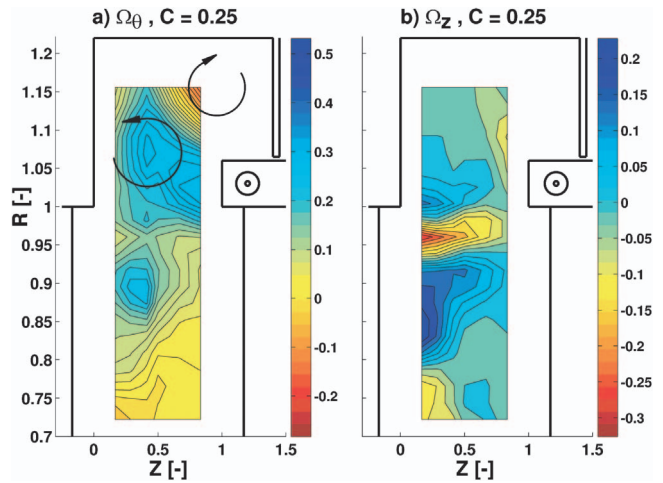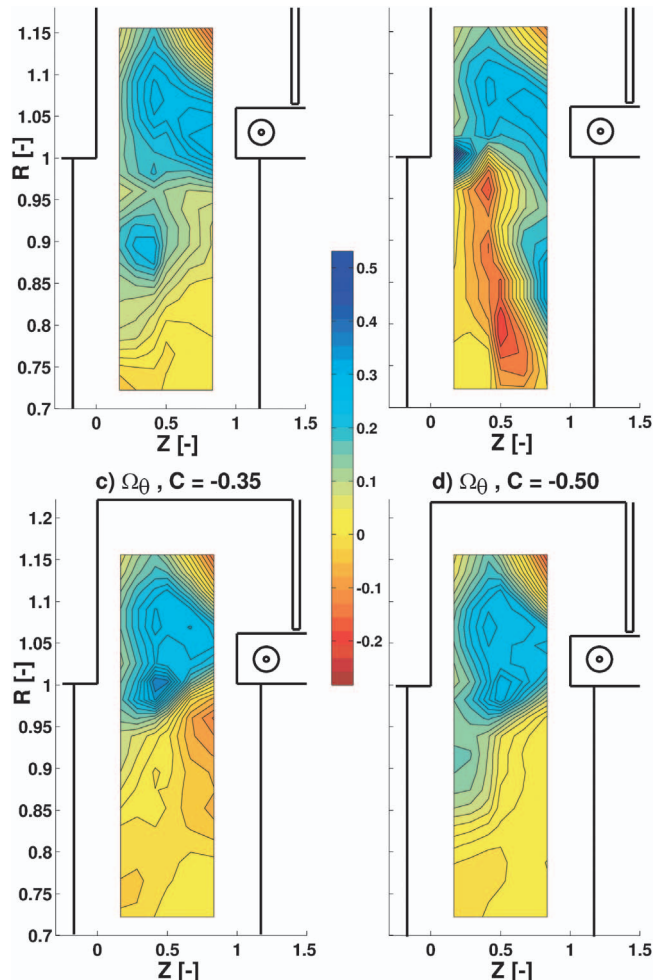**Fig. 5** Radial velocity $v_r[-]$, $R=1$ (tip radius)

Fig. 7 Circumferential vorticity $\Omega_\theta[-]$

static pressure at $R=1.06$ coincides with streaks of higher total pressure. The inflow region marked with the arrow encounters a low local static pressure. High kinetic energy fluid is pushed into the cavity.

The convective path of flow in and out of the cavity is shown with a contour plot of radial velocity in Fig. 5. The view is in the positive radial direction. The thick line at $C=0.35$ indicates the position of the trailing edge at $R=1$. At $Z=0$ and 1 thick lines mark the axial position of the inlet corner and the shroud leading edge. Positive and negative radial velocities can be observed parallel to a line of zero radial velocity indicated with a dashed line. Close to the upstream corner radial velocities are negative, since the toroidal vortex pushes fluid into the main flow. On the downstream side of the axial gap the vortex moves fluid particles into the cavity. In addition, the centrifugal forces induced by the rotating shroud leading edge surface contribute to the inflow.

Vorticity Field. Flow in the cavity is three dimensional with a high level of unsteadiness in pressure and velocity. Representing the flow structure in terms of vorticity in this case permits a better physical insight into the entrainment and loss generation using only a single scaler. Figure 6 presents the non-dimensional circumferential and axial vorticity components of a circumferential position of $C=0.25$. The vorticity is made nondimensional assuming solid body rotation and taking a reference angular speed calculated with the blade passing frequency. High positive tangential vorticity dominates the measurement volume inside the cavity. Maximum values occur in a round region at $Z=0.4$ and $R=1.07$ as well as in the vicinity of the shroud leading edge. Close to the corner formed by the sealing fin and cavity floor the sign of vorticity changes. This may indicate the presence of a second counterrotating vortex with the center approximately at $Z=1$ and $R=1.15$ as the circular arrow indicates.

The axial vorticity component shows an alternating pattern of high positive, high negative and back to high positive values at the $Z=0.17$ as R increases. Since axial vorticity in cylindrical coordinates is defined as $\omega_z = 1/r \partial r v_\theta / \partial r - 1/r \partial v_r / \partial \theta$, it is a measure of tangential shear, if radial shear is comparably small. The region of high and low axial vorticity at $R=1$ and $R=0.96$ is confining center of the tangential momentum wake, which was found in Fig. 3(*e*). The higher axial vorticity at $R=0.9$ as well as the lower at $R=0.96$ is induced by the overturning profile also found in Fig. 3(*e*) at $R=0.94$. As the gradients in tangential velocity decrease with Z, the axial vorticity also decreases. Note that some negative axial vorticity is induced from the rotating shroud leading edge.

A combined view of axial and tangential vorticity reveals the center of the toroidal vortex. The condition for the center of a toroidal vortex is zero vorticity in radial and axial direction, which is fulfilled in the local maximum of tangential vorticity at $R=1.073$ and $Z=0.41$. Closer to the shroud the tangential vorticity stays positive. However, the axial vorticity becomes negative. These two conditions can be explained with a skewed boundary layer induced by the tangential shear and the radial pumping effect of the rotating shroud and rotor leading edge. An important finding is, that the center of the toroidal vortex is found to be at a slightly higher span than it was determined with circumferential averaged data in Fig. 3(*b*). This indicates a pitch wise variation of the vortex center.

In Fig. 7, the tangential vorticity component at different circumferential positions is presented. Taking $C=0.25$ as a starting point, the diagrams Fig. 7(*a*) through *d* follow the convective direction of the toroidal vortex at $C=-0.05$, -0.35, and -0.5. In position $C=-0.05$ the main flow shows a high negative tangential vorticity. It is generated by the change of negative radial migration present in the blade wake with increasing Z. The high positive tangential vorticity at $R=1$ and $Z=0.17$ indicates the point on the pressure side of the stator wake where the inflow to the cavity starts. Comparing with Fig. 5, it seems that at $C=-0.35$, the region of high tangential vorticity is detached from the cavity corner and has
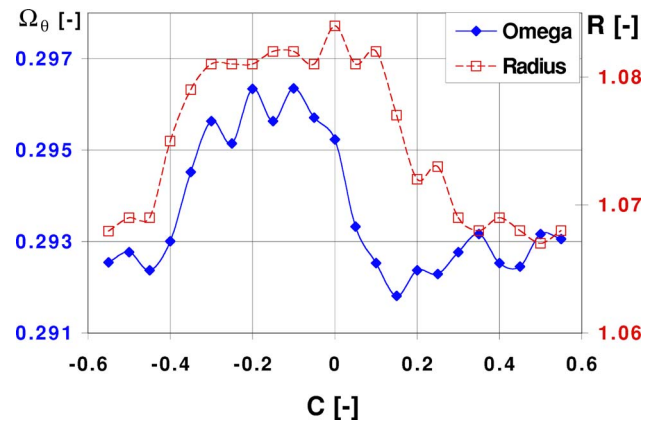

Fig. 8 Vorticity and radial position of the toroidal vortex

moved into the midaxial gap position. This movement is continued in the next circumferential position while the magnitude of vorticity diminishes. At the end of the periodic cycle the region of higher vorticity merges with the flow region close to the shroud as can be observed in Fig. 6(*a*). It is through this process that vorticity is entrained into the toroidal vortex.

The radial position and the angular speed defined at the center of the toroidal vortex are presented in Fig. 8. As the cavity flow swirls in negative C direction, the vortex encounters stretching and tilting in the absolute frame. The cause of the spinning up and down of the vortex can be found in the static pressure field given in Fig. 4(*b*). Within the cavity at $C=0.4$ a local maximum of static pressure is observed, and vorticity of the toroidal vortex is low. The fluid within the vortex accelerates due to a favorable tangential static pressure gradient. At $C=-0.1$ the vortex reaches a low pressure field and vorticity is high. While passing one stator pitch the vortex is pushed outward to $R=1.08$ and the moves back to the lower radius $R=1.07$. The maximum absolute difference in radial position is 1.4 mm which is 7% of the cavity height. The resolution of the measurement grid in axial direction is not sufficient to detect an axial displacement of the vortex. Therefore, the axial position is given to $Z=0.41$ as discussed in Fig. 6.

Mass Flows Involved. The leakage mass flow, which passes the labyrinth, can be estimated using an empirical correlation. The correlation applied is given in Traupel [15],

$$\dot{m}_{\text{leak}} = Se\sqrt{p\rho} \tag{1}$$

where S is the gap area and e denotes the discharge coefficient. The latter depends on the pressure ratio and the number of sealing fins and was determined to be 0.17. With the conditions present in the inlet cavity to the labyrinth and the average gap width of 0.36% blade span the leakage mass flow is calculated to 0.52% of the main mass flow.

Table 2 compares the estimated leakage mass flow with the integrated probe measurements. The corresponding locations of integration are given in Fig. 9. Non-slip boundary conditions at $Z=0$ and $Z=1$ are considered in the integration procedure. The continuity of mass within the cavity states that all investigated mass flows must satisfy the equation

Table 2 Mass flows, % of main mass flow

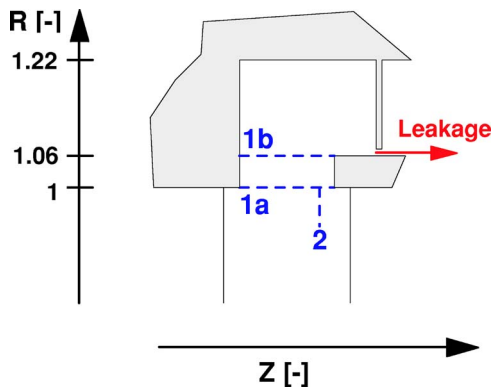| Station	In ($v_r > 0$)	Out ($v_r < 0$)	Sum
1(a)	1.56	−1.44	0.12
1(b)	2.42	−1.85	0.57
2	⋯	−1.52	⋯
Traupel	⋯	⋯	0.52

Fig. 9 Stations of mass flow integration

$$\dot{m}_{\text{leak}} = \dot{m}_{\text{in}} + \dot{m}_{\text{out}} \qquad (2)$$

Integrating the radial velocity components at position 1a, gives a lower net mass flow than the estimated leakage mass flow. The grid spacing in axial direction is too coarse to capture the flow gradients close to the shroud leading edge. In addition, the toroidal vortex is cut far away from the center, which reduces the radial velocity components. At area 1b, much more rotating mass is involved, since this plane cuts the vortex close to the center. Furthermore, the new boundary layer at the shroud leading edge has grown, which results in an integrated mass flow close to the leakage mass flow.

In station 2 an area of $0.93 < R < 1$ and $-0.45 < C < -0.1$ was integrated. This area fulfills two conditions. First, the streamlines have passed the outflow region on the suction side of the wake, e.g., in Fig. 5 $C = 0.15\ldots0.2$ and $Z = 0.25$. Second, the radial velocity is negative. The fluid particles enter the rotor passage. The axial velocity component sums up to 1.52% of the main mass flow, which is about three times higher than the leakage mass flow.

Integrating the tangential velocity components from $R = 0.99$ to $R = 1.22$ and $Z = 0$ to $Z = 1$, a swirling mass flow of 0.3% is found. The missing part of the cavity flow of $Z > 1$ was estimated to have 0.1% assuming an average tangential velocity as in the measured part of the cavity flow. The swirling mass flow in the boundaries of $R = 0$ to 0.99, and form trailing to leading edge was estimated at 1.7%. Therefore, the cavity flow comprises an estimated 24% of the swirling mass flow between the blade rows.

Relative Frame of Reference. In this section the measurement results of the virtual four sensor probe are presented in the relative frame of reference. Figure 10 shows the time averaged relative
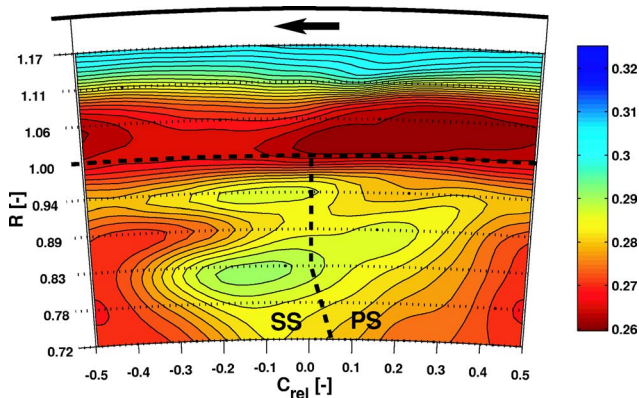

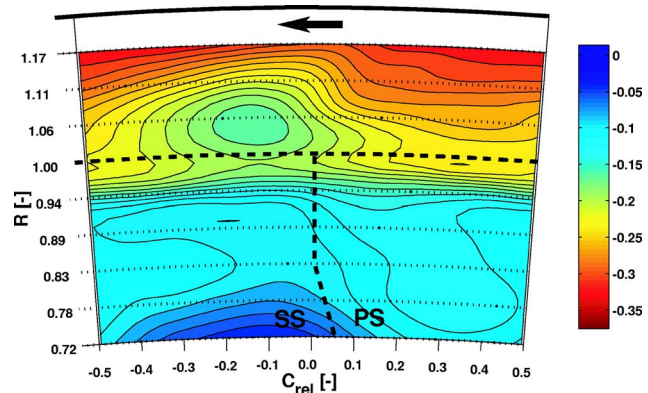**Fig. 10 Time averaged relative total pressure $C_{\text{porel}}[-]$ rotor relative, $Z = 0.5$**

total pressure. The tip radius is indicated with a thick dashed line. The leading edge position of the rotor is given by the vertical dashed line at $C_{\text{rel}} = 0$. The view is upstream and the arrow indicates the sense of rotation of the coordinate system.

Within the cavity the relative total pressure shows a wavy structure but has a lower variation than in the main flow region. At the cavity floor, the relative total pressure is higher than upstream of the shroud leading edge.

The incoming flow field to the rotor passage is dominated by a high relative total pressure region at $C_{\text{rel}} = 0$. The pressure contours are a result of two superimposed effects of the rotor blade on the upstream flow field. One is the leading edge potential field being responsible for an increase in static pressure. The other is found in the through flow distribution which is set up in a rotor passage due to the turning of the flow. The highest velocity is present on the suction side of an airfoil, where the local axial through flow reaches a maximum. The upstream effect of this interaction causes a higher relative dynamic head on the suction side of the leading edge. Figure 10 confirms this observation, where a region of higher relative total pressure at $C_{\text{rel}} = -0.15$ and $R = 0.81$ is present.

The relative circumferential velocity distribution at $Z = 0.5$ is given in Fig. 11. The cavity flow is swirling at a lower tangential velocity than the rotational speed of the rotor. Close to the cavity floor the values are high negative. The center of the cavity vortex at $R = 1.07$ is accelerated and decelerated according to the static pressure field. The cavity vortex fluid moves into positive C_{rel} direction. The fluid is accelerated out of the high static pressure region across the leading edge position until it reaches the maximum relative velocity at $C_{\text{rel}} = 0.4$. The static pressure there is therefore low. Close to the rotor leading edge the static pressure field induced by its potential field is clearly evident. Figure 12 shows a high static pressure upstream of the rotor leading edge. This pressure field propagates into the cavity at the speed of sound. In the main flow region a low pressure faces the rotor passage.

The potential field causes the distribution of relative radial velocity as presented in Fig. 13. In the time average the tip end wall of the rotor passage ($R = 1$) exceeds positive and negative radial flow over the entire pitch. Additional radial inflow must occur closer to the shroud leading edge ($Z > 0.83$) since the radial velocity is highly positive at $R = 1.08$ and $C_{\text{rel}} = 0.25$. Surprisingly, the highest positive radial velocity is not found at $C_{\text{rel}} = 0$ directly above the leading edge. One reason could be that the relative movement of the fluid particles from the location of the inflow ($Z > 0.83$, $C_{\text{rel}} = 0$) up to the location of measurement results in a circumferential shift. Looking at the relative tangential velocity (Fig. 11), one can observe values of around -0.2 in the relevant area and an average radial velocity of 0.1 can be given. The di-
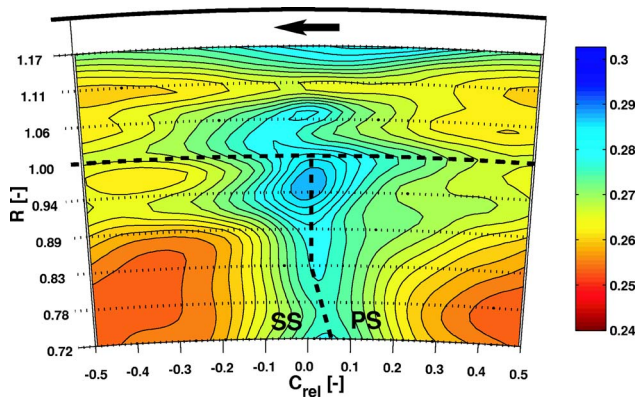
Fig. 11 Time averaged relative tangential velocity $v_{\theta\text{rel}}[-]$ rotor relative, $Z = 0.5$

Fig. 12 Time averaged static pressure $C_p[-]$ rotor relative, $Z = 0.83$

rection of relative convection is indicated from the vector addition of the corresponding arrow of the radial and tangential velocity components. The resulting vector points from the intersection point of the stator leading edge and shroud to the maximum of radial velocity.

Unsteady Flow Field. The unsteady flow field is discussed with the help of Figs. 14 and 15, which show the non-dimensional total pressure and the non-dimensional tangential vorticity component. One period of rotor blade passing is resolved with four time frames. The data are given in the absolute frame of reference. The thick dashed lines indicate the blade tip radius as well as the leading edge position of the rotor. For clarity the latter is shown as a straight line.

The total pressure sequence starts with the rotor leading edge aligned with the stator wake. Comparing Figs. 4(a) and 14(a) the loss core has an increased value due to the potential effect. Following the time sequence the loss core region undergoes large changes in position, size and magnitude of pressure. If the open rotor passage is facing the loss core, as in $t/T=0.5$, the loss core covers a large area and values are low due to the accelerating lower static pressure.

Directing the attention to the cavity flow, regions of high and low total pressure are apparent. They move with rotor blade velocity. The high pressure region is $\Delta C=0.15$ ahead of the rotor leading edge position. Note, that it is more round shaped and covers 30% of pitch, whereas the low pressure region is more narrow shaped and covers 70% of pitch. The low pressure region also coincides with the region of high negative relative tangential velocity in Fig. 11.

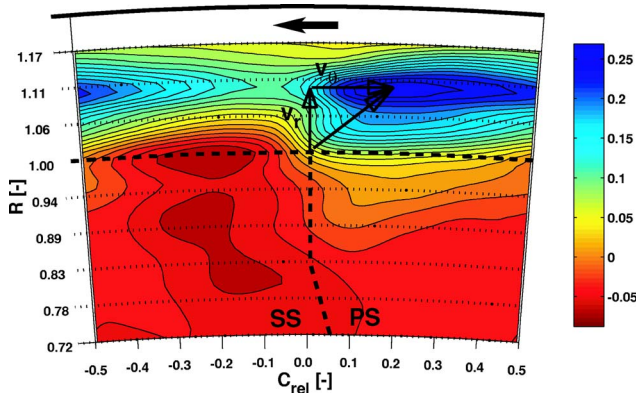The wavy shear layer has changed the form in comparison to

the time averaged picture. At $C=0$ in the initial time step the shear layer enters the main flow as deep as $R=0.94$. The S shape with the center at $C=-0.1$ is more pronounced. At $t/T=0.25$ it reaches to $R=0.91$ but has a minimum total pressure at $R=0.96$ and $C=0$. The outflow area, as it was determined in Fig. 4, undergoes unsteady periodic variations. The changes to the position of inflow ($C=-0.25, R=0.98$), however, are less affected by the rotor interactions.

The rotor passage experiences an unsteady flow field as boundary condition. The mass flow is varying in time, since the area and velocity are changing with time. Recalling the results found of Table 2 in Fig. 9, unsteady fluctuations will also be encountered. Further investigations are planned to quantify the unsteady mass flow interactions with the rotor tip area.

The time sequence of the nondimensional circumferential vorticity component as given in Fig. 15 shows the unsteady vortex evolution within the cavity as well as the secondary flow field of the stator exit flow. At the first time step high positive values at $C=0.1$ and $R=0.89$ indicate the position of the passage vortex. The region of high negative values at $C=-0.05$ and $R=0.8$ coincides with the tangential total pressure gradient in Fig. 14. Radial migration within the wake and the loss core can have this effect on vorticity. The loss core region faces the rotor leading edge. As the rotor moves in time, both regions change their size and value. At $t/T=0.5$, the covered area is large and the measured vorticity values are lower than at the beginning of the sequence. Thus, the rotor passage is facing the loss core region.

The center of the toroidal vortex is found at radii around 1.1. This is located higher than the position determined with the five hole probe measurements in Fig. 8. Regions of high and low vorticity alternate in a similar manner as the total pressure in Fig. 14. The high vorticity coincides with low total pressure regions. Looking at the first time step $t/T=0$ the pitch wise variation of vorticity at $R=1.1$ ranges from 0.1 to 0.4. The maximum time averaged value found in Fig. 6 was 0.3. The vortex changes rotational speed in both space and time. The amplitude of the unsteady vorticity fluctuation is larger than the time averaged, pitch wise variations measured with the five hole probe in Fig. 8. The sign of vorticity does not change in time.

Furthermore, the unsteady mechanism of vorticity entrainment into the toroidal vortex can be discussed. The inflow region at $R=1$ and $C=-0.35$ encounters a local positive maximum of tangential vorticity [Figs. 4(a) and 8(b)]. While the region of high vorticity within the cavity passes this position, both areas merge together ($t/T=0.74$). Due to higher gradients vorticity is also transferred into the low vorticity regions of the toroidal vortex at this point ($t/T=0.25$).

Summary

Comprehensive Flow Model.

Overview. The flow field of the inlet cavity and the interaction zone is dominated by a three-dimensional, periodic unsteady static pressure field. Four independent sources of pressure fields are present:

- stator pressure field (uncovered turning);
- rotor pressure field (leading edge);
- cavity recess (step in and out); and
- annular casing (radial pressure gradient).

The periodic unsteadiness stems from the relative movement of the rotor pressure field. Due to the interference of the stator and rotor pressure field, the kinematic flow parameters, e.g., flow angles, velocity components, mass flows, experience high and low amplitudes, which depend on space and time.

The kinematic boundary condition to the flow area is set up by the stator exit flow containing wakes, boundary layers and secondary flow structures. This results in specific areas of inflow and
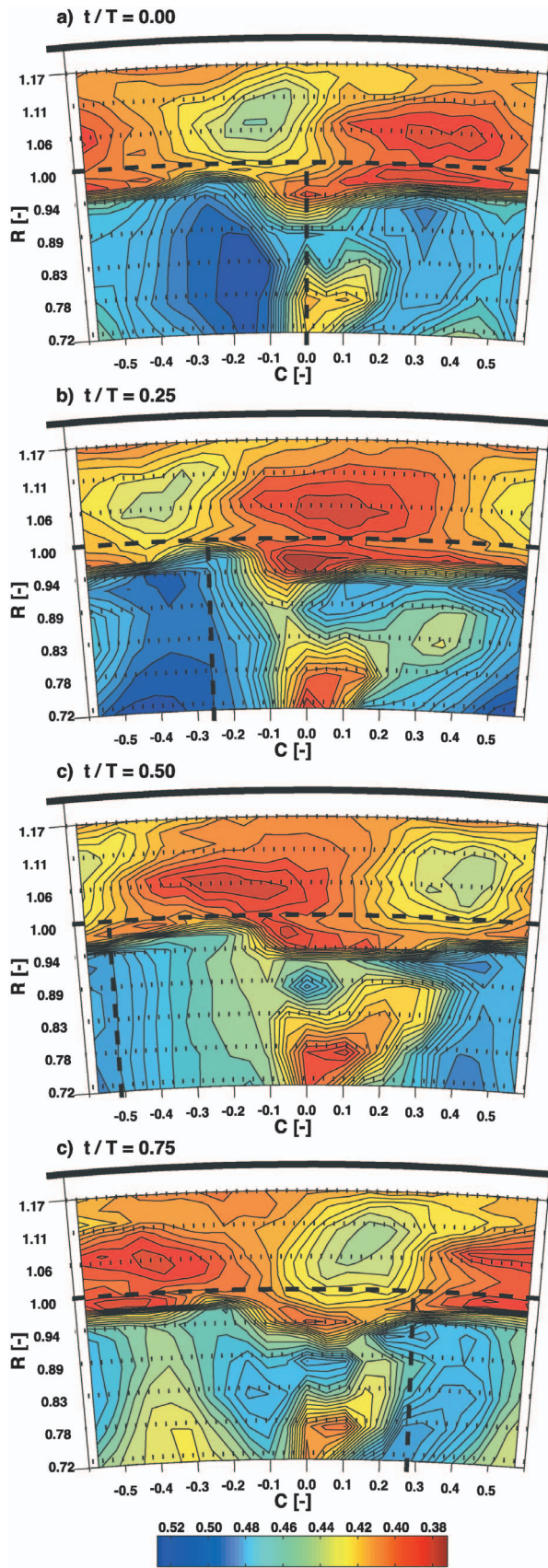

Fig. 13 Time averaged radial velocity $v_r[-]$ rotor relative, $Z = 0.83$

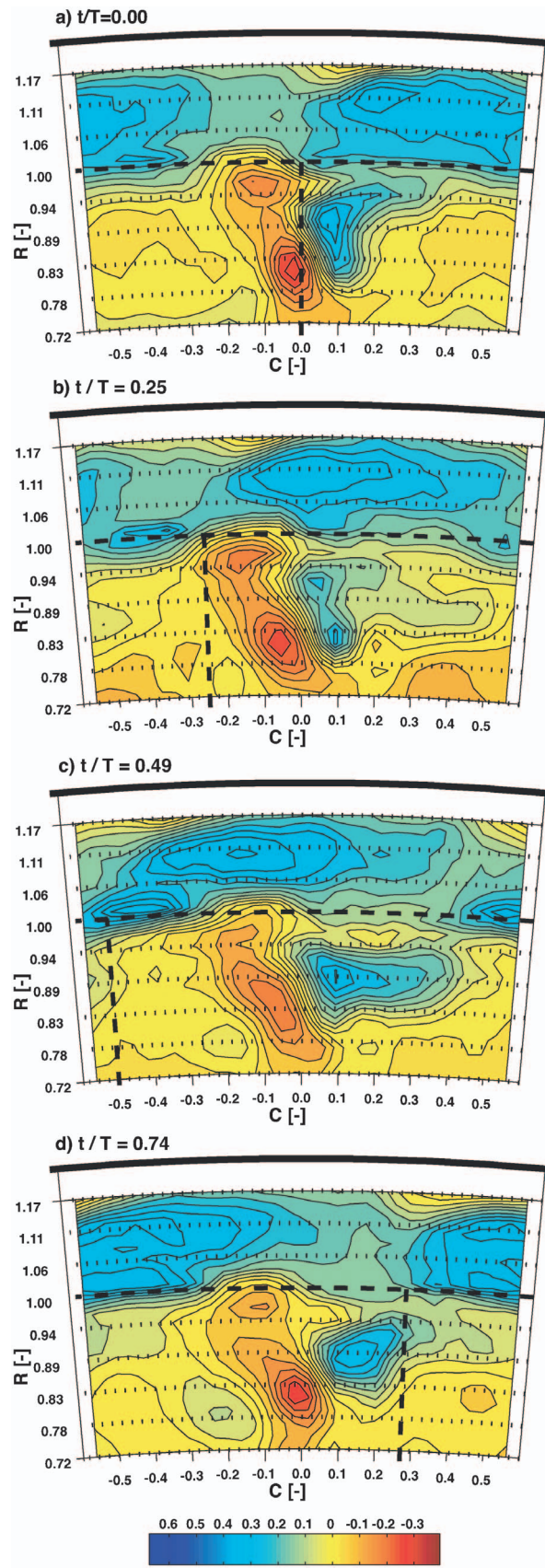**Fig. 14   Time sequence of total pressure $C_{po}[-]$, $Z=0.5$**

Fig. 15   Time sequence of tangential vorticity $\Omega_\theta[-]$, $Z=0.5$

Table 3 Identified drivers of the toroidal vortex

|	Stator	Rotor
Tangential momentum	In flow	Non-slip condition Potential field
Tangential vorticity	In flow Axial velocity shear profile	Radial pumping
Stretching	Potential field	Potential field

outflow for the cavity flow. Close to the exit of the flow area the kinematic effects are shaped by the radial pumping effect of the rotor leading edge alternating with the open rotor passage.

The interaction zone between main flow and cavity flow is dominated by a toroidal vortex. Additionally, this vortex moves at an average tangential velocity of 90% of the blade tip speed. This vortex undergoes stretching and tilting in space and time caused by different drivers of the cavity flow. They are summarized in Table 3.

Detailed Discussion. A sketch of the flow drivers is given in Fig. 16. The inflow and outflow regions are boundary conditions set by the exit flow field of the stator. The high potential fluid originating from the stator pressure side corner has enough kinetic energy to penetrate into the cavity. Radial equilibrium is not maintained in this area and the fluid follows a tangential direction, feeding tangential momentum to the cavity fluid. Due to the high axial velocity component, which is then turned into radial flow, the incoming fluid also contributes to the rotational movement of the vortex.

The outflow contains mixed cavity fluid of low total pressure, low tangential momentum, and negative incidence to the rotor tip profile section. This fluid affects the rotor passage flow field in an adverse way by increasing secondary flows and by doing less work on the rotor blades. Because of continuity, it balances the cavity inflow.

The cavity vortex system swirls at a lower velocity than the rotational speed of the shroud tip. This is due to mixing losses
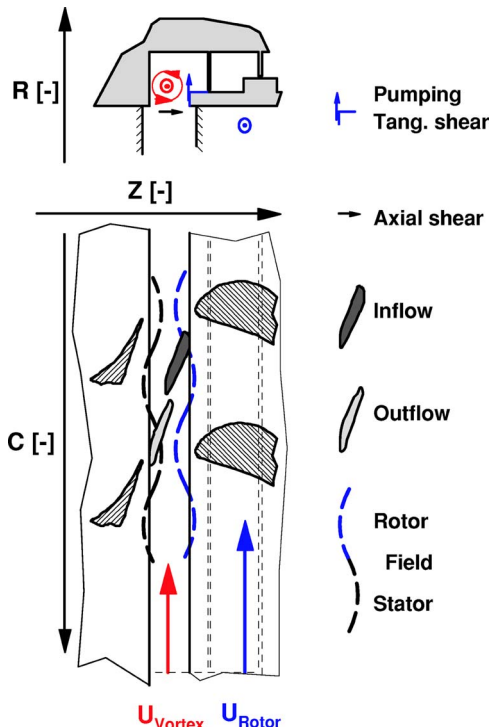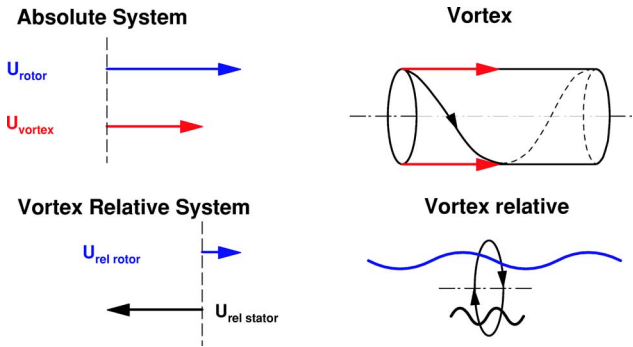
Fig. 17 Vortex relative system

within the vortices as well as to shearing effects of the boundary layer at the non-rotating walls. In addition the leakage mass flow transports tangential momentum into the next cavity.

In order to better understand the effects on the fluid movements, a flow relative system is helpful. A vortex relative coordinate system is proposed as described in Fig. 17. It rotates at the average tangential velocity of the toroidal vortex. By moving with the vortex in the swirling direction, rotor and stator events pass at two different relative velocities. These events correspond to two counter moving waves assuming rotor and stator pressure fields are standing sinusoidal waves in space. Then a dual frequency modulation acts on the vortex. Both frequencies satisfy the relation

$$f = f_{\text{rotor,rel}} + f_{\text{stator,rel}}. \tag{3}$$

In this case the frequencies are split into 17% of blade passing frequency for the rotor relative and 83% for the stator relative frequency. The wavelength of the two frequencies is also depicted schematically in Fig. 17.

Further investigations will be dedicated to derive a mathematical model by describing the flow in the vortex relative system. The goal is to model unsteady loss production terms and compare them to the experimental data in a quantitative way. A small perturbation analysis will then allow us to derive important parameters and scales for the loss production in this area. Additionally, the question might be answered as to whether unsteady loss is higher or lower than the steady loss. Future work will be dedicated to the mathematical modeling of the vortex and the quantification of steady and unsteady loss production terms with the help of the vortex relative system.

Impact on Efficiency. Using the available time averaged results, it is estimated that this labyrinth seal configuration results in a loss of about 1.6% per stage in efficiency for this turbine. The circumferential momentum of the leakage mass flow gets mixed out across the labyrinth. Measurements of the leakage jet entering the exit cavity indicate low circumferential momentum. The toroidal vortex by itself seems to contribute a small portion of efficiency loss around 0.1%. However, further losses in the rotor blade row due to the vortex interaction and the reentering cavity mass flow are not accounted for. These are estimated values based on the available data. It is planned that a more detailed integration and sensitivity analysis will be performed and presented at a later time. Additional measurements have been made with variations in seal clearance gap. Initial indications show that variation in the gap has a major effect on flow structures and turbine loss.

Conclusions

This paper presents a highly resolved experimental data set taken in an inlet cavity of a rotor tip labyrinth seal. The high resolution in space and time of flow angles and total and static pressure make it possible to derive further parameters, e.g., the velocity field or the vorticity field.

Fig. 16 Flow model: Side and above view

The drivers of the cavity flow could be identified. The unsteady flow interaction stems from the unsteady static pressure field interaction. The toroidal vortex found in the inlet cavity is described in detail. It is subject to unsteady vortex stretching and tilting. The total pressure fluctuations in the cavity outflow suggest an unsteady, low total pressure disturbance of the rotor tip region. Associated with this are a negative incidence and an average mass flow of 1.5% of the main mass flow. A vortex relative coordinate system swirling at the same average speed as the toroidal vortex is proposed.

Acknowledgment

Nomenclature

$$a = \text{speed of sound}$$
$$r, \theta, z = \text{cylindrical coordinate system}$$
$$h = \text{blade height, 90 mm}$$
$$z_{\text{cav}} = \text{axial cavity width, 15 mm}$$
$$n = \text{numbers of blades, 42}$$
$$f_{\text{blade}} = \text{blade passing frequency}$$
$$p = \text{blade pitch, } 360°/42$$
$$t = \text{time}$$
$$C = \text{non-dimensional circumferential position } \theta/p$$
$$\text{M} = \text{Mach number}$$
$$R = \text{non-dimensional radial height}$$

$$\frac{r - r_{\text{Hub}}}{r_{\text{Tip}} - r_{\text{Hub}}}$$

$$\text{Re} = \text{Reynolds number}$$
$$T = \text{blade passing period } 1/f_{\text{blade}}, \text{ temperature}$$
$$U = \text{blade tip speed}$$
$$Z = \text{non-dimensional axial distance } z/z_{\text{cav}}$$
$$v = \text{non-dimensional velocity } u_{\text{loc}}/U$$
$$C_p = \text{non-dimensional pressure}$$

$$C_p = \frac{p_{\text{local}} - p_{\text{stat,out}}}{p_{\text{total,in}} - p_{\text{stat,out}}}$$

$$\alpha = \text{yaw angle}$$
$$\beta = \text{pitch angle}$$
$$\Omega = \text{nondimensional vorticity } \omega/(4\pi f_{\text{blade}})$$

References

[1] Gregory-Smith, D. G., Ingram, G., Jayaraman, P., Harvey, N. W., and Rose, M. G., 2001, "Non-Axisymmetric Turbine End Wall Profiling," Proc. Inst. Mech. Eng., **215**(A6), pp. 721–734.
[2] Sauer, H., Muller, R., and Vogeler, K., 2001, "Reduction of Secondary Flow Losses in Turbine Cascades by Leading Edge Modifications at the Endwall," J. Turbomach., **123**, pp. 207–213.
[3] Denton, J. D., and Johnson, C. G., 1976, "An Experimental Study of the Tip Leakage Flow around Shrouded Turbine Blades," CEGB research Report No. CEGB-R/M/N848.
[4] Peters, P., Breisig, V., Giboni, A., Lerner, C., and Pfost, H., 2000, "The Influence of the Clearance of Shrouded Rotor Blades on the Development of the Flow Field and Losses in the Subsequent Stator," ASME Paper No. GT2000-0478.
[5] Hunter, S. D., Manwaring, S. R., 2000, "Endwall Cavity Flow Effects on Gaspath Aerodynamics in an Axial Flow Turbine: Part 1-Experimental and Numerical Investigation," ASME Paper No. GT2000-065.
[6] Wallis, A. M., Denton, J. D., and Demargne, A. A. J., 2001, "The Control of Shroud Leakage Flows to Reduce Aerodynamic Losses in a Low Aspect Ratio, Shrouded Axial Flow Turbine," Appl. Math. Model., **123**, pp. 334–341.
[7] Anker, J. E., and Mayer, J. F., 2002, "Simulation of the Interaction of Labyrinth Seal Leakage Flow and Main Flow in an Axial Turbine," ASME Paper No. GT2002-30348, ASME Turbo Expo, June, Amsterdam.
[8] Schlienger, J., Pfau, A., Kalfas, A. I., and Abhari, R. S., 2003, "Effects of Labyrinth Seal Variation on Multistage Axial Turbine Flow," ASME Paper No. GT2003-38128.
[9] Pfau, A., Treiber, M., Sell, M., and Gyarmathy, G., 2001, "Flow Interaction from the Exit Cavity of an Axial Turbine Blade Row Labyrinth Seal," J. Turbomach., **123**, pp. 342–352.
[10] Binder, A., 1985, "Turbulence Production Due to Secondary Vortex Cutting in a Turbine Rotor," J. Eng. Gas Turbines Power, **107**(4), pp. 1039–1046.
[11] Chaluvadi, V. S. P., Kalfas, A. I., Baniegbal, M. R., Hodson, H. P., and Denton, J. D., 2001, "Blade Row Interaction in a High Pressure Turbine," AIAA J., **17**(4), pp. 892–901.
[12] Pfau, A., Schlienger, J., Kalfas, A. I., and Abhari, R. S., 2003, "Unsteady, 3-Dimensional Flow Measurement Using a Miniature Virtual 4 Sensor Fast Response Aerodynamic Probe (FRAP)," ASME Paper No. GT2003-38128.
[13] Sell, M., Schlienger, J., Pfau, A., Treiber, M., and Abhari, R. S., 2001, "The 2-Stage Axial Turbine Test Facility LISA," ASME Paper No. GT2001-0492.
[14] Treiber, M., Kupferschmied, P., and Gyarmathy, G., 1998, "Analysis of the Error Propagation Arising from Measurements with a Miniature Pneumatic 5-Hole Probe," *Proc., 13th Symp. on Measuring Techniques in Cascades and Turbomachines*, Limerick, Ireland.
[15] Traupel, W., 1977, *Thermische Strömungsmaschinen*, Springer, Berlin.

Design and Test of an Ultralow Solidity Flow-Controlled Compressor Stator

K. R. Kirtley

P. Graziosi

GE Global Research,
Niskayuna, NY 12309

P. Wood

B. Beacher

H.-W. Shin

GE Aircraft Engines,
Cincinnati, OH 45215

A full annulus fluidic flow-controlled compressor stator ring was designed and tested in the third stage of a four-stage low-speed research compressor. The solidity of the flow-controlled stator was near unity and significantly below design practice with a commensurately high diffusion factor. The design intent was to reduce the vane count by 30% and load the stator to the point of stall at the design point, then employ flow control to restore attached boundary layers and regain design-point stage matching. The flow control applied, which maintained attached flow, was 1% of the compressor mass flow and was introduced via discrete steady jets on the suction side of the stator. The design method used steady Computational Fluid Dynamics (CFD) with the flow control jets simulated to drive stator exit angles, velocities, and blockage to match the baseline machine. The experiment verified the pretest predictions and demonstrated degraded compressor performance without flow control and restoration of the pumping characteristics of the baseline high solidity compressor when flow control was applied. An assessment of the engine cycle impact of the flow-controlled compressor shows a 2.1 point stage efficiency reduction for the increased loading. Extrapolation of the data and analysis to a high-speed compressor shows a more modest 0.5 point stage efficiency trade.
[DOI: 10.1115/1.1860374]

Introduction

Fluidic flow control is not a new concept but is an emerging technology in its application to manage the deleterious effect of diffusing boundary layers in aircraft engine components. Steady suction and blowing, pulsing, and synthetic jets are all means to remove low energy flow, replace momentum defects, or promote mixing that inhibit boundary layer separation. Ball [1,2], demonstrated the technique in offset S-type diffusers. From that point, the literature shows rapid growth in benchmark experiments of flow control and development of flow control actuation methods. Wadia and Mielke [3] patented a self-aspirated compressor concept, but the vision of flow control in the turbomachinery of gas turbine engines was not articulated in the engineering literature until Kerrebrock et al. [4] presented design ideas for an aspirated fan to significantly increase pressure ratio. Lord et al. [5] took a broader view and proposed methods to significantly increase loading and reduce engine length via aggressive controlled diffusion in multiple engine components. The performance of gas turbine engines is, for all intents and purposes, limited by boundary layer diffusion, and the compressor is perhaps the most limited. Carter et al. [6] demonstrated significant increases in diffusion factor for a linear compressor cascade using an embedded ejector pump designed to provide a combination of suction and blowing. The benefit of the suction-blowing combination over straight blowing is not clear, and ejector pumps are not particularly efficient devices in motivating fluid. To discriminate, the flow control benefits must be weighed against the system-level impact when applied to an engine. Bons et al. [7] applied unsteady pulsed vortex generator jets to control low-pressure turbine boundary layer separation. To maintain attached flow, their result shows a substantial reduction in required total momentum of flow control when a combination of low- and high-frequency unsteadiness is imparted to the vortex generator jets. The general benefit of flow control on diffusion in cascade tests was corroborated by a NASA Glenn test. Culley et al. [8] investigated flow control in a low-speed compressor by restaggering two individual stator vanes in the third-stage ring of a four-stage research compressor. The focus of their effort was to explore unsteady blowing techniques to remove separated flow from the restaggered vanes. Their results again show the benefit of unsteady blowing in reducing the total momentum required to maintain attached boundary layers with a commensurate reduction in loss. However, by virtue of controlling only two airfoils in the stator ring, the impact of flow-controlled airfoils on the full compressor could not be assessed.

Schuler et al. [9] tested a full transonic fan stage specifically designed with boundary layer suction to achieve a significant pressure rise. Suction slots on the fan and the Outlet Guide Vane (OGV) as well as the endwall were applied with a design suction requirement of 4.65% of the throughflow mass. Reinjection of this low energy flow into the engine cycle without significant penalty is an aerothermodynamic challenge. Still, the strong performance over its entire operating range shows that aspirated fans could have a future in engine design. But does flow control technology have a future in a core compressor? Can flow control be used to significantly increase loading and allow for reduced part count and length in an engine core without adversely impacting the overall specific fuel consumption after properly accounting for thermodynamic effects? The goal of the current effort is to answer these questions.

To test the concept of higher stage loading via flow control, an ultralow solidity flow-controlled stator has been designed to replace a highly loaded conventional uncontrolled third-stage stator and match the compressor. While Culley's [8] work focused on advanced actuation methods to remove separation and reduce loss, the current work is focused on design for flow control, stage matching, and compressor operability when flow control is employed. The current design philosophy can be simply stated: reduce the vane count by 30% and load the stator to the point of stall at the design point, then employ flow control to restore attached boundary layers and regain design-point stage matching.

Demonstrating aerodynamic viability of such a concept is not

Fig. 1 (*a*) **Solidity and** (*b*) **diffusion factor**

changes were applied to facilitate a steady flow control scheme and restore compressor matching back to the levels measured with the conventional stage 3 vanes.

First, the maximum thickness of the airfoil was increased 25% to accommodate a settling plenum inside the airfoil. The plenum was designed as large as possible and included a structural support that also guided the jet from the trunnion feed toward the rear of the plenum so as not to interfere directly with the individual blowing holes.

Second, the camber of each section was adjusted to match the baseline airfoil's absolute exit angle to within $\pm\frac{1}{4}$ deg since the flow-controlled vane was predicted to have a different deviation angle. This requirement led to slightly less camber at midspan and more near the endwalls. Assessment of each design attempt was made with CFD using surface source terms to represent the net flux of mass, momentum, and energy into the domain at the location of each blowing hole. The method is discussed by Hunter and Orkwis [13] and has been shown to give an accurate description of film cooling when sufficient mesh resolution is used.

Third, only suction-side blowing was contemplated to reduce the cost and complexity of the implementation. The total momentum of injection was modulated in an attempt to match the wake depth of the baseline airfoil and therefore the blockage experienced by the following rotor. The flow control levels were fixed while the camber was adjusted. Finally, some thought was given to a radial restack of the airfoil to better match the radial flow distribution of the baseline airfoil. The final decision made was to maintain a similar stacking relative to the higher solidity vane and rely on the CFD analyses, indicating that additional blowing holes at the outer part of the vane would keep the near-wall suction surface healthy.

An expected result when controlling a three-dimensional (3D) highly loaded diffuser is that the next-weakest wall will separate once the weakest wall becomes attached. Complete control could therefore require a complex design with endwall control and perhaps even pressure-side control. CFD analyses indicated that this design did not warrant such a scheme. In hindsight, not restacking the airfoil led to a nonoptimal result but did not diminish the successful outcome of the test.

The CFD analysis showed that a momentum scaling law applied in determining the extent to which flow separation was prevented over the suction side of the airfoil. Therefore the ratio of total blowing to total free-stream momentum flux was set as the key controlling parameter in designing the flow control holes. A total momentum ratio of 2.2% was found to produce wakes similar to the baseline high solidity stator. Then for a fixed total momentum, one can vary the hole size and produce Fig. 2.

The important point is that the required power (shown in ft-lbf/s) drops with increased hole diameter (in.) because the driving pressure ratio (blowing total to free-stream static) and the resulting Mach ratio (blowing to freestream) are reduced. Correspondingly, the blowing mass flow rate increases, but it is the required power that impacts the engine cycle. It is expected then that the higher mass flow rate delivered at lower pressure yields a lower overall penalty than lower mass flow rate delivered at higher pressure. Consequently, in an engine application, the hole size is chosen based on the desired momentum ratio and the available pressure at the extraction point for the blowing air. Although momentum scaling laws hold for this low-speed flow, the Mach number ratio must still be greater than 1 to repair a separated boundary layer [14]. Based on these considerations, a hole size of diameter 0.127 cm (0.05 in.) was chosen.

A very conservative flow control system was implemented. Nineteen equally spaced flow control holes were pointed in the streamwise direction at a 20 deg angle to the airfoil surface and set just aft of the suction peak but upstream of the computed separation point. Complicating the hole placement was the high suction-side curvature of the airfoil and the necessity to have a hole length to diameter ratio greater than 1.5 to guarantee the

sufficient to guarantee acceptance on an engine. The penalties on the engine system, which are incurred in order to gain the loading, must always be considered to offset the benefit. Choosing the right application in these terms is the real challenge of flow control. Therefore, a discussion of the engine cycle impact of a highly loaded flow-controlled compressor is presented.

Design of the Flow-Controlled Stator. The test vehicle was an advanced technology highly loaded high-reaction compressor with forward swept rotors detailed by McNulty et al. [10]. While the static pressure rise through the stators was modest, the loading was still high because the turning was significant. The diffusion factor for the baseline stator was around 0.5.

The baseline stator ring tested in GE Aircraft Engines' Low Speed Research Compressor (LSRC) had 74 airfoils with a span of 11.43 cm and a tip chord of 10.5 cm. The flow-controlled airfoil count was set at 53 for the simple reason that a stator retention ring for 53 IGV's already existed for the LSRC. The reduction in solidity produced the desired increase in diffusion factor of 25% and a 30% reduction of solidity to below unity at midspan (see Fig. 1).

With a midspan diffusion factor in excess of 0.6, boundary layer separation was anticipated and CFD analyses, which applied a steady Reynolds Averaged Navier-Stokes (RANS) solver [11,12] and GE Aircraft Engines' best practices, indicated massive boundary layer separation. With this level of degradation at the design point, the candidate airfoil solidity was fixed. Minor design

Fig. 2 Flow control characteristics versus hole diameter

Fig. 4 Flow-controlled airfoil installed in stator ring

desired 20 deg leaving angle for the blowing jets. Wall thickness and plenum volume also had to be considered. Two additional holes were placed near the tip along the chord in an effort to boost the casing flow because the CFD indicated a general weakness of the flow there. A bench test of the airfoil showed reasonable uniformity of the total pressure leaving each hole with the highest pressures near the trunnion feed and lowest near the hub. A photo of one of the 53 flow-controlled stators is presented in Fig. 3. The stator was set in the annulus via the trunnion on the right, and the hub was sealed during testing.

Flow control air for each airfoil was fed through the blade retention trunnion that was bored to 0.8 cm dia. Flexible tubing connected the airfoil feed to a toroidal plenum constructed of PVC pipe that surrounded the compressor case. Four separate pipes of equal length connected to shop air downstream of a valve fed the plenum. Figure 4 shows the installation of the flow-controlled airfoils, and Fig. 5 shows the assembled compressor in operation. Data were acquired during compressor operation that showed reasonable uniformity of flow feeding each stator. Maximum variation was 10% peak to peak.

Experimental Setup. GE's Low Speed Research Compressor (LSRC) is a four-stage machine designed to represent the essential features of modern high-speed core compressors. The successful transfer of design philosophies verified in the LSRC to high-speed
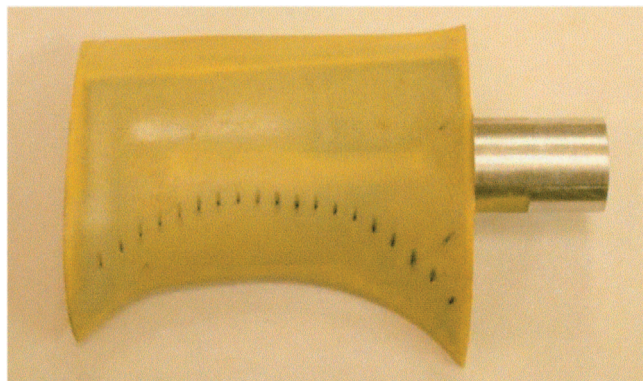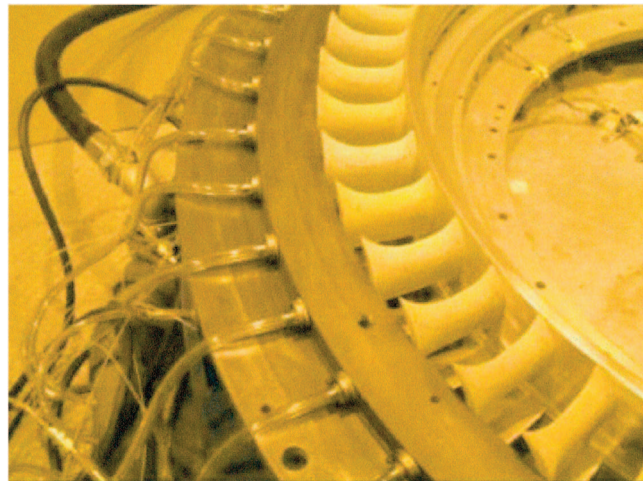
machines is well established. The design creates a repeating stage environment with identical rotors and stators. Rotor one is the limiting rotor and casing treatment is employed to extend its range. Detailed investigations are usually conducted on stage 3 because a repeating stage environment is fully established there. The facility is more completely described by Wisler [15].

The steady-state instrumentation embodies high-resolution pressure transducers, accurate to ±0.010% of the full scale values of either 0.068 or 0.136 bar (1 or 2 psi) and were used to record steady-state static and total pressures for determining overall compressor performance. Frequent calibrations were conducted during the test period. Surface static pressure data could not be acquired on the flow-controlled stator due to the presence of the internal plenum and the fact that the blade retention trunnion, normally used to extract the airfoil pressures, was used to deliver the flow control to the internal plenum. A strain-gage torque meter, accurate to ±0.07% of measured torque, was used to deduce shaft work input to quantify compressor efficiency. Overall measurement accuracy is as follows: flow and pressure coefficients are accurate to within ±0.15% and efficiency to within ±0.25 points. The velocity, flow angle, and unsteadiness characteristics entering and exiting the airfoil rows were measured with TSI 1240-20 "X" hot-film probe. Hot film calibration was done in a free jet, providing an estimated measurement accuracy of ±1.0% for velocity and ±0.5 deg for flow angle.

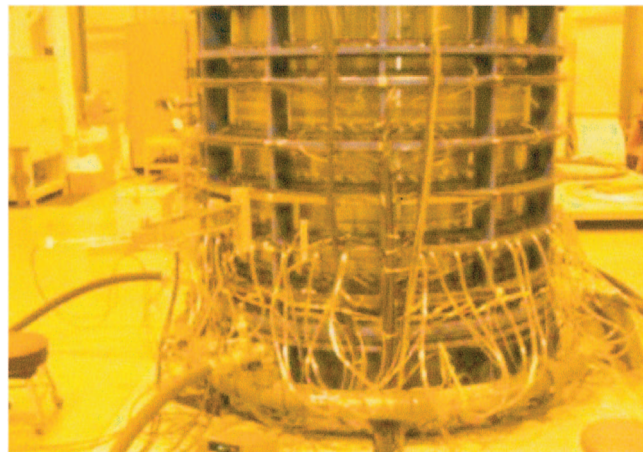Since the four-stage compressor was designed to create a re-

Fig. 3 Flow-controlled airfoil

Fig. 5 Assembled compressor

Journal of Turbomachinery
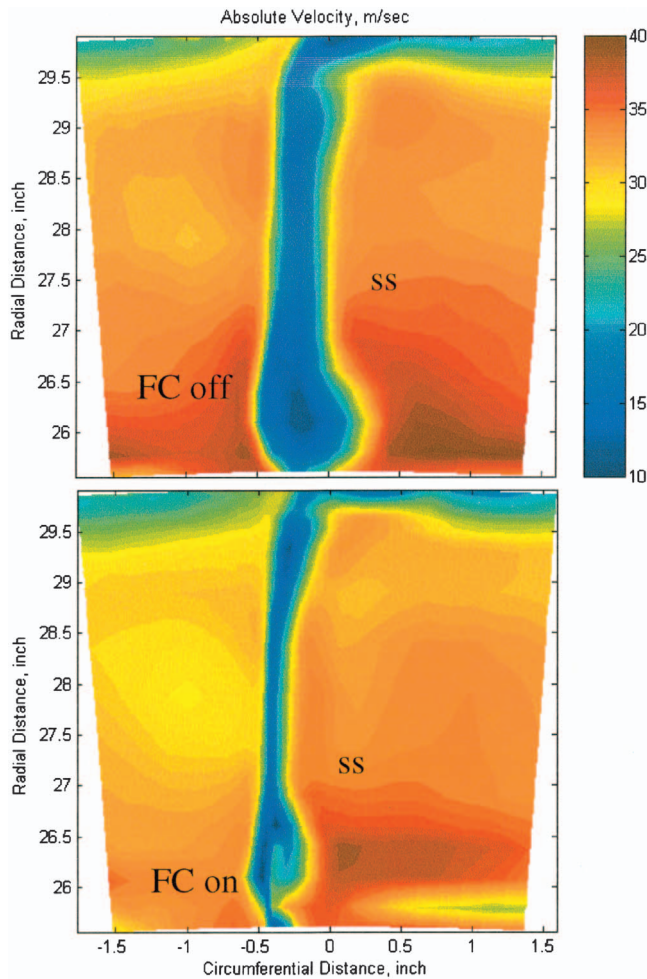
Absolute Velocity, m/sec

Fig. 6 Contours of stator 3 wake velocity

peating stage environment, comparisons of stages 3 and 4 give an indication of stage matching success. Quantitative comparison with the baseline high solidity configuration [10] is made however rotor 1 casing treatment, rotor tip clearances, and hub gaps are all slightly different from the baseline build.

The testing was continuous with and without flow control, and therefore, build-to-build uncertainty should not be a factor in the results. Except where indicated, the detailed data presented herein was acquired at the nominal design point at throttle point 16, an operating point near peak efficiency.

Flow-Controlled Stator 3 Wakes. A complete hot wire traverse of the stator 3 exit was made, and contours of absolute velocity at throttle 16 with and without flow control are compared in Fig. 6. The thick wake from the separated boundary layer was significantly reduced when flow control was applied. The reduction in blockage from the wake reduced the free-stream velocities commensurately with flow control applied. The radial distribution of flow also changed slightly. However, there was a general weakness in the outer diameter for both conditions. The suction-side flow control did not fully repair the region where large secondary flows and high endwall loading predominate. In fact, when flow control was applied, the loading of the stator went up and increased the endwall loading further. The CFD anticipated this weakness but not to the degree observed. The use of casing blowing or restacking of the airfoil may have been effective here in repairing the case weakness.

Measured stator wakes at several immersions versus the pretest CFD are shown in Fig. 7. What is apparent is that without blow-

ing, the ultralow solidity airfoil did not exhibit the massive separation anticipated by the CFD. Yarn tufts were glued to one of the flow-controlled airfoils, and they showed heavy agitation and backward flow without flow control. Because surface pressures were not measured, the tuft data were the only direct indication of the flow separation. However, when the flow control was applied, the tufts all turned downstream. The tufts closest to the trailing edge were still slightly agitated. The pretest CFD is close to the data with flow control on and verifies one of the design goals (i.e., provide only enough blowing to achieve attached flow with wakes similar to the baseline high solidity stator).

The fact that the ultralow solidity stator did not exhibit the levels of separation predicted by the CFD without flow control was disappointing because the flow control effect is maximized when repairing high levels of separation. The CFD mismatch without flow control could be due to many factors. The CFD did not include a boundary layer transition model in the analysis, and the LSRC exhibits regions of laminar flow that could impact the location of separation. Also, the two-equation turbulence model used tends to predict poorly the extent of separation.

Compressor Characteristics. With the flow control functioning as intended, the response of the compressor can be studied. Figure 8 shows the overall machine characteristics with and without the flow control as compared to the baseline compressor with the original higher solidity design 74 count stator 3 ring (see [10]).

With flow control off, the compressor performance is degraded from the baseline. When flow control is employed at 1% of the throughflow, the compressor pumping is restored to levels consistent with the baseline. Near throttle point 16, the flow-controlled stator configuration pumps very slightly lower than the baseline, but is higher as stall is approached. Unfortunately, there is a slight reduction in flow range from throttle point 16 to stall for this current configuration with and without flow control relative to McNulty's data [10]. This change in stall range is evident in Fig. 8 and is lowest with 1% flow control. McNulty et al. [10] point out that the forward swept rotor blade used in this build of the LSRC exhibited significant stall range due to spanwise flow redistribution across the rotor blade as the stall point was approached. The flow migrated toward the tip of the airfoil as small pockets of separation in the hub region formed as the blades were throttled close to their stall limit. The observed reduction in stall range measured during this testing is perhaps a result of a small flow rebalance into stage 4 downstream of the flow control vane. The design intent of the flow-controlled vanes focused on the radial and axial matching within the compressor at the design point. This stall line change implies that the radial matching was slightly different from the baseline machine close to stall. Unfortunately, only very limited traverse data exists at stall to support this assertion, but radial flow profiles in later figures support it.

The compressor efficiency is plotted in Fig. 9. The low-speed approximation to the compressor efficiency equation is used to include the additional air passing through stage 4 [see Eq. (1)] and is based on the representation of the cycle in Fig. 10

$$\eta_{\text{free air}} = \frac{\dot{m}\Delta p_{1-3} + (\dot{m} + \dot{m}_{\text{blowing}})\Delta p_{3-4}}{\rho \tau \omega} \tag{1}$$

No other accounting has been made for the additional blowing mass and pressure supplied to stator 3. For this reason, this efficiency is referred to as the "free air," "useful work" efficiency in that the additional energy for the flow control air has been pumped up "for free," and the work done on the flow control air passing through stage 4 is regarded as useful work. The measured torque cannot be split and assigned to individual rotors so this free air representation is the best available characterization. Still, as anticipated, the entire machine has regained 0.7 points in efficiency without accounting for the cost of compressing the flow control air. That cost will be accounted in the system-level model. The peak efficiency is about 0.2 points lower than the baseline but is
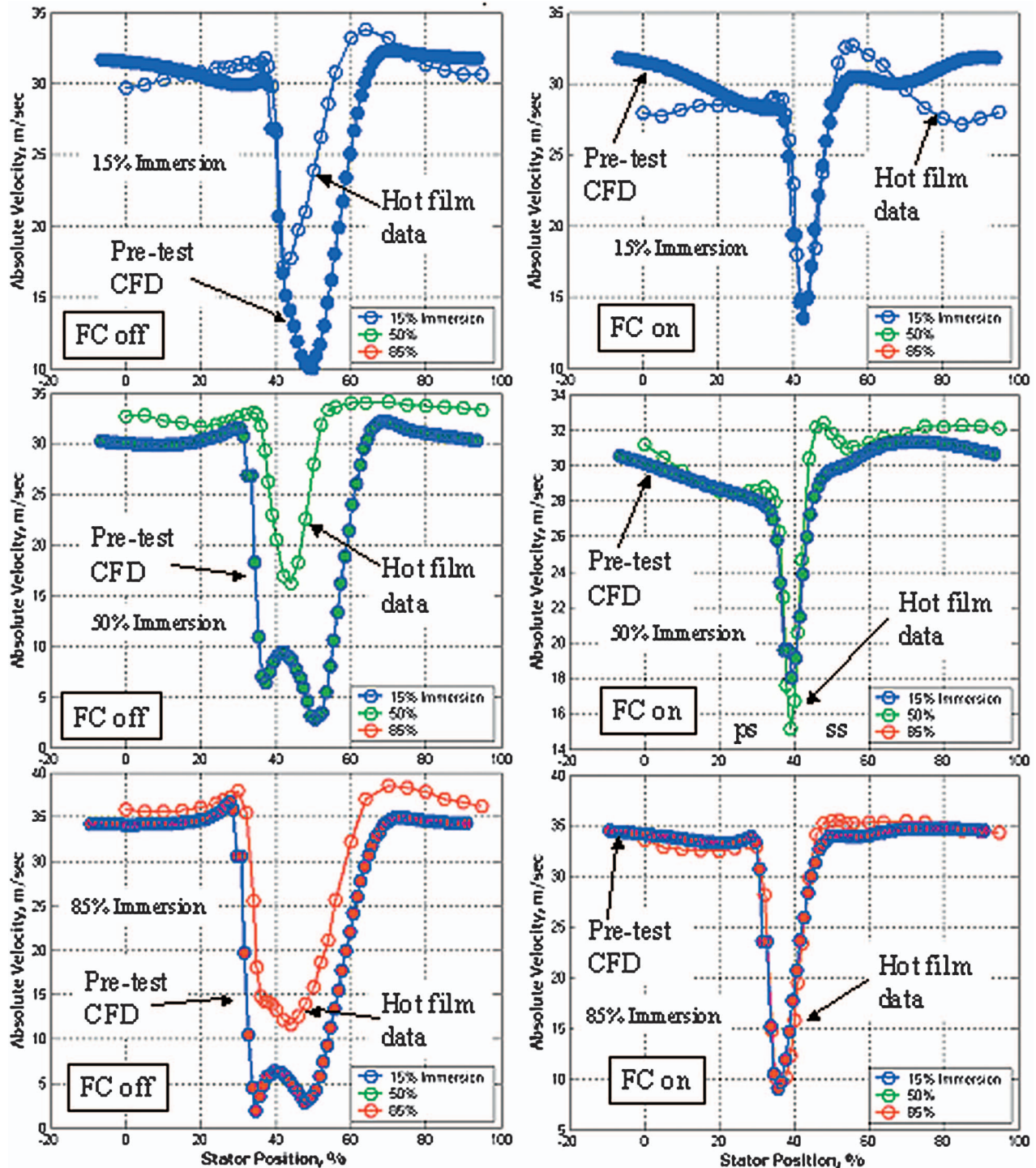
Fig. 7 (a) Stator 3 wake profiles, flow control off; and (b) stator 3 wake profiles, flow control on

0.3–0.5 points higher at lower flows and significantly higher at high flows.

Figures 11 and 12 show the effect on the compressor of incrementally increasing the blowing rate from zero to 1.5% of the throughflow at throttle point 16. At 0.25%, the momentum injected is low enough that its addition is detrimental because the velocity ratio is less than one and further weakens the boundary layer flow through a retarding shear force.

At 0.5%, equivalent performance to the no blowing configuration is achieved. At 0.75% blowing, the injected momentum is sufficient to delay separation and reduce the stator 3 deviation

angle. In response, rotor 4 moves toward its design incidence. Past 1% blowing, separated flow is fully removed and the gain in performance is mostly from the additional total pressure blown into the compressor. Still, the baseline compressor performance near throttle point 16 could be recovered with 1.25% blowing.

The efficiency gains can be studied similarly in Fig. 12. Insufficient blowing is harmful, and gains diminish once the flow is fully attached. The improvement in efficiency from 1.25% blowing to 1.5% is essentially due to the free extra compression from the flow control system and show that the gains from 0.5% to 1.0% are more aerodynamic in nature. Again, the baseline com-

Fig. 8 Compressor pumping characteristic

Fig. 11 Compressor pumping with incremental flow control
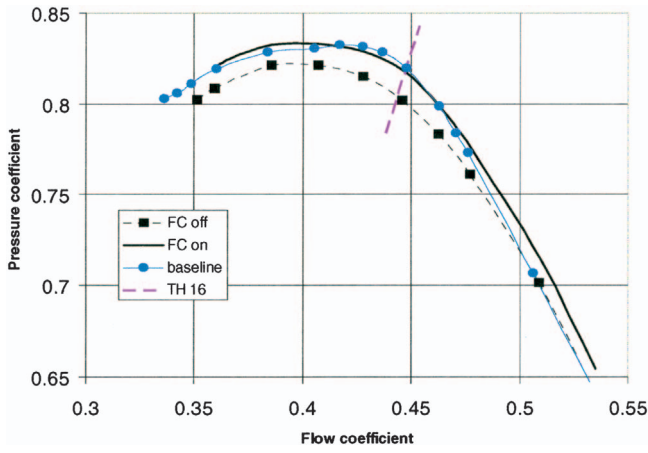
pressor performance could be matched with 1.25% blowing. The 0% and 1% incremental flow control data do not lay on the 0% and 1% performance curves because the latter represents the ensemble average of many tests, whereas the former represents a single test.

Stage Characteristics. Figure 13 shows the casing static pressure rise characteristics for each of the stages for both tests. Stage 1 and stage 2 are unchanged, as would be expected. Stage 3 shows a significant increase in performance because of reduced loss in the stator, but also due to the additional pressure from the blowing. If all of the total pressure of blowing were included in the casing static pressure by momentum mixing, then the pressure coefficient would increase by 0.02, which is an ideal maximum. So the additional gain in performance is a result of the reduced stator 3 losses. Not surprisingly, the stage 3 characteristic falls off toward stall because of the high loading. However, with flow control on, the characteristic slope is clearly healthier and the pres-

sure rise gain is well beyond that from just the blowing pressure.

The impact of flow-controlled stator 3 on the following stage 4 is dramatic at all operating points except near stall. The added total pressure of flow control should not confound this measured stage 4 static pressure rise since no mass is added past stator 3. However, some additional mixing does carry over. The gain in performance at throttle point 16 is real with the stage static pressure rise being increased to that measured in stage 2. This gain can
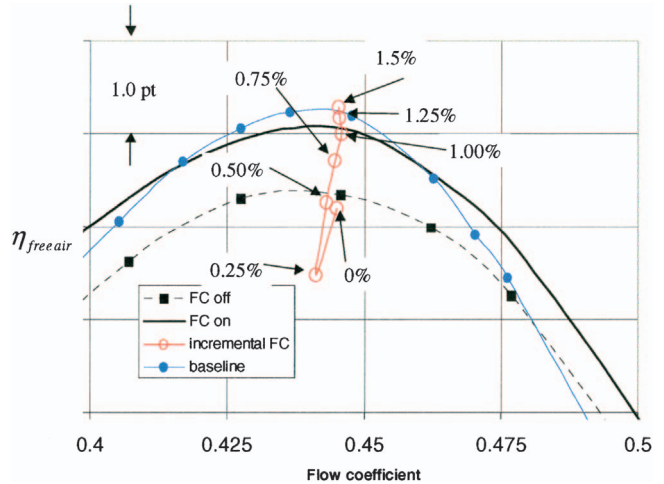
Fig. 12 Compressor efficiency with incremental flow control

Fig. 9 Compressor efficiency characteristic

Fig. 10 Free air cycle model
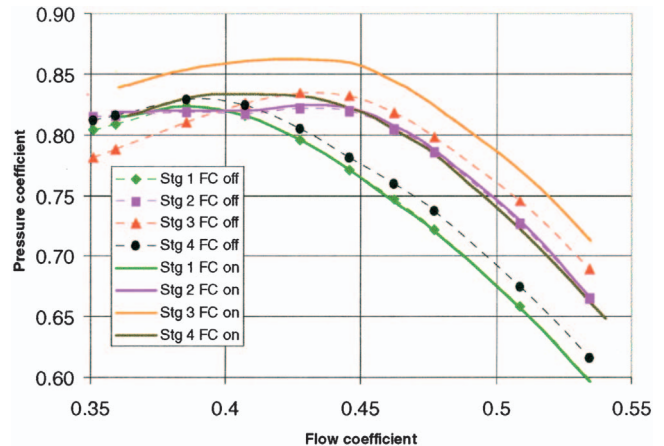
Fig. 13 Stage casing static pressure rise characteristics
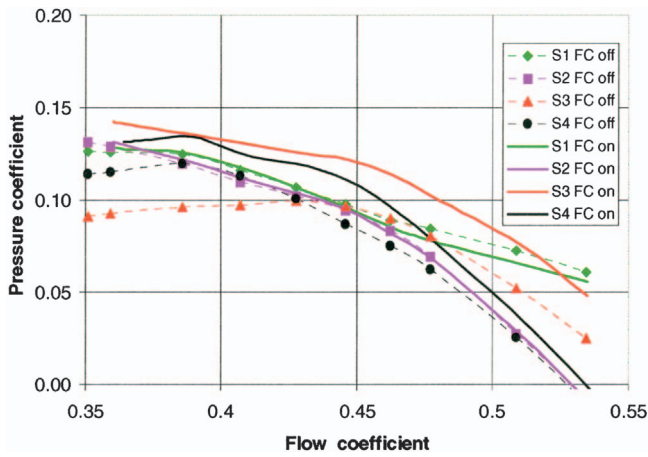
Fig. 14 Stator casing static pressure rise characteristics

Fig. 16 Stator 3 exit air angles

be regarded as due to the restored turning of stator 3 and its improved performance characteristics. However, the pressure rise characteristic of stage 4, while improved with the flow control and parallel to stage 3, is still somewhat disappointing relative to that of stage 4 with the baseline conventional stator 3 in front of it [10], which produced a 2.5% higher pressure rise. The additional flow control air is included in the flow coefficient for stage 4 components in Figs. 13–15 shifting their curves to the right by 1%.

The stator characteristics in Fig. 14 show the expected trend again of no change in stators 1 and 2 and improved performance of the flow-controlled stator 3. There is also a measurable gain in stator 4 performance. Some improvement in stator 4 performance would be anticipated because of the improved rotor 4 pumping.

Indeed, when flow control was applied, rotor 4 pressure rise was significantly improved, as seen in Fig. 15. All other rotors are unaffected when flow control is on or off, as would be expected. What is noticeable though is that near stall, the performance of rotor 4 does not show any benefit from flow control and, in fact, appears slightly worse. This lack of improvement in the characteristic near stall with 1% flow control is thought to be due to a radial flow redistribution through stage 4, discussed earlier, resulting in weakened endwall flows into the stage. Detailed traverse data at this condition would have been helpful in understanding why the stage 4 characteristic appears not to be benefiting to the extent measured on the operating line. Also, since the stage characteristics in Fig. 13 showed the same level of pressure rise at stall, there might be a slight measurement problem in splitting the

performance out between the rotor and the stator in this stage.

Effects of Flow Control on Stage Matching. The exit air angles measured with the hot-wire probe at the stator 3 exit are shown in Fig. 16. It is evident that the stator 3 exit flow angle, with 1% flow control, closely matches the design intent. This close agreement is gratifying in that achieving the design intent swirl distribution from the vane at throttle point 16 was the primary design requirement for axial matching. This result verifies the design process for a multistage environment where axial stage matching is important. With the flow control off, the reduction in turning associated with the thicker boundary layer is clearly evident across most of the span. In Fig. 6 it is noticeable that near the tip the flow control appeared to be ineffective. Attempts to boost the tip flow with extra blowing holes were included in the design, but the flow is dominated by a secondary vortex and the 1% flow control did not improve the turning there.

The impact on the rotor 4 relative flow angles is shown in Fig. 17. The increased stator 3 deviation for no flow control reduces the incidence onto rotor 4 as expected over most of the span. Near the tip, where the flow control appeared to be less effective, rotor 4 relative air angle is largely unchanged. For reference, the rotor 3 relative inlet air angles are also shown, and they can be seen to be

Fig. 15 Rotor casing static pressure rise characteristics
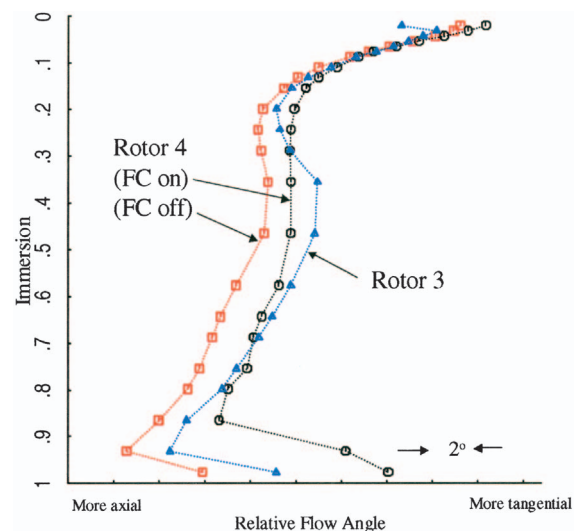
Fig. 17 Rotor inlet relative air angles
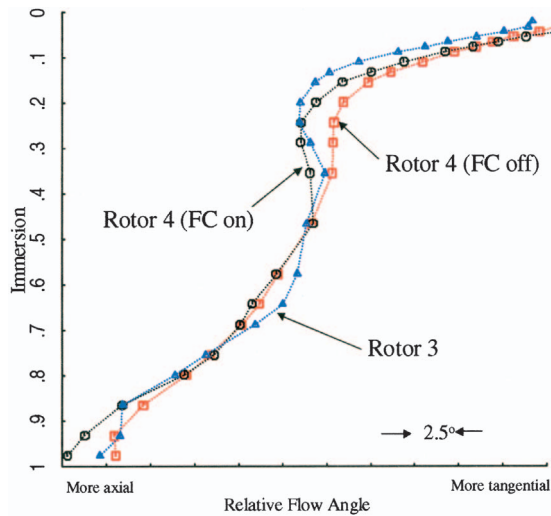
Fig. 18   Rotor exit relative air angles

Fig. 20   Rotor total pressure rise coefficient

very similar to those measured with the flow control on. The additional 1% mass flow at the stator 3 exit should only account for a 0.2 deg shift. These rotor 3 inlet angles are derived from hot-wire measurements taken aft of stator 2, and additionally confirm that the flow control vane was meeting its design intent with the flow control on.

The relative air angles leaving rotor 4, both with and without flow control operating, are shown in Fig. 18, based on hot-wire measurements at entry to stator 4. Additionally, the air angles from rotor 3 are also shown. Good agreement can be seen, indicating that rotor 4 turning was not significantly affected during the testing with the flow-controlled stator 3.

The impact on stator loss is shown in Fig. 19. The total pressure drop coefficient is defined from Kiel head probe total pressure traverses and is based on the difference between the inlet and exit measured total pressure divided by the tip speed dynamic head. This normalization is consistent with the pumping characteristics in the preceding figures. The total pressure reduction for the flow control vane, therefore, includes the benefits of both the higher pressure flow control air and the improved suction surface boundary layer. For comparison, the drop measured across stator 2, a conventional higher solidity stator vane, is shown. As computed by momentum mixing, the maximum possible contribution from
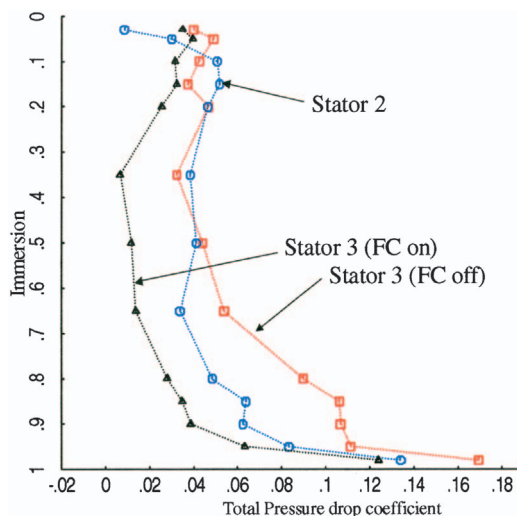
the blowing pressure accounts for only 0.02 of the observed change; the remainder is aerodynamic. A proper accounting of the blowing pressure is made in the system-level analysis discussed later and not included as a mass weighted adjustment to the stator inlet pressure.

Although it was explained that the axial matching had been maintained with the flow-controlled vane, there is evidence that the radial matching of the rotor behind the vane may have been slightly impacted. Figure 20 shows the measured total pressure rise across rotor 4 with flow control on (normalized by tip speed dynamic head) compared to that measured across rotor 3. There is evidence of stronger hub flow and weaker tip flow with the flow-controlled vane in front of the rotor, which is consistent with the excellent hub performance and slightly disappointing tip performance of the flow-controlled vane. Only limited traverse data were measured close to stall, so it is not possible to directly conclude whether this is contributing to the poorer throttle range measured with the flow control on. However, it does highlight the additional design challenge of not only maintaining the axial stage matching, but the radial matching as well. Missing on either of these goals could adversely affect the stall range of the compressor.

System Level Penalty. In an engine cycle study, the gain from increasing loading by 30%, as done here, must be offset by the penalty to achieve it. A complete engine cycle analysis to determine the net benefit is unique to each engine and beyond the scope of this paper. However, a straightforward analysis can be employed to find the stage efficiency penalty of the flow-controlled stator.

Naturally, the blowing air must come from a high-pressure source downstream of the flow-controlled stage. In a multistage high-pressure compressor, the flow control air could be supplied from a location that would be a number of stages downstream. For the LSRC, which is a four-stage compressor, insufficient pressure is available within the compressor to supply the air for stage 3. A system study, however, can still be conducted using the following approach. The flow control air can be extracted from the exit of the compressor, and a supplemental pump can be used to represent the work from downstream stages (see Fig. 21). A pump efficiency similar to the stage efficiency of the baseline stages is assumed.

For such a model, the compressor efficiency is then

Fig. 19   Stator total pressure drop coefficient

$$\eta_{\text{compressor}} = \frac{\text{power}_{\text{ideal}}}{\text{power}_{\text{actual}} + \text{power}_{\text{blowing}}} \quad (2)$$

and expanding in terms of measurable quantities gives

Fig. 21 Flow-controlled stator cycle model

$$\eta_{\text{compressor}} = \frac{\dot{m}\Delta p_{1-4}}{\rho\tau\omega + \dot{m}_{\text{blowing}}(p_{\text{blowing}} - p_4)/(\eta_{\text{pump}})} \quad (3)$$
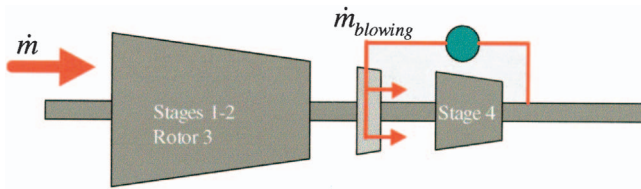
where state 4 is downstream of the flow control extraction. Equation (3) represents the cycle model in Fig. 21. Comparison of Eqs. (1) and (3) shows a drop in the numerator and a rise in the denominator.

The flow-controlled stator model in Fig. 21 can be applied to assess the potential penalty on stage efficiency in terms of how such a flow-controlled vane would impact the compressor performance in an engine cycle analysis. If the blowing air is extracted at the rotor exit (or better yet behind the following stator), then the power required to pump a given mass flow to the desired plenum pressure can be calculated. The required plenum pressure is fixed by the desired blowing Mach ratio and adjusted to account for duct losses of the flow control system. For this system-level study, the duct size is assumed to pass the flow control air at Mach 0.05. Accounting for the duct losses and expansion loss as flow enters into the airfoil plenum and assuming a flow control hole discharge factor of 0.85 the blowing power can be found. Furthermore, if the rotor efficiency is assumed constant and the stage is assumed to deliver a fixed exit total pressure, then the ideal stage power and the blowing power are known and only the total pressure drop across the flow-controlled stator is required. This drop should not adjust the stator inlet pressure to include the mass-averaged contribution from the blowing because the blowing pressure cost is already accounted for in the blowing power.

The stage efficiency is then the ratio of the ideal power to the sum of the stage power and blowing power. For various levels of blowing and stator loss reduction, Fig. 22 shows the stage efficiency penalty associated with the flow control stator. For the current design, the pretest CFD analysis indicated a stator total pressure drop (including the benefits of the higher-pressure flow control air) at only 35% of the baseline high solidity stator for a
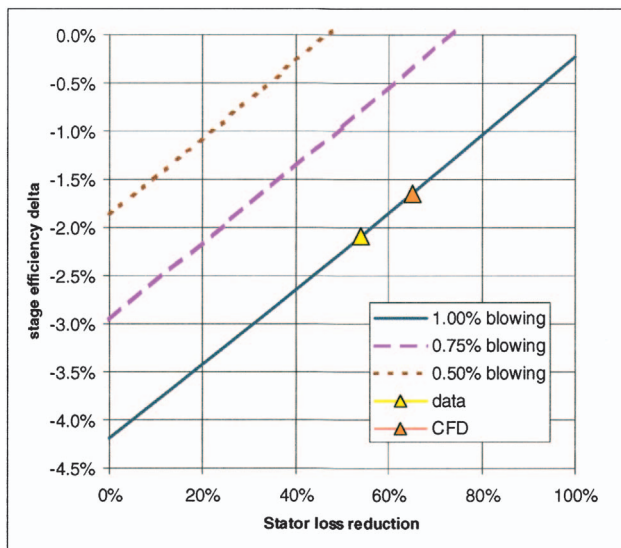
65% reduction. The result is a 1.6 point penalty in stage efficiency for the 30% increase in stator loading using 1% blowing air. Such a level may be considered as not an unreasonable trade-off when engine cost of ownership and weight are considered. Still, if flow control jet mixing loss is large and flow control is not as effective at reducing loss as indicated by the pretest CFD, then the penalty can be severe. Likewise, if flow control actuation can be optimized to reduce the flow requirements to 0.5% blowing, then very small penalties can be achieved. The experimental data showed a reduction of 54% in total pressure drop across the stator versus the baseline high solidity stator. Using this reduction, the stage efficiency penalty grows to 2.1 points, slightly larger than that predicted during the design using CFD.

Figure 22 also shows the qualitative effect of reducing the momentum ratio required and, hence, the blowing mass flow rate for a fixed area. The current configuration is very conservative, and through a more sophisticated flow control design, lower Mach ratios, and perhaps unsteady actuation, reduced blowing requirements could lead to a significant reduction of the stage efficiency penalty.

This form of system analysis must be performed in order to determine the merit of any flow control scheme in an engine application. In this study, being a low-speed compressor, the cycle impact on the required blowing power from pressure losses due to restrictions, pipe losses, and expansions from moderate Mach numbers into plenums, etc., is large. To that end, an extension of this system-level analysis to a flow-controlled stator vane in a high-speed compressor yields only a 0.5 point stage efficiency impact due to higher pressure ratios. For the high-speed analysis, similar assumptions were made including the stator loss reduction data and flow control Mach ratio, but the flow control was extracted from two stages downstream. The penalty comes from repumping the hot flow control air. The result must be qualified by the uncertainty of the actual high-speed stator loss reduction, the expansion loss into a small high-speed stator plenum, and the blowing hole discharge factor at the higher Mach numbers.

Conclusions

Direct application of steady flow control technology to a highly loaded stator embedded in a multistage compressor has been achieved. The major goals were all met, namely, degrade the compressor performance by exceeding design limits without flow control and restore compressor performance by applying flow control. The fact that the ultralow solidity stator without flow control was not as massively separated as anticipated by the CFD reduced the expected benefits. Perhaps an even lower solidity airfoil could have been used, but the strong secondary flows that developed in the ultralow solidity stator could not be ameliorated by the suction-side flow control alone. The test data showed that although the axial matching had been achieved, there was evidence that the tip flow in rotor 4 downstream of the flow-controlled vane had been weakened thereby contributing to the slight reduction in stall range measured with the flow control on. The radial mismatch highlights one of the challenging aspects of designing a compressor to work with flow control. A restack of this airfoil to improve the weakness at the casing is perhaps in order for better radial matching. Improvements to the flow control system and method of delivery are also being considered. Moving to lower Mach ratios for blowing while maintaining total momentum is also a desirable next step.

The test has also provided results that can be used in evaluating the system-level impact of flow control in an engine. For the LSRC, the penalty for pumping the flow control required to achieve the 30% increase in loading was 2.1 points in stage efficiency. Extension to a high-speed machine showed a more modest 0.5 point stage efficiency penalty.

The fact that flow control has been demonstrated to be effective for this ultralow solidity stator does not mean the technology would be applied in this manner. The weight reduction for fewer

Fig. 22 Compressor cycle impact map for the LSRC

stators is not great when one considers the stator rings are still in place with no reduction in engine length. A more promising approach could be to use flow control to reduce the number of stages within a compressor. Designers have routinely traded efficiency for reduced stage count based on a system level study yielding a net operating cost reduction. However, the complexity, cost, weight, and fail-safe nature of the flow control piping, valving, and vanes must also be considered as part of such a study. Alternatively, flow control could be used in specific applications where an extreme broad operating range is required for a particular airfoil.

Acknowledgments

Nomenclature

$$A = \text{annulus area}$$
$$c = \text{chord}$$
$$H = \text{total enthalpy}$$
$$p = \text{static pressure}$$
$$P = \text{total pressure}$$
$$r = \text{radius}$$
$$s = \text{blade spacing}$$
$$U = \text{blade speed}$$
$$V = \text{absolute total velocity}$$
$$W = \text{relative total velocity}$$
$$\dot{m} = \text{mass flow rate}$$
$$\tau = \text{torque}$$
$$\omega = \text{rotation rate}$$
$$\rho = \text{density}$$
$$\frac{H_{ref}}{\frac{1}{2}U_{tip}^2}\left[\left(\frac{\Delta p}{P_{in}}+1\right)^{(\gamma-1/\gamma)}-1\right] = \text{pressure rise coefficient}$$
$$\eta = \text{torque efficiency}$$
$$1-V_{exit}/V_{in}+\Delta(rV_\theta)/(2\sigma rV_{in}) = \text{diffusion factor}$$
$$\sigma = \text{solidity } (c/s)$$
$$\dot{m}/(\rho_{avg}AU_{tip}) = \text{flow coefficient (inlet)}$$
$$(r_{tip}-r)/(r_{tip}-r_{hub}) = \text{immersion}$$
$$\gamma = \text{ratio of specific heats}$$
$$\Delta = \text{change from inlet to exit}$$
$$\tan(V_\theta/V_z) = \text{absolute flow angle}$$
$$\tan(W_\theta/V_z) = \text{relative flow angle}$$

Subscripts

$$avg = \text{compressor average}$$
$$blowing = \text{flow control blowing}$$
$$free\ air = \text{no-penalty cycle model}$$
$$in = \text{compressor inlet}$$
$$ref = \text{compressor bellmouth}$$
$$\theta = \text{tangential direction}$$
$$z = \text{axial direction}$$

References

[1] Ball, W. H., 1983, "Experimental Investigation of the Effects of Wall Suction and Blowing on the Performance of Highly Offset Diffusers," AIAA Paper 83-1169.

[2] Ball, W. H., 1984, "Test of Wall Blowing Concepts for Diffuser Boundary Layer Control," AIAA Paper 84-1276.

[3] Wadia, A. R., and Mielke, M. J., 1996, "Self Bleeding Rotor," US Patent 5,480,284.

[4] Kerrebrock, J. L., Reijnen, D. P., Ziminsky, W. S., and Smilg, L. M., 1997, "Aspirated Compressors," ASME Turbo Expo 1997, June 2-5, Orlando, FL, USA, ASME, New York ASME Paper No. 97-GT-525.

[5] Lord, W. K., MacMartin, D. G., and Tillmann, T. G., 2000, "Flow Control Opportunities in Gas Turbine Engines," AIAA Paper 2000-2234.

[6] Carter, C. J., Guillot, S. A., Ng, W. F., and Copenhaver, W. W., 2001, "Aerodynamic Performance of a High Turning Compressor Stator With Flow Control," AIAA Paper 2001-3973.

[7] Bons, J. P., Sondergaard, R. and Rivir, R. B., "The Fluid Dynamics of LPT Blade Separation Control Using Pulsed Jets," ASME Turbo Expo 2001, June 4-7, New Orleans, LA, USA, ASME, New York, ASME Paper No. 2001-GT-0190.

[8] Culley, D. E., Bright, M. M., Prahst, P. S., and Strazisar, A. J., 2003, "Active Flow Separation Control of a Stator Vane Using Surface Injection in a Multistage Compressor Experiment," ASME Turbo Expo 2003, June 16-19, Atlanta, GA, USA, ASME, New York, ASME Paper No. GT2003-38863.

[9] Schuler, B. J., Kerrebrock, J. L., and Merchant, A., 2002, "Experimental Investigation of an Aspirated Fan Stage," ASME Turbo Expo 2002, June 3-6, Amsterdam, Netherlands, ASME, New York, ASME Paper No. GT2002-30370.

[10] McNulty, G. S., Decker, J. J, Beacher, B. F., and Khalid, S. A., 2003, "The Impact of Forward Swept Rotors on Tip-Limited Low-Speed Axial Compressors," ASME Turbo Expo 2003, June 16-19, Atlanta, GA, USA, ASME, New York, ASME Paper No. GT2003-38837.

[11] Jennions, I. K., and Turner, M. G., 1993, "Three Dimensional Navier-Stokes Computations of Transonic Fan Flow Using an Explicit Flow Solver and an Implicit k-ε Solver," ASME J. Turbomach. **115**, pp. 261–272.

[12] Turner, M. G., and Jennions, I. K., 1993, "An Investigation of Turbulence Modeling in Transonic Fans Including a Novel Implementation of an Implicit k-ε Turbulence Model," ASME J. Turbomach. **115**, pp. 249–260.

[13] Hunter, S. D., and Orkwis, P. O., 2000 "Endwall Cavity Flow Effects on Gaspath Aerodynamics in an Axial Flow Turbine: Part II - Source Term Model Development," ASME Turbo Expo 2000, May 8-11, Munich, Germany, ASME, New York, ASME Paper No. 2000-GT-0513.

[14] Johnston, J., 1999, "Pitched and Skewed Vortex Generator Jets for Control of Turbulent Boundary Layer Separation: A Review," ASME/JSME 1999 Fluids Engineering Division Summer Meeting, July 18–23, San Francisco, CA, USA, ASME, New York, ASME/JSME Paper No. FEDSM99-6917.

[15] Wisler, D. C., 1985, "Loss Reduction in Axial Flow Compressors Through Low-Speed Model Testing," ASME J. Eng. Gas Turbines Power **107**, pp. 354–363.

Vortex-Wake-Blade Interaction in a Shrouded Axial Turbine

J. Schlienger[1]
e-mail: joel.schlienger@ch.abb.com

A. I. Kalfas

R. S. Abhari

Turbomachinery Laboratory,
Swiss Federal Institute of Technology,
Sonneggstrasse 3,
8092 Zurich, Switzerland

This paper presents time-resolved flow field measurements at the exit of the first rotor blade row of a two stage shrouded axial turbine. The observed unsteady interaction mechanism between the secondary flow vortices, the rotor wake and the adjacent blading at the exit plane of the first turbine stage is of prime interest and analyzed in detail. The results indicate that the unsteady secondary flows are primarily dominated by the rotor hub passage vortex and the shed secondary flow field from the upstream stator blade row. The analysis of the results revealed a roll-up mechanism of the rotor wake layer into the rotor indigenous passage vortex close to the hub endwall. This interesting mechanism is described in a flow schematic within this paper. In a second measurement campaign the first stator blade row is clocked by half a blade pitch relative to the second stator in order to shift the relative position of both stator indigenous secondary flow fields. The comparison of the time-resolved data for both clocking cases showed a surprising result. The steady flow profiles for both cases are nearly identical. The analysis of the probe pressure signal indicates a high level of unsteadiness that is due to the periodic occurrence of the shed first stator secondary flow field. [DOI: 10.1115/1.1934263]

Introduction

In recent years of turbine flow research, great importance is given to the time-varying flow field and the related generation of unsteady loss in a blade row. Denton [1] identifies different sources of loss for shrouded axial turbines. One source of loss is generated in the endwall flow field, when the leakage flow interacts with the main flow field and the endwall's secondary flow vortices. This mechanism is one reason for the reduction of the blade loading and the stage performance. The detailed unsteady flow measurement and the understanding of the flow physics is thus a key requirement in achieving further improvements of turbine efficiency.

The relative motion between the rotating and stationary turbine blades causes the rotor indigenous secondary flow and potential flow field, that is induced by the rotor and stator blades, to periodically interact with each other (Sharma et al. [2]). The evolution and convection of the stator and rotor hub vortices and wakes through the downstream blade rows are therefore triggered by the instantaneous relative position of the rotor and stator blades. The associated unsteady flow effects, that originate in the interaction of the wake with the secondary flow vortices and the blade geometry, contributes to a large extent to the generation and redistribution of unsteady loss. The convection of the upstream stator flow field through the downstream rotor passage is explained in the work of Miller et al. [3]. The shed stator vortices influence the formation of the rotor indigenous hub passage vortex as seen from numerical simulations.

The mechanism of the wake-blade interaction has been reported in several publications (including Hodson [4]) and is generally important for high aspect ratio and high lift airfoils as used in low pressure turbines. Major contributions in the field of unsteady vortex-blade interactions for unshrouded single or 1.5 stage turbines are found in the work of Binder et al. [5], Boletis and Sieverding [6], and Sharma et al. [2]. However, only a few publications report on the time-resolved vortex-blade interaction mechanism for a shrouded single stage turbine (i.e., Chaluvadi et al. [7] or Behr et al. [8]). The unsteady interaction of a vortex with

a stationary blade row is experimentally investigated in Chaluvadi et al. [9] using delta wings as vortex generators at the hub inlet of a single stage turbine. The influence of an upstream rotor trailing edge on this mechanism is, however, not included in this experiment and needs some further investigations.

The paper focuses on the interaction of the rotor hub vortices with the rotor wake and the downstream stator leading edge of a two stage shrouded axial turbine. The associated unsteady variation of the relative total pressure, incidence angles and level of unsteadiness is analyzed and discussed in detail.

The unsteady flow field is ideally measured by detailed time-resolved flow field measurements using miniature fast response aerodynamic pressure probes (FRAP) Kupferschmied [10]. The high aspect ratio of 10:1 between the blade minimal throat and the head diameter of the fast response probe leads to a minimal blockage effect of the probe shaft within the measured flow field. Finally, the measurement technique provides the fully three dimensional time-resolved flow field of the turbine.

The results are presented as contour plots for the relative total pressure at different time steps and in combination with the derived secondary flow velocity vectors. The evolution of the flow profiles (e.g., relative total pressure) is given as pitchwise mass-averaged space–time diagrams and explained in detail.

In the work of Chaluvadi et al. [7], the turbulence level was measured with hot-wire probes and used as a marker for the generation of loss in a turbine stage. In the present study, the stochastic fluctuations of the dynamic head, that is measured with the fast response probes, is expressed as turbulence level, as proposed in the work of Ruck [11] and Koeppel [12] for fast response pneumatic probe techniques.

Experimental Method

Research Facility. The measurements were performed in the low speed two stage axial research turbine at the Turbomachinery Laboratory of the ETH Zurich (Fig. 1, Schlienger [13]). The rig consists of an axial turbine, a closed loop duct system, a radial compressor, a water/air cooler and a venturi nozzle for accurate massflow measurements within ±0.5% accuracy of the overall mass flow. The delivered turbine power is absorbed by a DC generator, that accurately controls the rotor speed within ±1 rpm.

The turbine is operated at a constant pressure difference across the two stages. The inlet temperature is kept constant at $45\,^\circ\text{C}$ and varies within $\pm 0.2\,^\circ\text{C}$ over one day. The specific turbine operating

Fig. 1 Low speed 2-stage axial turbine LISA

Probes	α (deg)	β (deg)	C_{pt} (%) Dyn. Head	C_{ps} (%) Dyn. Head	Ma (%)
FRAP	0.3	0.5	3%	5%	3%
5-Hole	0.3	0.3	2%	3%	1%

lock averaged using 80 rotor passing events and the rotor trigger reference signal. The obtained raw data files of the FRAP probe measurements are processed with the software program HERKULES (Schlienger [13]). The code is based on the Matlab programming language syntax. The overall processing time for 700 grid points per blade pitch, that covers typically one area traverse (17 GByte), is less than 4 h on a 3.2 GHz pentium processor. The pneumatically averaged flow field is finally measured with a miniature 5-hole cobra probe that uses a tip diameter of only 0.9 mm.

Probe Measurement Plane. The time-varying secondary flow field and the associated vortical system at the rotor exit plane are measured with detailed probe area traverses in the first stage exit plane in area I as shown in Fig. 2.

A typical spatial resolution of the measurement grid for a FRAP or 5-hole probe consists of 31 grid points per radial traverse (hub to tip) and 21 traverses at equidistant circumferential positions per blade pitch, resulting in 651 grid points. The temporal resolution is 108 samples per blade passing period, which leads to a measurement set of nearly 70,000 data points for one blade pitch.

Results

The measurement results of the steady and time-resolved flow field are shown in this section. The comparison of the pneumatic (5-hole) and time-averaged (FRAP) result is given as pitchwise mass-averaged flow profiles as a function of blade span for the absolute total pressure C_{pt} and the stator incidence angle $\Delta\alpha$ relative to the blade design data.

The second section focuses on the unsteady interaction of the rotor hub vortices with the rotor and stator blades. The evolution of the flow field within area (I) is presented as contour area plot for the rotor relative total pressure C_{ptr} and for eight consecutive time steps within one blade passing period. Of particular interest are the associated incidence angles and the level of flow unsteadiness.

The stochastic part of the FRAP pressure measurement is further analyzed and expressed in terms of the turbulence intensity factor Tu_p (see Ruck [11] and Koeppel [12]). The stagnation pressure P^0 in the flow field is similar to the center hole pressure P_1 of a virtual-four sensor FRAP probe. This assumption is representative for a probe relative flow yaw angle variation of less than ±10 deg and still acceptable for larger relative flow angles. Based on these assumptions, the turbulence intensity Tu, which is usually derived from hot-wire velocity measurements, is correlated with the random variation of the stagnation pressure Tu_p using inviscid and incompressible flow principles. This concept was

point is given in Table 1. The pressure drop is stable to within ±40 Pa (±0.1% of total pressure drop) for a typical measurement time of one day.

The airfoil design is typical as for modern gas turbines. The moderate blade aspect ratio of 1.8, in combination with the labyrinth leakage flow field, enhances the secondary flow effects in the endwall area which leads to an averaged typical flow pitch angle of up to 20 deg. A set of highly sophisticated fast response pressure probes are required for the detailed measurements of this complex unsteady three-dimensional flow.

Probe Technology. The unsteady flow field is measured with two single sensor fast response aerodynamic pressure probes at a sampling frequency of 200 kHz (Kupferschmied et al. [10]). In this case, the FRAP probes are used as a pair in virtual 4-sensor mode for the measurements of the 3D time-resolved flow field. The measured flow parameters are the flow yaw (α) and pitch (β) angles, the total and static pressure coefficients (C_{pt} and C_{ps}) and the Mach number (Ma) at frequencies of up to 20 kHz. The measurement accuracy is given for Table 2 for the different probes that are used for this experiment.

A trigger signal, with a measured accuracy of ±1/108 of blade pitch, relates the four consecutive FRAP probe pressure measurements in space and time. The local flow vector is then reconstructed from those four pressures at each spatial coordinate using the aerodynamic probe calibration model. The raw data is phase-

Table 1 Typical operating point of the low speed 2-stage axial research turbine

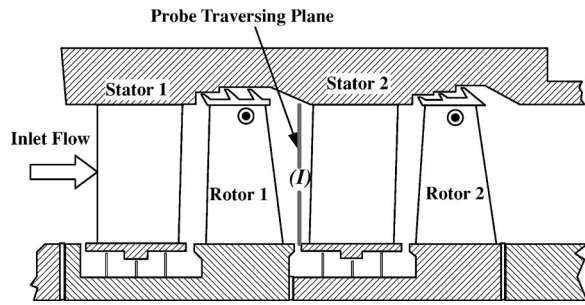| Rig parameter	Value	Accuracy
Rotor speed	2625 rpm	±1 rpm
Pressure ratio	1.32	±0.02%
Aspect ratio (span/ax.chord)	1.8	⋯
Blade count (rotor/stator)	42/42	⋯
Outer tip diameter	0.8 m	±0.05 mm
Mach number Ma (rotor/stator)	0.1/0.35	⋯
Reynolds number Re (axial chord)	2×10^5	⋯

Fig. 2 Probe traversing plane at the exit of the first turbine stage (area I)

verified with the comparison of FRAP measurements (pressure measurement) with LDA (laser doppler anemometry) data for the stochastic velocity field of a centrifugal compressor (Koeppel [12]).

Steady Flow Field at First Stage Exit Plane. The flow field at the exit of the first stage is shown in Fig. 3 for the pitchwise mass-averaged total pressure coefficient C_{pt}. The results of the 5-hole probe are superimposed to the time-averaged flow measurements of the FRAP probes in order to validate the accuracy of the different measurement techniques. The spanwise averaged measurement results for two probe techniques differ by less than 0.001 of C_{pt} (2% of dynamic head) for the entire blade span. A peak difference of 10% dynamic head between the two flow profiles is registered at 28% blade span, which is within the secondary flow dominated area.

The results indicate the presence of considerable secondary flow structures between the rotor hub at 0%–40% of blade span (see circle A). The total pressure varies within 22% of dynamic head due to the effects of the secondary flow vortices on the endwall flow. The re-entering labyrinth leakage flow at the upstream stator hub shroud generates a large nonuniform inlet flow profile into the first rotor blade. The leakage flow rolls-up into a strong rotor hub passage vortex and affects the total pressure distribution at the hub (Schlienger et al. [14]).

The flow profile on the right-hand side of Fig. 3 shows the averaged deviation $\Delta\alpha$ of the absolute flow yaw angle α relative to the design intention α_{design}. The hub passage vortex causes a considerable positive incidence on the stator leading edge of +18 deg at 10% blade span. The over- and underturning of the flow field is due to the induced velocity field of the passage vortex which causes a negative incidence of −8 deg in the upper part of the flow area at 25% blade span. At the blade tip section, a posi-
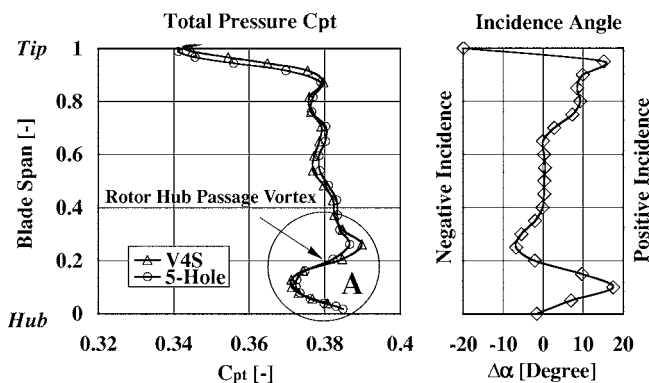
tive incidence of up to 20 deg is measured within 70%–95% of the blade span. This deviation is due to the blade design intention at the tip section.

Unsteady Flow Field at First Stage Exit Plane. The flow field at the rotor hub exit plane (area I) is highly three-dimensional due to the leakage flow at the rotor inlet and exit plane and the high level of flow turning in the blade passage (Langston et al. [15]). These boundary conditions lead to strong secondary flow vortices at the rotor hub, which alters in strength and position during a blade passing event, as seen in this part.

The results of detailed unsteady flow measurements show that the relative motion between the rotor and stator blades affects the convection of the rotor wakes and vortices through the downstream turbine stage. The associated interaction mechanism of the vortices with the wakes, the rotor, and the stator blades is measured in detail and presented in this section. The time-resolved evolution of the flow field is shown for the rotor relative total pressure C_{ptr} and for eight consecutive time steps t/T within one blade passing period T.

The secondary flow field is superimposed onto the contours of the relative total pressure and shown as vector plots (Figs. 4 and 5). The definition of the secondary flow velocities is given in Eq. (1),

$$\mathbf{u}_{\text{sec}} = \mathbf{u}_i - (\mathbf{e}_{\text{mean}} \cdot \mathbf{u}_i)\mathbf{e}_{\text{mean}} \qquad (1)$$

The velocity $\mathbf{u}_{\text{sec}}$ is the local secondary flow vector, $\mathbf{u}_i$ the local main flow vector, and $\mathbf{e}_{\text{mean}}$ is the mean area unit vector for the entire flow field at time step t_i. The secondary flow velocity field is recomputed for every new time step. The different vortices are identified in using the local minima of the static pressure, the secondary flow field and the derived vorticity distribution.

Classical secondary flow theories (Hawthorne [16]) assigns the vortical structure on top of the passage vortex to the trailing edge vortex that is combined with the vorticity that is developed in the suction surface boundary layer. An other secondary flow model (Goldstein and Spores [17]) associates the vortical structure on top of the passage vortex to the horse-shoe suction side leg vortex.

The measured secondary flow vectors reveal three separate vortices at different locations in the rotor hub section. The major vortex is the passage vortex and is referenced with *PV*. The small region of high vorticity on top of the *PV* is a combination of horse shoe suction side leg vortex (*HSs*), trailing shed vorticity and suction surface vorticity. A corner vortex (*Cvs*) is found at 5% blade span at the hub of the rotor blade.

The shape of the rotor wake is derived from the measured pitchwise averaged relative flow yaw angle $\beta(r)$ and the axial distance $X(r)$ between the probe and the rotor trailing edge. The corresponding equation for the wake displacement $\Delta_w(r)$ in circumferential direction is given in Eq. (2), with the parameter r as the radial position.

$$\Delta_w(r) = \tan\beta(r) \cdot X(r) \qquad (2)$$

The instantaneous position of the rotor trailing edge is known from the blade trigger and the rig geometry. The deformed wake shape $\Delta_w(r)$ is added to the rotor trailing edge geometry, which leads to the sketched shape of the wake.

Discussion of Unsteady Flow Results. The evolution of the different vortices into the downstream stator passage is determined by the relative position of rotor and stator blades and by the stator leading edge potential field, that acts as a radial stagnation line on the evolution and convection of the unsteady flow structures. Any of those rotor indigenous vortices, such as the passage vortex (PV), horse shoe suction side vortex (HSs), or corner vortex (Cvs) will experience a severe bending and stretching as they interact with the downstream stationary stator blades. The unsteady flow measurements that are presented in this paper give a realistic insight into this complex flow mechanism and are dis-

Fig. 3 Total pressure C_{pt} at area I and stator incidence angle Da (relative to design intention)

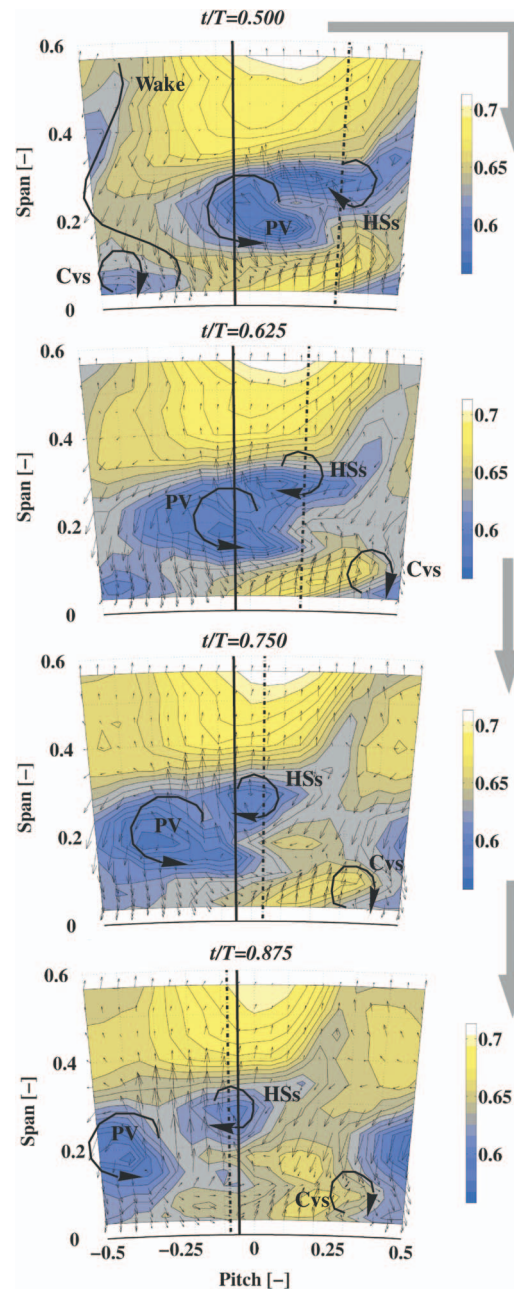**Fig. 4 Relative total pressure and secondary flow vectors at different time steps (area I)**
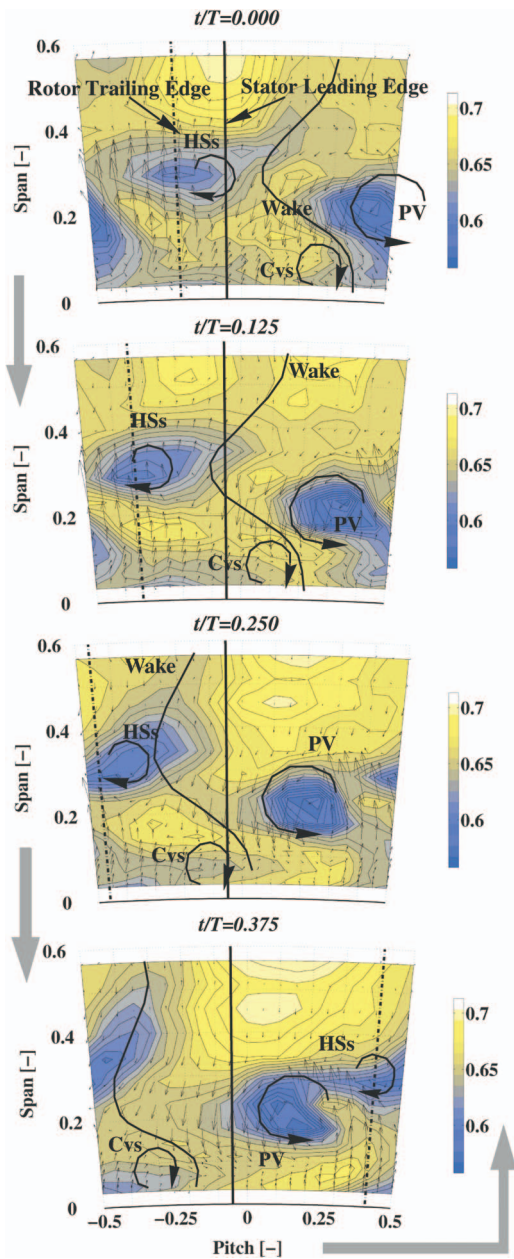
Fig. 5 Relative total pressure and secondary flow vectors at different time steps (area I)

cussed next.

Classical vortex flow theory predicts a static pressure and relative total pressure minimum peak within the core of a vortex tube. This fact is used, together with the secondary flow vectors, to localize the different vortical flow structures within the contour plots of Figs. 4 and 5. With regards to those results, the regions of low relative stagnation pressure are therefore associated to the rotor indigenous secondary flow vortices and the remnants of the upstream first stator endwall flow.

At $t/T=0$ a drop of relative stagnation pressure of 0.08 C_{ptr} (30% relative dynamic head) is found in the core of the passage vortex (PV) when compared to the average level at the hub. This drop remains nearly constant within the entire blade passing period. The size of this local drop in the contour plot varies with time and relative position of the rotor and stator blade rows. The effect of the corner vortex on the stagnation pressure is marginal and is neglected in this discussion.

A flow structure is seen on top of the passage vortex for the entire blade passing period, indicating that this structure is rotor related and associated to the suction side leg of the horse shoe vortex HSs or to the rotor trailing edge vortex. The relative stagnation pressure deficit due to the HSs vortex is half when compared to the passage vortex. The corresponding drop of relative stagnation pressure in the HSs flow structure remains nearly constant within the blade passing period, but the affected flow area doubles for certain time steps ($t/T=0.5-0.75$).

In general, a region of high vorticity often results from high shear and dissipative flow effects that occur within e.g., secondary flow dominated regions within a turbine stage. In particular the strong passage vortex at the rotor exit flow field is held responsible for this result, as found in the experiments for time steps $t/T=0.5$ to $t/T=0.75$. Remarkable is the large area that is covered by the stagnation pressure deficit (70% of blade pitch) at 20% radial span.
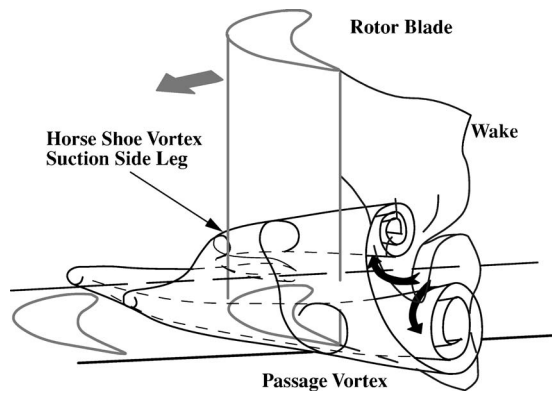
Fig. 6 Schematic of roll-up mechanism of the wake into the secondary flow vortices

Fig. 7 Space–time diagram for incidence angle Da at 25% rotor blade span (underturning) (I) 0% stator–stator/(II) 50% stator–stator

Additional analysis of the unsteady 3D flow data indicates an increase of 220% of pitchwise averaged streamwise vorticity at a radial height of 0.15 between $t/T=0.25$ to $t/T=0.75$ (Schlienger [13]). This dramatic increase of streamwise vorticity originates from a streamwise stretching of the dominant rotor passage vortex tubes and from the periodic shedding of high vorticity that is generated in the upstream first stator endwall flow field and convects downstream through the first rotor blade row into the measurement volume.

Apart of the vortices that influence the stagnation pressure distribution at the rotor exit, the wake layer also contributes to a loss of stagnation pressure. The wake and its shape is identified in the contour plots of Figs. 4 and 5 and marked by a solid line when using Eq. (2). The shape of the wake is influenced by its proximity to the passage vortex that induces a secondary flow velocity field on to the main flow. The radially aligned wake layer is skewed around the streamwise axis and rolled up into the vortical system at the rotor hub the closer the wake approaches it. High loss fluid is entrained from the wake layer into the endwall secondary flow field as shown in Fig. 6.

The identified vortices interact with the radial vorticity filaments of the rotor wake layer and redistributes high loss fluid in the hub area of the rotor blade row. At times, the wake does not exist as a measurable quantity ($t/T=0.5-0.75$) as it is entrained by the streamwise vortical flow structures. The downstream stator potential field affects, through a change of the rotor exit velocity field, the convection of the upstream rotor indigenous secondary flow and wake structures into the downstream stator blade passage.

Influence of Upstream Stator Flow Field. The secondary flow structures from the first stator blade row are shed into the downstream rotor passage, which affects the formation of the rotor indigenous vortices. The resulting flow structure at the rotor exit faces the downstream second stator blade row with its potential pressure field. The stagnation pressure distribution and the incidence angles in the rotor exit plane depend on the relative position of the first and second stator blade rows (clocking effect). A possible way to assess the influence of stator clocking on the unsteady flow field in the measurement area is by shifting the first stator blade row by half a stator pitch relative to the second stator. This way, the different flow structures are forced to interact at different time instances and positions with the downstream second stator. Any differences of the unsteady flow field for both cases are then associated with the effect of stator clocking. This procedure reveals best the nature of the interaction mechanism and quantifies those differences of incidence angles and relative total pressure due to clocking.

The initial configuration with the axially aligned first and second stator blades are defined as 0% stator–stator case, the second
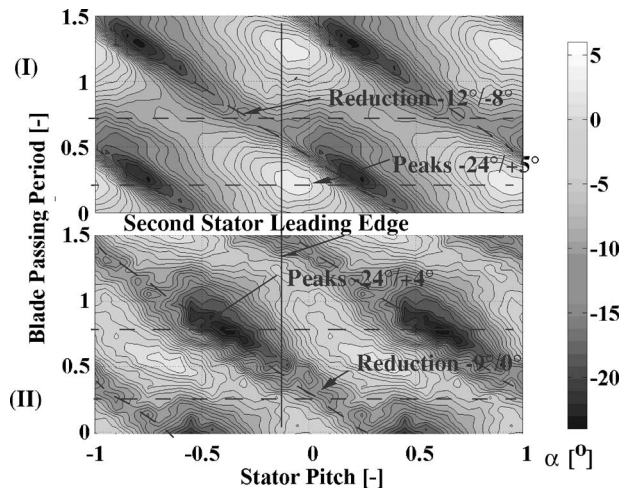
case with the half blade pitch shift of the first stator blade row as 50% stator–stator, respectively. Figure 7 shows the space–time diagram for both configurations for the incidence angle $\Delta\alpha$ at 25% blade span. The flow at 25% span is underturning by −8 deg on average, as seen in Fig. 3. The influence of the rotor relative flow field is visible as inclined contour pattern that is parallel to the dashed lines. The influence of the stator stationary flow field is visible as contour pattern that is perpendicular to the stator pitch axis.

For $t/T=0.25$ the peak incidence reaches a level of −24 deg and +5 deg close to the second stator leading edge at 0 and 0.2 stator pitch. For $t/T=0.75$, those peaks are considerably reduced down to −12 deg and −8 deg. The previous analysis of the measured data showed a maximum deficit of relative stagnation pressure for this time step. Hence, at $t/T=0.25$ the secondary flow field is mainly defined by the rotor indigenous vortices, in particular the passage vortex, that leads to the largest variation of the incidence angle. At $t/T=0.75$, the shedding of the upstream first stator secondary flow field occurs and destroys the strong secondary flow structure at the rotor hub, which reduces the pitchwise variation of incidence angle from 29 deg down to 4 deg. Such a low variation of incidence angle would be positive for the stator blade design. But this beneficial stabilizing effect goes in parallel with a drop of relative stagnation pressure that reduces blade performance and stage efficiency.

The incidence peaks are shifted by 50% in circumferential direction when clocking the first stator by half a blade pitch, as seen in Fig. 7(II). The peak values of positive and negative incidence remain in the same order of magnitude as for case (I). A reduction of incidence angle implies a reduction of over- and underturning of the flow field and thus less secondary flow velocity, which is equivalent to a weakened rotor hub passage vortex. This effect is pronounced in case (I) at $t/T=0.75$ and in case (II) at $t/T=0.25$, which is when the remnants of the shed first stator secondary flow structures passes the measurement area.

Figure 8 shows the corresponding space-time diagram for the relative total pressure C_{ptr} at 25% span. The first comparison of the contour plot for case (I) and case (II) shows a remarkable difference of stagnation pressure variation for the baseline and the clocked turbine stage configuration. With aligned first and second stator blades (case I) the stagnation pressure varies within 0.68 and 0.56 of C_{ptr}, whereas for case (II) there is a variation of within 0.68 to 0.52, which is equivalent to 63% of the relative dynamic head.

The remnants of the shed first stator secondary flow field
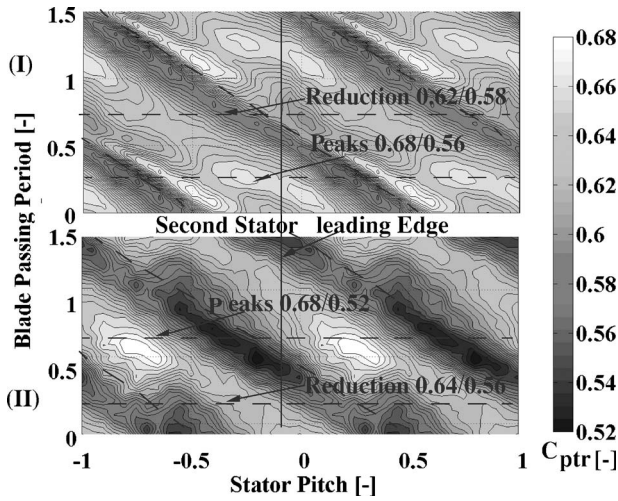
Fig. 8 Space–time diagram for relative total pressure coefficient at 25% blade span (I) 0% stator–stator/(II) 50% stator–stator

crosses the rotor exit plane at t/T=0.75 in case (I) and t/T =0.25 for case (II). The stagnation pressure contours for case (I) suggest less variation when compared to case (II). This means, that the periodic shedding of the first stator secondary flow struc-

Fig. 9 Effects of stator–stator clocking on mass-averaged flow profiles (at first rotor exit)

tures onto the downstream stator blade are generating high stagnation pressure variations as they convect in between the second stator leading edges at half a blade pitch. In case, that those structures hit the second stator leading edge (case I), the stagnation pressure variation remains moderate. The stator blade potential pressure field reduces the flow unsteadiness by enforcing an acceleration and deceleration effect on the velocity field at the rotor exit plane, as seen in the comparison of Fig. 8 (I) and (II). The results suggest, that the influence of the shed upstream stator flow on the vortex-wake-blade mechanism mainly affects the peaks of unsteady relative total pressure variation rather than the peaks of incidence angle in front of the stator blade.

The comparison of the pitchwise mass averaged steady flow profiles for the absolute flow angle α and relative stagnation pressure C_{ptr} is shown for both clocking positions in Fig. 9. The time-averaged incidence angles and the relative total pressure do not differ between the two cases (I) and (II) at both 10% and 25% blade span. Although the space–time diagrams (Figs. 7 and 8) showed measurable differences of the instantaneous values, the time-mean values do not.

This surprising result suggests that the interaction mechanism of the observed flow features, even though they occur at different time instances and locations, remains primarily kinematic with no influence of the time averaged values. This important conclusion implies that stator clocking does not generate any effects (positive or negative) that alter the averaged flow field in front of the second turbine stage.

The analysis of the unsteady flow data is summarized in Tables 3 and 4. The steady flow field shows no considerable differences at the hub section within the area of the rotor hub passage vortex dominated flow area between 0%–40% blade span. The result shows a minimal radial migration of the rotor hub vortex towards the hub as a result of the shifted upstream first stator hub endwall flow field.

It is concluded, that the shed vortices from the upstream first stator hub secondary flow field influence the pitchwise variation of unsteady incidence angles and relative stagnation pressure but leaves the time-averaged flow profiles unaffected. The over- and underturning effect at the rotor hub is therefore mainly a result of the rotor indigenous passage vortex, that induces this strong secondary velocity field on the main flow.

Pitchwise Mass-Averaged Unsteady Flow Profiles. The previous section showed an influence of the first stator secondary flow field on the unsteady flow field in the downstream rotor exit area. Stator clocking did not influence time-mean flow profiles but obviously has an effect on the unsteady flow profile distribution as shown in this section.

The results of time-resolved flow field measurements are in general presented as animated flow fields. Alternatively they could be expressed as pitchwise mass-averaged space–time diagrams as

Table 3 Summary of incidence angles $\Delta\alpha$ on second stator blade row for 25% and 10% blade span (I) 0% stator–stator/(II) 50% stator–stator

Blade span	Design α (deg)	Mean (I/II) $\Delta\alpha$ (deg)	Max. (I/II) $\Delta\alpha$ (deg)	Min. (I/II) $\Delta\alpha$ (deg)
25%	−34	−8/−7.9	−3.6/2.9	−23/−24
10%	−40	15.4/16.2	28/26.4	8.1/2.9

Table 4 Summary of relative total pressure C_{ptr} at rotor exit plane I for 25% and 10% blade span (I) 0% stator–stator/(II) 50% stator–stator

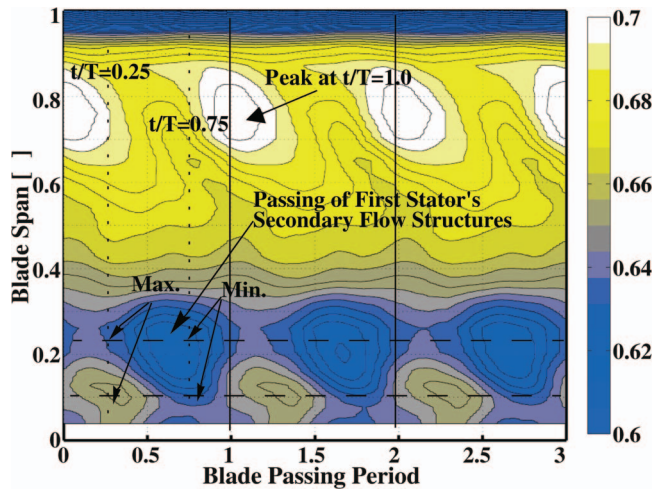| Blade span	Mean (I/II) C_{ptr}	Max. (I/II) C_{ptr}	Min. (I/II) C_{ptr}
25%	0.63/0.63	0.68/0.68	0.56/0.52
10%	0.66/0.65	0.67/0.65	0.61/0.59

Fig. 10 Pitchwise mass-averaged space–time diagram for relative total pressure C_{ptr} for area (I)

shown in Figs. 10 and 11. The measured data for the flow area (e.g., flow yaw angle) is pitchwise mass-averaged for each timestep t_i and given as a function of blade span r. The result is a space–time diagram for a given number of blade passing periods. An example is shown in Fig. 10 for the relative stagnation pressure C_{ptr} at the rotor exit plane of area I. The results of three consecutive blade passing events (phase lock averaged data) are plotted versus the blade span for the selected flow parameters. The contour lines for a steady flow field (e.g., from 5-hole probe measurements) would show contours that are parallel to the time axis. The identified fluctuations of C_{ptr} along the time axis are thus a result of unsteady flow effects and are evaluated on the basis of the proposed diagram type.

The two time steps for $t/T=0.75$ and $t/T=0.25$ are shown as dotted lines on the contours of Fig. 10. The presence of secondary flow vortices at the rotor hub influences the relative total pressure as seen at 25% blade span (underturning).

With increasing time, the relative total pressure drops from a peak of 0.64 at 25% blade span and $t/T=0.25$ down to 0.61 at $t/T=0.75$ (11% of relative dynamic head). A similar drop is observed at 10% blade height (overturning).

At 40% blade span, the relative stagnation pressure remains nearly constant over time. The rotor blade loading is therefore constant and thus not affected by secondary flow vortices from the
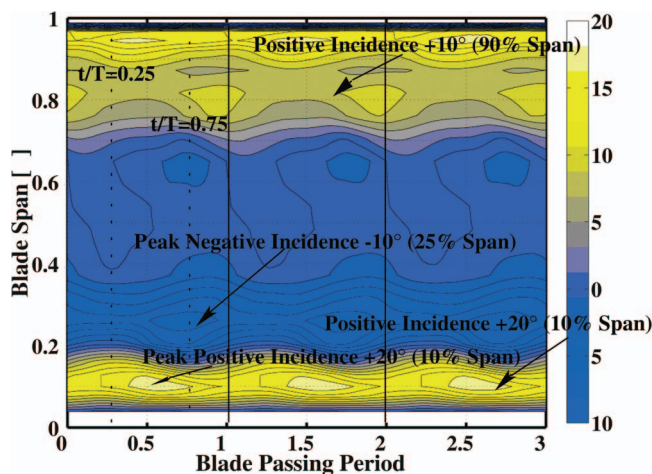
first rotor or upstream stator flow field. The time-resolved flow measurements show a massflow variation of ±0.6% of the overall massflow for one blade passing event, which is equivalent to a quasi-steady operating point of the turbine stage. The temporal variation of C_{ptr} at the rotor hub (dashed lines) is therefore related to the remnants of the first stator secondary flow field in the rotor exit area and to the interaction effects of the rotor related secondary flow vortices with the wake and the downstream stator blade profiles.

At the tip section of the rotor exit plane a variation of 0.02 C_{ptr} is found at 80% radial span, which is equivalent to 8% of relative dynamic head. This variation is either due to the interaction of the rotor wake with the downstream stator blade row or it results from the shed upstream first stator tip passage vortex. The evaluation of the corresponding contour plot for the clocked turbine stages shows a temporal shift of the observed peak, which associates this peak to the shed flow structure of the first stator rather than to the wake–blade interaction.

The measured variation of total pressure (Fig. 10) is associated with the time-resolved incidence angle $\Delta\alpha$ for three blade passing events, as shown in Fig. 11. The incidence angle is defined here as the angle between the measured instantaneous pitchwise averaged absolute flow angle α and the design intention for the stator blade.

The contour plots of Fig. 11 shows nearly zero incidence on the stator leading edge within the midspan area (between 40%–70% of blade span). The overall unsteady fluctuation of pitchwise mass-averaged incidence angle is considered as moderate and reaches a fluctuation amplitude of ±3 deg of absolute incidence angle at certain blade span positions during one blade passing event. The measured variation is equivalent to nearly 5% of rotor blade loading. The major impact is seen at the endwalls at both hub and tip. The strong secondary flow hub vortices in the rotor passage causes an average negative and positive incidence angle of up to −10 deg with ±3 deg of variation (at 25% span) and at 10% span an incidence angle of +15 deg and a variation of ±3 deg at the rotor hub. The tip section shows a nearly constant positive incidence of +10 deg relative to the blade design at 90% blade span.
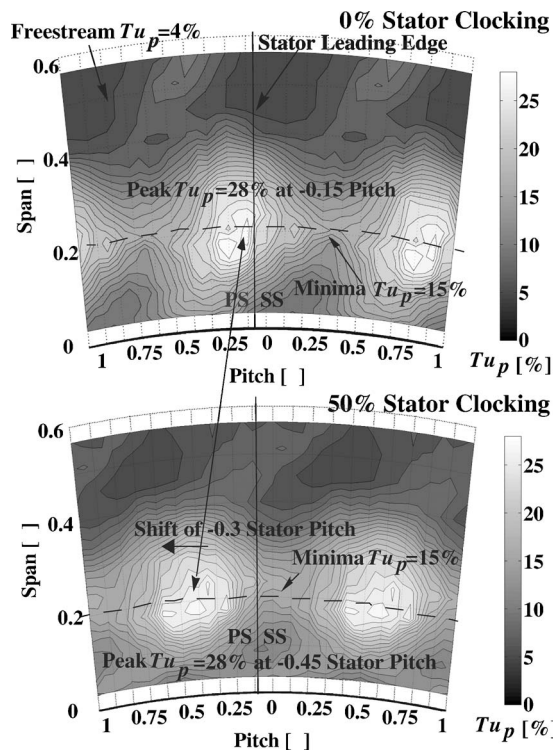
Analysis of Stochastic Pressure Signal

The turbulence level in the main flow field can be derived from the time-resolved pressure measurement under certain conditions. If the measured relative probe flow yaw angle remains within ±10 deg, then the derived stagnation pressure $P^0(t)$ is reasonably comparable to the measured center hole pressure $P(t)$ of a 3-sensor or virtual 3-sensor probe. It is assumed that the static pressure fluctuation is of secondary order when compared to the dynamic head variations P_{dyn}. The random signal of the center hole pressure $P'(t)$ is thus representative and equivalent to the random variation of the dynamic head $P'_{dyn}(t)$ (see Koeppel [12]). A turbulence intensity level Tu_p is introduced that relates the stochastic pressure variation $P'(t)$ to the dynamic head pressure $P_{dyn}(t)$ according to Ruck [11].

$$Tu_p = \frac{1}{2} \cdot \frac{\sqrt{\overline{P'^2}}}{P_{dyn}} \quad (3)$$

The derived turbulence level is assumed to be isotropic ($u' = v' = w'$) and is only valid for incompressible flows. The dynamic head P_{dyn} is derived from the probe measurements and calibration model and finally phase lock averaged in order to obtain the deterministic part of the dynamic head.

The introduced turbulence level is derived for the exit flow field of the first rotor hub section in order to evaluate the distribution of random unsteadiness at the rotor hub. In the work of Binder et al. [5] an area of high unsteadiness is observed at the blade pressure side at the inlet to the rotor blade where the upstream stator passage vortex interacts with the rotor blade leading edge.

Fig. 11 Pitchwise mass-averaged space–time diagram for incidence angle $\Delta\alpha$ (relative to design)

Fig. 12 Time-averaged turbulence level Tu_p of dynamic head at exit of first rotor for 0% stator clocking (baseline) and 50% stator clocking

This level of unsteadiness is also observed in the present analysis of the Tu_p level and shown in Fig. 12 as a time-averaged contour plot at the rotor hub section. The data analysis has been repeated for the clocked version (case II) and shown bellow the baseline contour plot. A freestream turbulence of $Tu_p=4\%$ is measured for both configurations (case I and II), which is representative for turbulence levels at the exit of first turbine stages.

The secondary flow dominated area between 10% and 35% blade span shows a very high averaged turbulence level of up to 28% due to the influence of the rotor hub passage vortex and the remnants of the first stator's secondary flow field at the rotor exit. The position of the second stator leading edge is sketched as a solid line at -0.1 blade pitch. A high level of random unsteadiness of +28% Tu_p is identified at the stator blade pressure side whereas a drop of Tu_p down to 15% is observed at half the blade pitch at 20% blade span.

In both cases (baseline and clocked version), the turbulence peak remains at a constant level of 28% Tu_p. The average turbulence level at 10% blade span shows a moderate difference of +10% versus +15% of Tu_p as a result of the stator clocking. However, the turbulence peak of 28% is shifted by only 30% blade pitch in negative circumferential direction when clocking the first stator blade row by half a blade pitch. The observed reduced circumferential shift of the turbulence peak (30% instead of 50%) suggest the following conclusions. The turbulence peak is primarily influenced by the periodic appearance of the shed first stator secondary flow structures that convect through the measurement volume. Clocking the first stator blade row implies a clocking of its endwall secondary flow field and as such a clocking of the area of high unsteadiness in the downstream flow field. The fact that the turbulence peak has only shifted by 30% blade pitch instead of half a blade pitch is surprising.

Conclusions

This paper has shown the key effects of the interaction between the rotor wake, the turbine blades, and the secondary flow vortices that are formed in the rotor and stator blade passages. The characteristic of the unsteady flow field at the rotor hub exit is primarily a result of the interaction between the rotor indigenous passage vortex and the remnants of the secondary flow structures that are shed from the first stator blade row. The clocking of the first stator blade row does not affect the time averaged flow profiles but clearly influences the circumferential positions of the peak values for the relative stagnation pressure, the incidence angles and the stochastic fluctuations of the dynamic head at the rotor exit. The strength of those effects have a potential to influence the formation of secondary flow structures in the downstream blade rows. Finally, the measurements reveal an interesting mechanism between the passage vortex and the wake, that is rolled up into the secondary flow vortical system at the rotor hub, as a result of the induced secondary velocity field of the passage vortex.

Acknowledgment

Nomenclature

C_{ps} = static pressure coefficient
C_{pt} = absolute total pressure coefficient
C_{ptr} = relative total pressure coefficient $C_{ptr}=(P^0_{\text{rel,local}}-P^0_{\text{Turbine out}})/(P^0_{\text{Turbine in}}-P_{\text{Turbine out}})$
$\vec{e}$ = mean unit vector (area)
P^0_{rel} = relative total pressure (Pa)
P' = random part of pressure signal (Pa)
P_{dyn} = dynamic head (Pa)
t = time (s)
T = blade passing period (s)
Tu_p = turbulence level of stagnation pressure (%)
U = rotor speed (m/s)
$\vec{u}_{\text{sec}}$ = local secondary flow vector (m/s)
$\vec{u}_i$ = local main flow vector (m/s)
v = velocity (m/s)
X = axial distance (trailing edge to probe)
Δ_w = circumferential wake displacement
α = absolute flow yaw angle (deg)
β = relative flow yaw angle (deg)
$\Delta\alpha$ = deviation relative to design intention (deg)

References

[1] Denton, J. D., 1993, "Loss Mechanisms in Turbomachines," The 1993 IGTI Scholar Lecture. J. Turbomach., **115**, pp. 621–656.
[2] Sharma, O. P., Butler, T. L., Joslyn, H. D., and Dring, R. P., 1985, "Three-Dimensional Unsteady Flow in an Axial Flow Turbine," AIAA J., **1**, pp. 29–38.
[3] Miller, R. J., Moss, R. W., and Ainsworth, R. W., 2003, "The Development of Turbine Exit Flow in a Swan-Necked Inter-Stage Diffuser," ASME GT-2003-38174, Atlanta, Georgia.
[4] Hodson, H. P., 1985, "Measurements of Wake Generated Unsteadiness in the Rotor Passages of Axial Flow Turbines," ASME J. Eng. Gas Turbines Power, **107**, pp. 337–344.
[5] Binder, A., Förster, W., Mach, K., and Rogge, H., 1986, "Unsteady Flow Interaction Caused by the Stator Secondary Vortices in a Turbine Rotor," ASME 1986-GT-302.
[6] Boletis, E., and Sieverding, C. H., 1991, "Experimental Study of the Three-Dimensional Flow Field in a Turbine Stator Preceded by a Full Stage," ASME J. Turbomach., **113**, pp. 1–9.

[7] Chaluvadi, V. S. P., Kalfas, A. I., Hodson, H. P., Ohyama, H., and Watanabe, E., 2003, "Blade Row Interaction in a High Pressure Steam Turbine," ASME J. Turbomach., **125**, pp. 14–24.

[8] Behr, T., Porreca, L., Mokulys, T., Kalfas, A. I., and Abhari, R. S., 2004, "Multistage Aspects and Unsteady Effects of Stator and Rotor Clocking in an Axial Turbine with Low Aspect Ratio Blading," ASME GT-2004-53612, Vienna, Austria.

[9] Chaluvadi, V. S. P., Kalfas, A. I., and Hodson, H. P., 2003, "Generating a Vortex to Study Vortex Interaction in an Axial Flow Turbine," 5th European Conference on Turbomachinery 2003, Conference Proceeding, pp. 1029–1038.

[10] Kupferschmied, P., Köppel, P., Gizzi, W. P., and Gyarmathy, G., 2000, "Time-Resolved Flow Measurements with Fast-Response Aerodynamic Probes in Turbomachines," Meas. Sci. Technol., **11**, pp. 1036–1054.

[11] Ruck, G., 1989, "Ein Verfahren zur instationären Geschwindigkeits- und Turbulenzmessung mit einer pneumatisch messenden Keilsonde," Mitteilung des Instituts No. 33, University of Stuttgart, Germany.

[12] Koeppel, P., 2000, "Instationäre Strömung in Turbomaschinen: Analyse Zeitabhängiger Sondenmessungen," Ph.D thesis Nr. 13500, ETH Zurich, Switzerland.

[13] Schlienger, J., 2003, "Evolution of Unsteady Secondary Flows in a Multistage Shrouded Axial Turbine," Ph.D. thesis, No. 15230, ETH Zurich, Switzerland.

[14] Schlienger, J., Pfau, A., Kalfas, A. I., and Abhari, R. S., 2003, "Effects of Labyrinth Seal Variation on Multistage Axial Turbine Flow," ASME Atlanta 2003-GT-38270.

[15] Langston, L. S., Nice, M. L., and Hooper, R. M., 1977, "Three Dimensional Flow Within a Turbine Cascade Passage," ASME J. Eng. Power, **99**, pp. 21–28.

[16] Hawthorne, W. R., 1955, "Rotational Flow Through Cascades," Q. J. Mech. Appl. Math., **8**, Pt. 3, Sept., pp. 266–279.

[17] Goldstein, R. J., and Spores, R. A., 1988, "Turbulent Transport on the Endwall in the Region Between Adjacent Turbine Blades," ASME J. Heat Transfer, **110**, pp. 862–869.

Flow Mechanism for Stall Margin Improvement due to Circumferential Casing Grooves on Axial Compressors

Aamir Shabbir

University of Toledo and
NASA Glenn Research Center,
21000 Brookpark Road, MS 5-9,
Cleveland, OH 44135
e-mail: aamir.shabbir@grc.nasa.gov

John J. Adamczyk

NASA Glenn Research Center,
21000 Brookpark Road, MS 5-9,
Cleveland, OH 44135

A computational study is carried out to understand the physical mechanism responsible for the improvement in stall margin of an axial flow rotor due to the circumferential casing grooves. Computational fluid dynamics simulations show an increase in operating range of the low speed rotor in the presence of casing grooves. A budget of the axial momentum equation is carried out at the rotor casing in the tip gap in order to understand the physical process behind this stall margin improvement. It is shown that for the smooth casing the net axial pressure force at the rotor casing in the tip gap is balanced by the net axial shear stress force. However, for the grooved casing the net axial shear stress force acting at the casing is augmented by the axial force due to the radial transport of axial momentum, which occurs across the grooves and power stream interface. This additional force adds to the net axial viscous shear force and thus leads to an increase in the stall margin of the rotor. [DOI: 10.1115/1.2008970]

Introduction

Several papers have been published that demonstrate the improvement of stall margin of axial flow compressors and fans by using circumferential casing grooves. There have also been a number of papers which have attempted to uncover the flow mechanism by which casing grooves provide an increase in stall margin. However, this understanding is still not complete and more work is needed not only in understanding the flow mechanism but also in bringing it to a level where it can easily be used by turbomachinery designers.

The earliest studies that attempted to understand the physics behind the improvement in stall margin of an axial flow compressor rotor attributed to circumferential casing grooves were those of Osborn et al. [1], Moore et al. [2], Bailey [3], and Prince et al. [4]. Some of the other related studies from this time period are those of Griffin and Smith [5], Koch and Smith [6].

Takata and Tsukuda [7] experimentally tested five different forms of grooves in order to establish their effectiveness and to determine the mechanism responsible for the stall margin improvement. They concluded that the tangential momentum imparted by the flow exiting the grooves resulted in an increase in stall margin. Paulon and Dehondt [8] carried out a theoretical study of casing treatment. Smith and Cumpsty [9] examined axially skewed casing grooves and found that the unsteady flow generated by this treatment was of secondary importance in increasing stall margin. Lee and Greitzer [10] used axially skewed grooves in their experimental study in order to clarify some of the issues regarding the fluid mechanics associated with their use. The unique design of their experiment (stator with a rotating hub) allowed them to study the effect of flow injection and removal in a controlled manner. They concluded that both flow injection and removal by the grooves increased the stall margin but neither could be regarded as the sole mechanism for stall margin improvement.

Crook et al. [11] also examined axially skewed grooves using computational fluid dynamics (CFD). They concluded that the two main reasons for stall margin improvement for this form of casing treatment were removal of low relative total pressure fluid from the power stream and the suppression of flow blockage in the core of the tip leakage vortex. Kang et al. [12] from their experimental study on recessed casing treatment concluded that stall margin improvement was due to removal of low relative total pressure fluid from the power stream into the recessed casing treatment. They also concluded that the increase in stall margin was not due to the decrease in flow incidence in the rotor tip region. Rabe and Hah [13] studied the effectiveness of circumferential grooves on the stall margin of a transonic compressor both experimentally and computationally. They suggested that the reason for stall margin improvement was reduced incidence near the pressure side of the rotor leading edge which in turn caused an alteration of the local flow distribution. They also found that shallow grooves were very effective in extending stall margin.

The current computational study is aimed at investigating the flow mechanism that is responsible for stall margin improvement attributed to circumferential groove casing treatment. The results of the study are applicable to casing critical low speed compressors. The objective of the work is to verify the following hypothesis.

1. For the smooth casing the net axial pressure force at the casing in the tip gap is balanced by the net axial viscous shear force.
2. For the grooved casing the net axial pressure force at the casing in the tip gap is balanced by the net axial shear force and the net axial force due to the radial transport of axial momentum. The later acts across the interface between the grooves and the power stream. When the magnitude of axial viscous shear force drops, the net axial force due to the radial transport of axial momentum is able to compensate for it thereby extending the operating range of the compressor.
3. Relative to a smooth casing, the grooved casing reduces the growth rate of flow blockage of a rotor at a given flow coefficient. Furthermore, the growth rate of blockage is dependent upon the near casing viscous flow field over the tip gap.
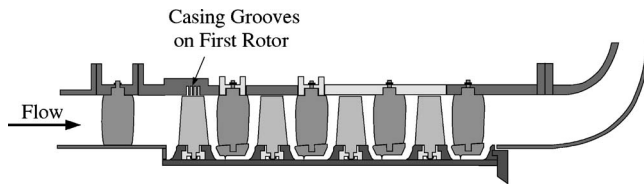
Fig. 1 A side view of the low speed axial compressor taken from Prahst and Strazisar (2003)

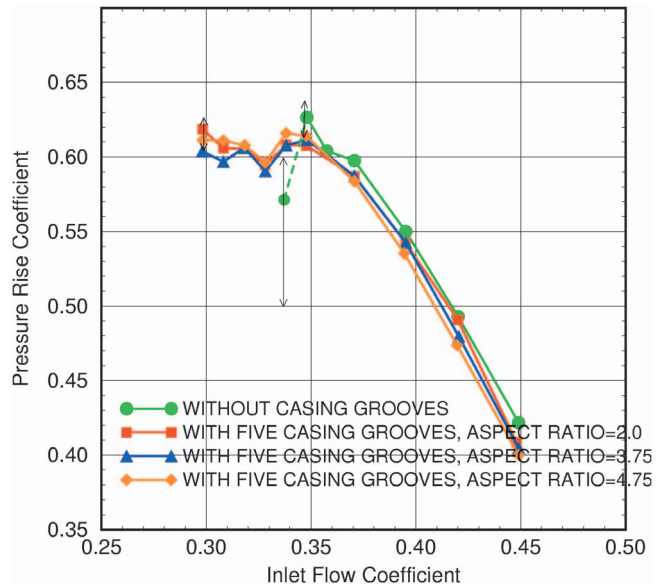Fig. 2 Pressure rise across the rotor with and without the casing circumferential grooves

The outline of the paper is as follows. First we will briefly describe the geometry of the rotor used in this study and the CFD tool employed. In the results section we first present the rotor pressure rise characteristic for a smooth casing and with circumferential casing grooves. Both sets of results are based on CFD simulations. These results demonstrate the CFD tool's ability to predict an improvement in stall margin due to the use of circumferential casing grooves.

An axial momentum budget analysis is presented for a control volume located adjacent to the casing of finite but very small radial extent spanning one rotor pitch and extending from the rotor leading edge to the rotor trailing edge. This budget analysis is used to show the fluid mechanics introduced by circumferential casing grooves at the casing over the rotor. Estimates of flow blockage at various operating points are presented in order to show the growth rate of flow blockage for a smooth casing and for a casing with circumferential grooves. This is followed by a set of results which show the impact of the near casing viscous flow region on the growth rate of flow blockage. Finally a procedure for establishing the effectiveness of an individual groove on stall enhancement is presented. This procedure can be used to guide the design of circumferential grooved casing treatment. Note that the current study is aimed at understanding the stall margin improvement provided by circumferential casing grooves using steady state CFD. Therefore it cannot be used to investigate the generation of instabilities and their temporal and spatial growth which happens prior to stall.

Test Compressor

The test compressor used for the current study is the low speed axial compressor (LSAC) at NASA Glenn Research Center which has an inlet guide vane followed by four identical stages (Fig. 1.). LSAC geometry is similar to the GE low speed research compressor and is designed to study the rear stages of a core compressor. The blades of the LSAC were adapted from a GE design (Wisler [14]). The GE design was executed for NASA with the objective of reducing the end wall losses of an axial flow compressor. The outer diameter of the LSAC flow path is 1.219 m and the hub-to-tip ratio is 0.8. The rotational speed is 958 rpm and the rotor tip speed is 61.15 m/s. For both sets of simulations the rotor tip clearance to chord ratio is 1.6% (for the simulations with circumferential grooves clearance is measured with respect to ungrooved portion of casing). More details about the compressor can be found in Wellborn et al. [15] and Culley et al. [16].

The first rotor of the compressor uses casing treatment in the form of five casing grooves of equal width. In order to reduce the computational work we simulated the first rotor of this compressor in isolation. The simulations are carried out with and without the grooves. The axial location and the width of the five grooves used in the current CFD study are identical to the ones used in the experiment. The first groove starts at approximately 6 mm from the leading edge of the rotor tip. Each groove is 6 mm wide (11.7% of rotor tip axial chord) with a gap of 3 mm (5.7% of rotor tip axial chord) between each of the grooves. Three different heights of the grooves were used while keeping their axial width unchanged. This gave us three sets of simulations with groove aspect ratios of approximately 2, 4, and 5.

The mesh used in the current study had 182 grid cells in the axial direction of which 99 grid cells were between the leading and trailing edges of the rotor. The mesh has 63 cells in the span wise direction, and 51 cells in the blade to blade direction. Eight cells were employed to grid the tip gap region in the base line mesh. The rotor tip was grided so that the tip gap was part of the computational domain and therefore no tip gap flow model was employed. Each of the circumferential grooves used ten grid cells in the axial direction. In the radial direction 28 grid cells were used for the 5:1 aspect ratio groove, 26 for the 4:1 aspect ratio groove, and 21 for the 2:1 aspect ratio groove.

The numerical procedure solves the three-dimensional Reynolds averaged Navier–Stokes and energy equations using the four step Runge–Kutta scheme (Adamczyk et al. [17]). The standard two equation $k-\epsilon$ model was used to calculate the turbulent eddy viscosity along with an improvement in the form of a variable eddy viscosity coefficient as described in Shabbir et al. [18]. Spalding's formula [19] was used to set the wall boundary conditions for the mean flow equations as well as the turbulence model (Shabbir and Turner [20]). The inlet boundary conditions consisted of the span wise profiles of total pressure, total temperature, radial and tangential flow angles. These were obtained from the numerical simulations of the full compressor.

The results to be presented in this paper are normalized using the following definitions. The pressure coefficient is defined as $(\Delta P_T)/(1/2)\rho_{ref}U_{tip}^2$ where ref refers to the conditions at the inlet of the compressor (upstream of inlet guide vane). ΔP_T is the mass averaged total pressure rise across the rotor. U_{tip} is the tip speed of the rotor. The mass flow $\dot{m}$ is defined in terms of a flow coefficient $\dot{m}/(\rho_{ref}A_{ref}U_{tip})$.

Speedlines

The pressure characteristics derived from the isolated rotor simulations are summarized in Fig. 2. For the smooth casing configuration the flow coefficient of 0.350 was the last converged point obtained. (The error bars on some of the points represent the envelope of pressure coefficient variations. The simulations do not converge to a single value for these points and instead approach a limit cycle.) When five casing grooves are used the rotor does not stall until the flow coefficient is reduced to 0.300, clearly extending its operating range. This increase in range is found to exist for

all three groove aspect ratios. Over the flow range of the smooth casing simulations the use of casing grooves lowers the pressure rise slightly.

In the experiments the smooth casing configuration stalls just below a flow coefficient of 0.34. For the circumferential groove configuration the compressor stalls just below a flow coefficient of 0.300. The insensitivity of the stall point to the groove aspect ratios which were investigated is consistent with the unpublished experimental findings of Prahst and Strazisar [21].

Axial Momentum Equation

The present work hypothesizes that circumferential groove casing treatment reduces the growth rate of flow blockage relative to a smooth casing. In addition the growth rate of flow blockage is controlled by the near casing flow field over the rotor tip. In order to prove this hypothesis we begin by analyzing the near casing flow in order to gain a quantitative understanding of the relevant fluid mechanics associated with a smooth casing and one with circumferential grooves. There are several ways of accomplishing this task, the use of the equations of motion being one of them. Specifically we will analyze the balance between the various terms which appear in the axial momentum equation, since the pressure rise across the rotor can be explicitly derived from it.

Since we are numerically solving the axial momentum equation for a finite control volume, we will start with its finite volume formulation. The first step in this direction is integration of the axial momentum equation over a finite grid cell. Then using the divergence theorem the volume integral is expressed as a surface integral. For a flow which is steady in time (rotor frame of reference) the resulting equation is

$$\int_s \left[\rho V_z V_r dA_r + \rho V_z V_\theta dA_\theta + (\rho V_z V_z + P)dA_z \right]$$
$$= \int_s \left[\tau_{rz} dA_r + \tau_{\theta z} dA_\theta + \tau_{zz} dA_z \right], \qquad (1)$$

where the integration is over the appropriate surfaces of the grid cell. Equation (1) represents the conservation of axial momentum for an individual grid cell. It states that the net axial force due to the transport of axial momentum in the three directions is balanced by the net axial pressure force and the net axial stress force acting on the radial, tangential and axial faces of the grid cell. The stresses in Eq. (1) include both the viscous and Reynolds stresses. The Reynolds stresses are approximated by the eddy viscosity model, as was described earlier in the paper.

To help understand the nomenclature used in this paper let us look at the pressure force term in the above equation. Using the sketch of Fig. 3 (grid cell is shown with face normals parallel to the axial, radial and tangential direction) the net pressure force acting on the cell can be rewritten as

$$\int_s P dA_z = \int_{z1}^{z2} P dA_z = P_{z2}(A_z) - P_{z1}(A_z) = \Delta(PA_z), \qquad (2)$$

where P_{z1} and P_{z2} are the values of pressure on the two axial faces. The two axial faces of the grid cell have the same axial area, A_z, for the grid cell considered here and to be used later. (In general, for an arbitrary control volume there are also contributions from the projections of the areas A_r and A_θ in the axial (z) direction.) For brevity we can write this as $\Delta(PA_z)$. Using this notation Eq. (2) can be rewritten as

$$\Delta(\rho V_z V_r A_r) + \Delta(\rho V_z V_\theta A_\theta) + \Delta(\rho V_z V_z A_z) + \Delta(PA_z)$$
$$= \Delta(\tau_{rz} A_r) + \Delta(\tau_{\theta z} A_\theta) + \Delta(\tau_{zz} A_z). \qquad (3)$$

The meaning of $\Delta(\ )$ for each of the terms is evident from the grid cell surface area which appears in that term. Thus $\Delta(\rho V_z V_r A_r)$ is the net axial force due to the transport of the axial momentum
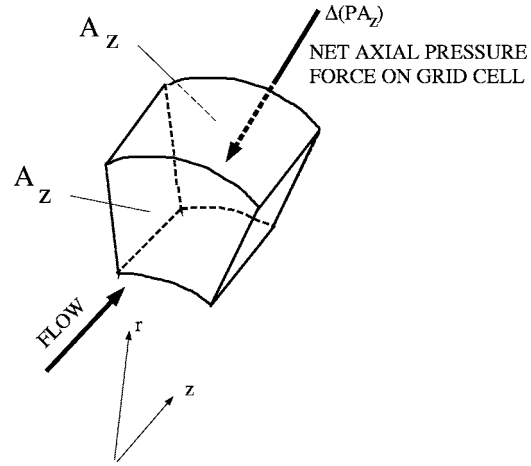

Fig. 3 A sketch of the grid cell illustrating the nomenclature of Eqs. (1)–(3) by using the example of net axial pressure force

across the radial faces of the grid cell. Similarly $\Delta(\tau_{rz} A_r)$ is the net axial stress force which acts on the radial surfaces of the grid cell.

Now consider the control volumes (one for smooth casing, other for grooved casing) at the casing in the tip gap as illustrated in Fig. 4. Each of these control volumes starts slightly upstream of the rotor leading edge and ends just downstream of the rotor trailing edge. In the tangential direction each extends one blade pitch. In the radial direction each extends only one grid cell. (Ideally we would like it to be of differential thickness in the radial direction.) Note that the geometry of the rotor used in the current study has a constant radius casing. The grid topology at the casing in the tip gap follows the casing flow path. For the control volumes shown in Fig. 4 the magnitude of the surface area normal to the axial direction at the rotor inlet and exit plane are the same.

Our objective is to understand the balance between the various terms of the axial momentum, Eq. (3), for both control volumes shown in Fig. 4. We want to know which terms plays a major role in supporting the net axial pressure force. Equation (3) is for an individual grid cell. The control volume in Fig. 4(a) has a number of such grid cells in the axial and tangential directions. Therefore, if we sum Eq. (3) in the tangential and the axial directions we obtain

$$\sum_{\theta,z} \Delta(\rho V_z V_r A_r) + \sum_{\theta,z} \Delta(\rho V_z V_\theta A_\theta) + \sum_{\theta,z} \Delta(\rho V_z V_z A_z) + \sum_{\theta,z} \Delta(PA_z)$$
$$= \sum_{\theta,z} \Delta(\tau_{rz} A_r) + \sum_{\theta,z} \Delta(\tau_{\theta z} A_\theta) + \sum_{\theta,z} \Delta(\tau_{zz} A_z). \qquad (4)$$

For brevity we have used the nomenclature $\Sigma_z \Sigma_\theta (\ ) = \Sigma_{\theta,z}(\ )$. This equation represents the balance of axial momentum for the control volumes of Fig. 4. Equation (4) will be used in conjunction with the results from the numerical simulations to determine which terms of the equation balance the net axial pressure force. First we will discuss the smooth casing configuration.
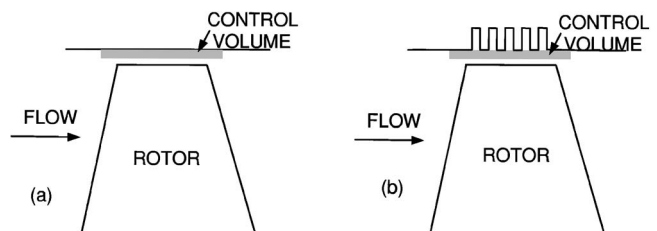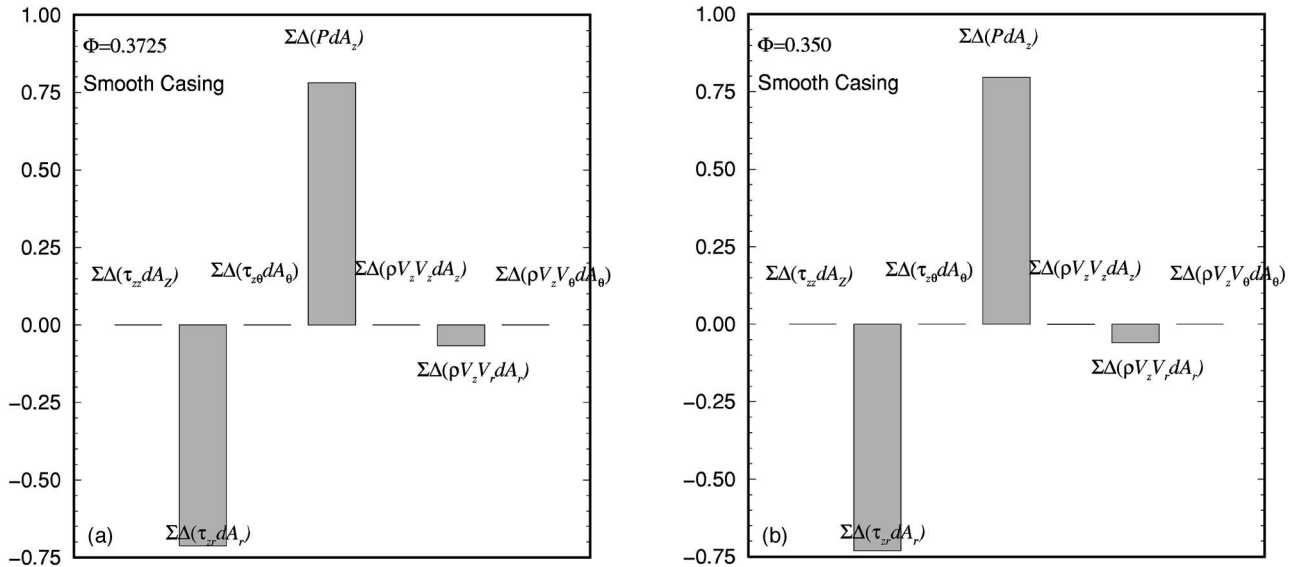

Fig. 4 A sketch illustrating the control volume at the casing used for analyzing the axial momentum equation

Fig. 5 The balances of the axial momentum equation for the smooth casing control volume defined in Fig. 4(*a*). Note that the summation nomenclature Σ in the figure means $\Sigma_{\theta,z}$.

Before we proceed with the analysis of the smooth casing configuration it is instructive to comment on the magnitude of each of the terms which appear in Eq. (4) based on physical arguments alone. We will assume the control volume to be of differential thickness in the radial direction. Since the pressure rise across the rotor is of primary interest the net axial pressure force will be retained. Because of periodicity (which is assumed in the current computational procedure) in the tangential direction the net transport of axial momentum in the tangential direction $\Sigma_{\theta,z}\Delta(\rho V_z V_\theta A_\theta)$ as well as $\Sigma_{\theta,z}\Delta(\tau_{\theta z}A_\theta)$ will be zero. Since the velocity vanishes at the casing, the two remaining momentum transport terms as well as $\Sigma_{\theta,z}\Delta(\tau_{zz}A_z)$ will also be zero. Therefore in the limit as the radial thickness of the control volume approaches zero, Eq. (4) reduces to

$$\sum_{\theta,z}\Delta(PA_z) \rightarrow \sum_{\theta,z}\Delta(\tau_{rz}A_r) \quad as \ \Delta r \rightarrow 0 \tag{5}$$

Equation (5) simply implies that the net axial pressure force is balanced by the net axial viscous shear force acting on the radial faces of the control volume.

The balance of Eq. (5) based on simulations for smooth casing are shown in Fig. 5 for the flow coefficients of 0.3725 and 0.350, which was the last converged point that was calculated for the smooth casing. The various terms are normalized by $\rho_{ref}U_{tip}^2 A_{z_{total}}$ where $A_{z_{total}}$ is the total area of the axial face of the control volume. The balances for the other flow coefficients are similar and, therefore, are not shown.

We find that the net axial pressure force is balanced by the net axial shear force and the axial force due to the radial transport of axial momentum. Recall that the analysis presented in this section showed that the momentum transport term should vanish as the radial extent of the control volume approached zero. Results from a grid refinement study done in support of the present work showed this to be the case. The bar diagrams in Fig. 5 show the momentum transport term to be less then 10% of the pressure force. For the CFD simulation shown the net axial pressure force is almost totally balanced by the net axial shear force. We therefore conclude that for the control volume in Fig. 4(*a*) of differential thickness in the radial direction the net axial pressure force is balanced by the net axial viscous shear force. This confirms the first hypothesis which was stated in the Introduction and is schematically illustrated in Fig. 6.

Grooved Casing. Before discussing the results for the grooved casing let us revisit Eq. (4) for the control volume shown in Fig. 4(*b*). A portion of the top surface of this control volume is occupied by the grooves where there is a slip velocity. The flow can move across this surface either from the power stream into the grooves or vice versa as shown in Fig. 7. Figure 7 shows a flow image from the simulation with casing grooves to aid in understanding the flow field near the casing. It shows the distribution of radial velocity very close to the interface between the casing grooves and the power stream flow. The figure shows how the fluid is transported into and out of the grooves. This information is not new but is shown to orient the reader relative to the flow field
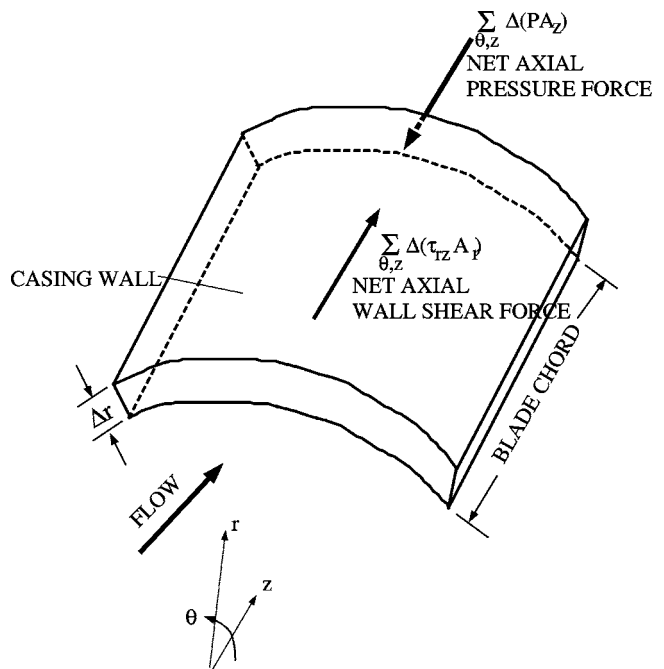
Fig. 6 A sketch illustrating the balance of axial momentum equation for the casing control volume for smooth casing as defined in Fig. 4(*a*)
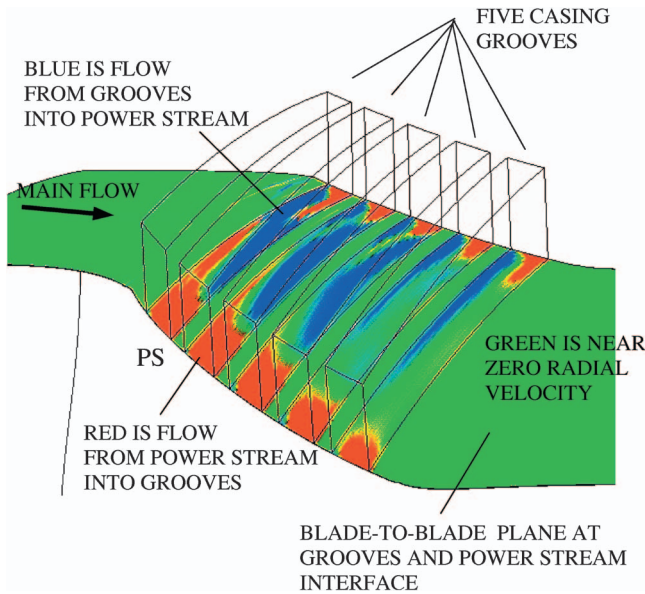
Fig. 7 An oblique view of the blade-to-blade plane at the casing showing the radial velocity distribution

generated by the grooves. Takata and Tsukuda [7] refer to the flow flowing from the grooves into the power stream as jets and noticed that it is the dynamic effect of these jets impinging on the power stream flow that provides stall margin improvement. The flow from the power stream into the casing grooves is referred to as flow removal in the literature. In addition to the radial transport across the groove power stream interface there is also a free shear layer which exists between the flow in the grooves and the power stream.

Before presenting results for the grooved casing we shall analyze Eq. (4) to see if any of the terms can be eliminated based on physical arguments. We shall maintain the net axial pressure force since it is directly related to the pressure rise across the rotor. We expect that the axial force due to $\sum_{\theta,z}\Delta(\tau_{rz}A_r)$ will be of the same order of magnitude as the pressure force because of the large radial gradient of axial velocity that exists in the near casing region. Due to periodicity in the tangential direction the tangential

transport of axial momentum as well as the force due to $\sum_{\theta,z}\Delta(\tau_{\theta z}A_\theta)$ will be zero, as was the case for the smooth casing. Due to the slip velocity at the groove power stream interface we cannot a priori rule out the force due to the radial and axial transport of axial momentum as well as the force due to $\sum_{\theta,z}\Delta(\tau_{zz}A_z)$ as was done for the smooth casing. Therefore, based on physical arguments Eq. (4) can be reduced to

$$\sum_{\theta,z}\Delta(\rho V_z V_r A_r) + \sum_{\theta,z}\Delta(\rho V_z V_z A_z) + \sum_{\theta,z}\Delta(PA_z)$$

$$\overset{?}{\rightarrow} \sum_{\theta,z}\Delta(\tau_{rz}A_r) + \sum_{\theta,z}\Delta(\tau_{zz}A_z) \quad as \ \Delta r \rightarrow 0 \quad (6)$$

The use of $\overset{?}{\rightarrow}$ in Eq. (6) is to highlight the fact that we do not know a priori the magnitude of some of the terms in this equation. Results for the balance between the terms which appear in Eq. (6) for grooved casing are presented in Fig. 8 for flow coefficients of 0.350 and 0.320. The balances for the other flow coefficients are similar. We observe that the net axial pressure force is balanced by the net axial shear force and the net axial force due to the radial transport of axial momentum. Thus Eq. (6) can be reduced to

$$\sum_{\theta,z}\Delta(PA_z) \rightarrow \sum_{\theta,z}\Delta(\tau_{rz}A_r) - \sum_{\theta,z}\Delta(\rho V_z V_r A_r) \quad as \ \Delta r \rightarrow 0 \quad (7)$$

and is schematically illustrated in Fig. 9.

Comparing the bar diagram for a flow coefficient of 0.350 in Fig. 5 to the corresponding bar diagram in Fig. 8 shows that the net axial pressure force with and without casing grooves are comparable. For the grooved casing configuration the magnitude of the net axial shear force is seen to be approximately 2/3 of that for the smooth casing configuration. With grooves present the remaining axial force needed to balance the axial pressure force is associated with the radial transport of axial momentum which occurs at the groove power stream interface.

Figure 8 shows that at the flow coefficient of 0.320 (recall smooth casing stall coefficient 0.340) the axial pressure force is virtually equal to that in Fig. 5 at a flow coefficient of 0.350. As the flow coefficient is reduced from 0.350 to 0.320 the reduction in the net axial shear force is augmented by an increase in the magnitude of the net axial force associated with the radial transport of axial momentum across the groove power stream interfaces. This augmentation is necessary in order to balance the net
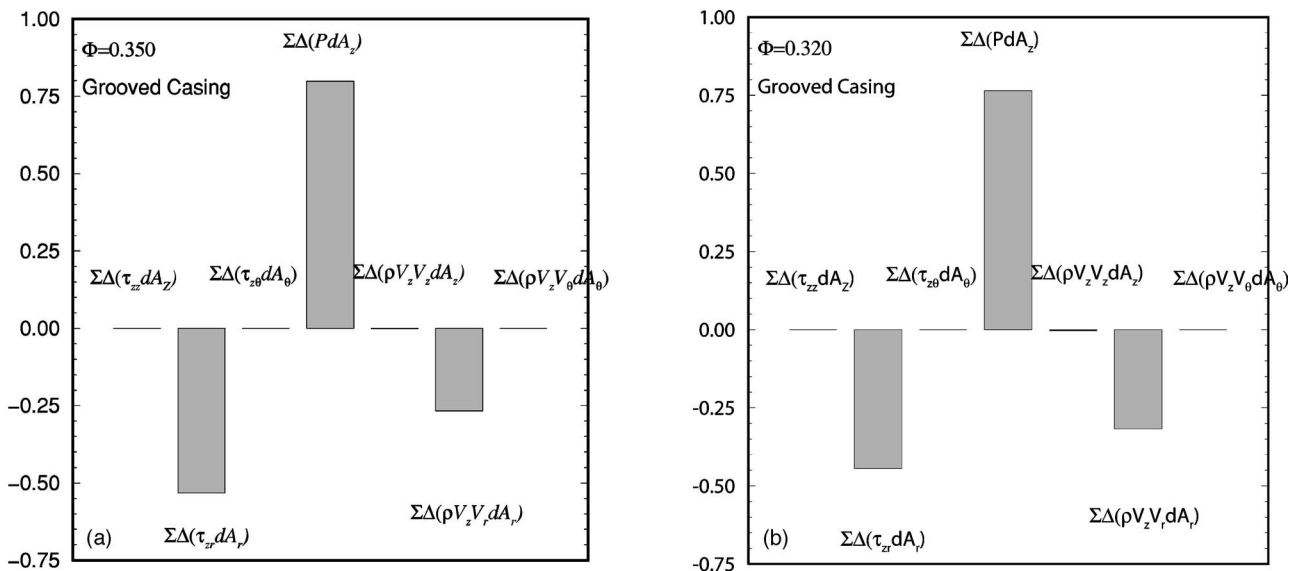
Fig. 8 The balances of the axial momentum equation for the grooved casing control volume defined in Fig. 4(b). Note that the summation nomenclature Σ in the figure means $\Sigma_{\theta,z}$.
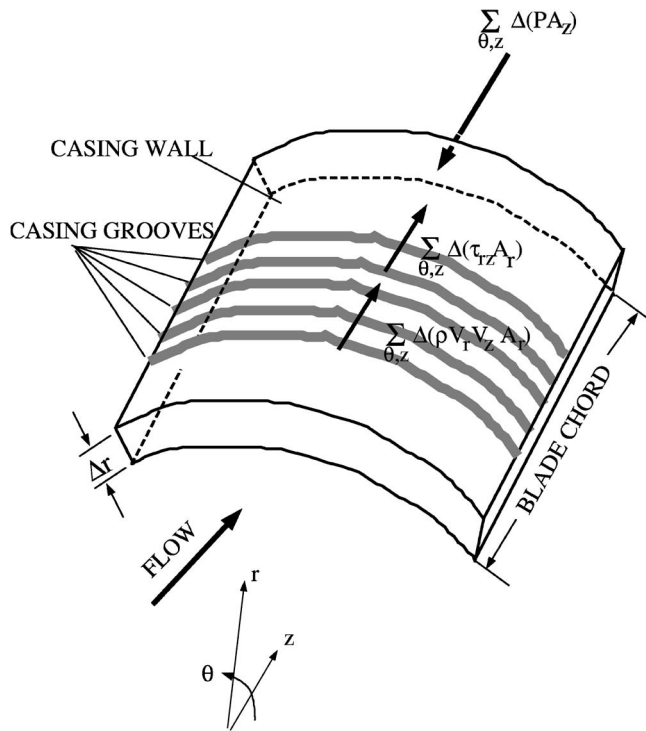
Fig. 9 A sketch illustrating the balance of axial momentum on the casing control volume with casing grooves as defined in Fig. 4(*b*)

axial pressure force and is absent in the case of a smooth casing. It is the fluid mechanics introduced at the casing by the transport process which leads to an increase in stall margin relative to a smooth casing configuration. This confirms the second hypothesis which was stated in the Introduction and is schematically illustrated in Fig. 9.

Individual Groove Contributions. We next assess the contribution of each groove to the net axial shear force and the net axial force due to the radial transport of axial momentum to the control volume in Fig. 4(*b*). This assessment is accomplished by determining the magnitude of these two forces as a function of axial position from the rotor leading edge. To estimate the magnitude of these two forces we first sum Eq. (3) across the tangential pitch of the rotor. The circumferential summation is then followed by a sum to a fixed axial location. The results are values for the net axial shear force and the net axial force due to the radial transport of axial momentum at a given axial location. The values for a flow coefficient of 0.350 and 0.320 are presented in Fig. 10. For comparison purposes the result for the net axial shear force for the smooth casing configuration at a flow coefficient of 0.350 is also presented. The normalized value of 0.73 at 100% chord is the net axial shear force on the control volume of the smooth casing configuration. For this configuration aft of 20% of chord the shear force is monotonically decreasing at nearly a constant rate.

Figure 10 also shows the contribution to the net axial force due to the radial transport of axial momentum. As discussed in section entitled Smooth Casing, the magnitude of this term for a smoothed casing approaches zero as the radial thickness of the control volume vanishes. This term must also approach zero on the land of the grooved casing as the radial thickness of the control volume vanishes. The fact that in both cases this term is finite is due to the small radial extent of the control volumes in Fig. 4. The results presented in Fig. 10 show that the consequence of this term not vanishing at the solid surfaces of the control volume on the quantitative behavior of the axial force balance is small.

The five shaded bands which appear in Fig. 10 denote the axial
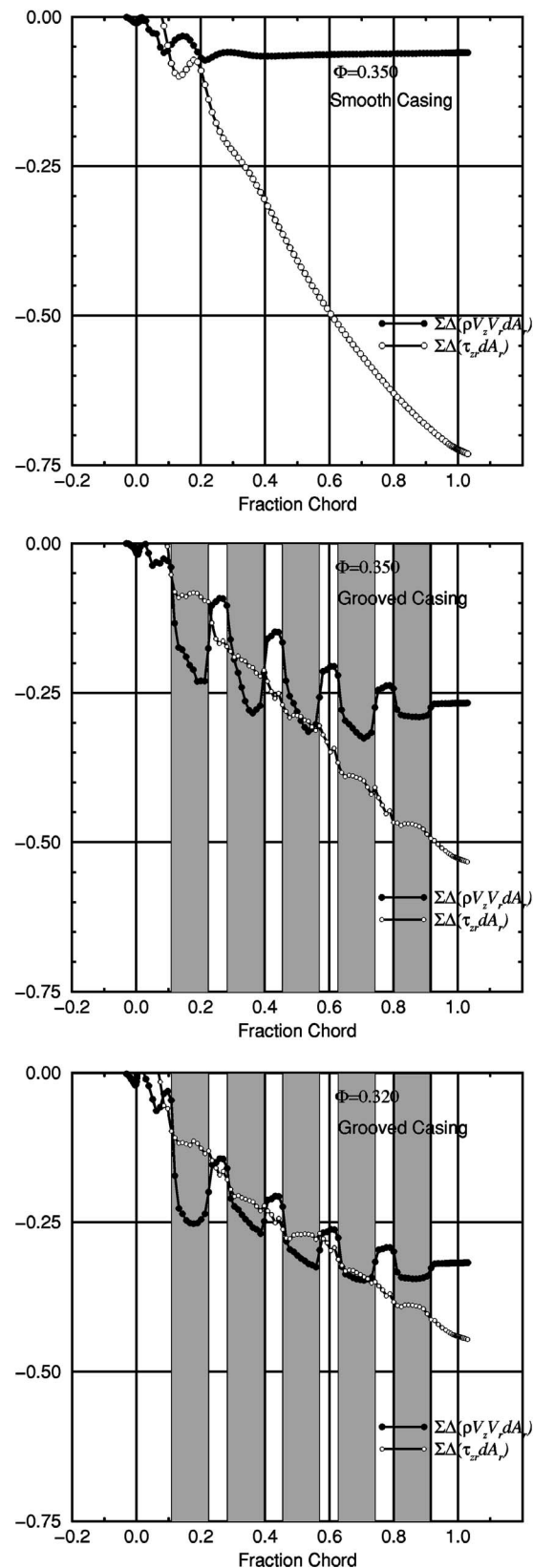
Fig. 10 Evolution of the cumulative sum in the axial direction for the axial shear force and the force due to the radial transport of momentum for the control volume shown in Fig. 4. Note that before doing the axial sum, these quantities have already been summed in the tangential direction and the summation nomenclature Σ in the figure legend means Σ_θ.

location of the five casing grooves. As in the case of the smooth casing configuration at a flow coefficient of 0.350, aft of 20% of chord the magnitude of net axial shear force decreases at nearly a constant rate with axial distance, the rate, however, being less than that for the smooth casing configuration. The presence of the free shear layer at the groove power stream interface does not appear to impact the character of the shear force distribution. This implies that the free shear layer is supporting the pressure rise across the rotor to the same degree as the shear layer on the groove land.

Figure 10 shows that the gain in the axial force due to the radial transport of axial momentum over the front portion of the groove is substantial. This gain is offset by a loss near the trailing edge of the groove which is only slightly less than the gain. The net result is a gain in the magnitude of the axial force associated with the radial transport of axial momentum across the groove power stream interface. The simulation results at a flow coefficient of 0.320 have similar trends to that at a flow coefficient of 0.350. One sees that the contribution to the net axial force due to the radial transport of axial momentum is greater at a flow coefficient of 0.320 than at 0.350. over the entire rotor chord. The net contribution of an individual groove to the axial force necessary to balance the net axial pressure force decreases the further the groove is from the rotor leading edge. Indeed the last groove appears to contribute little in support of the axial force necessary to balance the net axial pressure force. An assessment of the impact of the last groove on the stall margin of the rotor is presented in the section Application of Current Approach.

Flow Blockage Analysis

In this section we will show the impact of circumferential grooved casing treatment on flow blockage. No universally accepted definition of flow blockage exists and the majority of approaches use the fact that "you know it when you see it." In this study we will use the definition proposed by Khalid et al. [22] which expresses blockage in terms of the ratio of the "blocked" flow area to the total passage flow area. We will present these blockage values along with flow field pictures of the axial velocity, in order to relate these values to flow structure. This analysis is carried out for an r, θ plane located just downstream of the rotor trailing edge.

Flow blockage calculations results are presented in Fig. 11. With casing grooves present, only the results for the 2:1 aspect ratio configuration will be shown. The results for the other aspect ratio configurations are very similar. At the flow coefficient of 0.3725 the axial velocity distribution looks very similar for simulations with and without casing grooves. The blockage calculations using the method of Khalid et al. [22] is little more than 7% for both cases. At the flow coefficient of 0.350 the flow blockage for the smooth casing is 12.27% which is higher than the 9.57% for the grooved casing. The axial velocity contour plots clearly show that there is more flow blockage near the rotor tip for the smooth casing configuration. We further note from the axial velocity contours that the blockage near the hub suction corner in both cases is about the same. This is the last smooth casing simulation which converged. The contour plots in Fig. 11 give a qualitative picture as to how the casing flow is modified by circumferential grooves.

We next show the flow blockage in the outer 50% of span as a function of flow coefficient for the smooth casing configuration and with 2:1 aspect ratio casing grooves present. This comparison is presented in Fig. 12. From the speed lines shown in Fig. 2 the stall flow coefficient for the smooth wall configuration is near 0.340 while with grooves present it is below 0.300. For the smooth wall configuration Fig. 12 shows that the rate at which flow blockage increases becomes very large as the flow coefficient approaches 0.340. This behavior in the rate of growth of flow blockage near stall is consistent with that first observed by Khalid et al. [22]. At the flow coefficient of 0.340 the corresponding plot for the grooved casing configuration shows only a modest growth
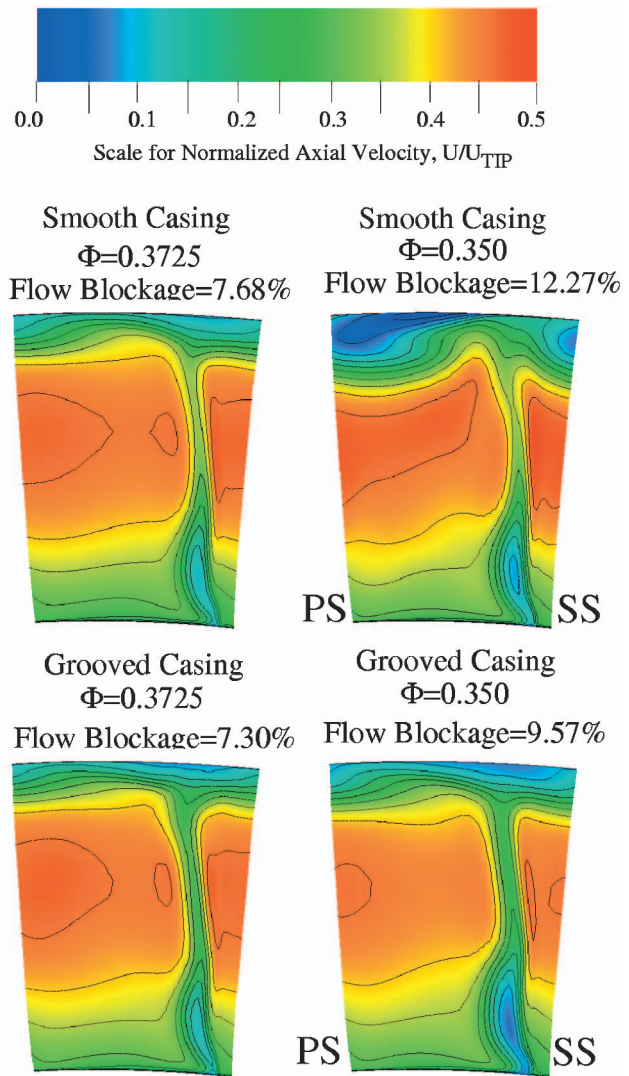

Fig. 11 The normalized axial velocity contours in an axial plane just downstream of the rotor trailing edge for smooth and grooved casing

rate. The growth in flow blockage with a reduction in flow coefficient for the grooved casing configuration does not change dramatically even as the flow coefficient approaches 0.300. The radial transport of axial momentum imparted by the grooves to the power stream results in a reduction in the growth rate of blockage as the flow coefficient is reduced. The reduced growth of flow blockage due to the presence of circumferential casing grooves results in an increase in rotor stall margin. Figure 12 confirms the first part of the third hypothesis stated in the Introduction, namely circumferential groove casing treatment impacts the rate at which flow blockage increases near stall.

Zero Shear on Casing. The third part of the hypothesis underpinning the present work states that the near casing flow region impacts the rate of blockage growth and thus impacts the rotor stall margin. To gain insight into the role of the near casing viscous flow region on blockage growth a series of simulations were performed in which the shear stress at the casing was set to zero, Van Zante et al. [23], Tan and Greitzer [24]. This results in a slip velocity at the casing which eliminates the development of the near casing viscous flow layer. The resulting pressure characteristic is shown in Fig. 13 along with the smooth casing characteristic from Fig. 2. Clearly there is large difference in the two character-
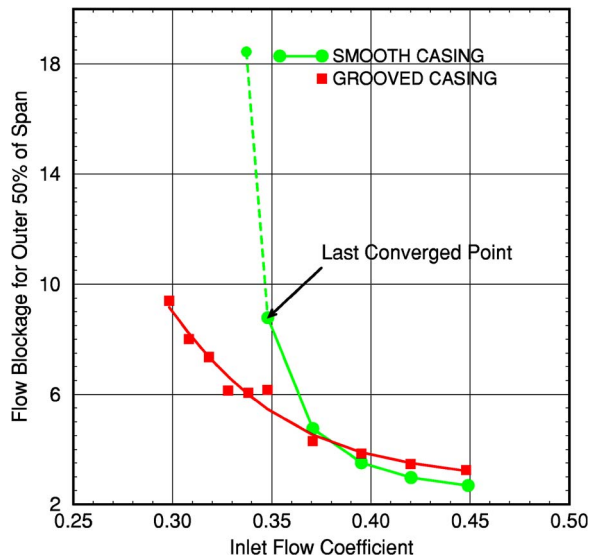
Fig. 12 Comparison of blockage growth as function of flow coefficient for smooth and grooved casings. Flow blockage is defined as $(A_{\text{Blocked}}/A_{\text{Total Passage}}) \times 100$.

Φ=0.395
Flow Blockage=8.17%
Zero Shear on Casing

Φ=0.3725
Flow Blockage=12.6%
Zero Shear on Casing

Fig. 14 The normalized axial velocity contours in an axial plane just downstream of the rotor trailing edge for the case of zero shear at the casing wall. See Fig. 5 for scale.

istics. The characteristic for the case in which the casing viscous flow layer is absent lies below that with the casing viscous layer present over the entire flow range. The peak pressure rise without the casing viscous layer is 0.52 while that with the viscous flow layer is 0.62, an increase of nearly 20%. In addition, the characteristic without the viscous flow layer rolls over at a higher flow coefficient than the corresponding characteristic with the viscous flow layer.

Figure 14 shows the contours of normalized axial velocity in an axial plane just downstream of rotor trailing edge for the flow coefficients of 0.395 and 0.3725. The corresponding figure with the casing viscous layer present is in Fig. 11. On both plots the respective flow blockage is noted and is primarily associated with the low axial velocity region near the casing. Comparing Figs. 11 and 14 one clearly sees less flow blockage in the rotor tip region when the casing viscous layer is present.

The two plots shown in Fig. 15 show the dramatic impact of the near casing flow field on flow blockage growth. This figure proves
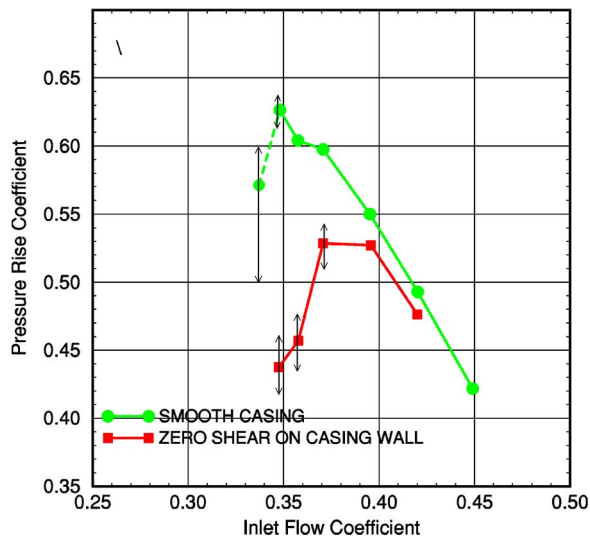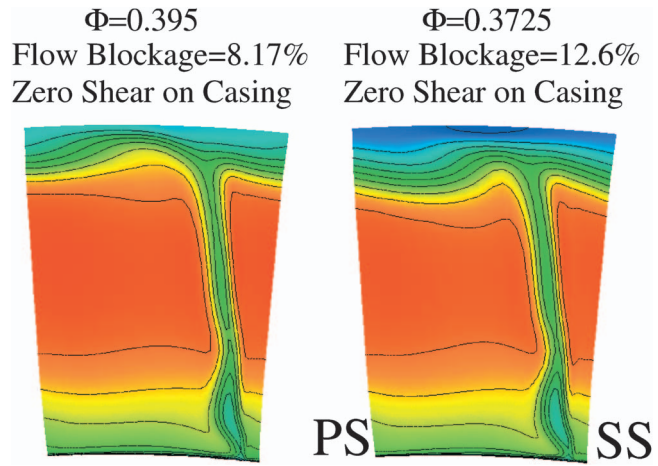
the second part of the third hypothesis underpinning the present work. The near casing flow region over the rotor tip, therefore, plays a major role in establishing the growth rate of flow blockage. It is this flow region that is first impacted by the presence of circumferential grooved casing treatment, the result being (compared to a smooth casing) a reduction in the growth of flow blockage.

Application of Current Approach

Figure 10 shows that the last groove contributes very little to the axial force associated with the radial transport of axial momentum. This implies that removing this groove should not alter the operating range of the grooved casing configuration. A set of simulations were executed for a configuration in which the last groove was omitted to test this hypothesis. The results of these simulations are summarized in Fig. 16 in the form of a pressure rise characteristic. For comparison purposes the corresponding characteristic with five grooves is also shown. The four groove configuration provides the same pressure rise and the same operating range as the five groove configuration.

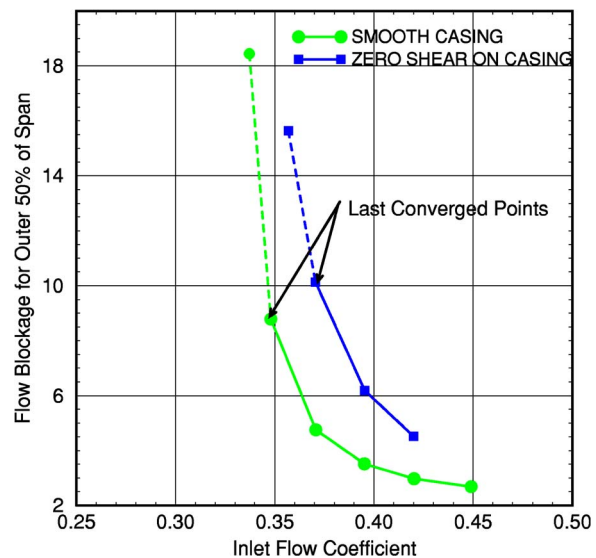Fig. 13 Speedline corresponding to zero shear at the casing wall

Fig. 15 Comparison of blockage growth as function of flow coefficient for smooth casing and zero shear casing. Flow blockage is defined as $(A_{\text{Blocked}}/A_{\text{Total Passage}}) \times 100$.
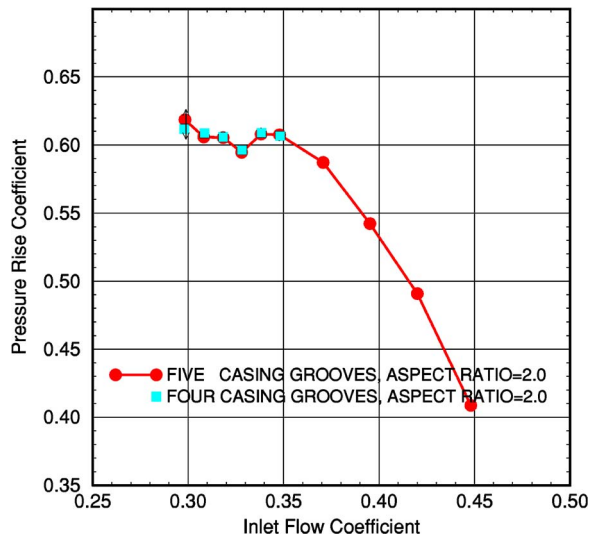
Fig. 16 Comparison of the pressure rise coefficient of the four grooved casing with the five grooved casing

The evolution of the axial shear force and the axial force due to the radial transport of axial momentum is shown in Fig. 17 for the four grooves configuration. The flow coefficient is 0.320 and the control volume is sketched in Fig. 4(*b*). Comparing the plots in this figure to their respective counterparts in Fig. 10, one sees that between 20% and 80% of chord they are nearly identical. Figures 10 and 17 establish that the impact of the fifth groove on stall margin is minimal and that this groove could be removed.

This simple study illustrates the usefulness of the current approach of using an axial momentum budget analysis applied to a control volume adjacent to the casing to ascertain the contribution of each groove to stall margin improvement thereby providing guidance in selecting the number of grooves required.

Summary and Conclusions

A computational study was carried out to uncover the flow mechanism responsible for the extension in the operating range of
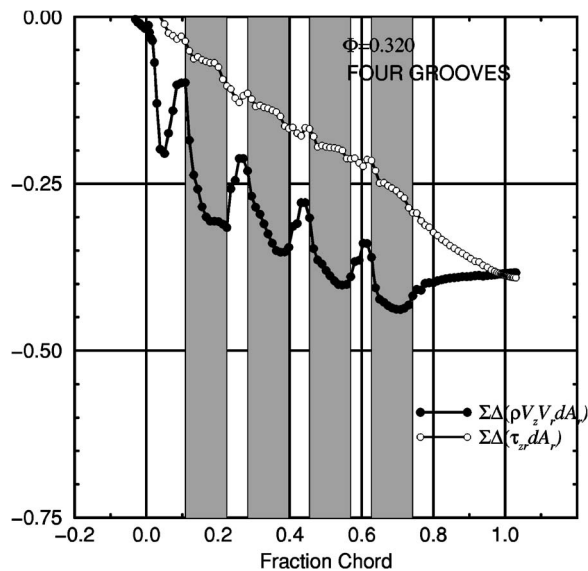

Fig. 17 Evolution of the cumulative sum in the axial direction for the axial shear force and the force due to the radial transport of momentum for the control volume shown in Fig. 4(*b*) for the four casing grooves configuration

an axial flow compressor due to the use of circumferential casing grooves. The geometry used for this purpose was a low speed rotor. This study entailed simulations of a smooth casing configuration as well as one with circumferential grooves. The results of the study are applicable to casing critical low speed compressors and are summarized as follows:

1. Numerical simulations showed that with the addition of circumferential casing grooves the stall flow coefficient of the rotor could be reduced from 0.340 to 0.300. Three different sets of grooves with aspect ratios of approximately 2, 4, and 5 were simulated. All of these aspect ratios provided the same increase in the operating range.
2. Results of simulations were used in a budget analysis of the axial momentum equation for a control volume adjacent to the casing. It was found that for smooth casing the net axial pressure force at the casing in the tip gap is balanced by the net axial viscous shear force.
3. For the grooved casing the net axial pressure force at the casing in the tip gap is balanced by the net axial shear force and the net axial force due to the radial transport of axial momentum. The later is comparable in magnitude to the net axial shear force. It is concluded that the radial transport of axial momentum across the groove and power stream interface is the flow mechanism that provides the increase in the stall margin.
4. A blockage analysis showed that the rate at which flow blockage grows near stall is reduced when a grooved casing is present over the rotor. It was further shown that the casing viscous flow layer had a substantial impact on the rate at which flow blockage increased near stall. These two results confirmed the hypothesis namely that the near casing viscous flow field over the rotor tip plays a key role in the development of blockage.
5. The analysis presented in the paper was further used to assess the effectiveness of each groove in imparting the radial transport of axial momentum to the power stream. It showed that the five groove casing treatment investigated in this study could be replaced by one in which the last groove was eliminated. The four groove configuration provided the same pressure rise characteristic as the five groove configuration.

Acknowledgment

Nomenclature

A_r = radial surface area of the grid cell and is normal to the radial direction
A_z = axial surface area of the grid cell and is normal to the axial direction
A_θ = tangential surface area of the grid cell and is normal to the tangential direction
$\dot{m}$ = the mass flow rate
P = static pressure
P_T = total pressure
r = radial coordinate
ref = reference conditions, taken at the inlet of the inlet guide vane
u_τ^* = skin friction velocity

U_{tip} = tip speed at the casing

V_r = mean radial velocity

V_z = mean axial velocity

V_θ = relative mean tangential velocity

y = distance from the wall

y^+ = distance from the wall in wall units, $= \rho y u_\tau^* / \mu$

z = axial coordinate

Δr = radial thickness of the control volumes shown in Fig. 4

ρ = density

Φ = flow coefficient $= \dot{m} / (\rho_{\text{ref}} A_{\text{ref}} U_{\text{tip}})$

θ = tangential coordinate

τ_{rz} = axial component of the sum of the viscous and turbulence stress tensor which acts on the radial surfaces of the control volume

τ_{zz} = axial component of the sum of the viscous and turbulence stress tensor which acts on the axial surfaces of the control volume

$\tau_{\theta z}$ = axial component of the sum of the viscous and turbulence stress tensor which acts on the tangential surfaces of the control volume

μ = molecular dynamic viscosity

References

[1] Osborn, W. M., Lewis, G. W., and Heidelberg, L. J., 1971, "Effect of Several Casing Treatments on Stall Limit and on Overall Performance of an Axial-Flow Compressor Rotor," NASA TN D-6537.

[2] Moore, R. D., Kovich, G., and Blade, R. J., 1971, "Effect of Casing Treatment on Overall and Blade-Element Performance of a Compressor Rotor," NASA TN D-6538.

[3] Bailey, E. E., 1972, "Effects of Grooved Casing Treatment on the Flow Range Capability of a Single-Stage Axial-Flow Compressor," NASA TM X-2459.

[4] Prince, D. C., Wisler, D. C., and Hilvers, D. E., 1974, "Study of Casing Treatment Stall Margin Improvement Phenomena," NASA CR-134552.

[5] Griffin, R. G., and Smith, L. H., 1966, "Experimental Evaluation of Outer Case Blowing or Bleeding of Single Stage Axial Flow Compressor Part I—Design of Rotor and Bleeding and Blowing Configurations," NASA CR-54587.

[6] Koch, C. C., and Smith, L. H., 1968, "Experimental Evaluation of Outer Case Blowing or Bleeding of Single Stage Axial Flow Compressor Part IV—Performance of Bleed Insert Configuration No. 3," NASA CR-54590.

[7] Takata, H., and Tsukuda, Y., 1977, "Stall Margin Improvement by Casing Treatment—Its Mechanism and Effectiveness," J. Eng. Power, **99**, pp. 121–133.

[8] Paulon, J., and Dehondt, D., 1982, "Influence of Casing Treatment on the Operating Range of Axial Compressors," ASME Paper No. 82-GT-103.

[9] Smith, G. D. J., and Cumpsty, N. A., 1985, "Flow Phenomenon in Compressor Casing Treatment," ASME J. Eng. Gas Turbines Power, **117**, pp. 532–541.

[10] Lee, N. K. W., and Greitzer, E. M., 1990, "Effect of Endwall Suction and Blowing on Compressor Stability Enhancement," ASME J. Turbomach., **112**, pp. 133–144.

[11] Crook, A. J., Greitzer, E. M., Tan, C. S., and Adamczyk, J. J., 1993, "Numerical Simulation of Compressor Endwall and Casing Treatment Flow Phenomena," ASME J. Turbomach., **115**(3), pp. 501–512.

[12] Kang, C. S., McKenzie, A. B., and Elder, R. L., 1995, "Recessed Casing Treatment Effects on Fan Performance and Flow Field," ASME Paper No. 95-GT-197.

[13] Rabe, D. C., and Hah, C., 2002, "Application of Casing Circumferential Grooves for Improved Stall Margin in a Transonic Axial Compressor," ASME Paper No. GT-2002-30641.

[14] Wisler, D. C., 1977, "Core Compressor Exit Stage Study: Volume 1—Blade Design," NASA CR 135391.

[15] Wellborn, S., Okiishi, T. H., and Strazisar, A. J., 1996, "Effects of Shrouded Stator Cavity Flows on Multistage Axial Compressor Aerodynamic Performance," NASA CR 198536.

[16] Culley, E. C., Bright, M. M., Prahst, P. S., and Strazisar, A. J., 2003, "Active Flow Separation Control of a Stator Vane Using Surface Injection in a Multistage Compressor Experiment," Proceedings of the ASME TURBO EXPO.

[17] Adamczyk, J. J., Celestina, M. L., Beach, T. A., and Barnett, M., 1990, "Simulation of Three-Dimensional Viscous Flow within a Multistage Turbine," Trans. ASME, J. Appl. Mech., **112**, pp. 370–376.

[18] Shabbir, A., Zhu, J., and Celestina, M. L., 1996, "Assessment of Three Turbulence Models in a Compressor Rotor," ASME Paper No. 96-GT-198.

[19] Spalding, D. B., 1961, "A Single Formula for the Law of the Wall," J. Appl. Mech., **28**, pp. 455–458.

[20] Shabbir, A., and Turner, M. G., 2004, "A Wall Function for Calculating The Skin Friction with Surface Roughness," ASME Paper No. GT2004-53908.

[21] Prahst, S., and Strazisar, A. J., 2003 (private communication).

[22] Khalid, S. A., Khalsa, A. S., Waitz, I. A., Tan, C. S., Greitzer, E. M., Cumpsty, N. A., Adamczyk, J. J., and Marble, F. E., 1999, "Endwall Blockage in Axial Compressors," ASME J. Turbomach., **121**, pp. 449–509.

[23] Van Zante, D. E., Strazisar, A. J., Wood, J., Hathaway, M. D., and Okiishi, T., 2000, "Recommendations for Achieving Accurate Numerical Simulation of Tip Clearance Flows in Transonic Compressor Rotors," ASME J. Turbomach., **122**, pp. 734–742.

[24] Tan, C. S., and Greitzer, E. M., 2004 (private communication).

Effect of Hole Geometry on the Thermal Performance of Fan-Shaped Film Cooling Holes

Michael Gritsch

Will Colban[1]

Heinz Schär

Klaus Döbbeling

ALSTOM (Switzerland) Ltd.,
Brown Boveri Str. 7,
Baden 5401, Switzerland

This study evaluates the impact of typical cooling hole shape variations on the thermal performance of fan-shaped film holes. A comprehensive set of experimental test cases featuring 16 different film-cooling configurations with different hole shapes have been investigated. The shape variations investigated include hole inlet-to-outlet area ratio, hole coverage ratio, hole pitch ratio, hole length, and hole orientation (compound) angle. Flow conditions applied cover a wide range of film blowing ratios M = 0.5 to 2.5 at an engine-representative density ratio DR = 1.7. An infrared thermography data acquisition system is used for highly accurate and spatially resolved surface temperature mappings. Accurate local temperature data are achieved by an in situ calibration procedure with the help of thermocouples embedded in the test plate. Detailed film-cooling effectiveness distributions and discharge coefficients are used for evaluating the thermal performance of a row of fan-shaped film holes. An extensive variation of the main geometrical parameters describing a fan-shaped film-cooling hole is done to cover a wide range of typical film-cooling applications in current gas turbine engines. Within the range investigated, laterally averaged film-cooling effectiveness was found to show only limited sensitivity from variations of the hole geometry parameters. This offers the potential to tailor the hole geometry according to needs beyond pure cooling performance, e.g., manufacturing facilitations. [DOI: 10.1115/1.2019315]

Introduction

In state-of-the-art gas turbine cooling schemes film cooling is a well-accepted and widely used means to keep the surface temperatures of components with high thermal loads like first stage vanes and blades at acceptable limits. Coolant air is released through so-called film holes on the surface and is supposed to form a protective layer on the surface that protects the surface from hot gas exposure. Recent improvements in the manufacturing process have led to a greater flexibility in choosing a proper shape for these holes. Standard film cooling schemes have used cylindrical holes but increasing attention is given to holes with a diffuser shaped exit (so-called fan-shaped holes) due to superior thermal performance compared to cylindrical holes. The flow deceleration in the diffuser section of the hole reduces the momentum of the coolant jet and thus the penetration of the coolant into the hot gas flow. The coolant stays attached to the surface and forms an effective film. Additionally, the diffuser provides an improved lateral spreading of the coolant and thus a more uniform film on the surface since neighboring cooling jets start merging immediately downstream of the injection location

Although film holes with noncylindrical exit shape have received increasing attention during the last years, there are only very few studies that try to find out which are the governing geometrical parameters that really affect the thermal performance of the hole. Most of the studies focused on a comparison of fan-shaped hole performance versus a standard cylindrical cooling hole [1–3] or on a comparison of global film cooling schemes employing cylindrical and/or fan-shaped holes, e.g., comparing a

double row of cylindrical holes vs. a single row of fan-shaped holes [4,5] or combining rows of cylindrical and fan-shaped holes [6].

Gritsch et al. [7], Thole et al. [8], Gritsch et al. [9–11] compared the performance of two different fan-shaped holes in terms of film-cooling effectiveness and heat transfer coefficients. They found that the thermal performance of a hole that diffuses in both lateral and streamwise direction (laidback fan-shaped hole) is superior to a hole that only diffuses in lateral direction, in particular at high blowing ratios. The area ratio of both holes were almost identical (AR=3.0 for the lateral diffusing hole and AR=3.1 laidback fan-shaped hole). Saumweber et al. [12] investigated a row of holes that had identical shapes as those of Gritsch et al. at elevated turbulence levels. They found that the fan-shaped and the laidback fan-shaped hole performances were very close. The same type of hole shapes have also been investigated for leading edge cooling applications [13]. The performance of the laidback fan-shaped hole was found to be superior to the fan-shaped hole for this case.

Bell et al. [14] provided film effectiveness data for a row of fan-shaped holes diffusing only in lateral direction and a row of holes diffusing only in forward direction. Since the area ratios of their fan-shaped holes are only in the order of 1.65 the thermal performance of both shaped hole geometries was found to be very close to standard cylindrical holes.

Kohli and Bogard [15] compared two fan-shaped holes featuring the same lateral diffusion angle but different forward diffusion angles of 15 and 25 deg. The hole with the larger forward diffusion angle was expected to keep the coolant jet closer to the surface. However thermal performance of this hole in terms of film cooling effectiveness was found to be lower than for the hole with the smaller forward diffusion angle due to flow separation in the diffuser part of the hole.

Lutum et al. [16] studied film-cooling effectiveness for a row of holes diffusing in both lateral and forward directions as compared to holes diffusing in lateral direction only. Hole shapes were very close to those from Gritsch et al. They report that the performance of the hole with an additional forward diffusion performed slightly

---

Copyright © 2005 by ASME   **Transactions of the ASME**

Table 1 Test rig operation conditions

Main flow	Temperature	T_t	340 K
	Pressure	P_t	1.0 bars
	Mach number	Ma	0.3
	Reynolds number	Re_D	22,000
	Turbulence level	Tu	4%
	BL thickness at film injection	δ/D	0.5
Coolant	Pressure	P_t	<1.4 bars
(carbondioxide)	Temperature	T_t	295 K
	Density ratio	DR	1.7
	Blowing ratio	M	0.5,…,2.5

worse and attribute this behavior to local flow separations within or just downstream of these laid back shaped holes.

Numerical studies [17–19] carried out on fan-shaped film hole geometries suggest that the flow field structure inside the film hole is highly complex. The hole geometrical parameters have an major impact on the flow field inside and at the exit of the hole and, consequently, on the thermal performance of the film hole.

The findings from previous studies underline the importance of in-depth knowledge of the impact of individual hole geometrical parameters. It is obvious that compared to a standard cylindrical film hole, the number of geometrical parameters that define the hole shape is profoundly increased. Beside the parameters that define a cylindrical hole [hole diameter, hole length, and the orientation of the hole axis on the surface—typically referred to as inclination and orientation (or compound) angle] there are further parameters that basically describe the shape of the diffuser-shaped exit portion of the hole. These include the starting point of the diffuser as well as the diffuser angles in streamwise and lateral direction. With those parameters fixed, the area ratio of the hole, and—with a given hole-to-hole pitch—the coverage ratio are set. These two typically serve as the standard parameters defining a fan-shaped film hole. When a film cooling design is done these parameters can be used to tune the thermal performance. However, it is crucial to know the impact of each of the dominating hole geometry parameters on the thermal performance.

Furthermore, it needs to be considered that the manufacturing process of these fan-shaped holes has a profound impact on the hole shape. For laser-drilled holes, it is cost efficient to use the same drilling process parameters for a complete row of film holes. This can cause a change in hole shape since the wall thickness of a blade typically varies in radial direction. Also blade-to-blade casting tolerances lead to different hole shapes on different blades. Moreover, tolerances in the manufacturing process can cause major hole-to-hole shape variations. When defining a manufacturing process, it is therefore extremely helpful to know which hole geometry parameters have a big impact on the thermal performance and which do not. Ultimately, those having a big effect need to be tightly controlled.

Since there are obviously no studies reported in the open literature that can provide detailed insight this study aims to assess the effect of a number of geometrical parameters of typical fan-shaped holes on thermal performance. Detailed film-cooling effectiveness distributions and discharge coefficients are used for evaluating the thermal performance of a row of fan-shaped film holes. An extensive variation of the main geometrical parameters describing a fan-shaped film-cooling hole is done to cover a wide range of typical film-cooling applications in current gas turbine engines.

Due to the large body of data, this study concentrates on the film-cooling effectiveness data. For an overall assessment of the film-cooling performance, also heat transfer coefficients need to be considered [20–22]. Those have been measured in parallel and will be presented in a follow-up paper.

## Experimental Apparatus and Procedure

Wind Tunnel and Film-Cooling Injection System. The present investigation is carried out in a continuous flow wind tunnel delivering main flow air—up to 1 kg/s—into a test section of 50 mm × 130 mm cross section. An electrical 34 kW heater increases the main flow temperature to about 340 K. After passing through a flow settling device and some flow straightening grids and honeycombs the flow is accelerated in a bell-mouth shaped nozzle to Mach numbers in the order of 0.3. A turbulence grid located about 45 D upstream of the film-cooling ejection location created a turbulence intensity level of 4% at the ejection location. The length of the test plated mounted to the test section is 800 mm which allows for measuring the film-cooling effectiveness data up to 110 D downstream of the ejection location. The test plates consist of a polyurethane foam featuring a low thermal conductivity of about 0.1 W/mK providing nearly adiabatic conditions for the experiments. Each of the test plates features a row of fan-shaped film-cooling holes consisting of five holes. The metering diameter of these holes is 4 mm. The holes are fed from a 130 × 70 mm plenum underneath the test plate. The coolant flow rate provided to the coolant plenum is directly measured by means of a gas meter.

Despite that the present study focuses on the effect of hole geometry parameters, it is made sure that the main flow parameters, e.g., the blowing ratio and the density ratio are kept in engine-representative ranges. Carbondioxide is used as coolant for the experiments in order to achieve enginelike coolant-to-main flow density ratios of about 1.7. Table 1 summarizes the operating conditions.

Measurements of Film Effectiveness and Discharge Coefficients. Surface temperature measurements are carried out by means of an infrared thermography system (FLIR ThermaCAM 3000). The sensor of this system is detecting radiation in the 8 μm to 9 μm range. The IR camera is mounted above the test section of the wind tunnel (Fig. 1). The wall opposite to the test plate is equipped with four circular KCl windows that are
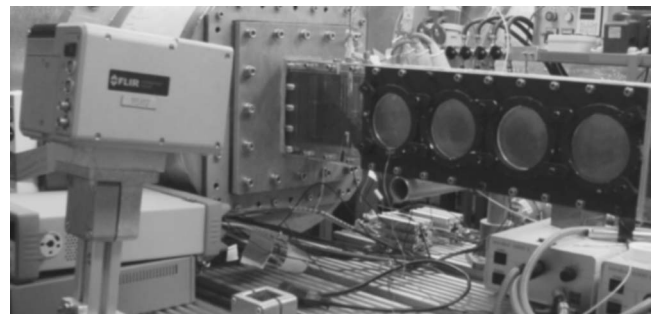
Fig. 1 Test rig setup
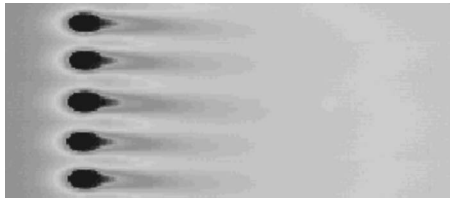
Fig. 2 Local surface temperature distribution downstream of film ejection location, Config.D

highly transparent to infrared radiation ($\tau = 0.93$) in the wavelength range of the sensor. The radiation collected from the test plate is digitized into an array of 240×320 pixels. Accounting for the optical setup used a spatial resolution of 0.3 mm $\times$ 0.3 mm per pixel is achieved. The camera is mounted on a rigid stand that could slide in the streamwise direction allowing for images to be taken through each of the four windows for every test case.

The test plate surface is covered by black paint with a known emissivity of 0.95. A number of K type thermocouples are distributed on the test plate surface which are used for an *in situ* calibration of the thermography system in order to increase the accuracy of the surface temperature measurements and, thus, of the film cooling effectiveness data, following the approach described by Martiny et al. [23]. The local film-cooling effectiveness is then based on the local surface temperature, coolant supply total temperature, and the main flow recovery temperature

$$\eta = \frac{T_{aw} - T_{m,\mathrm{rec}}}{T_{c,t} - T_{m,\mathrm{rec}}} \tag{1}$$

Before applying this equation, the surface temperature readings have been corrected for back-side losses by heat conduction through the test plate material which have been estimated employing a thermocouple measuring the back-side temperature of the test plate. Due to the low thermal conductivity of the test plate material and the rather thick test plate, back-side heat losses are found to be small (less than a 2% effect on film-cooling effectiveness). Furthermore, the heat radiation from the test plate to the opposite wall and—through the windows—to the lab surroundings have been estimated. Since the experiments are carried out at a main flow temperature level only about 40 K above ambient temperature, radiation effects are found to be small (less than 1% effect on film-cooling effectiveness). A typical local surface temperature distribution is given in Fig. 2.

In order to quantify the flow losses, discharge coefficients have been measured as well. The discharge coefficient is defined as the ratio of real and ideal mass flow through the film hole.

$$C_D = \frac{m_{c,\mathrm{real}}}{m_{c,\mathrm{ideal}}} \tag{2}$$
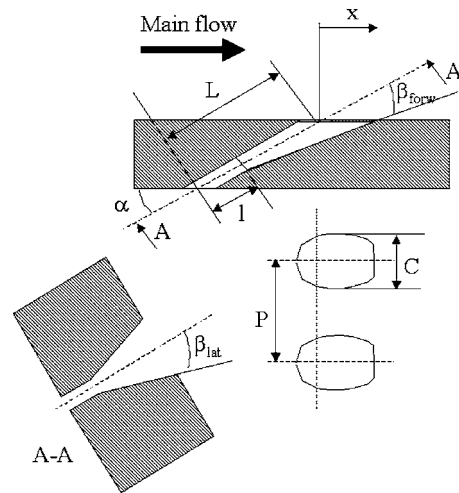
The ideal mass flow is defined by assuming isentropic, one-dimensional expansion across the hole from coolant total pressure to main flow static pressure level.

$$m_{\mathrm{ideal}} = A_c p_{t,c} (p_m/p_{t,c})^{(\kappa+1)/2\kappa} \sqrt{\frac{2\kappa}{(\kappa-1)RT_{t,c}} \left[(p_{t,c}/p_m)^{(\kappa-1)/\kappa} - 1 \right]} \tag{3}$$

The crosssection of the initial cylindrical hole portion is used as the metering area A_c.

$$A_c = \frac{\pi}{4} D^2 \tag{4}$$

The calculation of the blowing ratio

Fig. 3 Film-cooling hole geometry

$$M = \frac{m_c/A_c}{(\rho u)_m} \tag{5}$$

is based on the hole inlet cross-sectional area as well.

Experimental Uncertainties

Experimental uncertainties are estimated following the partial derivative method of Moffat [24]. Accounting for the individual uncertainties in setting the flow (main flow Mach number δ Ma $= 0.01$, blowing ratio $\delta M = 0.02$, and density ratio δDR$= 0.02$) and measuring temperatures ($\delta T = 0.4$ K), the relative overall uncertainty in film-cooling effectiveness is estimated to be in the range 1.5% to 9%. The lower value corresponds to locations with good film protection ($\eta = 0.7$) while the higher value is valid for locations with poor cooling ($\eta = 0.05$). The uncertainty in discharge coefficients ranges from 1.2% to 4.2% for the conditions applied during this study.

Film-Cooling Configurations

An initial assessment was carried out to find out which geometrical quantities describing the shape of a film-cooling hole can be easily controlled/changed and/or are prone to manufacturing uncertainties. Those of this list that are suspect to have a big impact on the film-cooling performance have been selected for this study. These include

- The length of the hole, L/D.
- The hole exit-to-inlet area ratio, AR.
- The hole pitch, P/D.
- The hole coverage (hole exit width-to-pitch ratio), C/P.
- The hole compound angle, γ.

Note that the hole inclination angle α, although having a major impact on film-cooling performance, is kept constant at 30 deg for all test cases presented in this paper. The length of the cylindrical inlet portion is $\ell = 2D$ for all hole geometries investigated (Fig. 3).

A test matrix of 16 different hole geometries has been created. These 16 geometries can be pooled into subsets; each subset is meant for investigating a single geometrical parameter from the list above. The challenge has been to single out these effects since typically if one parameter is changed others are also affected. Therefore, the test matrix and the hole geometries associated have been carefully selected to allow for differentiating the impact of individual geometrical hole parameters. For instance, Configs A to C are supposed to investigate the effect of the length of the fan-shaped hole portion. Note that all other geometrical quantities in Table 2 below are kept constant. This implies, that Configs A to C

Table 2   Film-cooling hole geometries investigated

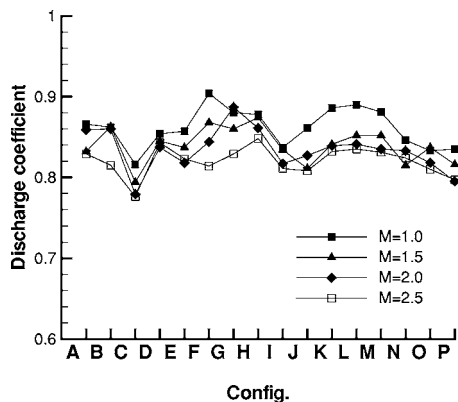|	Config	L/D	AR	P/D	C/D	β_{lat} (deg)	β_{forw} (deg)	γ (deg)
L/D effect	A	11.5	3.5	6	0.49	6	2	0
	B	9.5	3.5	6	0.49	7	4	0
	C	7.5	3.5	6	0.49	7	11	0
P/D effect	D	11.5	4.2	4	0.65	4	8	0
	E	11.5	4.2	6	0.43	4	8	0
	F	11.5	4.2	8	0.32	4	8	0
C/P effect	G	11.5	2.5	6	0.31	2	4	0
	H	11.5	2.5	6	0.37	4	2	0
	I	11.5	2.5	6	0.39	4	0	0
	E	11.5	4.2	6	0.43	4	8	0
	K	11.5	4.2	6	0.57	7	2	0
	L	11.5	4.2	6	0.63	9	0	0
AR effect	M	11.5	3.5	6	0.43	4	4	0
	E	11.5	4.2	6	0.43	4	8	0
	L	11.5	4.2	6	0.63	9	0	0
	N	11.5	4.7	6	0.63	8	3	0
Compound angle	E	11.5	4.2	6	0.43	4	8	0
	J	11.5	4.2	6	0.43	4	8	45
	O	11.5	4.2	6	0.43	4	8	60
	P	11.5	4.2	6	0.43	4	8	45[a]

[a]One-side diffusion hole.

do not feature identical diffuser portions with just the length of the diffuser portion varying but are rather individual designs in order to make sure that the area ratio and the coverage ratio are kept unchanged.

The parameter ranges were chosen according to what is typically found in engines rather than covering the full feasible range. For example, the area ratio AR was varied from 3.5 to 4.7. Lower values are of course feasible, but the objective was to get a sensitivity of the film effectiveness with area ratio within the typical range applied in engines. Some of the parameters investigated, e.g., the hole length, might be more typical for land-based gas turbines than for aero engines.

Experimental Results

Discharge Coefficients. In order to quantify the flow losses associated with injection of the coolant flow into the main flow discharge coefficients have been measured for all hole configurations investigated. Measured discharge coefficients are presented in Fig. 4 for blowing ratios $M=1.0$ to 2.5. Generally, the discharge coefficients were found to be in the 0.8 to 0.9 range—decreasing with increasing blowing ratio since the diffusion and the associated pressure recovery gets less effective at higher flow rates. The pressure recovery is somewhat affected by the hole diffuser shape. However, differences from configuration to configuration are rather small—typically less than 10%. The discharge coefficients agree well with those found by Hay and Lampard [25] and Gritsch

et al. [26] et al. who both reported C_D values of 0.8 for hole geometries and flow conditions that are not identical but similar to those applied in the present study.

Film-Cooling Effectiveness. In order to benchmark the experimental setup and procedure, experimental film-cooling effectiveness data are compared to results from previous studies (see Table 3). The comparison is made based on laterally averaged film-cooling effectiveness. Only studies employing engine-like density ratios DR are considered.

The data of Config D (P/D=4) are used in order to compare them in particular to data of Saumweber et al. [6] and Dittmar et al. [5] (both P/D=4) who present data in the far field of the injection location up to $x/D=50$. The results (Fig. 5) reveal excellent agreement with the data of Dittmar et al. [5] and—in the near field—with the data of Gritsch et al. [7]. Kohli and Bogard [15] tested hole geometries with a smaller P/D=3 and consequently found higher laterally averaged film-cooling effectiveness. Although Lutum et al. [16] employed a larger pitch of P/D=6 film effectiveness is higher than those of the present study. Their investigation was carried out on a convex surface which is known to enhance film-cooling effectiveness for low blowing rates and thus to counterbalance the effect of the larger pitch. Overall, it can be stated that the present data agree well with data from previous investigations bearing in mind that the hole shapes and operating conditions differ to some extent from study to study.

Effect of Length-to-Diameter Ratio. Lutum and Johnson [27] found that for cylindrical film holes the hole length-to-diameter ratio L/D has basically no effect on the film cooling effectiveness for L/D>5. The present study extends this finding to fan-shaped

Fig. 4   Discharge coefficients for all holes investigated

Table 3   Literature data sets considered for comparison with current study

	M	P/D	DR	Tu (%)	α (deg)
Dittmar et al. [5]	0.5	4	1.3	9	45
Gritsch et al. [7]	0.5	4[a]	1.85	1.4	30
Saumweber et al. [6]	0.5	4	1.75	5.1	30
Lutum et al. [16]	0.5	6	1.78	5	30
Kohli and Bogard [15]	0.5	3	1.6	0.2	55
Current study, Config D	0.5	4	1.7	4	30

[a]Single-hole data are converted to a "virtual pitch" of P/D=4 as given in [6].
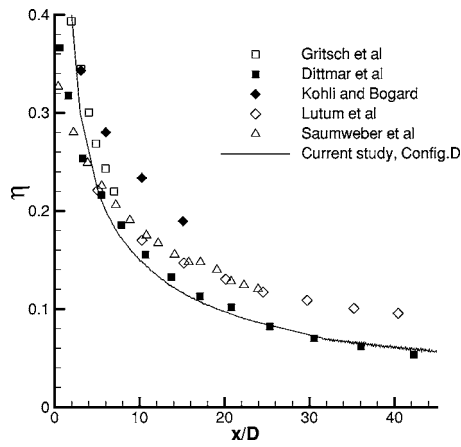
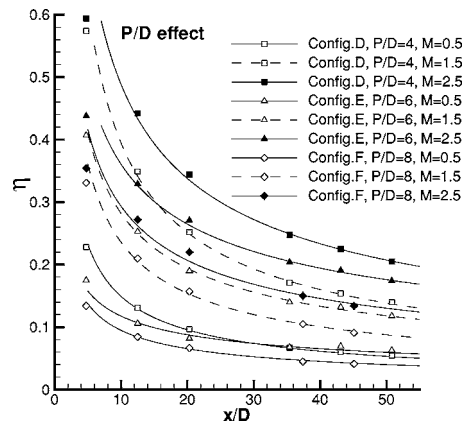**Fig. 5 Laterally averaged film-cooling effectiveness, comparison to literature data sets**

Fig. 7 Effect of hole-pitch-to-diameter ratio on laterally averaged film-cooling effectiveness

hole geometries. For the three L/D ratios investigated during this study (L/D=7.5, 9.5, and 11.5) the film-cooling effectiveness was found to be essentially the same, see Fig. 6. Since the cylindrical inlet section length was kept constant for all Configs. A, B, and C, it can be stated that the length of the hole diffuser section does not have an impact on the film effectiveness. Note that—as already mentioned in the previous chapter—Configs. A, B, and C feature the same coverage and the same area ratio. The diffuser section of each of these holes has been individually designed to meet these criteria.

Effect of Pitch-to-Diameter Ratio. The pitch-to-diameter ratio P/D is a measure for the number of holes per unit span and—for a given blowing ratio—the amount of cooling per unit span. Therefore, it is no surprise that the hole configuration Config D (P/D =4) provides a higher film-cooling performance as compared to config E (P/D=6) and F (P/D=8), Fig. 7. However from a cooling performance point of view what is the optimum P/D ratio? Since film cooling effectiveness is often assumed to scale with the reciprocal of the P/D ratio. Figure 8 presents the laterally averaged film-cooling effectiveness normalized with D/P.

If the film-cooling effectiveness would solely depend on the amount of coolant spent per unit span the curves for the different configurations should collapse. The data for P/D=6 and 8 are indeed in good agreement (except in the vicinity of the injection location) while the data for P/D=4 are somewhat lower. Apparently, for P/D=4 the holes are too close to each other to make efficient use of the coolant spent.
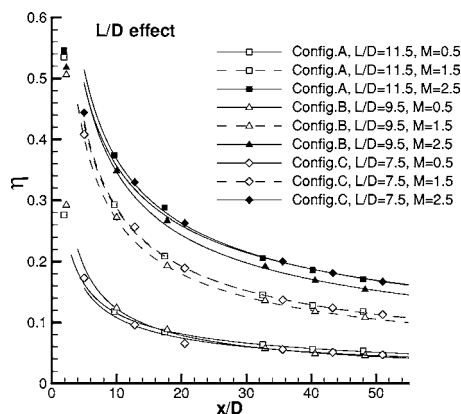
Effect of Hole Coverage. The hole coverage C/P is defined as the ratio of hole exit width and hole pitch which basically defines the width of the coolant film emerging from a film hole. Frequently, this parameter is assumed to describe the potential of the coolant to spread out laterally and form a self-contained film with the coolant emerging from its neighbor holes. Data have been measured for three rather low C/P ratios (0.31, 0.37, 0.39) for AR=2.5 (Fig. 9), and three rather high C/P ratios (0.43, 0.57, 0.63) for AR=4.2 (Fig. 10). Since the AR ratio is kept constant, low C/P ratios indicate that the hole is mainly forward diffusing while for high C/P ratios the hole is mainly laterally diffusing. Surprisingly, for $M=0.5$ and 1.5 all data collapse to a single curve, showing that the C/P ratio does not have an impact on the film-cooling effectiveness for these blowing ratios. For $M=2.5$, however, film-cooling effectiveness increases with C/P, indicating that the lateral diffusion is somewhat more effective than the forward diffusion.

Effect of Area Ratio. The area ratio AR is defined as the ratio of cross-sectional areas at hole exit and inlet. This parameter is assumed to describe the potential of the hole to diffuse the coolant in the fan-shaped portion of the hole and, thus, to reduce the momentum of the coolant. Lower momentum leads to less penetration into the main flow and consequently higher film cooling performance. Data have been measured for three area ratios (3.5, 4.2, and 4.7). Since for a fair comparison the coverage needs to be kept constant, two area ratios (3.5 and 4.2) were investigated for C/P=0.43 (Fig. 11), and another two area ratios (4.2 and 4.7) for C/P=0.63 (Fig. 12). Since the C/P ratio is kept constant, high AR
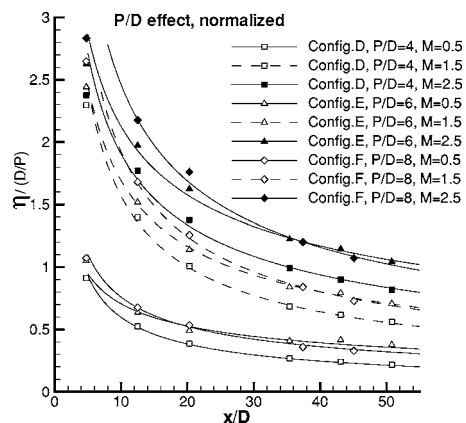

Fig. 6 Effect of hole-length-to-diameter ratio on laterally averaged film-cooling effectiveness

Fig. 8 Effect of hole-pitch-to-diameter ratio on laterally averaged film-cooling effectiveness, normalized

Fig. 9 Effect of coverage ratio on laterally averaged film-cooling effectiveness at AR=2.5
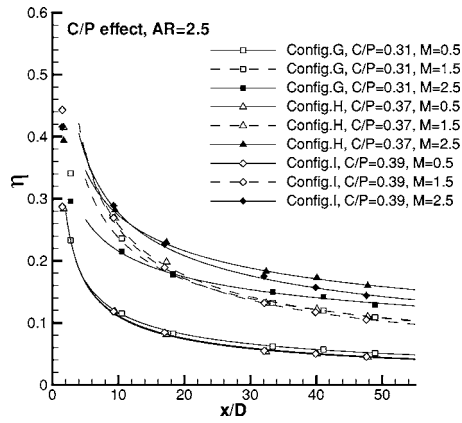

Fig. 12 Effect of area ratio on laterally averaged film-cooling effectiveness at C/P=0.63

ratios indicate that the hole is more forward diffusing than for a lower AR ratio. As for the C/P parameter, all data were found to collapse indicating that the AR ratio does not have an impact on film-cooling performance within the range investigated. The selected AR ratios cover what is typically found on engine airfoils. It should be noted though that the results may look different for lower AR ratios than investigated in this study.

Effect of Compound Angle. For cylindrical film holes, adding a compound angle is known to improve the lateral spreading of
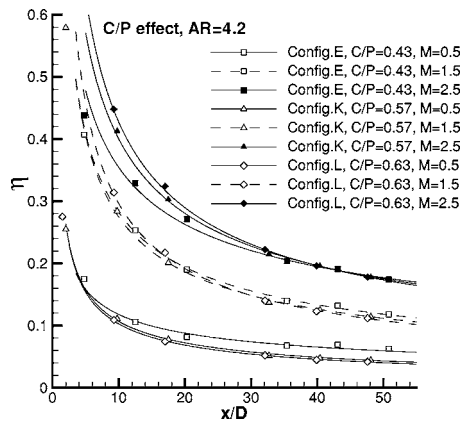

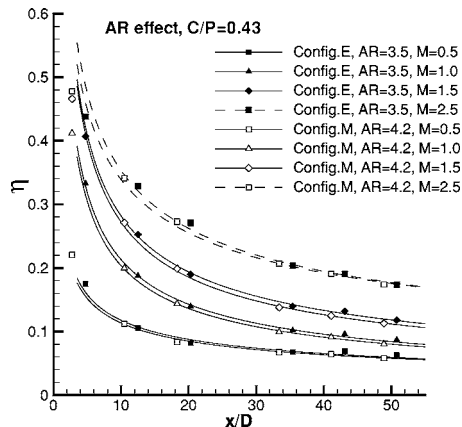**Fig. 10 Effect of coverage ratio on laterally averaged film-cooling effectiveness at AR=4.2**
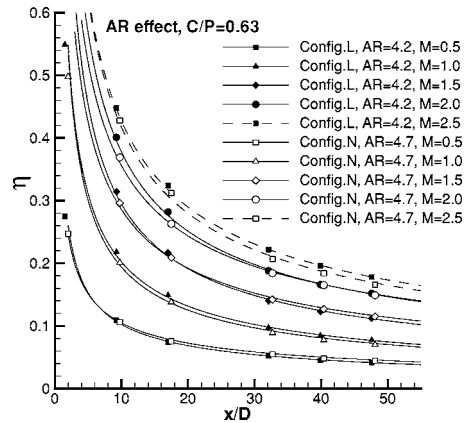

Fig. 11 Effect of area ratio on laterally averaged film-cooling effectiveness at C/P=0.43

the coolant and reduce the penetration of the coolant jets into the main flow. This results in enhanced film-cooling effectiveness data, but typically at the expense of higher heat transfer coefficients due to intensified interaction of coolant and main flow.

Whereas cylindrical holes with compound angles have been investigated for years, it was just recently that some results on compound shaped holes were published.[5,14,28–30] Although poor lateral spreading or penetration into the main flow are generally not an issue for fan-shaped holes, putting a compound angle on a fan-shaped hole is beneficial under certain circumstances and has thus received increasing attention. Therefore, the current study is looking into the effect of adding a compound angle to a fan-shaped hole on film-cooling effectiveness. Three different compound angles ($\gamma=0$ deg, 45 deg, and 60 deg) have been investigated (Fig. 13). At low to medium blowing ratios ($M=0.5$, 1.5), adding a compound hole seems to have no major impact on film-cooling effectiveness, while at high blowing ratios ($M=2.5$) the performance of the holes featuring a compound angle is somewhat lower than for a straight hole. The difference between a 45 deg and 60 deg is negligible. Apparently, putting a compound angle leads to elevated interaction of the noncoflowing coolant and main flow which reduces the protective effect of the film.

One option to overcome this problem is to change the diffuser portion of the hole in a way that the diffuser is not symmetric anymore but employs a one-sided diffusion. This means that the lateral diffusion angle on the windward side of the diffuser is smaller than the one on the leeward side $\beta_{\mathrm{lat},w}<\beta_{\mathrm{lat},l}$ (Fig. 14). This would cause the flow leaving a hole to be directed more in the main flow streamwise direction. Figure 15 shows a compari-
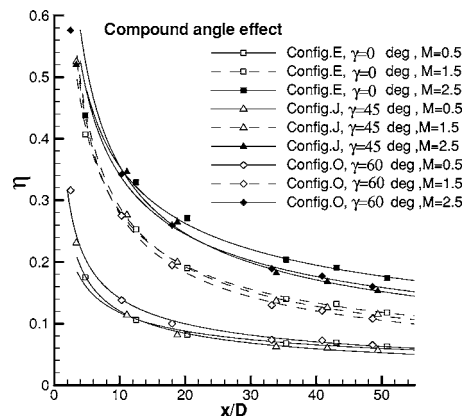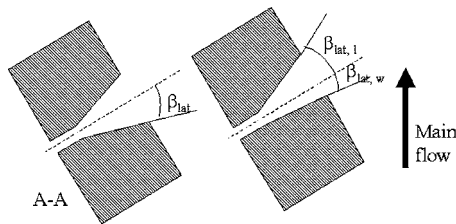

Fig. 13 Effect of compound angle on laterally averaged film-cooling effectiveness

Journal of Turbomachinery

Fig. 14 Symmetric (left) and nonsymmetric diffuser portion of the film-cooling hole

son of a hole with a symmetric diffusion to a hole with a one-sided diffusion. Apparently, there is some benefit in terms of film-cooling effectiveness that can be gained by reshaping the hole at medium to high blowing ratios.

Summary

An experimental study has been carried out to investigate the impact of various hole geometry parameters on the discharge coefficient and film-cooling effectiveness of fan-shaped film-cooling holes. This study is unique since a detailed compendium of all major hole parameters is provided. The key findings may be summarized as follows:

- Pressure losses quantified by means of discharge coefficients are not profoundly affected by the geometry of the fan-shaped hole. All C_D values were found to be in a 0.8 to 0.9 range.
- Within the range investigated, most hole geometry parameters only have a weak impact on laterally averaged film-cooling effectiveness.

  (1) The effect of hole length to diameter ratio is small.
  (2) The effect of pitch-to-diameter ratio is as expected large as it determines the amount of coolant spent per unit span.
  (3) The effect of coverage ratio and area ratio is basically negligible.
  (4) Putting a compound angle has some detrimental affect at high blowing ratios which can be overcome by using non-symmetric diffusion.

- Since many of the parameters investigated do only have a small impact on filmcooling effectiveness the cooling designer may be more tolerant on the hole shape if requirements from manufacturing process necessitate to do so
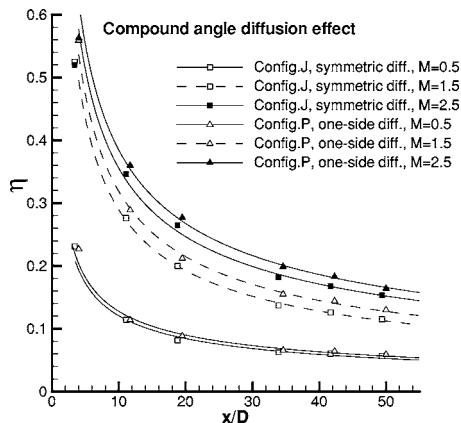
Fig. 15 Effect of compound angle diffusion on laterally averaged film-cooling effectiveness

Nomenclature

$$
\begin{aligned}
AR &= \text{Hole inlet-to-exit area ratio} \\
C_D &= \text{Discharge coefficient} \\
C &= \text{hole width, exit side, mm} \\
D &= \text{Film-cooling hole diameter, mm} \\
DR &= \text{Density ratio} \\
I &= \text{momentum flux ratio} \\
L &= \text{Film-cooling hole length, mm} \\
l &= \text{Length of hole cylindrical inlet portion, mm} \\
Ma &= \text{Mach number} \\
M &= \text{Blowing ratio} \\
m &= \text{Mass flow rate through the film-cooling hole, kg/s} \\
p &= \text{Static pressure, Pa} \\
p_t &= \text{Total pressure, Pa} \\
P &= \text{hole-to-hole pitch, mm} \\
R &= \text{Gas constant} \\
Re_D &= \text{Reynolds number based on film hole diameter} \\
T_t &= \text{Total temperature, K} \\
Tu &= \text{Turbulence intensity, \%} \\
\alpha &= \text{Angle of hole inclination (deg)} \\
\beta &= \text{Hole diffusion angle, deg} \\
\delta &= \text{boundary layer thickness, m} \\
\gamma &= \text{Angle of hole orientation (compound angle), deg} \\
\kappa &= \text{Ratio of specific heats} \\
\eta &= \text{Laterally averaged film-cooling effectiveness} \\
\rho &= \text{Flow density, kg/m3}
\end{aligned}
$$

Subscripts

$$
\begin{aligned}
c &= \text{Internal flow conditions (``coolant'')} \\
m &= \text{External flow conditions (``mainflow'')} \\
rec &= \text{Recovery conditions} \\
AW &= \text{Adiabatic wall conditions} \\
lat &= \text{lateral (spanwise) diffusion} \\
forw &= \text{forward (streamwise) diffusion} \\
l &= \text{leeward side} \\
w &= \text{windward side}
\end{aligned}
$$

References

[1] Goldstein, R. J., Eckert, E. R. G., and Burggraf, F., 1974, "Effects of Hole Geometry and Density on Three-Dimensional Film Cooling," Int. J. Heat Mass Transfer, **17**, pp. 595–607.

[2] Makki, Y. H., and Jakubowski, G., 1986, "An Experimental Study of Film Cooling From Diffused Trapezoidal Shaped Holes," AIAA paper no 86-1326.

[3] Yu, Y., Yen, C-H., Shih, T. I-P., Chyu, M. K., and Gogineni, S. 1999, "Film Cooling Effectiveness And Heat Transfer Coefficient Distributions Around Diffusion Shaped Holes," ASME paper No.-99-GT-34.

[4] Dittmar, J., Gritsch, M., Schulz, A., Kim, S. and Wittig, S., 1999, "Advanced Cooling of Gas Turbine Blades: Effect of Hole Geometry and Film Cooling Performance," *8th Colloquium on Turbomachinery*, TMPRC Seoul National University, Seoul, Korea, June 27th–July 3rd.

[5] Dittmar, J., Schulz, A. and Wittig, S., 2003, "Assessment of Various Film-Cooling Configurations Including Shaped and Compound Angle Holes Based on Large-Scale Experiments", ASME J. Turbomach., **125**, pp. 57–64.

[6] Saumweber, Ch., Schulz, A., and Wittig, S., 2004, "Interaction of Film Cooling Rows: Effects of Hole Geometry and Row Spacing on the Cooling Performance Downstream of the Second Row of Holes," ASME J. Turbomach., **126**, pp. 237–246.

[7] Gritsch, M., Schulz, A., and Wittig, S., 1998, "Adiabatic Wall Effectiveness Measurements of Film-Cooling Holes With Expanded Exits," ASME J. Turbomach., **120**, pp. 549–556.

[8] Thole, K. A., Gritsch, M., Schulz, A., and Wittig, S., 1998, "Flowfield Measurements for Film-Cooling Holes With Expanded Exits," ASME J. Turbomach., **120**, pp. 327–336.

[9] Gritsch, M., Schulz, A., and Wittig, S., 2000, "Film-Cooling Holes with Expanded Exits: Near Hole Heat Transfer Coefficients," Int. J. Heat Fluid Flow,"

21, pp.146–153.

[10] Gritsch, M., Saumweber, C. Schulz, A. Wittig, S. and Sharp, E., 2000, "Effect of Internal Coolant Crossflow Orientation on the Discharge Coefficient of Shaped Film-Cooling Holes," ASME J. Turbomach., **122**, pp.146–153.

[11] Gritsch, M., Schulz, A., and Wittig, S., 2003, "Effect of Internal Crossflow on the Effectiveness of Shaped Film-cooling Holes," ASME J. Turbomach., **125**, pp. 547–554.

[12] Saumweber, Ch., Schulz, A., and Wittig, S., 2003 "Free-StreamTurbulence Effects on Film Cooling With Shaped Holes," ASME J. Turbomach., **125**, pp. 65–73.

[13] Reiss, H., and Bölcs, A., 2000, "Experimental Study of Showerhead Cooling on a Cylinder Comparing Several Configurations Using Cylindrical and Shaped Holes," ASME J. Turbomach. **122**, pp.161–169.

[14] Bell, C. M., Hamakawa, H., and Ligrani, P. M., (2000), "Film Cooling from Shaped Holes," ASME J. Heat Transfer, **122**, pp. 224–232.

[15] Kohli, A., and Bogard, D., 1999, "Effects of Hole Shape on Film Cooling with Large Angle Injection," ASME Paper No. 99-GT-165.

[16] Lutum, E., von Wolfersdorf, J., Weigand, B., and Semmler, K., 2000, "Film Cooling on a Convex Surface With Zero Pressure Gradient Flow," Int. J. Heat Mass Transfer, **43**, pp. 2973–2987.

[17] Giebert, D., Gritsch, M., Schulz, A., and Wittig, S., 1997, "Film-Cooling From Holes With Expanded Exits: A Comparison of Computational Results With Experiments," ASME Paper No. 97-GT-163.

[18] Hyams, D. G., and Leylek, J. H., 1997, "A Detailed Analysis of Film Cooling Physics, Part III: Streamwise Injection with Shaped Holes," ASME Paper No. 97-GT-271.

[19] Kohli, A., and Thole, K. A., 1998, "Entrance Effects on Diffused Film-Cooling Holes," ASME Paper No. 98-GT-402.

[20] Metzger, D. E., Carper, H. J., and Swank, L. R., 1968, "Heat Transfer With Film Cooling Near Non-Tangential Injection Slots," ASME J. Eng. Power, **90**, pp. 157–163.

[21] Gritsch, M., Baldauf, S., Martiny, M., Schulz, A., and Wittig, S., 1999, "The Superposition Approach to Local Heat Transfer Coefficients in High Density Ratio Film Cooling Flows," ASME Paper No. 99-GT-168.

[22] Sen, B., Schmidt, D. L., and Bogard, D. G., 1996, "Film Cooling With Compound Angle Holes: Heat Transfer," ASME J. Turbomach., **118**, pp. 800–806.

[23] Martiny, M., Schiele, R., Gritsch, M., Schulz, A., and Wittig, S., 1996, "In Situ Calibration for Quantitative Infrared Thermography," *Proceedings of the 3rd International Conference on Quantitative Infrared Thermography (QIRT '96)*, Stuttgart, Germany, September 2–5.

[24] Moffat, R. J., 1988, "Describing the Uncertainties in Experimental Results," Exp. Therm. Fluid Sci., **1**, pp.3–17.

[25] Hay, N., and Lampard, D., 1995, "The Discharge Coefficient of Flared Film Cooling Holes," ASME Paper No. 95-GT-15.

[26] Gritsch, M., Schulz, A., and Wittig, S., 1998, "Discharge Coefficient Measurements of Film-Cooling Holes With Expanded Exits," ASME J. Turbomach., **120**, pp. 557–563.

[27] Lutum, E., and Johnson, B., 1999, "Influence of the Hole Length-to-Diameter Ratio on Film Cooling with Cylindrical Holes", ASME J. Turbomach. **121**, pp. 209–216.

[28] Cho, H., Rhee, D., and Kim, B., 1999, "Film Cooling Effectiveness and Heat/Mass Transfer Coefficient Measurements around a Conical-Shaped Hole with Compound Angle Injection," ASME Paper No. 99-GT-38.

[29] Brittingham, R. A., and Leylek, J. H., 2000, "A Detailed Analysis of Film Cooling Physics, Part IV: Compound-Angle Injection With Shaped Holes," ASME J. Turbomach. **122**, pp.133–145.

[30] Yu, Y., Yen, C-H., Shih, T. I-P., Chyu, M. K., and Gogineni, S., 1999, "Film Cooling Effectiveness and Heat Transfer Coefficient Distribution Around Diffusion Shaped Holes," ASME Paper No. 99-GT-34.

Corso Padova

Jeffrey Barton

Michael G. Dunn

Gas Turbine Laboratory,
Ohio State University,
Columbus, OH 43235

Steve Manwaring

Gamaliel Young

GE Aircraft Engines,
Cincinnati, OH 45215

Maurice Adams, Jr.

Michael Adams

Machinery Vibrations, Inc.,
Chagrin Falls, OH 44022

Development of an Experimental Capability to Produce Controlled Blade Tip/Shroud Rubs at Engine Speed

An experimental capability using an in-ground spin-pit facility specifically designed to investigate aeromechanic phenomena for gas turbine engine hardware rotating at engine speed is demonstrated herein to obtain specific information related to prediction and modeling of blade-casing interactions. Experiments are designed to allow insertion of a segment of engine casing into the path of single-bladed or multiple-bladed disks. In the current facility configuration, a 90 deg sector of a representative engine casing is forced to rub the tip of a single-bladed compressor disk for a selected number of rubs with predetermined blade incursion into the casing at rotational speeds in the vicinity of 20,000 rpm. [DOI: 10.1115/1.1934429]

1 Introduction

Contemporary gas turbines rely on complex blade-casing rub-in-systems to improve the tip clearance behavior during operation from initial service to maximum lifetime [1,2]. Typically a rub-in-system in the compressor section of the engine may consist of a specific circumferential area of the metal alloy case shaped to accept coatings of materials selected for in-service wear and, when required, fire shielding. A momentary eccentricity of a few tenths of 1 mm between a blade and the engine case, which may occur because of an abrupt maneuver in flight or in a hard landing, may cause the tips of a few airfoils to incur the rub-in surface.

Blade-to-case rubs can degrade the operation of an engine through the induction of high amplitude shaft vibration and severe blade/seal wear, and may lead to catastrophic failure of the engine in the worst occurrence. Precisely for these reasons, engines are already routinely tested for containment and survival of blade out events. But to enable the formulation of a comprehensive design methodology for rub-in-systems, particularly one capable to predict and take advantage of the potential offered by new and emerging rotor/blade concepts, advances in several underlying technologies are needed. Among them are: rotor dynamics under severe disturbances [3–6], forced vibrations of bladed disks [7–9], impact dynamics [10–13], and abradability of materials [14].

While the studies reported earlier and in the companion literature have provided excellent conceptual frameworks for developing the desired design methodology, there is much need for controlled experimental data obtained in experiments conducted with real engine components. The experimental capability described in this paper is intended to fill such need.

In the development of the facility and experimental method reported, considerable emphasis was placed on engine manufacturer input regarding the facets of the rub phenomena where results would yield the highest design-advance payoff. Characterizing blade impact dynamics at engine speed was highest on the industry list. Seminal work on blade contact forces during rubbing has been published by Ahrens et al. [12]; however, the measurements were done at a rotational speed about one order of magnitude below those typical of aircraft engines. In addition, engine hardware was not used in this earlier research activity. By contrast, characterizing the high-frequency disturbances occurring at blade first contact and at detachment during repeated rub events is important in the current research program and justifies the preference for experimenting with engine hardware rotating at design speed.

2 Experimental Arrangement

The arrangement of an in-ground spin-pit facility (SPF) specifically designed to investigate aeromechanic phenomena for gas turbine engine hardware rotating at engine speed is described in this section. The underground containment tank that houses both the rotating component and a high-stiffness spindle is cylindrical (1.52 m in diameter by 0.65 m high), and has 0.90 m diameter openings at the top and at the bottom. Figure 1 is a photograph of the facility with the protective top cover in place.

Vertical axis spin testing for design validation of turbomachinery components dates back to World War II applications, which sought to solve problems with military aircraft turbochargers. However, the research projects envisioned from the inception of this facility design dictated the use of a high-stiffness spindle. This requirement forced a significant departure from the common way to conduct a spin test, whereby a rotor is suspended in the heavily armored vacuum tank from a flexible shaft. That shaft arrangement allows the rotor to find its own balance axis and eliminates the need for extreme precision in mounting and balancing. Unfortunately, it is unsuitable to reproduce blade-to-case rubs that can degrade the performance of the engine through introduction of high amplitude shaft vibration and severe blade/seal wear.

Thus the first major subsystem component required for the facility is a vertical and high-stiffness spindle capable of operating

Copyright © 2005 by ASME
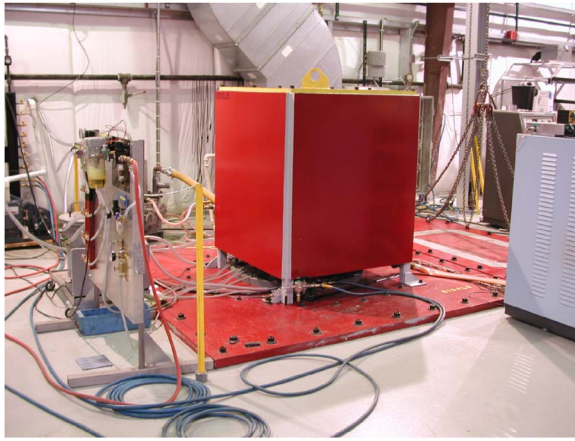
Fig. 1 General view of facility (with protective top cover)

Fig. 2 Section of spindle

at 20,000 rpm for a reasonable period of time. The system utilized here incorporates hybrid bearings and an oil mist lubrication system. This component will be described in more detail later in the paper.

A second major subsystem required to investigate blade-to-case rubs is a fast-acting mechanism that allows insertion of the engine casing into the path of the bladed rotor. Such a mechanism was designed and developed to research asymmetric and full rotor clearance closure for engine stages. In single blade asymmetric clearance closure investigations, a rapid contact of the bladed rotor with its housing is simulated as would occur in an abrupt flight maneuver. In full rotor clearance closure, an extended contact of the bladed rotor with its housing is simulated as could be experienced in some flight phases due to temporary thermal imbalances in different parts of the engine. The known requirements for those types of investigations have defined the general layout of the electromechanical, pneumatic, and measurement subsystems of the facility. The fast-acting incursion mechanism is described in detail later in this paper.

In addition to the two major subsystems noted earlier, a few other facility design features are key in making the facility a versatile tool for performing research on many areas of aeromechanics, including rubs, blade excitation, and blade dampers. A modern high-efficiency air turbine is used to spin-up rotors with large moment of inertia in a few minutes. Moderate vacuum is maintained in the containment tank during operation to eliminate high air friction losses and to reduce the risk of explosion of metal dust or oil fog during an experiment. A high-speed slip ring and hollow spindle is used to conduct strain gauge signals from an instrumented airfoil to the laboratory data collection instrumentation.

2.1 High Stiffness Spindle. The vertical spindle of the SPF shown in Fig. 2 is capable of operating at 20,000 rpm. It consists of a hollow shaft supported on high speed, ceramic hybrid, angular contact ball bearings. The shaft is driven from the top by a reversible air motor. The single stage engine rotor is bolted beneath the spindle assembly and is surrounded by the containment test chamber. The outer spindle housing is made from an aluminum forging. A steel sleeve is inserted into the aluminum housing and serves as the bearing housing. Figure 3 show a photo of the spindle assembly with the slip ring and the drive cover removed. The connector assembly and drive are exposed at the top of the upper housing.

The first critical speed of the spindle is higher than the maximum operating speed. The analysis of the high-stiffness bearing arrangement indicates a shaft critical speed of 23,500 rpm for the design manufacturing tolerances and assumed operating temperature effects.

2.2 Incursion Mechanism System. The function of the incur-

sion mechanism is to move the engine-case segment into the blade path at an exact time for a precise distance and duration, which then determines the number of blade strikes. After a few strikes, the mechanism retracts the casing out of the blade path.
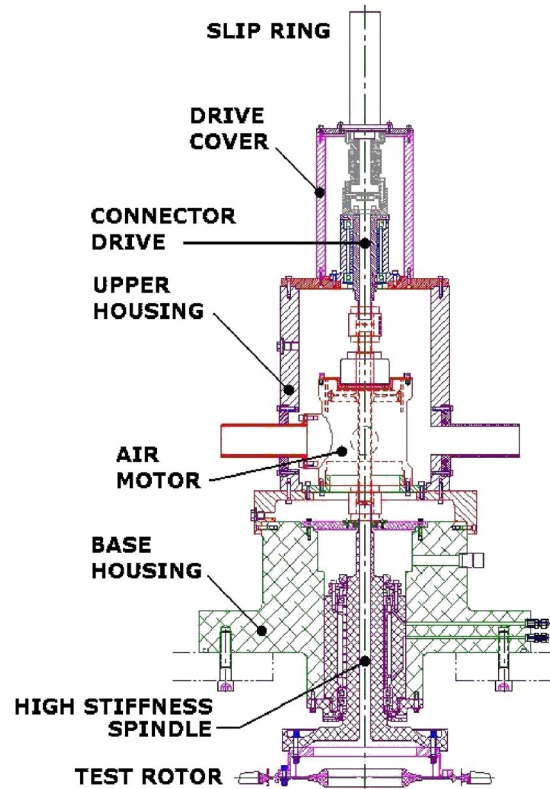
The experimental configuration allows insertion of a segment of engine casing into the path of single or multiple bladed disks while the disk is operating at engine speed. In the current configuration, a 90 deg sector of a representative engine casing is forced to rub the tip of a single bladed compressor disk for a limited number of times with predetermined blade incursion into the cas-

Fig. 3 Spindle photo

CASING SEGMENT SUPPORT RING ASSEMBLY

Fig. 4 Incursion mechanism support ring

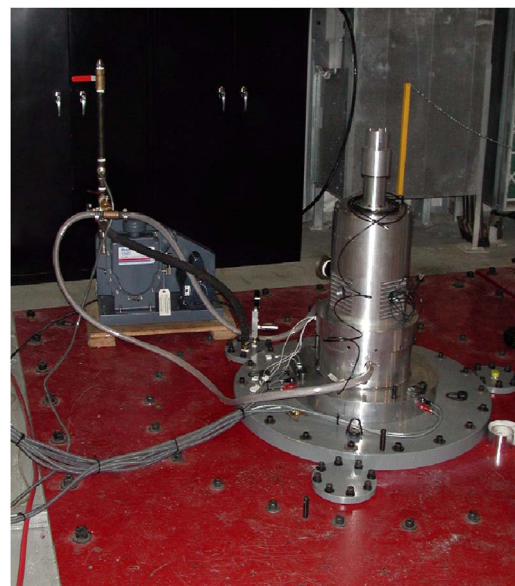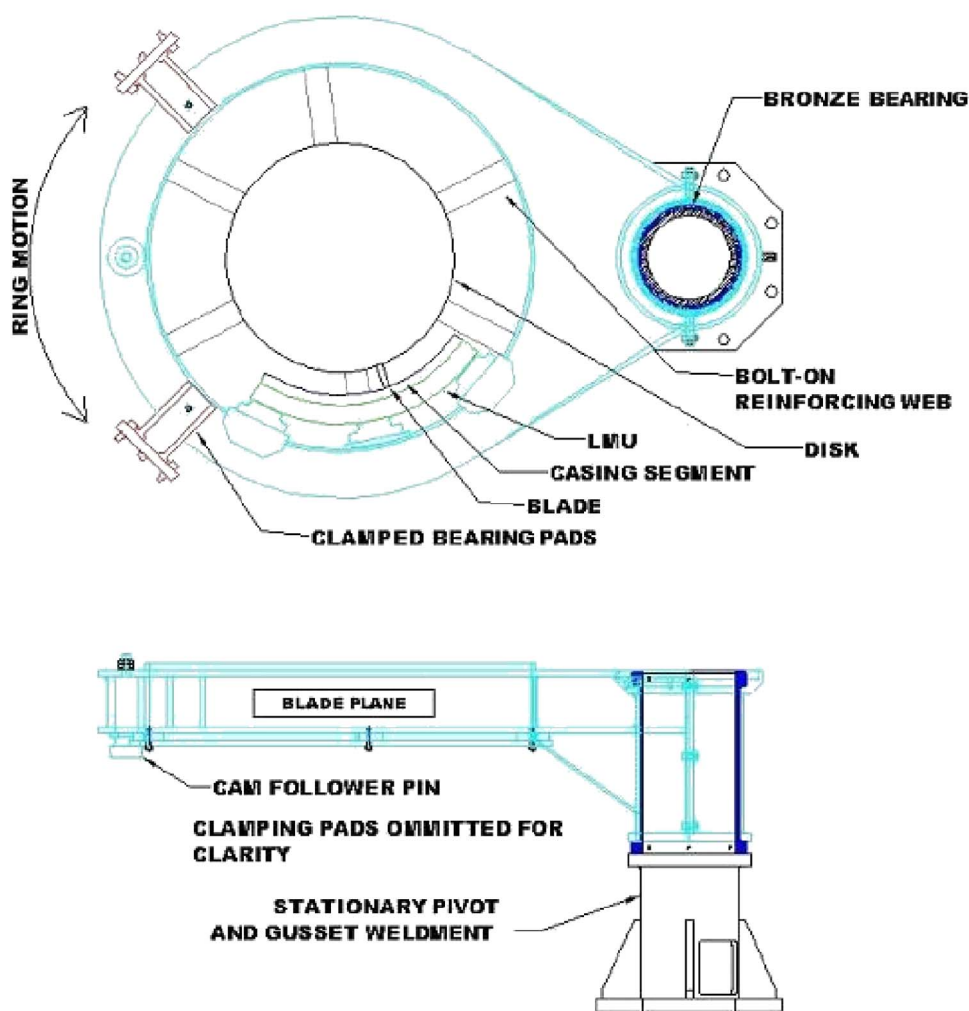ing. For the facility development measurements described herein, the speed at the time of rub was on the order of 17,000 rpm. For this rotational speed, the instrumented airfoil returns to the same circumferential position in 3.8 ms, thus several contacts between blade and shroud are experienced before the eccentricity disturbance is removed. The compressor disk and blade rotate on a vertical rigid spindle that is operated by an air turbine. The casing sector is mounted on a unit based on three piezoelectric load cells and attached to a support ring that swivels in the horizontal plane. The single throw by a fast acting gas piston attached to a cam follower is coupled to the support ring and brings the casing in and out of the path of the rotating blade for a few rubs over a time interval of about 20 ms. The incursion of the rubs is prescribed by setting the initial position of the mechanism in increments of 5 μm.

The incursion mechanism can be broken down into three major subsystems. The structural subsystem consists of a support ring that carries the casing segment along during its motion, a linear cam device that controls the motion, and high-stiffness components anchoring all elements of the system to the containment tank. The actuation subsystem moves the cam block on a linear slide via a pneumatically operated piston and its associated controls. The third subsystem comprises the motion instrumentation and triggering electronics.

The function of the support ring is to carry the casing segment that is mounted to the load-measuring unit (LMU) through its travel cycle into and back out of the blade path. The ring surrounds the disk and pivots on a near zero clearance cylindrical bearing. The stationary pivot point of the bearing is a hollow steel shaft surrounded by a bronze oil-impregnated sleeve. Support for this pivot is provided by a gusseted weldment that attaches to the bottom surface of the containment tank. A cam-follower pin is built into the support ring at the location 180 deg from the pivot. The pin follows a sliding cam profile to effect ring motion. Vertical ring movement is held to less than 125 μm by a set of oil impregnated bronze bearing pads held in a "C" clamp like assembly. The pads are in contact with the ring reinforcement webs. There is a second bolt-on reinforcing web that spans the lower diameter of the ring to help maintain dimensional stability under load. Figure 4 shows a schematic of the structural subsystem and identifies its main elements. Figure 5 shows a picture of the subsystem.

A slot in the cam block guides the cam-follower pin on the support ring. The block is mounted on a linear slide and both are moved thru their travel with a pneumatic piston. The slide and block travel path is along the centerline that extends from the ring follower pin to the ring pivot. A shock absorber is mounted near the end of the slide base to prevent over travel. This assembly is mounted to an adjustable and lockable mechanism that travels perpendicularly to the slide movement to provide initial static adjustment. Support for these components is a table mounted to the
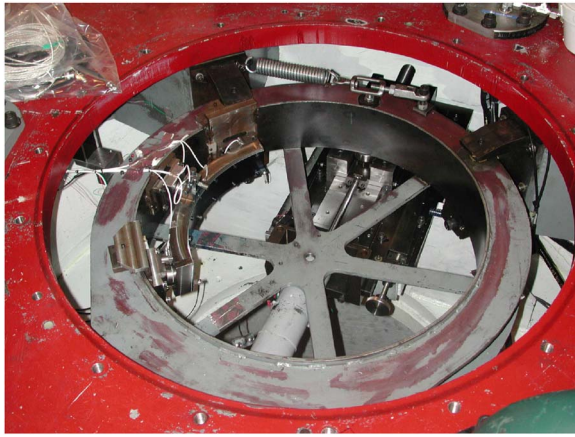
Fig. 5 Incursion mechanism photo

bottom surface of the vessel with substantial welded gussets to the vessel sides for stability. Figure 6 shows a schematic of the subsystem and identifies the main components.

The slide is of a square gib design with a 23 cm saddle (moving component) and a 51 cm base for a 28 cm total travel. Anti-
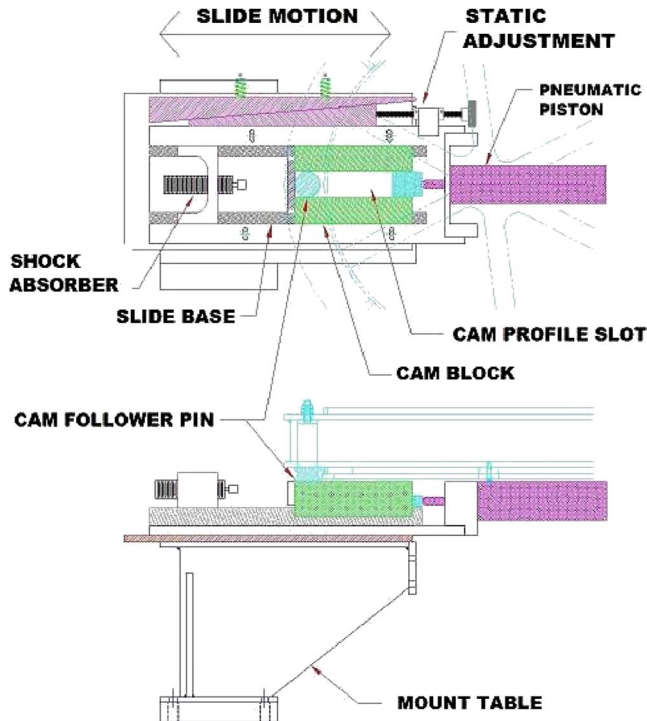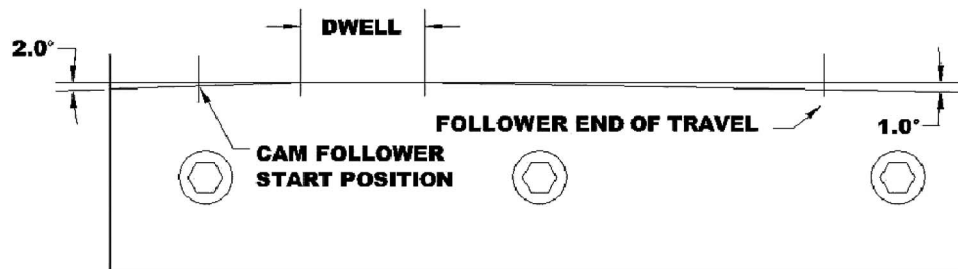

Fig. 6 Incursion mechanism, cam, and slide

friction surfaces are Roulon® and are set for zero clearance by adjusting a line of setscrews. Rated static loads are 170 kN in the vertical plane and 18.8 kN in the horizontal plane. The intended design of this slide is for high speed, high load, and high accuracy machinery. The high load rating and close tolerances allow for accuracy and minimal overshoot in ring travel.

The cam block is machined from C1018 steel (ASTM-A108) and bolted and pinned to the slide saddle. This particular steel was chosen for the finish quality obtainable and desired for a smooth surface at the follower pin contact. The profile of the cam is shown in Fig. 7. This profile, along with the travel speed characteristics provide for incursion timing (the casing must be fully extended into the blade path in less than one revolution), and length of time that the casing is in the blade path (referred to as dwell time). Maximum incursion distance is also controlled. Then, the casing must be retracted out of the blade path and the cam block/slide saddle slowed safely to a stop. The piston actuator is double acting with a 65 mm bore capable of 4.37 kN force.

The diagram of Fig. 8 shows the pneumatic and electrical components, and pressure instrumentation for controlling and monitoring the pressurization of the actuator piston. The reservoir is positioned close to the extend Valcor® valve in order to ensure adequate volume to the piston and is pressurized with gaseous helium. The Valcor® is an axial flow fast-acting full flow valve. Actuation times are on the order of 12 ms and very repeatable. The interval timer accepts either a local or remote trigger and has user programmable times for delay time and on time. The Valcor® valve requires a high initial voltage and so has its own supply in a metal enclosure separate from the control room. Pressure readouts are used as displays for initial setup, and paralleled to oscilloscopes and the data acquisition system for performance diagnostics. The retract side of the piston is connected to a three way valve using vacuum at prefire setup, shop air for post-test retraction, and a vent to ambient to relieve retract pressure. The operation of the subsystem is described later in Sec. 3.

2.3 Load Measuring Unit. The segment of engine casing against which the blade rubs is carried by a metric support that includes three load cells. Each piezoelectric load cell measures three force components. Two end cells are placed below the load line, which is located in the midplane of the engine case. The center cell is located above. The arrangement is designed to minimize the moment loads on each cell and to obtain moment information around three mutually perpendicular axes from the entire unit.

Five accelerometers are also mounted on the LMU, which is shown in Fig. 9. Three radial directions are measured at locations very close to each load cell. A triaxial block, which is mounted near the center load cell, is equipped with the remaining two accelerometers that measure one axial and one circumferential direction in the middle of the LMU.

As in the actual engine, the radius of the casing cylinder is greater than the radius of the circular path followed by the blade tips under normal operating conditions. A tight but finite clearance is maintained at the rub-in-system surface. This condition is applied to ensure that no impact of the blade will occur first at the

Fig. 7 Cam profile
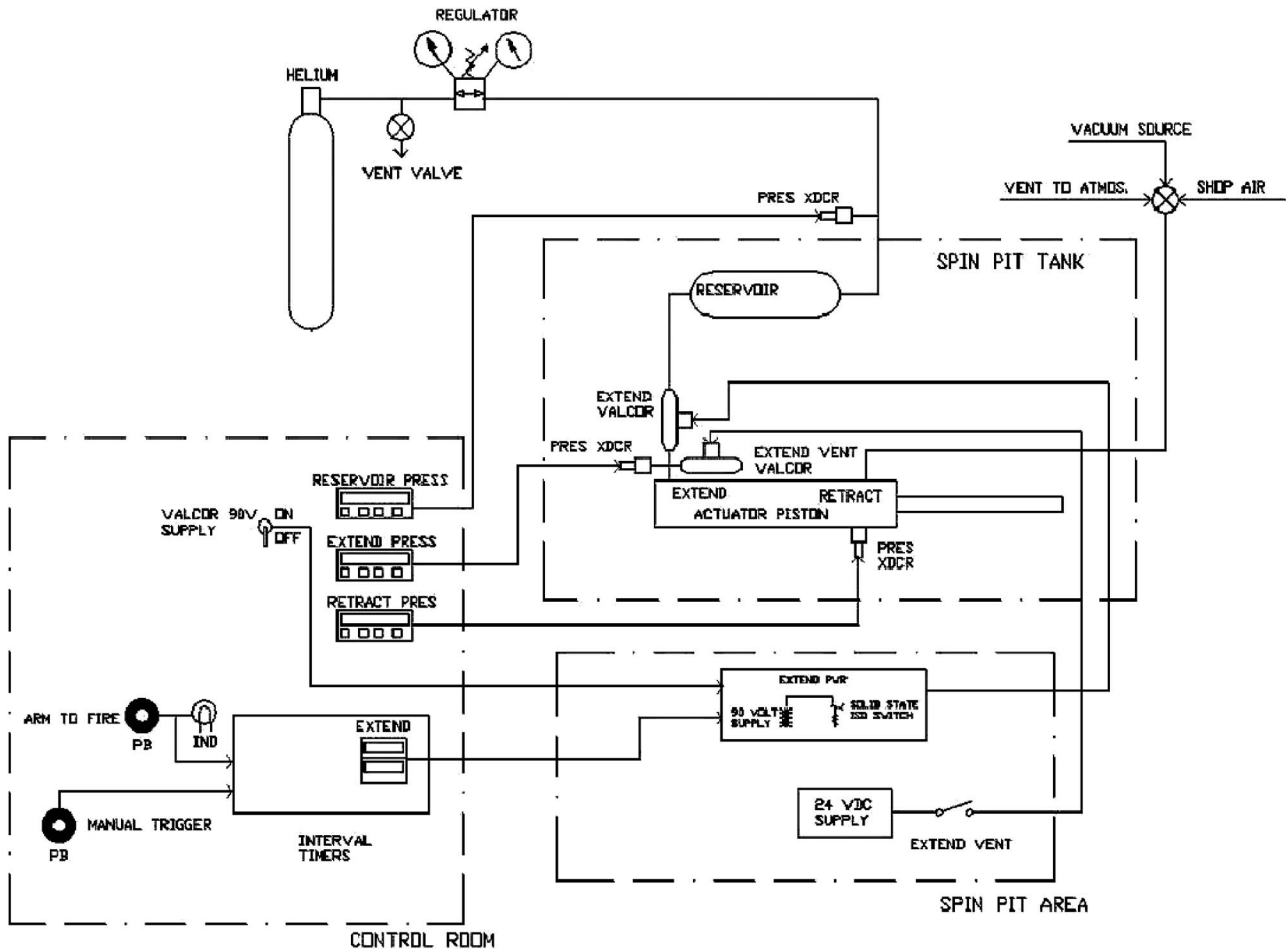
Fig. 8   Pneumatic control system

edge of the LMU for all chosen values of eccentricity between casing and rotor in the experiments. In addition, the corners of the casing sector are beveled for added margin of safety.

3   Operation

During a typical experiment the rotor is spun-up to the target speed in less than 3 min. As the rotor speed approaches the target value selected for a rub to occur, the angular acceleration is gradually decreased so that the airfoil impact with the shoe occurs effectively at a constant value of rpm. A few rubs are obtained as follows. First, the casing movement toward the spinning blade tip

is initiated by the triggering system described later in this section. This results in the motion shown in Fig. 10. Also shown in the figure are the markers that indicate the passing of the blade over the LMU for duration of about 1 ms. Second, during the casing motion, the tip sweep line is crossed as depicted in the figure. After this point in time, the LMU is in the path of the spinning

Fig. 9   Load measuring unit LMU

Fig. 10   Casing motion and incursion region

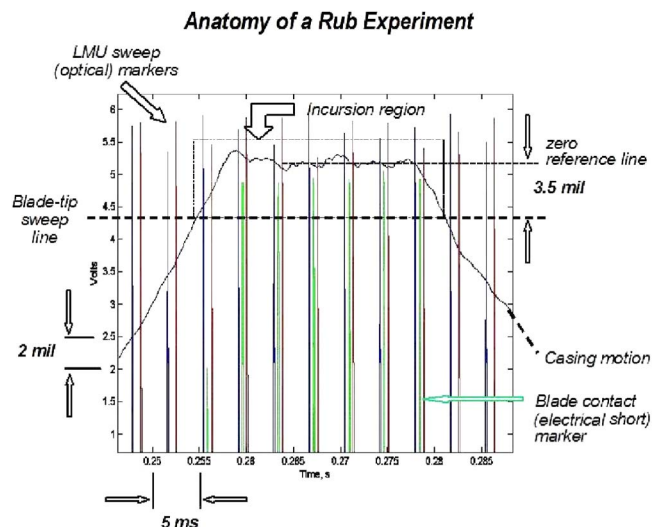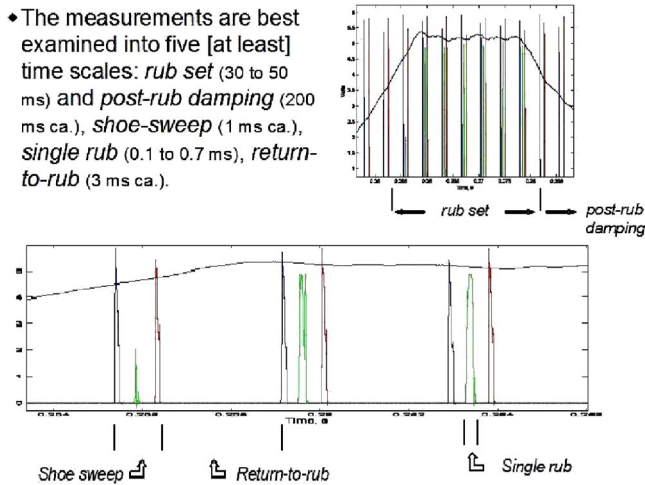♦ The measurements are best examined into five [at least] time scales: *rub set* (30 to 50 ms) and *post-rub damping* (200 ms ca.), *shoe-sweep* (1 ms ca.), *single rub* (0.1 to 0.7 ms), *return-to-rub* (3 ms ca.).

Fig. 11   Time Scales of blade rubs

Fig. 12   Triggering of case motion

blade and a rub is obtained as soon as the blade returns over the LMU sector. This is shown by the appearance of the blade contact marker in the figure. Except for a range of very small incursions, the rubs begin with the casing still advancing toward the spinning blade. The more severe the incursion, the more rubs occur before the casing locks into the zero-lead region shown in Fig. 10.

Third, during the time that the casing is in the maximum incursion position, up to six rubs can take place for the values of rotational speed at which experiments were conducted. In fact, due to the settings chosen in the triggering circuit, five rubs were obtained in most cases. All zero-lead incursions occur with the same nominal interference between the path of the blade tip and the arc of the casing. The deviation of the actual interference from the nominal value was monitored in repeated experiments and found to be less than ±3.8 μm.

Fourth, the continuing motion of the cam forces the casing to begin to retreat. In this phase, the rubs continue because the casing is still inside the incursion region. As before, the more severe the incursion, the more rubs occur before the casing clears the exit boundary of the incursion region.

Finally, the casing crosses the tip sweep line and the rubs end. In the experiments performed to this date, the maximum incursion imposed was for 400 μm and resulted in a total of 15 rubs.

It is important to note that the measurements obtained during each experiment should be examined according to a number of different time scales. Five scales are illustrated in Fig. 11. In order of decreasing duration they are: the time of damping of blade excitation after a set of rubs, the time spanned by an entire set of rubs, the time for one revolution, the time interval a blade spends in free oscillation after a rub and before returning for a subsequent rub, the time interval during which the blade sweeps over the LMU, and the duration of an individual rub.

It is precisely to identify during an experiment the different scales of the rub phenomena that two types of markers are recorded while operating the SPF. First contact is detected by a sensor and is used to begin data acquisition in one type of experiments (disk/blade growth experiments) as described later. In the second type of experiments (ramp-incursion experiments) that are discussed in greater detail in this paper, the shoe motion toward the spinning blade is manually initiated and is followed, after a suitable delay, by the signal to begin data acquisition. In either case, the data acquisition system is already running in sample-and-hold mode at the precise instant when the command to acquire is received, and a prerub hold time is programmed into it. Thus any of the measurement histories shows typically a prerub value for about 200 ms, the onset of the rub event, the dynamic response resulting from the impact of the airfoil with the shoe, the
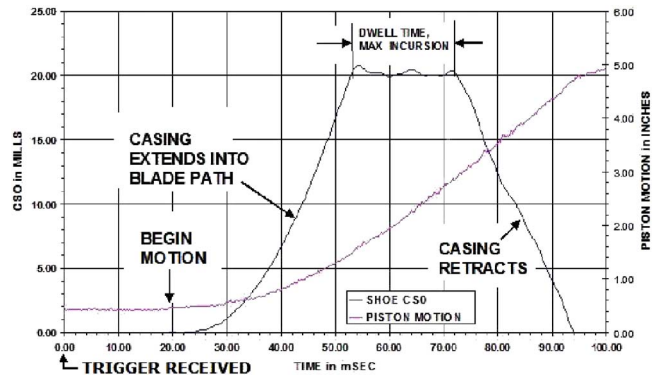
release of the airfoil immediately following detachment from the shoe, the vibrational response of the airfoil as it spins around once more after having been excited by the impact, the effect of repeated impacts, and the decay in dynamic response after the conditions causing the incursion have been removed. Typical histories last 829 ms and consist of a few to several rubs depending on the type of experiment.

It is important to relate the above sequence of events to rub occurrences in flight. It is clear that in the experiments just like in flight, for a given incursion depth or severity of a rub event, the rate of incursion in each strike will be positive, null or negative during different phases of the set of rubs that makes up an event. By comparing measurements obtained at different experimental conditions, the effects of incursion depth and rate of incursion can be separated. In the middle rub of Fig. 11, one can see the blade detaching and reattaching during a single strike interval.

Furthermore, the effects of rub repetition can be identified. For the example shown in Fig. 11, the first rub is clearly brief and is followed by rubs of equal duration (250 μs) later. Although not a full engagement, the 1st rub is important because it imparts to the airfoil an initial vibratory motion. In addition, in zero-lead rubs, the deviation of the actual interference from the nominal value was monitored in repeated experiments and found to be less than ±3.8 μm (±1.5 mil). Rub Nos. 2 and 3 are equal in duration and incursion depth. However, as the blade comes around after each rub it is excited and one would intuitively expect that rub Nos. 2 and 3 will be different in blade vibratory response and in tip loads during contact to the casing. The extent to which this was found to be true is discussed in Sec. 4 later.

The actuation of the incursion mechanism system is obtained as follows (reference should be made to Fig. 8 earlier). Initially, the air piston is retracted with shop air, vented, and the retract side brought to a vacuum. Both extend side Valcor® valves are closed and the reservoir is charged with helium. The interval times are set and the timer is armed and ready for either a manual or remote trigger. When a trigger is received the timer waits for the delay time then fires the Valcor® valves through its power supply for a set-on time. The piston then pushes the cam block through its travel.

Ring and attached LMU, casing segment initial position, and casing actuated motion are measured with a capacitance probe referred to as the casing stand off (CSO) sensor. Lion Precision manufactures the probe and associated electronics. This system has a certified resolution of 0.36 μm, a range ±1 mm, and a bandwidth of 16,800 Hz. The output is in volts. Cam block motion is measured with a LVDT manufactured by UniMeasure. It has a 25.4 cm stroke and has an in-house calibration of 0.3%. Several combinations of cam profile, helium pressure, and valve timing were tried during a total of 51 trial runs. The last of these runs is plotted in Fig. 12.

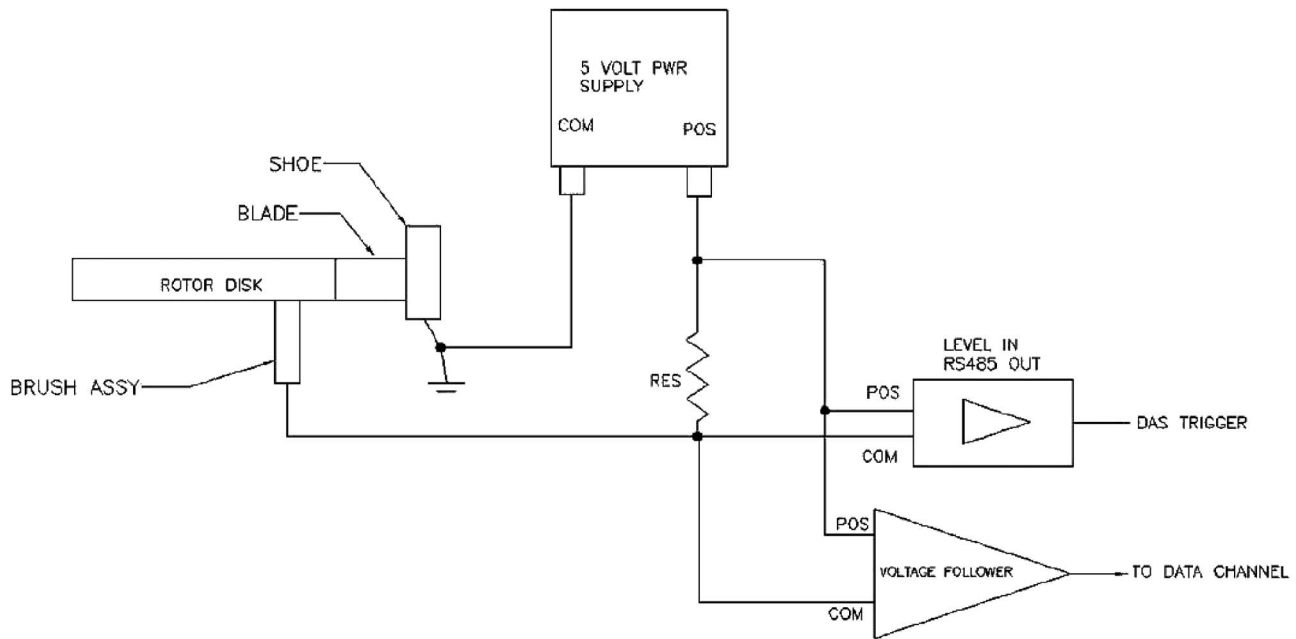In disk/blade growth experiments, rubs of progressively in-

Fig. 13 Blade contact trigger circuit

creasing severity were obtained by using the expansion of the rotating component under increasing rotational speed as the mechanism driving the interference relative to a stationary casing. The total number of rubs obtained in these experiments was greater than the number of rubs in the ramp-incursion case by at least one order of magnitude. The focus of this class of experiments is on the vibratory response of the blade when undergoing a multitude of excitation cycles.

The trigger to start both the data acquisition and incursion systems must be precisely controlled. Two different triggering schemes were used. One for the disk/blade growth experiments where the casing segment is stationary and the blade grazes it as a result of tip growth. The other for the ramp-incursion experiments where the casing is suddenly brought into the blade path. The high-speed data acquisition has a selectable window in which to collect data and record the rub events, therefore it must trigger at the appropriate moment. The incursion mechanism is stationary for the disk/blade growth experiments, requiring no trigger. For the ramp-incursion experiments it must be precisely timed.

For the disk/blade growth experiments, a voltage signal needed for the trigger to start the acquisition is produced when the blade tip first touches the casing segment. This is accomplished by setting the rotor to 5 V and the casing to ground. The blade tip touching the shoe completes a circuit and triggers the data system. Figure 13 shows a simplified diagram.

The triggering circuitry for the ramp-incursion experiments is fairly involved. The object is to get the casing sector to move out and set in place during the time interval when the blade cannot interfere with the casing surface. This time interval spans several blade revolutions, as can be seen from Fig. 10. Using a selectable time delay from a trigger that is related to instantaneous blade position, the object is achieved by delay increments equal to a fraction of one revolution. An optical sensor placed to sense blade passage at the leading edge of the shoe supplies the trigger signal. The incursion system timer can resolve to a millisecond, which is too coarse for this application, so a delay generator capable of resolving 0.1 ms is placed in front. A manual trigger-enable switch disables the sensor trigger until the rotor set speed is reached. The data acquisition system is triggered with the incursion system timer so that casing movement can be monitored during the experiment and correct position relative to blade location can be verified. Figure 14 shows a simplified diagram.

The facility instrumentation is conveniently grouped into two categories: rotating sensors and stationary sensors.

The rotating sensors consist of miniature dynamic strain gauges arranged on the suction and pressure side of the blade. Excitation power and signal response are carried by electrical wires routed through the hollow shaft of the spindle to the rotating terminal of a slip ring unit. The stationary terminal of the unit is directly patched into the high-speed data acquisition system. In the present experiments all strain gauges were operated in constant current mode.

The primary stationary sensors consist of the three piezoelectric load cells that are part of the LMU and of the five piezoelectric accelerometers, also mounted on the LMU.

4 Results and Discussion

The measurements obtained simultaneously from load cells, accelerometers, and strain gauges during nearly a second of data acquisition time, when combined, offer a detailed description of the rub phenomena. The purpose of this paper is to describe the facility design and operation and the measurements later are used merely to illustrate the capabilities of the facility. Extensive results from specific applications and research projects will be the subject of subsequent papers. Load cell and strain gauge measurements are discussed briefly later. The measurements of acceleration are qualitatively very similar to those obtained from the load cells.

Typical measurement traces are shown in Fig. 15 and 16. In these figures, the initial prerub level of the sensor, the response during about 10 ms of multiple rubs, and the postrub sensor response are easily identified.

The three load cell measurements from top to bottom of Fig. 15 are for the first cell, center cell, and last cell passed by the blade during each revolution. Note how quickly after the rub interval the measured loads return to the prerub level. The two typical strain gauge measurements from top to bottom of Fig. 16 are for a gauge located at the tip and for a gauge located at the root of the blade, respectively. Note that the tip gauge indicates localized disturbances during the rubs, a temperature-induced displacement of the baseline, and no postrub oscillations. In contrast, the root gauge shows oscillations building up from rub to rub followed by an exponential decay after the last rub.
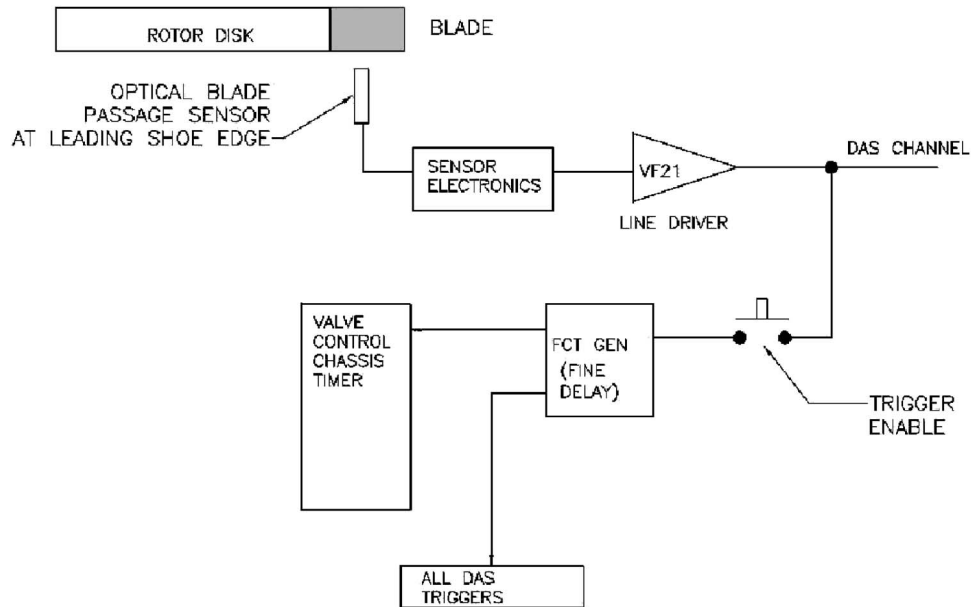
Fig. 14 Optical sensor trigger circuit

As the blade rubs on the engine-case segment attached to the LMU, blade tip loads are distributed to the three LMU load cells via the rigid transfer bar. Thus the LMU acts as a mechanical filter on the tip loads. A transfer frequency response function (FRF) algorithm is needed in relating engine-casing loads to load cell measurements. In brief, the theory for the FRF algorithm is based on characterizing the LMU dynamics by impulse vibration testing, whereby the output response at location x_0 is given by

$$u(x_0, t) = H_{oi}(\omega) F i e^{j\omega t}$$

where $H_{oi}(\omega)$ is the output FRF at location o per unit force applied at location i.

In order to implement the FRF algorithm we proceeded as follows. Prior to conducting rub experiments, input loads from an impulse hammer were applied at three locations, in three direc-

tions for each location. At the same time, nine response measurements were recorded from the load cells. The elements of the matrix $H_{oi}(\omega)$ were computed as ratios of measured outputs to known inputs in the frequency domain. Then the inverse of the output FRF matrix was computed and stored for later use in conjunction with rub measurements.

During a rub experiment, nine response measurements are recorded from an unknown force at the rub surface. It is precisely this resultant force that is computed from the known instantaneous blade position and from the inverse of the output FRF operating on the load cell measurements transformed to the frequency domain. The computation earlier is then repeated for a discrete set of blade positions during the rub.

At present, issues associated with the detailed requirements of impulse vibration testing have restricted the application of the FRF algorithm to two components of the blade tip load, the radial and the circumferential component. However, finite element structural modeling is in progress to remove such restriction. In the
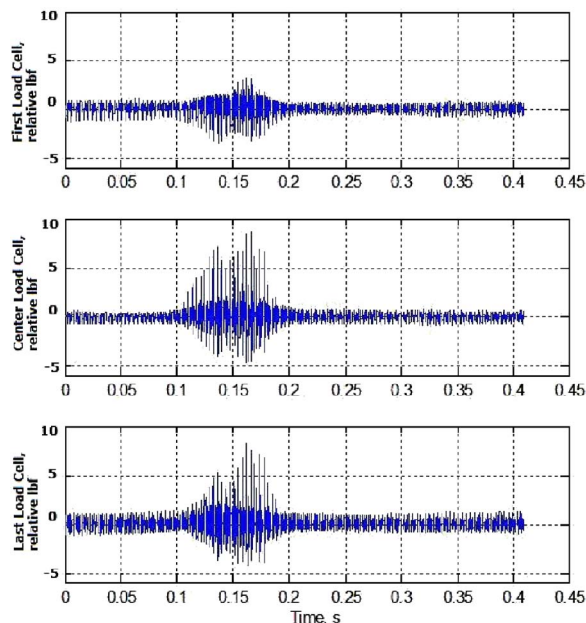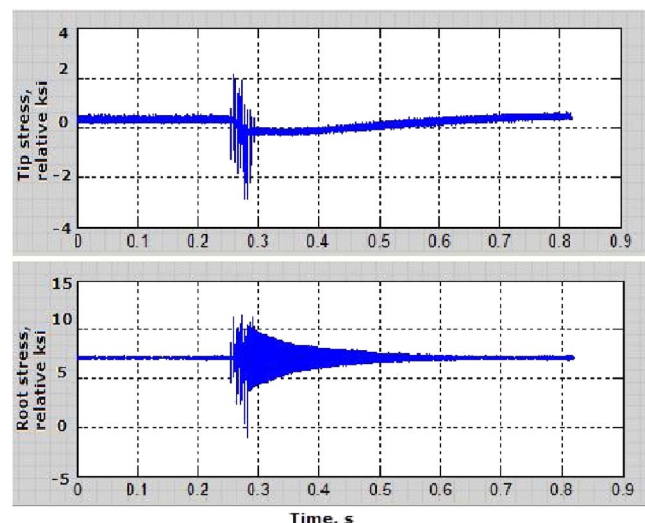

Fig. 15 Typical load cell measurements

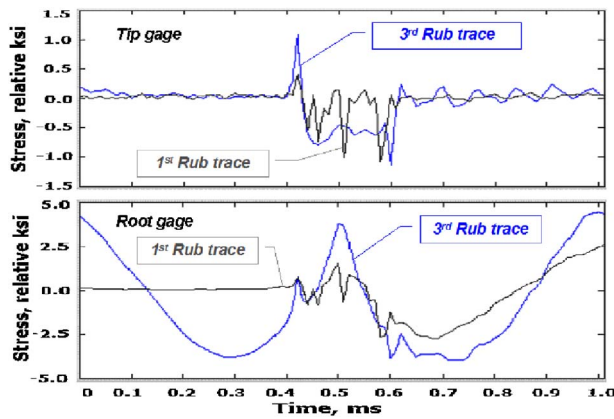**Fig. 16 Typical strain gauge measurements**

Fig. 17 Strain gauge measurements for shoe-sweep time scale

mean time, even with the restriction to two components, interesting comparisons of tip loads have been obtained and will be reported in the near future.

The strain gauge results at different airfoil locations are combined to extract modal information. Interpretation of the results is obtained after several steps of data reduction. The two major components of the data reduction technique are (a) a series of decompositions of the traces into time segments, and (b) spectral analysis of each time segment. The spectral analysis component of the data reduction technique applied conventional FFT processing applied to time segments as appropriate.

Much of the paper to this point has been devoted to describing the facility design and operation, but Figs. 10 and 11 given earlier and Fig. 17 given later illustrate an example of measurement of transient dynamics for the blade and casing vibroimpact response that is important to the industry. The reader attention is to be focused here on the shoe-sweep time scale to compare one of the zero-lead rubs, No. 3, to the first rub (see Fig. 11). Figure 17 shows the measurements again for the root gauge and the tip gauge. It is noticeable that the traces show distinct spikes at the beginning and end of the most perturbed region. The time interval between these two spikes correlates well in all experiments with the indications of electrical contact shown earlier as the blade-contact marker, so the first spike is taken as indicating an attachment stress wave and the last spike a detachment stress wave. In this case the blade contact lasted about 200 μs.

Looking first at the root gauge, the first rub is not a full engagement rub. The centrifugal load has been subtracted out and we see that relative stress is zero up to first attachment. Then there is some high frequency content probably related to a changing area of contact as the airfoil flexes and twists under load, and after a low frequency oscillation gradually develops. It is a first flex frequency that persists also at later times. The detachment spike is visible. Notice that it is a bit early relative to the companion event in the third rub. Again, this first rub is not a full engagement strike.

Now let us follow the third rub of the root gauge. The blade comes around and is excited in the first flex mode shape. It attaches first and it results in a history more suggestive of an increasing-decreasing contact area. Then it detaches and resumes the first flex motion.

Looking now at the tip gauge, the following occurs: the start of the first rub contact is clearly marked by a first positive spike followed by smaller disturbances because of varying contact area and local blade detachment. A distinct negative spike marks final blade detachment. In rub No. 3 the spike marking the initial blade impact is stronger and is followed by a more uniform load during

contact consistent with a deeper incursion. The detachment spike again ends the strike at about the same level encountered during rub No. 1.

It must be stressed that these are the durations involved in a real engine rub. It is necessary to understand the physics under these conditions, not at some longer duration that is easier to obtain experimentally. The detailed measurements provided in this paper have illustrated that the excitation state of the airfoil on the second and subsequent encounters with the shroud is very different from the initial encounter. This finding has resulted in re-evaluation of the modeling commonly used in design tools used for predicting the blade/shroud incursion interactions.

5 Conclusions

An in-ground spin-pit facility specifically designed to investigate aeromechanic phenomena for gas turbine engine hardware rotating at engine speed has been utilized successfully to obtain specific information related to prediction and modeling of blade-casing interactions as reported herein.

The results presented in this paper demonstrate that sudden incursions of varying severity can be controlled to increments of 5 μm. Rubs can be repeated for detailed investigation of tip loads and vibratory stresses. In addition, the amplification of blade oscillations under successive rubs can be quantified. In the future, refinements in tip load measurements will be obtained from finite elements modeling and the effect on rub forces from varying incursion rate will be investigated.

The purpose of this paper was to describe the development of the experimental capability along with results that demonstrate the operability of the facility and the importance of these results to the engine designer. It is interesting to note that a blade is capable of sustaining incursions that are more significant than might have been initially thought. The dynamics of high-frequency disturbances occurring at blade first contact and at detachment can be characterized relative to low-frequency oscillations in repeated rubs. An indication of tip loads can also be deduced from the measurements.

In combination with refined design methods and refined modeling of frictional forces, the greater understanding of the phenomena that affect blade-casing interactions is expected to result in savings in gas turbine maintenance costs applicable not only in propulsion engines but for stationary advanced power systems as well. Incursion measurements obtained using actual engine hardware at engine rotational speed have demonstrated the need for improved modeling of the event.

References
[1] Hermanek, F. J., Jr., 1970, "Coatings Lengthen Jet Engine Life," Metal Progress, **97**, pp. 104–106.
[2] Kosing, O. E., Scharl, R., and Schmuhl, H. J., 2001, "Design Improvements of the EJ 200 HP Compressor. From Design Verification Engine to a Future All Blisk Version," ASME Paper No. 2001-GT-0283.
[3] Muszynska, A., 1989, "Rotor-to-Stationary Element Rub-Related Vibration Phenomena in Rotating Machinery—Literature Survey," Shock Vib. Dig., **21**, pp. 3–11.
[4] Padovan, J., and Choy, F. K., 1987, "Nonlinear Dynamics of Rotor/Blade/Casing Interactions," ASME J. Turbomach., **109**, pp. 527–534.
[5] Gallardo, V., and Lawrence, C., 2004, "Turbine Engine Stability/Instability with Rub Forces," NASA TM-2004-212974.
[6] Adams, M. L., 2000, *Rotating Machinery Vibration: From Analysis to Troubleshooting*, Marcel Dekker, New York.
[7] Manwaring, S. R., and Wisler, D. C., 1993, "Unsteady Aerodynamics and Gust Response in Compressors and Turbines," ASME J. Turbomach., **115**, pp. 425–434.
[8] Weaver, M. M. et al., 2000, "Forcing Function Measurements and Predictions

of a Transonic Vaneless Counter Rotating Turbine," ASME Paper No. 2000-GT-0375.

[9] Kielb, J. J., Abhari, R. S., and Dunn, M. G., 2001, "Experimental and Numerical Study of Forced Response in a Full-Scale Rotating Turbine," ASME Paper No. 2001-GT-0263.

[10] Yigit, A., Ulsoy, A. G., and Scott, R. A., 1990, "Dynamics of a Radially Rotating Beam with Impact," ASME J. Vibr. Acoust., **112**, pp. 71–77.

[11] Jiang, J., Ahrens, J., Ulbrich, H., and Scheideler, E. M., 1998, "A Contact Model of a Rotating Rubbing Blade," *Proceedings of the 5th International Conference on Rotor Dynamics*, Darmstadt, pp. 478–489.

[12] Ahrens, J., Ulbrich, H., and Ahaus, G., 2000, "Measurement of Contact Forces During Blade Rubbing," IMechE Conf. Trans., pp. 259–268.

[13] Sinha, S. K., 2005, "Non-Linear Dynamic Response of a Rotating Radial Timoshenko Beam with Periodic Pulse Loading at the Free-End," Int. J. Non-Linear Mech., **40**(1), pp. 113–149.

[14] Laverty, W. F., 1981, "Rub Energetics of Compressor Blade Tip Seals," *Proceedings of the 3th International Conference on Wear of Materials*, pp. 714–721.

Averaged and Time-Dependent Aerodynamics of a High Pressure Turbine Blade Tip Cavity and Stationary Shroud: Comparison of Computational and Experimental Results

Brian R. Green

John W. Barter

GE Aircraft Engines,
Cincinnati, OH 45215

Charles W. Haldeman

Michael G. Dunn

Gas Turbine Laboratory,
Ohio State University,
Columbus, OH 43235

The unsteady aero-dynamics of a single-stage high-pressure turbine blade operating at design corrected conditions has been the subject of a thorough study involving detailed measurements and computations. The experimental configuration consisted of a single-stage high-pressure turbine and the adjacent, downstream, low-pressure turbine nozzle row. All three blade-rows were instrumented at three spanwise locations with flush-mounted, high-frequency response pressure transducers. The rotor was also instrumented with the same transducers on the blade tip and platform and the stationary shroud was instrumented with pressure transducers at specific locations above the rotating blade. Predictions of the time-dependent flow field around the rotor were obtained using MSU-TURBO, a three-dimensional (3D), nonlinear, computational fluid dynamics (CFD) code. Using an isolated blade-row unsteady analysis method, the unsteady surface pressure for the high-pressure turbine rotor due to the upstream high-pressure turbine nozzle was calculated. The predicted unsteady pressure on the rotor surface was compared to the measurements at selected spanwise locations on the blade, in the recessed cavity, and on the shroud. The rig and computational models included a flat and recessed blade tip geometry and were used for the comparisons presented in the paper. Comparisons of the measured and predicted static pressure loading on the blade surface show excellent correlation from both a time-average and time-accurate standpoint. This paper concentrates on the tip and shroud comparisons between the experiments and the predictions and these results also show good correlation with the time-resolved data. These data comparisons provide confidence in the CFD modeling and its ability to capture unsteady flow physics on the blade surface, in the flat and recessed tip regions of the blade, and on the stationary shroud. [DOI: 10.1115/1.1934410]

1 Introduction

Three-dimensional, viscous, steady, and unsteady computational fluid dynamics (CFD) analysis is being used routinely for designing airfoils for use in turbomachinery. Significant effort has been placed on validating CFD-based analysis tools for predicting the macroscopic flow details (e.g., loading, turning, loss) and most modern CFD-based tools are capable of adequately predicting these macroscopic details. CFD-based tools have matured to the point that they are capable of modeling complex geometric features. However, relatively little effort has been given to validating these tools for predicting the complex, but real, geometric features (e.g., turbine blade squealer tips, variable stator vane spindles, fillets, etc.) that are inherent in modern turbomachinery blade designs. These geometric features, while often small, can have a profound impact on the predicted secondary flows, leakage flows, and local heat-transfer.

As Dunn [1] points out, new engines are being designed with higher turbine inlet temperatures that are approaching the fuel stoichiometric temperature. This puts heavy emphasis on the cooling needs for combustors, turbines, and exhaust nozzles for reliability, durability, and survivability at these ever increasing turbine inlet temperatures. In the design phase of these components, heat-transfer predictions become routine and necessary to confirm metal temperatures are within the material capabilities. Problems associated with predicting heat-transfer are coupled with the turbine aerodynamics because proper prediction of the vane and blade surface-pressure distribution is essential for predicting the corresponding heat-transfer distribution (Dunn [1]).

Significant work, both experimental and numerical, has been directed at the calculation of the unsteady surface pressures in single-stage, high-pressure, rotating turbine stages. Studies by Venable et al. [2] began by looking at the time-averaged results while Busby et al. [3] looked at time resolved results of the interaction effects on the Allison Vane–Blade Interaction (VBI) turbine for three different axial spacings using four different two-dimensional (2D) and three different 3D Navier–Stokes codes. These predictions employed a coupled stage analysis for the unsteady predictions. Similar time-averaged and time-resolved predictions were also produced by Barter et al. [4] using the 3D, viscous, time-accurate code MSU-TURBO for the predictions. These predictions looked at two different analytical techniques, a coupled stage and a single blade-row analysis, for predicting the unsteadiness in the turbine stage. Kielb [5] used a quasi-3D un-

steady code to predict the aerodynamic forcing function on a turbine rotor due to the upstream vane. Predictions were performed on the blade surface at 50% and 85% span for a pair of vane-to-blade axial spacing.

Previous analytical predictions and experimental results were limited to the blade surface. Very few measurements have been aimed at acquiring time-resolved data sets for the blade tip and shroud regions. Even fewer attempts have been made to compare experimental data in these regions to analytical results. Dunn [6] used a short duration facility to obtain time-resolved pressure and heat flux measurements on the stationary shroud of the Garret TFE731-2 utilizing a flat tip blade geometry. Soon after, Metzger et al. [7] used a simplified model of the turbine rotor to predict time-averaged blade tip and shroud heat-transfer by using a Navier–Stokes solution of the blade passage and tip coupled with the Dittus–Boelter duct heat-transfer correlation. These simple one-dimensional calculations showed good agreement to the measured data for both the shroud and the blade tip heat transfer. Ameri and Steinthorsson provided computational results of time-averaged heat transfer on a flat tip blade and rotating shroud for the Garret TFE 731-2 turbine [8] and the first stage blade of the two-stage Shuttle Main Engine hydrogen side turbo pump [9] compared to experimental data obtained by Dunn et al. [10,11], respectively. These two computational results provided good agreement with the experimental data as well. A more recent study of a combined experimental and computational effort was reported by Bunker et al. [12] and Ameri and Bunker [13] aimed at investigating the time-averaged heat transfer on a first stage turbine blade for a flat tip power-generation gas turbine. The experiment used a three blade linear cascade with no outer shroud motion and the computational results showed, again, good agreement with the data.

Previous computational and experimental studies have been primarily focused on passage time-averaged and time-resolved surface pressures and blade tip and shroud time-averaged heat transfer. While time-resolved pressure data have been obtained for the stationary shroud above the rotating blade, to date, no data sets have been produced for the time-resolved behavior on a flat or recessed tip for a full-scale rotating turbine. According to Dunn [1], this is one of several missing pieces to CFD validation necessary for blade tip heat-transfer predictions. Another important aspect is the validation of this CFD code with complicated geometries. The recessed tip geometry and comparisons of shroud and tip surface pressures provides an opportunity for such a task. From this comes increased confidence in analysis techniques as applied herein.

1.1 Scope of Current Study. The current study covers an entire aerodynamic study of a rotating turbine blade, which includes both experimental data and the corresponding numerical predictions. The numerical predictions involve the use of unsteady CFD to predict the time-averaged behavior and the time-accurate behavior in the blade passage, and the time-accurate behavior in the blade tip, and stationary shroud regions. The experimental data is gathered from a full-scale rig that includes the high-pressure turbine (HPT) nozzle, a rotating HPT rotor, and the low-pressure turbine (LPT) vane. The rig was operated at the proper corrected engine design conditions (i.e., temperature ratio, pressure ratio, and rotation speed) to match a representative cruise condition for the turbine rig. The main focus of this study was on the HPT rotor tip and nonrotating shroud regions. However, the passage predictions were readily available from both the numerical and experimental investigations and are included for completeness.

The hardware used for the experimental rig, which consists of the HPT nozzle, HPT rotor, and LPT vane, is full-scale engine hardware. The engine hardware is representative of a single-stage HPT that would be found in commercial aviation turbomachinery. Typical commercial HPT hardware requires cooling flow for the vanes, blades, and disk cavities due to high combustor exit temperatures; however, for this experiment the cooling has been omit-

ted for simplicity. Another aspect of HPT rotor blades commonly found in commercial engines is a recessed (often termed a "squealer") tip. The rig consists of a majority of blades incorporating the flat tip geometry and several blades with the recessed squealer tip geometry of which both will be used for data comparisons. The experiments are performed in a short-duration, shock-tunnel facility that is located at The Ohio State University Gas Turbine Laboratory.

The numerical simulations use MSU-TURBO, a CFD code developed for resolving unsteady flow physics in turbomachinery. Following Barter et al. [4] and Green [14] only single blade row wake blade interaction (WBI) unsteady analyses are used for comparison. Both the flat tip and recessed tip were modeled in the analysis using high-fidelity multiblock grids and the boundary conditions were set to match the flow conditions in the rig.

2 Experimental Investigation

The experimental portion of this investigation provided the necessary results for a good comparative analysis to the numerical CFD predictions. The experiments involved the use of a full scale, rotating model of the one and a half stage high-pressure turbine. The experiments provided the detailed time-accurate measurements of the blade, blade tip, and shroud surface pressures on the rotating blade. With the turbine rig running at design point corrected conditions, the experiments were run as close to reality as possible. A brief description of the facility, the turbine stage and a more detailed description of the tip recess cavity and associated instrumentation, instrumentation at 15%, 50%, and 90% span on the blade suction and pressure surfaces will be provided in this section.

2.1 THE OSU Gas Turbine Laboratory (GTL) Facility. As previously mentioned, a shock-tunnel facility was used to gather the experimental measurements. The shock tunnel was used to provide a short duration of heated and pressurized gas directed through the rotating turbine model. For these experiments, air was utilized as the test gas. The entire experimental apparatus consisted of a shock-tube, an expansion nozzle, a large dump tank, and a device that housed the one and a half stage turbine and provided the flow path geometry, as shown in Fig. 1.

The actual construction and operation of the facility was first documented by Dunn [15] but more accessible descriptions of the operation of the facility have been reported in Dunn [16–18] as examples. The Turbine Test Facility (TTF) operates, and was used in these experiments, in two modes. One mode is the traditional shock-tube mode as described by Ref. [15]. A second mode, which has become more widely used for aerodynamic work (as opposed to heat-transfer work), is the blowdown mode. For the work presented here, all the experiments were performed in blowdown mode and are described more fully in Ref. [19] along with comparisons between the modes of operation. Since this facility has been reported in great detail over many years, readers unfamiliar with it are referred to the many other papers using this facility and no further discussion of the facility will be given here.

2.2 Description of the Turbine. The turbine rig is a transonic, single-stage, highly loaded high-pressure turbine vane and rotor with a low-pressure vane. There are thirty-eight high and low-pressure vanes with seventy-two rotating blades. All of the blades and vanes are uncooled for the purposes of these tests. In the absence of vane and blade cooling, the blades were rotated closed in order to maintain the proper flow function in the turbine. Both the rig and the CFD are run at the appropriate design corrected speeds and mass flow rates. The tip clearances were measured to be approximately 2.3% of the blade height.

The pressure sensors where variants of the Kulite XCQ-062-100A sensors mounted as static pressures (on the shrouds), or as chip sensors on the airfoils themselves. The shroud pressure sensors were mounted in a grid pattern with four lines of sensors at 0, 33%, 66%, and 100% of a blade passage, and at four axial loca-
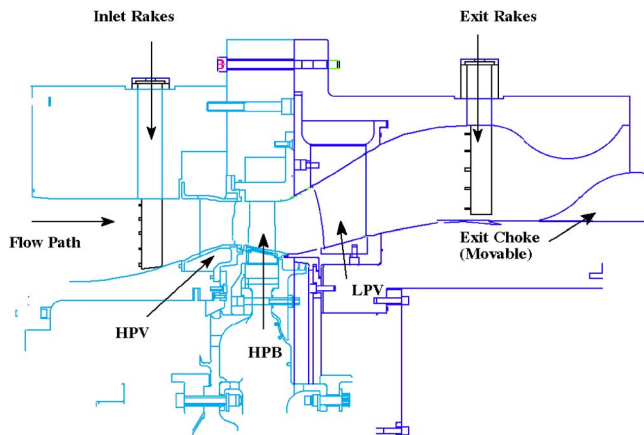
Fig. 1   Main flowpath

Fig. 2   Blade and blade tip grids for the flat and recessed tip O–H–O grids

tions at about −7%, 30%, 60%, and 90% blade chord. In this rig two different blade tip configurations were used at the same time. Two blades, one of each configuration, contained blade tip instrumentation with three to four pressure sensors installed in the tip region. However, only the recessed tip is currently available due to instrumentation problems with the flat tip blade.

The data acquisition system and basic calibration procedures have been described previously and have been summarized in Ref. [19]. As there is not much new information it will not be discussed in detail here other than saying that the data was all acquired at 100 KHz using a set of anti-aliasing filters set at 45 KHz. This insured that proper resolution of the time-resolved data was obtained.

3   Numerical Investigation

The numerical study was performed to obtain a set of data consistent with those obtained in the companion experimental program. The unsteady CFD analysis of the high-pressure turbine blade utilized a three-dimensional, Reynolds-averaged Navier–Stokes (RANS) CFD code, MSU-TURBO, to obtain the time-resolved pressure predictions. These predictions, when compared to the experimental data, provide confidence in the CFD code's ability to predict blade passage behavior as well as the unsteady behavior in the blade tip and shroud regions. Further detail of the numerical investigation will cover the goals of the predictions, background of the CFD code utilized, an in depth look at the computational modeling, and finally, some results obtained for comparison to the experimental data.

3.1   Background of CFD Code. For all CFD analyses, the time-accurate CFD code, MSU-TURBO, was used. MSU-TURBO is a three-dimensional, viscous, time-accurate code that solves the Reynolds averaged Navier–Stokes equations in Cartesian coordinates. The equations are spatially discretized using a modified upwind scheme (Whitfield et al. [20]) based on Roe [21] and Osher and Chakravarthy [22]. Temporal discretization is second-order accurate backward differencing and the governing equations are time marched using Beam and Warming's approximate factorization scheme with flux Jacobians computed using the flux-vector splitting technique of Steger and Warming [23] and viscous Jacobians computed numerically. Matrix inversion is accomplished using a symmetric Gauss–Seidel technique and multiple Newton subiterations are performed at each time step in order to minimize the linearization error. The turbulence model is incorporated into the code using the CMOTT κ-ε [24] model with wall functions.

Two analytical techniques for time-accurate analyses have been incorporated into MSU-TURBO. The first technique is a coupled blade-row analysis. This technique couples the time-dependant
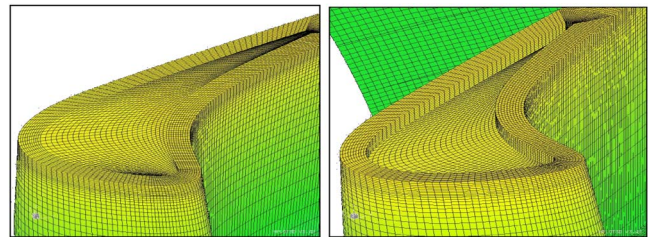
behavior of the three blade-rows (vane–blade–vane). For efficiency in the calculations, the domain of each blade–row is limited to a single passage and exact vane-to-blade-to-vane ratios are modeled using phase-lag boundary conditions at the periodic boundaries and blade–row interfaces. More detail on this modeling technique can be found in Chen and Barter [25]. The second technique is known as a wake blade interaction (WBI) model and is a single-blade-row analysis in which the disturbances from the upstream or downstream are introduced into the computational domain by an inlet or exit time-dependant boundary condition. This technique also utilizes a single passage for computational efficiency and proper blade counts are again modeled through the use of phase-lag boundary conditions at periodic boundaries. Greater details into this modeling technique can be found in Chen et al. [26].

3.2   Computational Modeling. A detailed set of multiblock grids was created using an O-mesh grid around the blade, H-mesh grids through the remainder of the passage, and a combination of O-mesh and H-mesh grids in the tip section. This combination of H-mesh and O-mesh grids in the tip facilitates creation of the recessed tip cavity needed to complete the study while keeping the flat-tip and the recessed tip passage grids identical. The passage grids were created and smoothed through the use of commercially available grid generation software. The grids contain sixty two cells in the blade-to-blade (theta) direction, one hundred and forty-eight cells axially on the blade surface, sixty cells radially on the blade surface, twelve cells radially through the tip clearance, and seven cells radially downward in the recessed tip cavity. The tip clearances were modeled identically to those measured in the experimental rig. The computational domains are extended from the trailing edge of the upstream vane to the leading edge of the downstream vane. Figure 2 shows the computational domain on the surface of the flat and recessed tip grid, and Fig. 3 shows the mesh refinement at approximately mid-span for both the flat and recessed tip grids.

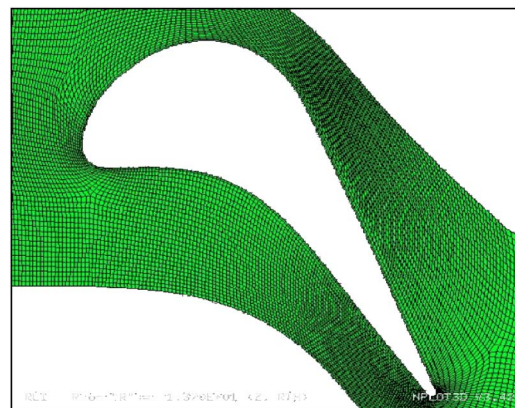The unsteady analyses are initialized from converged steady

Fig. 3   O–H–O mesh at approximately mid-span

solutions to minimize the amount of time needed to achieve a periodic solution. The unsteady WBI calculations were time-marched using four hundred and eighty time steps per period based on the adjacent (upstream) blade–row. This provides frequency resolution of up to 250 KHz, or approximately forty times vane passing frequency, however grid size will limit resolution. Five Newton subiterations were used at each time step to minimize linearization error. All analyses were performed on HPC3600 workstations in parallel using eight processors per blade-row. WBI solutions took approximately three days to achieve a periodic time-dependant solution.

3.3 Data Reduction of the CFD Results. For each set of CFD analyses, a large amount of data is available for post-processing. For this project, the static pressure on the blade surface, blade tip surface, and the shroud were desired. Specific locations were chosen based on the Kulite locations in the experimental rig. All data was extracted from the CFD solutions at each time step over a single vane-passing period. For the blade surface, the desired data was time-averaged and time-resolved static pressure data limited to the first harmonic amplitude and phase with respect to the upstream vane passing frequency. A discrete Fourier transform (DFT) was used to obtain the time-averaged and the first harmonic amplitude and phase for all points of interest. The time-averaged and Fourier harmonic amplitudes were then normalized by the turbine inlet total pressure.

Time-averaged and time-series data from the CFD was desired for the stationary shroud and the rotor blade tip. The blade tip data, as extracted, provided a time-series trace for each point of interest over the vane passing period. The stationary shroud time-series data, however, requires significantly more post-processing to achieve the blade-passing period. Grid points were mapped across the blade passage at four axial locations that coincided with Kulite positions as placed during the experiments. The corresponding surface pressure for each time step was then stored over one period of the unsteady solution. For ease in post-processing, the entire period was then interpolated to a constant tangentially spaced grid. Using the relationship of the rotor RPM to the time step as associated with the vane-passing period, the time-series data in the stationary reference frame was extracted. Final data comparisons were provided as a normalized pressure fluctuation. This fluctuation was calculated by normalizing the fluctuations about the period average.

4 Discussion of Results

The results of the study are provided in three parts, time averaged and time resolved (FFT) comparisons for the blade surface, time-resolved comparisons for the blade tip, and time-resolved comparisons for the stationary shroud above the rotating blade. The blade surface comparisons consist of surface pressures at three spanwise locations: 15%, 50%, and 90%. These comparisons are made to the available rig data to ensure that the predictions for the main passage are correct. This provides added confidence in the accuracy of the shroud and blade tip comparisons. The blade tip comparisons were made for the recessed tip only (as the flat tip data is currently unavailable) with four locations available for comparison. The final set of comparisons, those for the stationary shroud, was made only for the flat tip blades. This is because the majority of blades were of the flat tip configuration.

4.1 Blade Surface: Time-Averaged Pressure and FFT. The first set of comparisons covers the blade surface from both a time-averaged and a time-resolved standpoint. The time-resolved quantities have been limited to FFT data in the form of harmonic amplitudes and phase angles. Figure 4 shows the time-averaged comparisons of the CFD predictions and the data.

At 15% span, the comparisons show very good agreement on both the suction side and the pressure side. Near the leading edge, the CFD tends to over predict the acceleration on the suction side of the airfoil; however, differences between the measured and
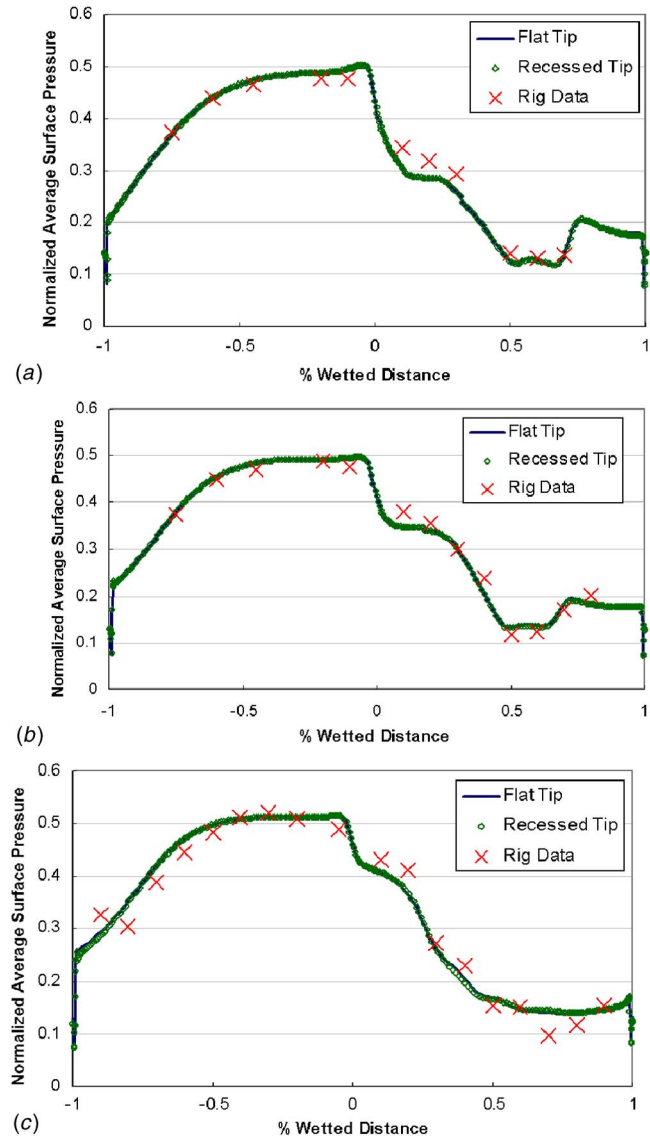
Fig. 4 Time-averaged surface pressures at (a) 15% span, (b) 50% span, and (c) 90% span

predicted surface pressures are minimal. A similar result was also achieved at 50% span on the suction side. Note that for both 15% and 50% span, the shock location on the suction side at about 60%–70% wetted distance is captured quite well. At 90% span, the CFD did not capture the suction side acceleration at about 65% wetted distance. The under prediction has been attributed to grid resolution issues around the shock location based on previous studies performed on this particular rotor by Green [14]. These grid resolution errors were a result of the grid expansion that happens during the smoothing process of the grid. In the CFD predictions, pressure spikes at the trailing edge of the blade can be seen at all spanwise locations. These spikes are caused by trailing edge separations in the CFD solutions and are most likely not real. While all of the blade surface data was measured on the flat tip configuration, at all spanwise locations, the flat tip predictions lie directly on top of the recessed tip predictions. This was an anticipated result and is pointed out for clarity.

Figures 5 and 6 show the FFT amplitudes and phase angles, respectively, for the vane passing frequency on the blade surface. The 15% span location shows the highest perturbation amplitudes with respect to the total inlet pressure. Over the majority of the pressure and suction surfaces, the CFD predictions and experi-
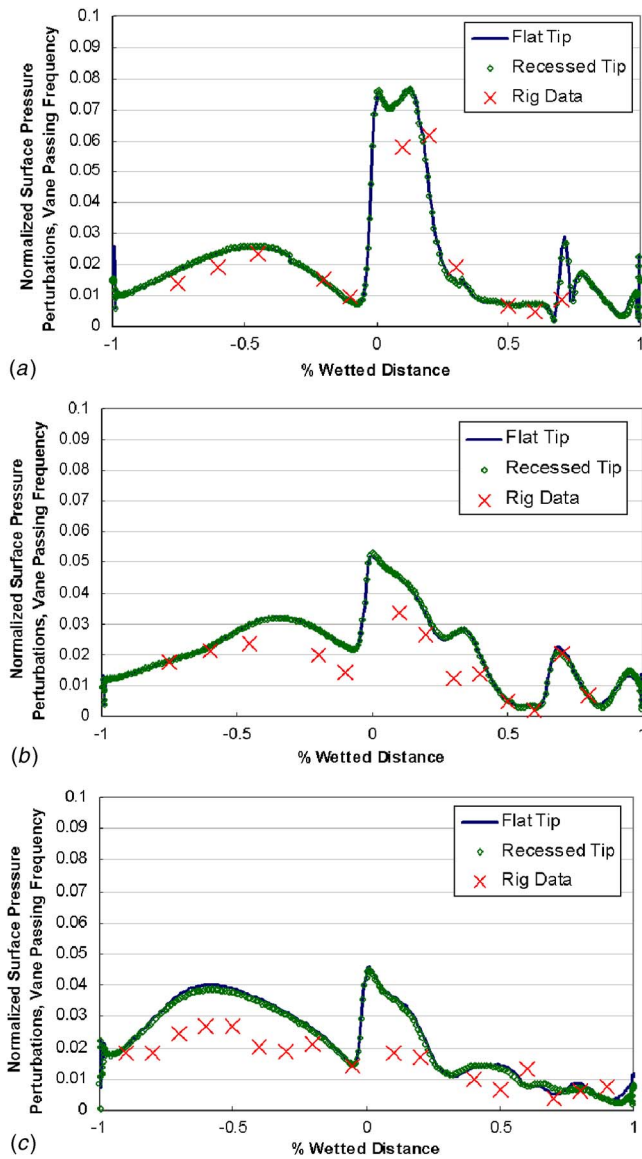
Fig. 5 Surface pressure perturbations for vane passing frequency at (*a*) 15% span, (*b*) 50% span, and (*c*) 90% span

Fig. 6 Surface pressure perturbation phase angle for vane passing frequency at (*a*) 15% span, (*b*) 50% span, and (*c*) 90% span

mental data are in very good agreement. However, at the leading edge of the blade, some discrepancies between predicted and measured amplitudes do exist. The error in the predicted amplitude is seen to be much lower at 15% span and increases at 50% and 90% span. At 50% span, the CFD over predicts the harmonic amplitudes in the vicinity of approximately ±40% of the wetted distance from the leading edge. The remainder of the pressure and suction side shows good agreement, particularly around the shock location at 60%–70% wetted distance on the suction surface. At 90% span, the same over prediction is seen at the leading edge and over most of the pressure surface of the airfoil; however, the suction surface does shows a good correlation between the CFD and the experimental data. Several possible reasons exist for the overprediction of the CFD. Such possible reasons include the modeling of nominal (as expected) geometry versus modeling of actual (as produced) rig hardware and improper prediction of secondary flows in the upstream nozzle, which affect nozzle exit swirl.

The phase angles, as shown in Fig. 6, complete the blade surface comparisons and tend to follow similar trends, as discussed for the vane passing frequency perturbations above. The phase
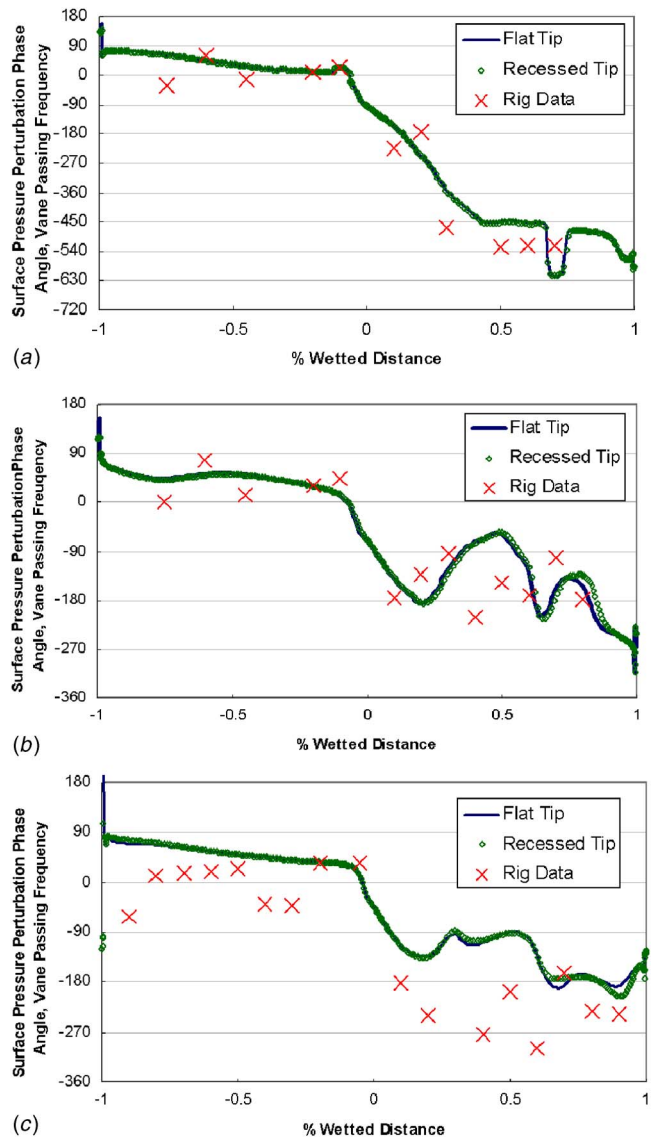
angles, both calculated and measured, show decent agreement at 15% and 50% span. But again, the phase angle comparisons at 90% span do show discrepancy between measured and predicted behavior on both surfaces.

At the 15%, 50%, and 90% spanwise locations, the flat tip CFD data lie directly on top of the recessed tip CFD data for both the time-averaged and FFT predictions. This is an interesting result and is pointed out for clarity only.

4.2 Blade Tip: Time-Average and Time-Series. The second set of comparisons was made for the blade tip region. For the blade tip region, four transducer locations were available, but only for the recessed tip. These transducer locations were characterized by a percentage of wetted distance, based on axial length of the recessed tip, and a percentage of pitch, based on the pitch width of the recessed tip. Figure 7 shows the transducer locations in the recessed blade tip.

The time-average data comparisons are shown in Fig. 8. These data are normalized to the inlet total pressure and designations are by gage number. The predicted time-averaged values on the blade tip do show some discrepancy to the measured rig data at all four locations. The largest of these discrepancies occurs at location
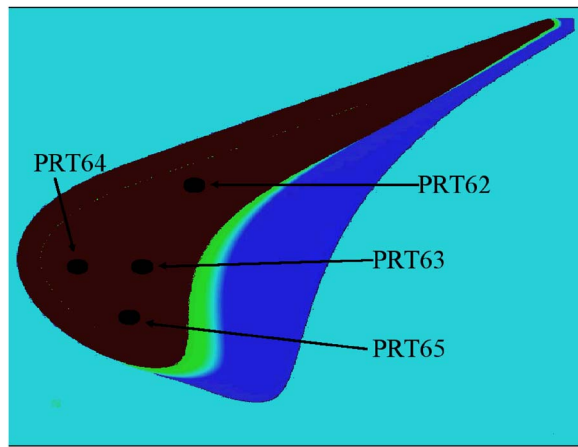
Fig. 7 Recessed blade tip Kulite locations

PRT63. At this location, the CFD predicts the static pressure on the blade tip to be approximately 14% higher than the measured data. The remaining three locations show differences of almost 10% at PRT62 down to 1% difference at PRT64.

The time-series data is shown as a percentage of vane passage, and duplicated for the second passage. These data are provided as a fluctuation about the average at that location and are normalized to the turbine inlet pressure. In Fig. 9, the four comparisons are shown for the CFD and the available rig data. The time series trends for all gages are in good agreement with the measured data, however, PRT62 and PRT65 miss the peak by over 50%. Similar to the blade surface, any number of possible reasons exists as to why this under-prediction has occurred. For the tip region, geometry variation and prediction of secondary flows would be crucial.

4.3 Stationary Shroud: Time Average and Time-Series. The last set of comparisons was to the stationary shroud above the rotating blade. The shroud data is shown on a percentage of the rotor passage and is duplicated for the second rotor passage. Similar to the tip comparisons, these data are provided as fluctuations about the average, normalized to the turbine inlet total pressure. There are four axial locations based on the axial length of the rotor (with negative values being upstream). Figure 10 shows these four locations with respect to the blade. A total of eight gages were available for the comparison.

The time-average comparisons between the CFD and the measured rig data can be seen in Fig. 11 below. The time-average measurement values were slightly under-predicted by the CFD were slightly under-predicted, however, trends of the data show
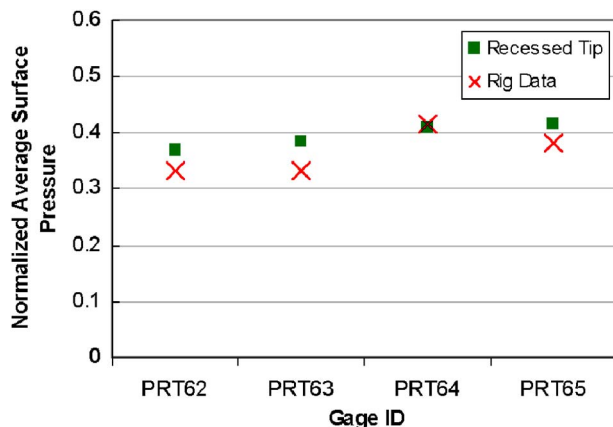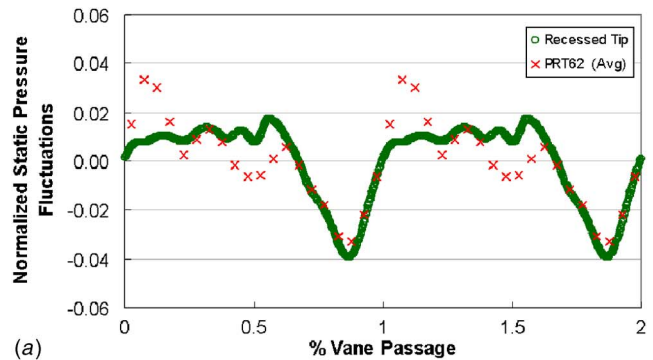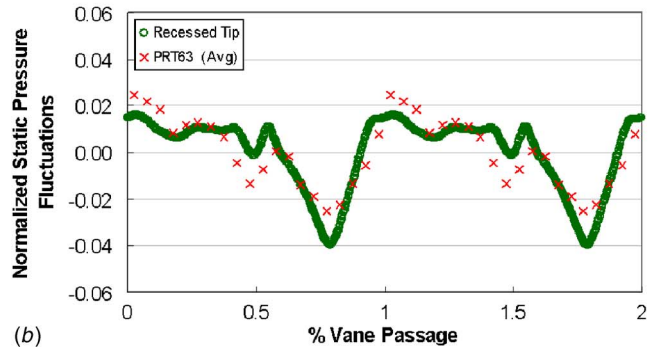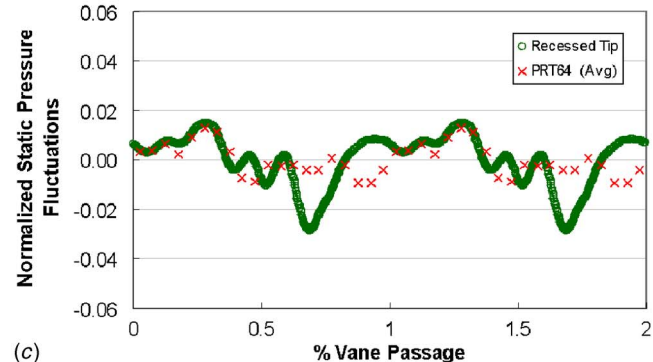

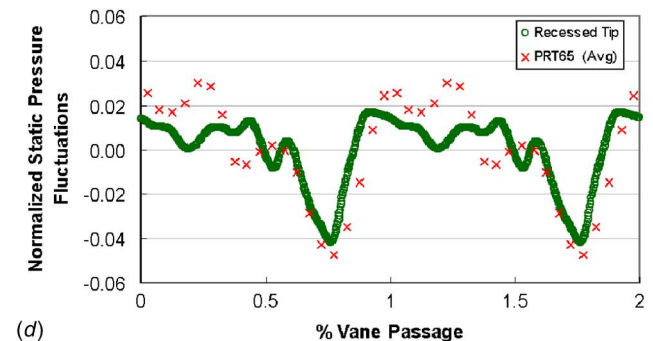**Fig. 8 Time-average comparisons for the blade tip designated by gage number**

Fig. 9 Surface pressure fluctuations for the recessed tip at (a) PRT62, (b) PRT63, (c) PRT64, and (d) PRT65

very good agreement.

The time-series comparisons are provided in Fig. 12. The first transducer location, Fig. 12(a) at −7% wetted distance, had four gages spaced at three different tangential locations. Included among these four gages was a repeat transducer one passage away. The predictions show good agreement with the overall trend of the rig data. Also note that the rig data for the four different gages show very little difference with exception given to the positive peaks. In Fig. 12(b) at 30.6% wetted distance, two gages were available and were one-third of a pitch apart. These comparisons
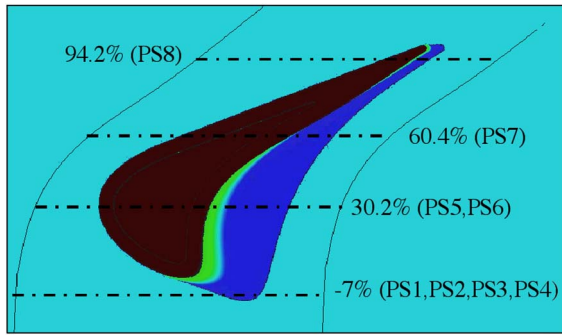
Fig. 10 Shroud Kulite sensor locations in the experimental rig

show good overall agreement with the trend and amplitude. The two rig transducers for this location show similar trends with respect to tangential location. The last two comparisons, in Fig. 12(c) at 60.4% and Fig. 12(d) at 94.2% wetted distance, contained only a single tangential location, and thus a single transducer. These comparisons show a very good correlation in both predicted trend and amplitude across the entire passage.

4.4 Flat and Recessed Tip Analytical Comparisons. Significant grounding of the flat and recessed tip unsteady CFD solutions has been accomplished through the use of the available experimental results. With this grounding complete, comparisons between the two analytical solutions in the tip and shroud regions can now be made to provide further insight into the time-averaged and unsteady differences between the flat and recessed tip solutions. The first set of analytical comparisons is for the tip region. Locations on the flat tip were selected to match the tangential and axial locations as previously shown for the recessed tip. The first comparison is made for the time-averaged surface pressure at each gage location. These comparisons are provided in Fig. 13 below. For all transducer locations, the flat tip results show significantly lower levels of time-averaged static pressure on the blade tip surface as compared to the recessed tip. This difference can be attributed to the fluid velocity across the tip cavity.

The relative Mach numbers from the time-averaged solution are shown in Fig. 14 below. The time-averaged recessed tip solution is on the left and the flat tip solution on the right. The tangential plane shows the contours of relative Mach numbers through the tip gap region on both solutions. The Mach numbers near the leading edge are fairly similar as the fluid enters the tip. The recessed tip solution shows a slight increase in Mach number across the tip until the fluid enters the main passage on the suction side whereas the flat tip solution shows a steady increase across its tip.

The next set of comparisons, shown in Fig. 15, are the unsteady pressure fluctuations for the flat and recessed tip solutions. At all
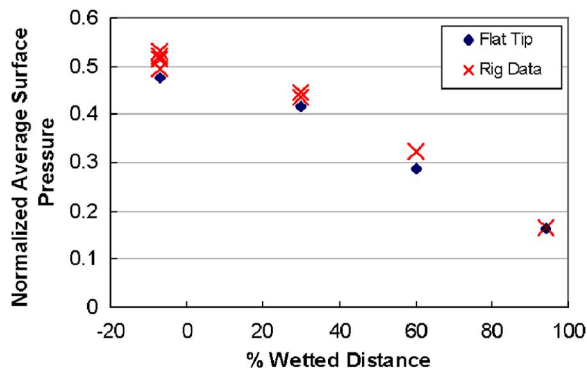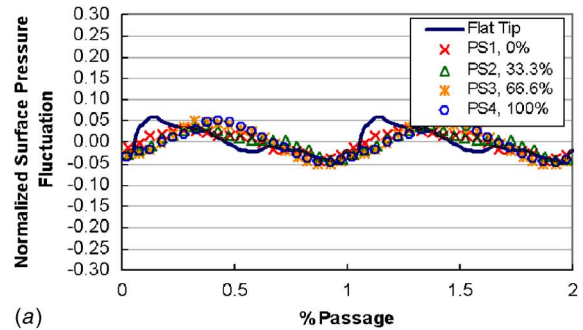

Fig. 11 Time-average comparisons for the stationary shroud
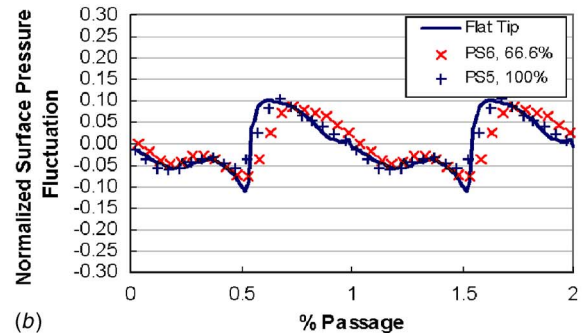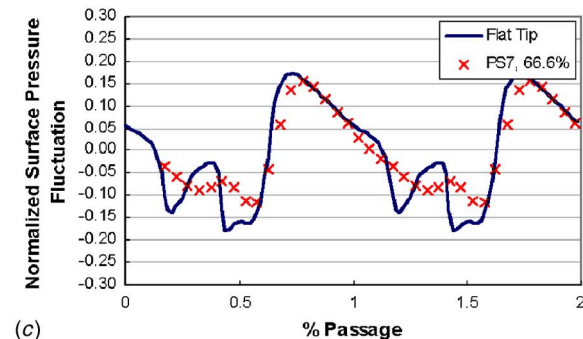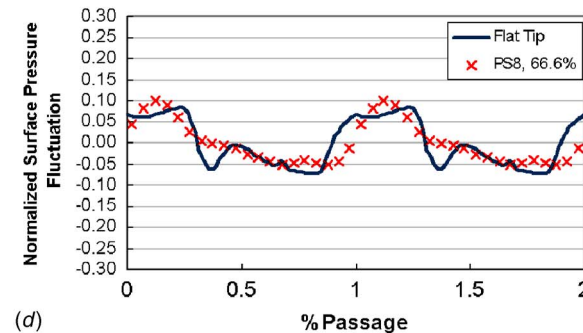
Fig. 12 Surface pressure fluctuations for the stationary shroud at (a) −7%, (b) 30.2%, (c) 60.4%, and (d) 94.2% wetted distance of the rotor blade above the flat tip

four locations, the flat tip solutions show much higher amplitudes of fluctuation. The maximum and minimum locations for the flat tip solutions are nearly twice that of the recessed tip solutions. The difference in amplitudes can be easily explained through exposure to the passage unsteadiness as the recessed tip provides protection from the main passage.

To help visualize the unsteady tip trends, Fig. 16 provides instantaneous contours of both static pressure and entropy. These plots are shown over a single vane-passing period with the instantaneous position within the time-series plot of the PRT63 location for both the recessed and flat tip solution. For each plot, the upper blade is designated by B1 and the lower blade by B2 and the
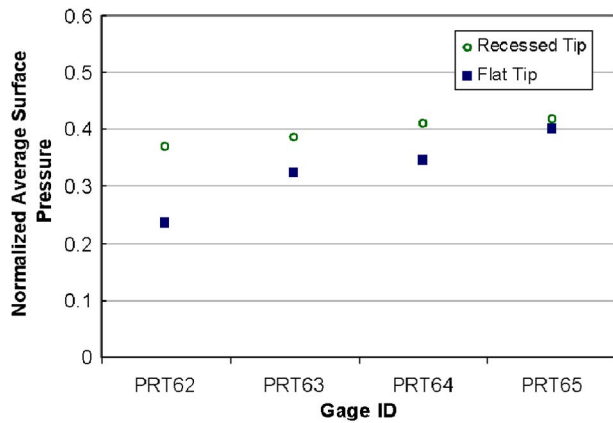
Fig. 13 Time-averaged tip comparisons of the flat and recessed tip analytical solutions

rotation of the blades is in the upward direction. Only the recessed tip passage solution is shown in Fig. 16 due to the qualitative nature of the plots. The attempt is to tie unsteady tip activity to the unsteady activity in the blade passage and only a few time points will be discussed.

There are two sources for unsteadiness from the upstream vane, the wake (VW) produced by vane losses and the shock emanating from the vane suction surface (designated VS). For $t/T=0.0$, the static pressure contours show the VS2 shock from the vane suction surface on the suction side leading edge of B2 and reflecting off the B1 pressure surface. From the entropy contours, the VW3 wake has been cut by B1 and is bending around B2. The surface pressures on both B1 tip geometries are slightly oscillating. The static pressure on the tip of B2 is rapidly increasing from its instantaneous minimum to its maximum. At time $t/T=0.1$, the VS2 shock has now moved to the pressure surface of B2 and is continuing to reflect off the B1 pressure surface. The VW2 wake is also starting to bend around B1 while the VW3 wake is ingested. The B2 tip gage is now at its maximum instanteous pressure with the B1 gage moving through small pressure oscillations on its way to its instantaneous minimum pressure. At time $t/T=0.4$, the backside of the VS1 shock (low static pressure region) is at the leading edge of B1 with the VS2 shock now reflecting off the B2 pressure surface. VW1 has now entered into the solution and VW2 continues to bend around B1. The tip surface pressures on B1 are now at their minimum while the B2 surface pressures are near average. The final time of note is $t/T=0.7$ where the VS1 shock is reflecting off another blade and hitting the B1 pressure surface. The VW2 wake has been cut by B1 and starting down the passage between B1 and B2. The PRT65 gage location on B2

Fig. 14 Relative Mach numbers entering the recessed and flat tip regions on a single tangential plane

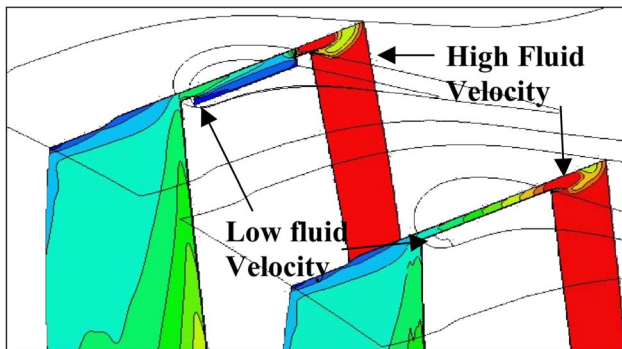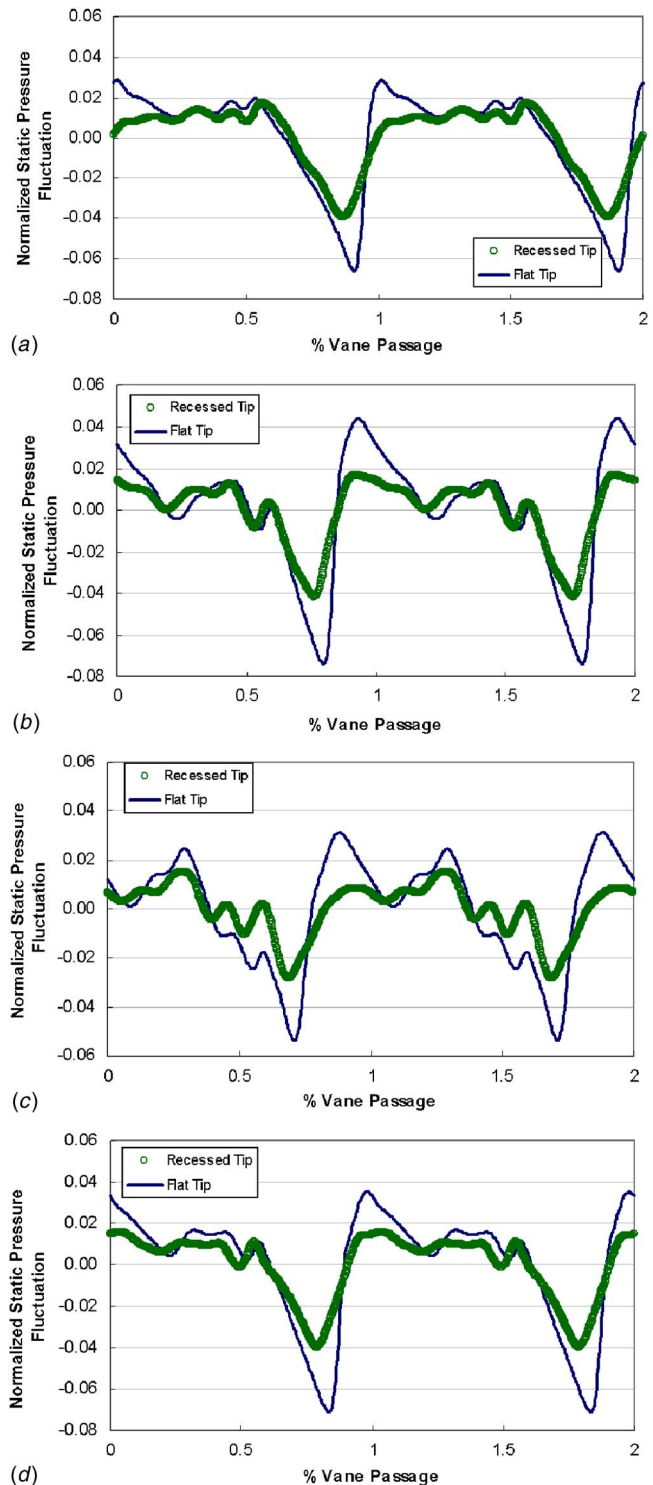**Fig. 15 Surface pressure fluctuation comparisons for the flat and recessed tip at (*a*) PRT62, (*b*) PRT63, (*c*) PRT64, and (*d*) PRT65**

shows some small oscillations and B1 is coming off its peak.

From analyzing these instantaneous solutions, it becomes apparent that the major peak and trough of unsteady pressure is directly related to the passing of the upstream vane shock across the rotating blade. When the shock hits the suction surface of the blade, the instantaneous pressure is near its minimum and as the shock moves across the leading edge to the pressure surface, the tip surface pressure increases into its maximum and drops off after
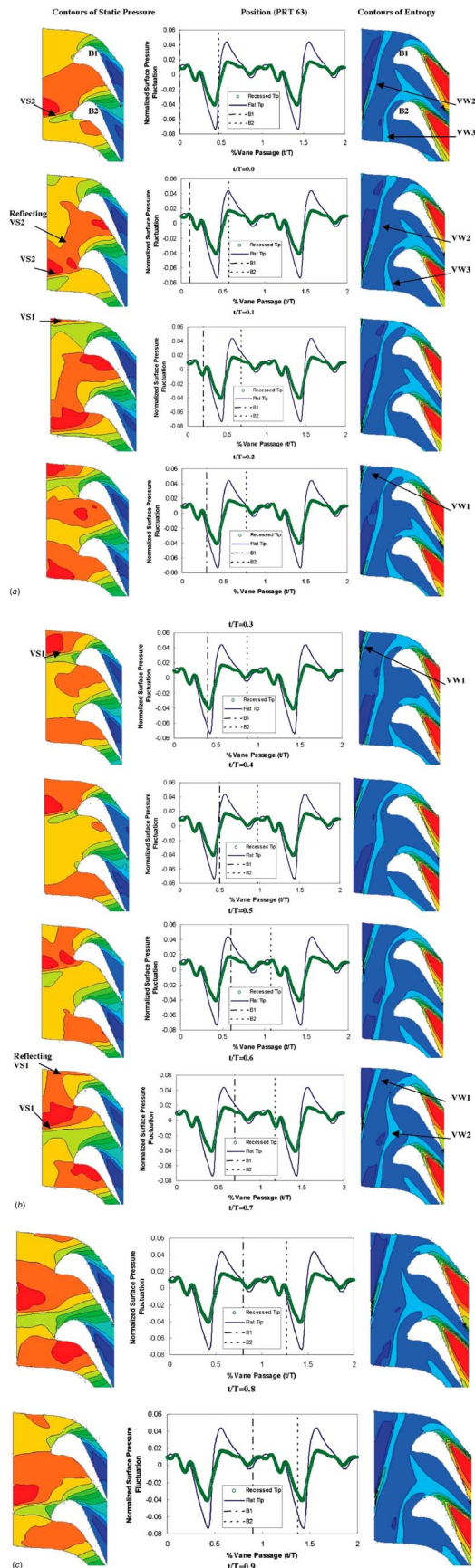
Fig. 16 Instantaneous contours of static pressure and entropy at 98% span in the recessed tip solution with the instantaneous position of within the recessed and Flat Tip PRT65 time-series solution
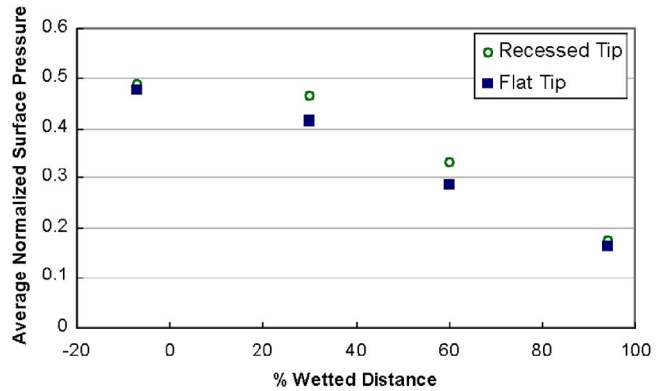
Fig. 17 Time-averaged surface pressure comparisons for the flat and recessed tip analytical solutions on the stationary shroud

the shock leaves the leading edge. The vane wakes cause oscillations in the time histories, however, their contribution to the total unsteady behavior is small compared to the upstream vane shock.

4.5 Flat and Recessed Tip Stationary Shroud Analytical Comparisons. The impact of two different tip geometries on the time-average and time-dependent static pressure on the shroud has also been examined. Similar to the blade tip region comparisons, shroud locations used for comparison were chosen to be identical to those used for the comparison to experimental data. Figure 17 provides the comparisons of the time-averaged shroud surface pressures. Ahead of the blade, at −7% wetted distance, and near the trailing edge, at 94% wetted distance, the time-averaged static pressures show very little difference between the flat and recessed tip solutions. At 30% and 60% wetted distance, the recessed solution shows an 11% and 16% increase, respectively, in the average surface pressure.

Figure 18 compares the static pressure time histories on the shroud for the flat and recessed blade tips. At each location, the time-series solutions for the flat and recessed tip show very similar trends and amplitudes with exception to the 60% wetted distance location in Fig. 18(c). Minor differences in the two solutions on the shroud are attributed to the difference in tip geometry, but overall, the tip geometry appears to have a small impact on the stationary shroud surface pressures. To add some insight into the unsteady pressure trends in Fig. 18, a single axial cut of static pressure was taken across two blades of both the recessed and flat tip in an instantaneous unsteady solution at each shroud sensor location. The instantaneous solution corresponds to $t/T=0.9$ in Fig. 16. Each set of plots for a given axial location are on the same scales.

Figure 19 presents the predicted static pressure contours for both the flat and recessed blade-tip configurations. At −7% wetted distance; the peaks of unsteady pressure are found to be in the passage between the two blades with valleys occurring as the blade passes the sensor. The small amplitudes are attributed to the sensor location being just in front of the blade and thus being influenced by the passing of the static pressure bow wave. At 30%, 60%, and 94% wetted distance; the peaks of instantaneous pressure were found to be on the pressure surface of the blade. And as the blade continues to rotate to the left, the instantaneous pressure begins to fall off. At 60% and 94%, the valley of instantaneous pressure occurs in the leakage vortex. For 60% wetted distance, the leakage vortex is still attached to the suction surface. However, at 94%, the leakage vortex is at mid passage between B1 and B2, as it is no longer attached to the blade surface. At 30% wetted distance, the leakage vortex has not formed and the valley in instantaneous pressure occurs at the suction side. Differences between the flat and recessed tip at 60% wetted distance are attributed to the leakage flows across the tip. For the flat tip solu-
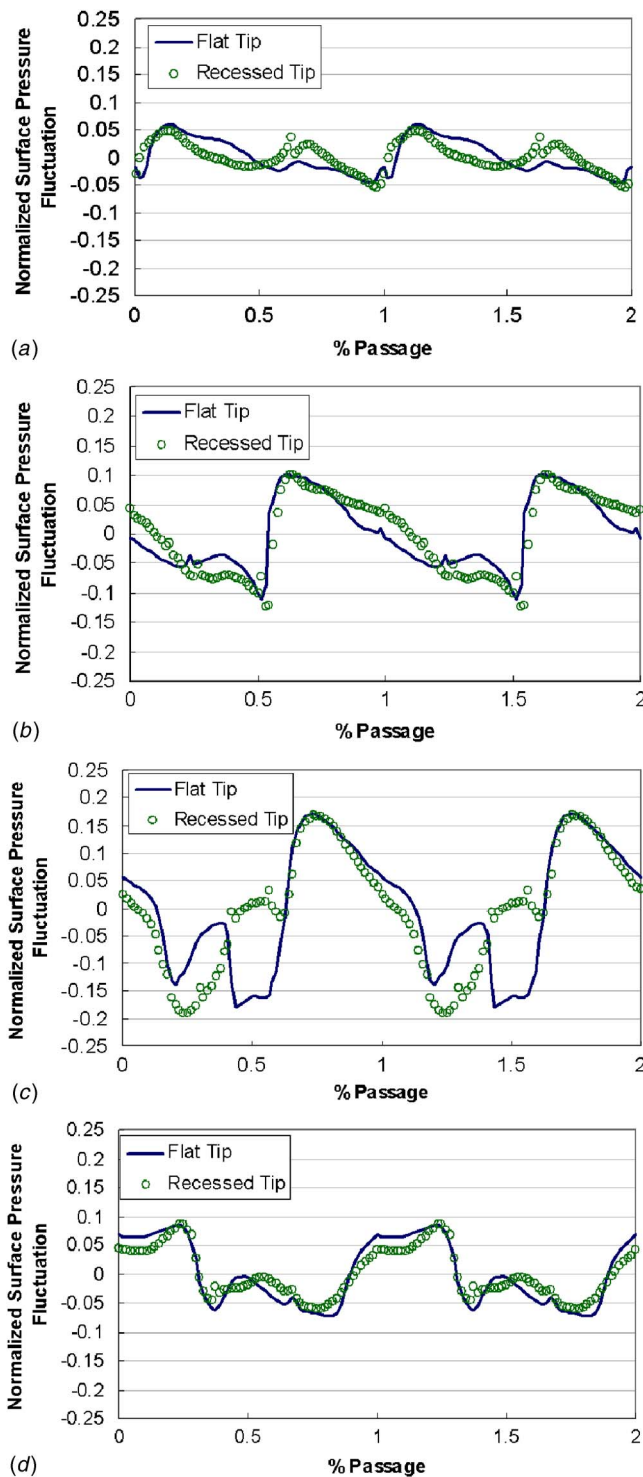
Fig. 18 Surface pressure fluctuation comparisons for the flat and recessed tip analytical solutions on the stationary shroud at (*a*) −7%, (*b*) 30.2%, (*c*) 60.4%, and (*d*) 94.2% wetted distance of the rotor blade

Fig. 19 Static pressure contours on an axial plane at (*a*) −7%, (*b*) 30%, (*c*) 60%, and (*d*) 94% wetted distance, forward looking aft for the recessed (1) and the flat (2) tip

5 Concluding Remarks

Measurements and predictions for a rotating blade in a one and a half stage turbine have been presented. These data and comparisons include the blade, blade tip, and stationary shroud from a time-accurate standpoint. The blade surface provided experimental data at 15%, 50%, and 90% span. The time-averaged comparisons show very good agreement on both the pressure and suction side of the airfoil. The only exception to this being the suction side acceleration at 90% span and 65% wetted distance. The predicted behavior was found to be weaker than the data suggests. This miss was found to be due to grid resolution issues at this location. The time-accurate comparisons for the blade surface were provided in the form of FFT (amplitude and phase) comparisons. The FFT comparisons show very good agreement with the measurements with both phase and amplitude over a majority of the blade surface. The leading edge of the blade, however, was found to have significant misses when compared with the measured data. The miss in predicted amplitude was found to be as good or better than similar published comparisons. The 15% span location showed the largest amount of unsteady surface pressure activity, especially on the suction surface near the leading edge. Just past the leading edge, unsteady pressure amplitudes, with respect to vane passing frequency, drop off rapidly. The blade tip comparisons were shown on a time-series basis with respect to the upstream vane passage. For each of the four available locations, both trends and amplitudes of the experimental measurements were predicted well by the CFD. Overall measured amplitudes were found to be less than 4% of the total inlet pressure. The last data set presented was for the stationary shroud above the rotating blade. Four different axial locations were shown from just in front

tion, the static pressure rises slightly, drops slightly and then increases across the tip gap going from the suction to the pressure surface. However, the recessed tip shows a larger rise in static pressure particularly around mid gap as the flow slows down in the recessed region. Thus, the differences on the shroud at 60% wetted distance can be attributed to the Mach numbers through the tip gap.

of the blade to the trailing edge. These time-series data sets were shown as a function of the rotor passage. Good correlation between the measured and predicted amplitudes and trends were achieved at all locations. Again, the overall agreement was found to be as good or better than similar previously published comparisons. Unsteady pressure amplitudes were found to be much larger for all of the shroud locations when compared to the blade tip locations. It is also interesting to note that the CFD predictions show higher frequency content than the measured data. This is a similar conclusion reached by Busby et al. [3].

While the blade surface computational and measurement comparisons are not new additions to the gas turbine literature, the pressure levels and histories for the blade tip and shroud regions provide a needed data set for turbine heat-transfer. These two regions offered the first look at a time-accurate code's ability to resolve the time-accurate behavior in the tip clearance region of a flat and recessed tip cavity. Analytical comparisons were also made between the flat and recessed tip blades for both the tip and stationary shroud. The tip comparisons show significant differences for both the time-averaged and time-accurate comparisons. Mechanisms for the unsteady pressure activity in the tip region were explored using the passage unsteady behavior. It was found that the major contributor to the unsteady pressure is the passing of the upstream vane while minor oscillations were due to the cutting and passing of the vane wakes. The stationary shroud analytical comparisons show very little difference between the recessed and flat tip solutions at all locations, with exception to the 60% location. This suggests that the blade tip configuration has very little impact on time-accurate behavior for the stationary shroud. Instantaneous peak pressures on the shroud were attributed to the passing of the pressure side of the blade. The lowest pressures on the shroud occurred with the passing of the blade suction surface and leakage vortex.

Overall, these data presented an excellent opportunity for comparing the accuracy of a modern time-accurate code prediction to experimental measurements for a modern high-pressure turbine. These data and comparisons provided confidence in the ability of this time-accurate CFD code to predict not only the blade passage, but also the blade tip and shroud unsteady pressures.

Acknowledgment

References

[1] Dunn, M. G., 2001, "Convective Heat-Transfer and Aerodynamics in Axial Flow Turbines," ASME Paper No. 2001-GT-0506.

[2] Venable, B. L., Delaney, R. A., Busby, J. A., Davis, R. L., Dorney, D. J., Dunn, M. G., Haldeman, C. W., and Abhari, R. S., 1998, "Influence of Vane–Blade Spacing on Transonic Turbine Stage Aerodynamics—Part I: Time-Averaged Data and Analysis," ASME Paper No. 98-GT-481.

[3] Busby, J. A., Davis, R. L., Dorney, D. J., Dunn, M. G., Haldeman, C. W., Abhari, R. S., Venable, B. L., and Delaney, R. A., 1998, "Influence of Vane-Blade Spacing on Transonic Turbine Stage Aerodynamics Part II: Time Resolved Data and Analysis," ASME Paper No. 98-GT-482.

[4] Barter, J. W., Vitt, P. H., and Chen, J. P., 2000, "Interaction Effects in a Transonic Turbine Stage," ASME Paper No. 2000-GT-0376.

[5] Keilb, J. J., "Experimental and Numerical Study of Blade Forced Response in a Full-Scale Rotating Turbine at Actual Engine Conditions," MS thesis, The Ohio State University, OSU GTL Doc. #1999_8_M6.

[6] Dunn, M. G., 1989, "Phase and Time-Resolved Measurements of Unsteady Heat-Transfer and Pressure in a Full-Stage Rotating Turbine," ASME Paper No. 89-GT-135.

[7] Metzger, D. E., Dunn, M. G., and Hah, C., 1990, "Turbine Tip and Shroud Heat-Transfer," ASME Paper No. 90-GT-333.

[8] Ameri, A. A., and Steinthorsson, E., 1996, "Analysis of Gas Turbine Tip and Shroud Heat-Transfer," ASME Paper No. 96-GT-189.

[9] Ameri, A. A., and Steinthorsson, E., 1995, "Prediction of Unshrouded Rotor Blade Tip and Shroud Heat-Transfer," ASME Paper No. 95-GT-142.

[10] Dunn, M. G., Kim, J., Cinvinskas, K. C., and Boyle, R. J., 1994, "Time-Averaged Heat-Transfer and Pressure Measurements and Comparison with Prediction for a Two-Stage Turbine," ASME J. Turbomach., **116**, pp. 14–22.

[11] Dunn, M. G., Rae, W. J., and Holt, J. L., 1984, "Measurement and Analysis of Heat Flux Data in a Turbine Stage—Part II: Discussion of Results and Comparison with Predictions," ASME J. Eng. Gas Turbines Power, **106**, pp. 234–240.

[12] Bunker, R. S., Bailey, J. C., and Ameri, A. A., 1999, "Heat-Transfer and Flow on the First Stage Blade Tip of A Power Generation Gas Turbine: Part 2–Experimental Results," Paper No. NASA TM 1999-209152.

[13] Ameri, A. A., and Bunker, R. S., 2000, "Heat-Transfer and Flow on the First Stage Blade Tip of A Power Generation Gas Turbine: Part 2-Simulation Results," ASME J. Turbomach., **122**, pp. 272–277.

[14] Green, B. R., 2004, "Time-Averaged and Time-Accurate Aerodynamics for the Recessed Tip Cavity of a Rotating High-Pressure Turbine Blade and the Stationary Outer Shroud," The Ohio State University, Columbus, OH.

[15] Dunn, M. G., Moller, J. C., and Steel, R. C., 1989, "Operating Point Verification for a Large Shock Tunnel Test Facility," Paper No. WRDC-TR-2027.

[16] Dunn, M. G., and Haldeman, C. W., 1995, "Phase-Resolved Surface Pressure and Heat-Transfer Measurements on the Blade of a Two-Stage Turbine," ASME J. Fluids Eng., **117**, pp. 653–658.

[17] Dunn, M. G., 1986, "Heat-Flux Measurements for the Rotor of a Full-Stage Turbine: Part 1–Time-Averaged Results," ASME J. Turbomach., **108**, pp. 90–97.

[18] Dunn, M. G., Bennett, W. A., Delaney, R. A., and Rao, K. V., 1992, "Investigation of Unsteady Flow Through a Transonic Turbine Stage: Data/Prediction Comparison for Time-averaged and Phase-Resolved Pressure Data," ASME J. Turbomach., **114**, pp. 91–99.

[19] Haldeman, C. W., 2003, "An Experimental Investigation of Clocking Effects on Turbine Aerodynamics Using a Modern 3D One and one-half Stage High Pressure Turbine for Code Verification and Flow Model Development, *Aeronautical and Astronautical Engineering*," Ohio State University, Columbus, OH, p. 345.

[20] Whitfield, D. L., Janus, J. M., and Simpson, L. B., 1988, "Implicit Finite Volume High Resolution Wave-Split Scheme for Solving the Unsteady Three-Dimensional Euler and Navier–Stokes Equations on Stationary or Dynamic Grids," Paper No. MSSU-EIRS-ASE-88-2.

[21] Roe, P. L., 1981, "Approximate Riemann Solvers, Parameter Vectors, and Difference Schemes," J. Comput. Phys., **43**, pp. 357–372.

[22] Osher, S., and Chakravarthy, S. R., 1984, "Very High Order Accurate TVD Schemes," ICASE Report No. 84-44.

[23] Steger, J. L., and Warming, R. F., 1981, "Flux Vector Splitting of the Inviscid Gasdynamic Equations with Application to Finite-Difference Methods," J. Comput. Phys., **40**, pp. 263–293.

[24] Shih, T. H., Liou, W. W., Shabbir, A., Yang, Z., and Zhu, J., 1995, "A New k-e Eddy Viscosity Model for High Reynolds Number Turbulent Flows," Comput. Fluids, **24**, pp. 227–237.

[25] Chen, J. P., and Barter, J. W., 1998, "Comparison of Time-Accurate Calculations for the Unsteady Interaction in a Turbomachinery Stage," AIAA Paper 98-3292.

[26] Chen, J. P., Celestina, M. L., and Adamczyk, J. J., 1994, "A New Procedure for Simulating Unsteady Flows Through Turbomachinery Blade Passages," ASME Paper No. 94-GT-151.

The Effects of a Trip Wire and Unsteadiness on a High-Speed Highly Loaded Low-Pressure Turbine Blade

M. Vera

H. P. Hodson

Whittle Laboratory,
University of Cambridge,
Cambridge, UK

R. Vazquez
ITP, Industria de Turbopropulsores,
Madrid, Spain

This paper presents the effect of a single spanwise two-dimensional wire upon the downstream position of boundary layer transition under steady and unsteady inflow conditions. The study is carried out on a high turning, high-speed, low pressure turbine (LPT) profile designed to take account of the unsteady flow conditions. The experiments were carried out in a transonic cascade wind tunnel to which a rotating bar system had been added. The range of Reynolds and Mach numbers studied includes realistic LPT engine conditions and extends up to the transonic regime. Losses are measured to quantify the influence of the roughness with and without wake passing. Time resolved measurements such as hot wire boundary layer surveys and surface unsteady pressure are used to explain the state of the boundary layer. The results suggest that the effect of roughness on boundary layer transition is a stability governed phenomena, even at high Mach numbers. The combination of the effect of the roughness elements with the inviscid Kelvin–Helmholtz instability responsible for the rolling up of the separated shear layer (Stieger, R. D., 2002, Ph.D. thesis, Cambridge University) is also examined. Wake traverses using pneumatic probes downstream of the cascade reveal that the use of roughness elements reduces the profile losses up to exit Mach numbers of 0.8. This occurs with both steady and unsteady inflow conditions. [DOI: 10.1115/1.1934446]

Introduction

In recent years, the ability of the wakes shed by an upstream row to promote transition under certain circumstances has been supplemented by selective roughening of the airfoil surface. Ramesh et al. [1] added to the effects of unsteadiness by selective roughening of the airfoil surface to decrease the profile loss of law pressure turbine (LPT) blades. Roman [2] used a roughness element to obtain a 12% greater lift with the same amount of relative loss than his datum ultra high lift profile. Therefore, roughness also provided a way of controlling losses on very highly loaded blades where large separation bubbles occur. Zhang and Hodson [3] after an extensive parametric study of the size, location, and sort of roughness gave the directions to achieve an optimum in terms of losses. All these experiments were carried out in low speed flows.

The applicability of these findings to high speed LPT blades needs justifying. The effect of roughness on high speed flows has been previously studied on flat plates. Brinich [4] showed that at high Mach numbers, the boundary layer could tolerate a bigger size of the roughness element. This conclusion was also found by Gibbins [5]. This author also showed that providing that there was no interaction with a supersonic mainstream flow, the effect of moderate, i.e., high subsonic, Mach numbers on the onset of transition was small.
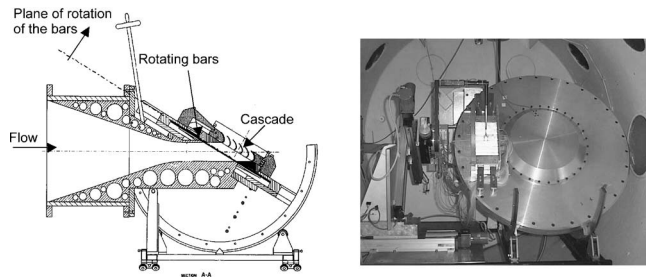
Klebanoff and Tidstrom [6] made use of stability arguments to show the mechanism by which the roughness elements induce an earlier boundary-layer transition. Their results supported the idea that the roughness hastens the downstream development of instabilities. They showed that the process of transition downstream of the wire was as if there was a wave selection process which ex-

hibited a nonlinear behavior, as one would expect from stability theory. From this theory, it is known that for a two-dimensional (2D) parallel incompressible flow, the minimum critical Reynolds number occurs for a 2D disturbance propagating in the same direction as the flow. This later statement is known as the Squires' theorem and it is a direct solution of the Orr–Sommerfeld equation for this type of flow. The latter seems to explain why the backward facing step was found to be the dominant mechanism controlling the process for 2D incompressible flows. This could also explain why three-dimensional roughness has less of an effect on transition than two-dimensional roughness elements.

The Squires' theorem no longer holds for compressible flows. Mack [7], showed that the higher amplification occurs for parallel disturbances up to approximately Mach 0.7. For higher Mach numbers, up to about Mach 3, nonparallel disturbances are more amplified. This could indicate that for this latter range of Mach numbers, a three-dimensional (3D) roughness element could be more efficient.

In the current work, the choice of the roughness element and its position have been based on low speed findings. The blade chord is about 40 mm. The roughness element used to trip the boundary layer in the current investigations was a cylindrical wire with a diameter of 60 μm. This size follows the criteria given by Zhang and Hodson [3] who indicated that the height of the roughness element should be of the order of 0.1% of the suction surface length of the airfoil to achieve an optimum in terms of losses. The wire was located in two different positions, i.e., at $60\% S_0$ or at $66\% S_0$. This also follows the criteria by Zhang and Hodson [3] who recommended placing the roughness between the blade suction peak and the separation onset location. According to the discussion presented in the paragraphs earlier, up to a Mach number about 0.7 the effect of the roughness element on the downstream position of transition is expected to be the same as in low speed flows. For higher Mach numbers, a larger 2D wire or a 3D roughness element would be necessary.

Fig. 1 Cross section (left) and rear view (right) of the high speed bar rotating rig

Table 1 CLT2 linear cascade and bar details

Chord (mm)	39.9
Axial chord (mm)	31.5
Pitch (mm)	39.1
Span (mm)	100
Design inlet flow angle (°)	48.7
Design outlet flow angle (°)	−69.2
Bar diameter (mm)	0.41
Bar passing frequency (kHz)	2400
Axial distance bars-cascade (mm)	19

In this paper, two Reynolds numbers are investigated, i.e., $Re_3 = 1.3 \times 10^5$ and $Re_3 = 2.0 \times 10^5$. For each Reynolds number the exit Mach number was varied between 0.61 and 0.83. For all the cases under consideration, the Reynolds number at the location of the wire is such that the wire will not promote transition at the location of the wire but it will affect the location of the onset of transition by moving it upstream, Gibbings [5].

Experimental Apparatus

The experiments were carried out in the transonic cascade facility at the Whittle laboratory. This is a continuous flow, closed-circuit variable density wind tunnel where the Reynolds and the Mach number can be fixed independently. Two vacuum pumps, working in parallel, are used to achieve subatmospheric pressures. A compressor is used to control the pressure ratio and thus the Mach number of the flow within the circuit. Before entering the cascade, the air passes through a honeycomb and screen in order to filter the air and to breakup any large scale structures that may exist in the flow. At the entry to the cascade, the flow is accelerated in a convergent nozzle. At the exit, it is discharged into the large exit plenum that contains the test section. The inlet freestream turbulence is 0.5%.

The presence of the wakes shed from an upstream blade row is simulated using a wake generator. The high speed bar wake generator consists of a number of cylindrical metal bars equally spaced at the outer periphery of a disk that rotates in a plane parallel to the leading edge plane of the cascade. In this way, the circumferential speed of the bars can be increased to the levels that are required in high speed cascade experiments. For the current case, the plane of rotation was located at 0.6 axial chord lengths upstream of the leading edges of the cascade in the axial direction. A cover encloses the rotating disk and bar assembly thus creating a sealed cavity containing the bars. This sealed cavity is needed to prevent the leakage that would occur if the cavity were opened to the plenum, i.e., to exit conditions. The cover has a rectangular opening aligned with the exit of the convergent nozzle over which the cascade is mounted. A cross section and a rear view of the high-speed bar rotating rig is presented in Fig. 1. A similar configuration has successfully been used in Oxford (Doorly [8]). For the current study, the bars are made of 0.41 mm diameter hypodermic tube. The bar passing frequency is 2400 Hz. This provides wakes of approximately the same strength and reduced frequency as an upstream stator, Vera et al. [9].

Static pressures upstream and downstream of the cascade are measured using 0.3 mm diameter wall pressure tappings. A conventional Pitot tube upstream of the row of bars measures the inlet total pressure. The inlet stagnation temperature is measured using a thermocouple placed within the inlet ducting upstream of the test section.

In order to know the inlet flow conditions to the cascade, the effect of the bars must be removed from the results. A calculation procedure is used to calculate mixed out conditions downstream of the bars. This calculation procedure and its validation are presented in Ref. [9]. It is based on the measured drag coefficient of the bars.

The profile used in the current test is a blade designed by ITP that is intended to meet the requirements for the removal of one stage of the LPT. This blade, CLT2, is a high lift, high turning profile designed to take account of the unsteady inflow conditions. The inlet angle is 48.7°, the exit angle is 69.2° and the lift coefficient is about 1.1. Further information is given in Table 1.

The cascade consists of six blades. The central passage of the cascade, i.e., the pressure side of one blade and the suction side of the adjacent one, was instrumented with 0.3 mm diameter static pressure tappings. Two slots were placed on the top and bottom of the cascade with movable aluminium sheets to regulate the mass flow through these slots in order to control the periodicity of the cascade.

Pitchwise traverses were performed behind the cascade to measure the profile loss. The traverse plane was placed at 0.5 axial chord lengths downstream of the trailing edge plane of the cascade in the axial direction. The traverses extended across the wakes covering two pitches of the cascade. These two pitches included the wakes of the two central blades. A fixed direction four hole Neptune probe, similar to the one used by Sieverding et al. [10], was used to measure the exit flow field. The local flow conditions were determined from the calibration curve of the probe. The Mach number, flow angle, and total pressure were used to provide the mixed-out values to calculate the profile loss coefficient. The calculation of the mixed out values of a 2D compressible wake has been presented in Ref. [11]. The KSI loss coefficient was calculated with an accuracy of ~0.1% of the exit dynamic pressure at the design condition.

Hot wire boundary layer traverses were performed over the rear part of the suction side of the CLT2 blade at 12 locations distributed between 69.2% and 99.2% S_0. At each position, the boundary layer traverses consist of 11 points exponentially distributed normal to the wall. The boundary layer traverses were performed up to a distance of 1.1 mm from the wall. The location of the wall was found with the method described by Hodson [12]. This process was performed at the operating conditions to account for the aerodynamic lifting of the probe and the small vibrations of the probe support. When the wall was found, the probe was moved 10 μm away from the wall in the perpendicular direction. This point has been taken as a reference ($Y_n = 0$ mm) for the plots presented in this paper.

The hot wire boundary layer traverses were carried out using a DANTEC 55P15 boundary layer probe with a 5 μm × 1 mm platinum-plated tungsten wire. The hot wire is operated in the constant temperature mode, using an overheat ratio of 1.8. A total of 64 ensembles were acquired at each of the eleven heights within the boundary layer. Each ensemble consists of 2048 points logged at 60 kHz. The correction of Cox [13] was used to take into account the effects of heat transfer to the blade surface.

In compressible flows, the heat transfer represented by the Nusselt number depends on the Mach number of the flow as well as on the Reynolds number so that

$$\frac{E^2}{T_w - T_0} = f(\text{Re}, M)$$
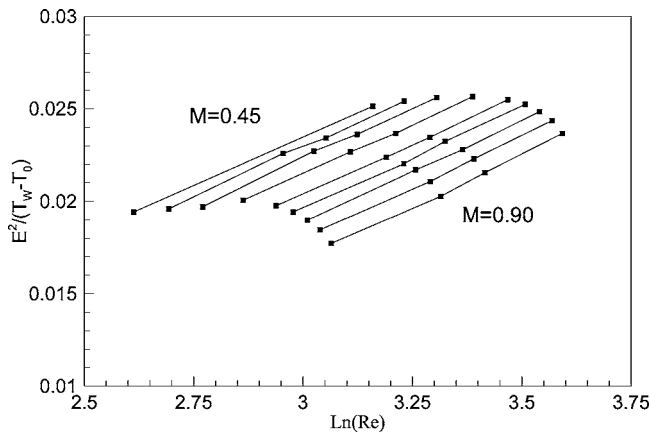
Fig. 2 Hot wire calibration map

Fig. 4 Isentropic blade surface Mach number distributions. Steady inflow. $Re_3 = 1.3 \times 10^5$.

where E is the bridge output voltage and T_W and T_0 are the temperature of the wire and the stagnation temperature of the flow respectively. Therefore, in using a hot wire in compressible flows a calibration map is required such as that shown in Fig. 2. This map presents the output of the hot wire as the Mach and Reynolds number are varied. Because the Reynolds number and the Mach number depend on static flow properties such as the density and temperature as well as the velocity of the flow, it is necessary to make assumptions in order to use the calibration map. In this case, it is assumed that the static pressure and the stagnation temperature are constant across the boundary layer. It is also noted that the wire temperature is constant. In steady, attached flows at the Mach numbers encountered here, these are reasonable assumptions. Flow unsteadiness and the curvature of the streamlines due to flow separation will compromise these assumptions to a limited extent. Therefore, it is important to highlight the fact that the character of the hot wire results is only qualitative. An overall picture of the flow field rather than quantitative values is sought.

Surface unsteady pressure measurements were carried out at midspan on the suction side of the CLT2 blade. For the surface unsteady pressure measurements, Kulite fast response transducers were utilized. The sensors, from the ultraminiature LQ-062 series (5 psid range) were flush mounted at different streamwise locations. The response of the sensors was linear. The slope measured for the calibration resulted in a sensitivity of approximately 560 Pa/V.

Results
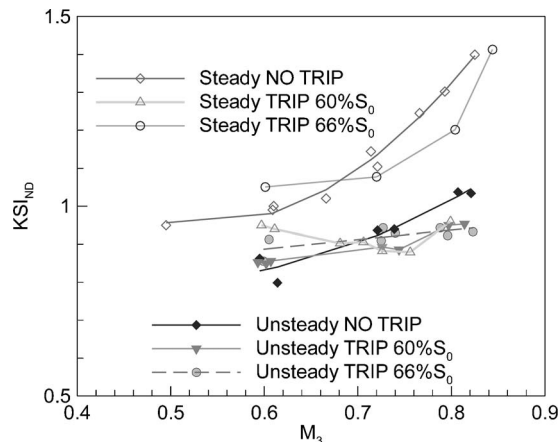
Time Mean Measurements. Figure 3 shows the normalized profile loss coefficient, KSI, against Mach number for the case of $Re_3 = 1.3 \times 10^5$. The results of the tripped boundary layer at 60% and 66% of the suction surface are shown together with the results from the smooth surface (no trip). The cases of steady and unsteady inflow conditions are presented in the same figure. The losses are normalized by the value obtained under steady inflow conditions with a smooth surface at $M_3 = 0.61$ and $Re_3 = 1.3 \times 10^5$.

Steady Inflow Conditions. Figure 3 shows that at $M_3 = 0.61$ the losses with the trip at $60\% S_0$ are 5% lower than the case of a smooth surface. On the other hand, the losses with the trip at $66\% S_0$ are 6% higher than the case of a smooth surface. Figure 4 shows the Mach number distribution for several conditions under steady inflow. For the case of $M_3 = 0.61$, the suction side separation bubble is clearly reduced in length when the trip is located at $60\% S_0$. However, it is not totally suppressed. This point plus the fact that the wire is promoting an earlier transition and thus, covering more surface with turbulent flow, means that the losses decrease by only 5%. According to Fig. 4, it seems as if the bubble is not affected when the wire is located at $66\% S_0$. Even so, in this case there is an increase in the losses with respect to the case of a smooth surface. This suggests that the roughness does not change the pressure distribution but that it is still affecting the flow, as indicated by the increase in losses.

At $M_3 = 0.74$, the 2D losses with the trip at $60\% S_0$ are about 20% lower than in the case of a smooth surface whereas the losses

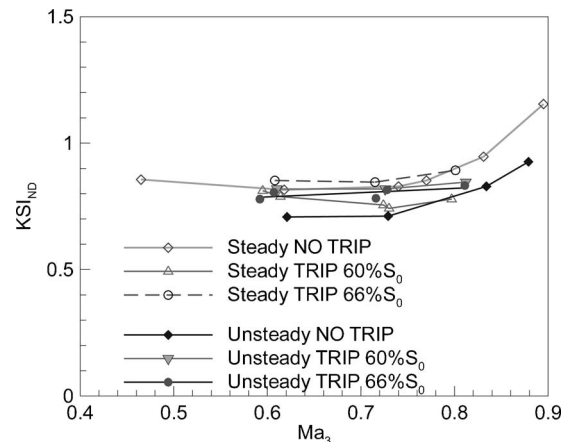**Fig. 3 Nondimensional KSI against Mach number. Steady and unsteady inflow. $Re_3 = 1.3 \times 10^5$.**

Fig. 5 Nondimensional KSI against Mach number. Steady and unsteady inflow. $Re_3 = 2.0 \times 10^5$.

with the trip at $66\%S_0$ are 2% lower than the case of a smooth surface. In Fig. 4, the same main features as in the case of $M_3 = 0.61$ can be identified. In addition, it is seen that the Mach number distribution is modified by the presence of the wire. This modification is due to the deceleration upstream and acceleration downstream of the wire. The Reynolds number of the wire, based on conditions at the wire location and the height of the wire has not changed with respect to the case of $M_3 = 0.61$. This is because the chord-based Reynolds number is unchanged and the shape of the Mach number distribution is only slightly altered. Therefore, the alteration of the pressure distribution occurs because the wire produces a bigger disturbance at higher Mach numbers due to the increased effects of compressibility on the shape of the streamlines.

With the trip at $60\%S_0$, the decrease in losses is larger at $M_3 = 0.74$ than at $M_3 = 0.61$. This is because, for a given size of bubble, the blockage is larger at higher Mach numbers. Thus, the benefit that arises from suppressing the bubble increases at the higher Mach numbers. In addition, when the Mach number is increased, the suction peak is moved aft and a stronger deceleration occurs. The point of steady separation changes only slightly when the suction peak is sent aft, therefore, the surface that can be covered by turbulent flow is approximately the same for all the Mach numbers under consideration. This factor is therefore not decisive in the comparison of losses between two different Mach numbers under steady inflow. By reducing the size of the bubble with the roughness element, a reduction of the thickness of the boundary layer at the rear of the blade can be achieved. This contributes to the reduction of losses. With the trip wire located at 66%, there is hardly any modification on the Mach number distribution, but the level of losses still changes with respect to the case of smooth surface.

In Fig. 3, the largest reduction of losses is found at $M_3 = 0.76$. The losses with the trip at $60\%S_0$ are 29% lower than the case of the smooth surface. For $M_3 = 0.8$ there is still a reduction in losses with respect to the case of a smooth surface. Nevertheless, it is seen that the trend of the losses has changed and the losses rise after having reached a minimum at $M_3 = 0.76$. The Mach number distributions for the case of $M_3 = 0.83$ are shown in Fig. 4. Mach 1 is reached at the location of the wire. This probably produces a decrease in the efficiency of the wire, as seen by Gibbins [5]. This lower efficiency of the wire could be due to an increase of the critical Reynolds number producing the amplification of instabilities as seen by Mack [7]. The reason why there is a minimum of loss around $M_3 = 0.76$, will be explained when considering the time resolved measurements.

Figure 5 shows the normalized profile loss coefficient against Mach number for the case of $Re_3 = 2.0 \times 10^5$. The losses are again normalized by the value obtained under steady inflow conditions with a smooth surface at $M_3 = 0.61$ and $Re_3 = 1.3 \times 10^5$. When increasing the Reynolds number, the losses decrease because a smaller separation bubble is found (the Mach number distributions for $Re_3 = 2.0 \times 10^5$ are not shown here). Therefore, the values of losses in Fig. 5 are lower than those at lower Reynolds number. The differences in the size of the bubble for different Mach numbers are also smaller. Thus, there will be less benefit from the suppression of the bubble and the losses will vary less with Mach number. In addition, the Reynolds number at the location of the trip has increased, which means that transition will be promoted earlier, thereby covering more surface with turbulent flow. The former point results in a flatter trend with Mach number in comparison with the lower Reynolds number case whereas the latter results in a tendency toward higher losses, resulting in less benefit in comparison with the case of the lower Reynolds number.

The earlier trends are seen in Fig. 5. When increasing the Reynolds number, and therefore reducing the size of the separation bubble, there is less opportunity for the roughness to produce a benefit. For the case of the trip element at $60\%S_0$, there is approximately a 10% reduction in losses at $M_3 = 0.74$. The case of

trip at $66\%S_0$ shows higher losses in comparison to the case of smooth surface up to $M_3 = 0.8$. The two curves cross at this point and, given the tendency of the curves, it seems as if a benefit from the roughness could be obtained for Mach numbers higher than 0.8. The suppression/reduction of the bigger separation bubble occurring at higher Mach numbers and, consequently, the reduction of the severity of reattachment are the factors contributing to this benefit.

Unsteady Inflow. In Fig. 3, the losses under unsteady inflow conditions are also presented. The first striking feature is that the curve for unsteady inflow and smooth surface crosses the curve for steady inflow and roughness at $60\%S_0$. Therefore, there is a certain condition at which the permanent reduction of the size of the bubble and associated losses that are caused by the roughness equals the loss reduction due to the periodic suppression of the bubble by the upstream wakes. At this point, it is useful to remind the reader that the reduced frequency decreases when the Mach number is increased and, hence, the separation bubble has more time to re-establish between the wake induced paths. If the reduced frequency had been kept constant, the crossing of these two curves would have probably occurred at higher Mach numbers (if no other effect was considered, i.e., shock waves). For incompressible flows, the reduced frequency has been proven to be of minor importance when using unsteadiness and roughness (Zhang and Hodson [3]). However, for high speed flows, the higher blockage from the bubble implies that any increase in height of the separated region could be detrimental for the losses.

According to Fig. 3, for the current size of the wire, 60 μm there is no superposition of the two effects roughness and unsteadiness. If both effects were additive, the fact that the curves of steady flow and roughness at $60\%S_0$ and the one of unsteady inflow and roughness at $60\%S_0$ cross at $M_3 = 0.72$ would imply no benefit coming from the unsteadiness. Since at this crossing point there is a benefit of 16% when comparing the curve of unsteady inflow without roughness with the curve of steady inflow without roughness, there is no superposition of effects. On the other hand, it seems that roughness and unsteadiness interact with each other in such a way that they reduce their mutual effectiveness under certain circumstances.
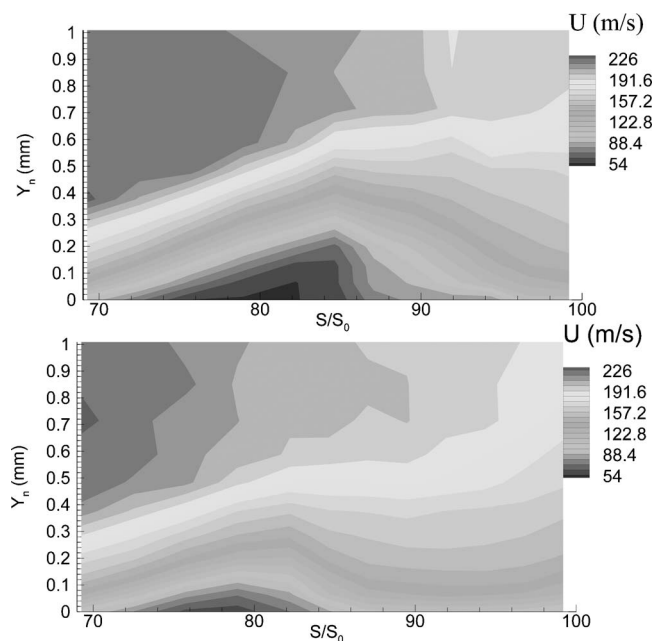
Fig. 6 Contours of ensemble averaged velocity on smooth surface (top) and with the trip at $60\%S_0$ (bottom). Steady inflow. $M_3 = 0.61$, $Re_3 = 1.3 \times 10^5$.
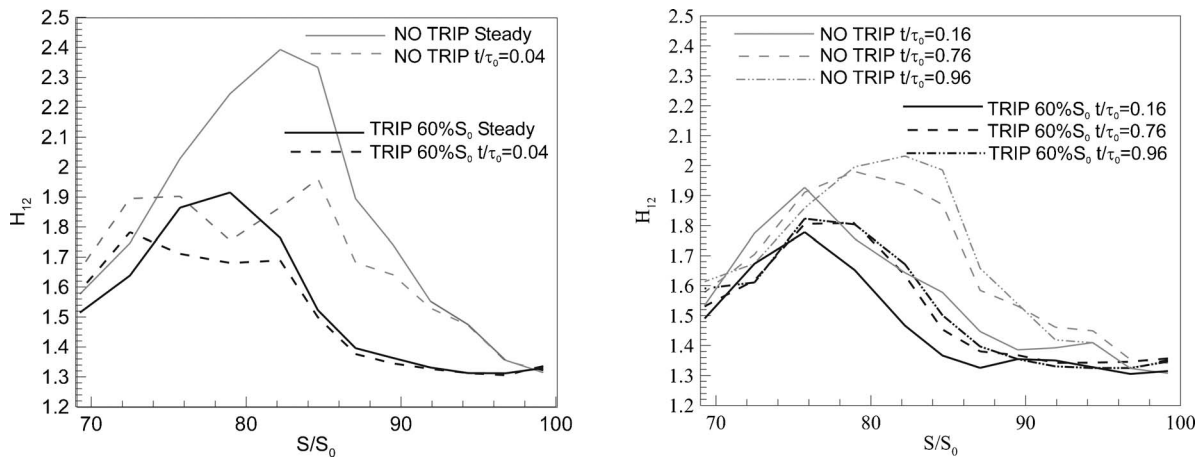
Fig. 7 Shape factor at different snapshots for the cases of a smooth surface and trip at 60%S_0. $M_3=0.61$, $Re_3=1.3 \times 10^5$. $f_r=0.48$.

In contrast to the case of steady inflow, the contribution of the roughness is similar for both positions of the roughness element (60% and 66%S_0) and at the same time, their level is similar to the case of smooth surface and unsteady inflow. This is because roughness and unsteadiness complement each other in suppressing the bubble. A benefit from the roughness elements is obtained only for the range of higher Mach numbers, which is where the bubble had not been efficiently suppressed with the unsteadiness alone. Another feature worth mentioning from Fig. 3 is that the presence of both roughness and unsteadiness does not increase the losses in comparison with the case of unsteady inflow and smooth surface.

Figure 5 shows the losses for the case of $Re_3=2.0 \times 10^5$ for unsteady inflow conditions as well as for the steady conditions. At this Reynolds number, the curve that represents the losses for the cases of steady inflow with roughness crosses the curve for the case of unsteady inflow with a smooth surface at higher Mach numbers ($Ma_3 \sim 0.8$) than for the case of $Re_3=1.3 \times 10^5$. This suggests that at this Reynolds number, the unsteadiness is better at reducing the losses than the roughness. In the range of Mach numbers between 0.61 and 0.74, the suction side separation bubble had been effectively suppressed by the unsteadiness. Therefore, the presence of a wire that trips the boundary layer does not imply any benefit but a penalty in terms of the losses. At higher Mach numbers, where this is not the case, the reverse may be true but data are currently not available to confirm this.

Time Resolved Measurements: Hot Wire Measurements. In this section, selected results from the hot wire traverses through the suction side boundary layer are presented. Further results can be found in Ref. [11].

Steady Inflow Conditions. Figure 6 shows the time mean velocity contours for the cases with and without roughness for the case of $Re_3=1.3 \times 10^5$ and $M_3=0.61$. The wire is located at 60%S_0. It is clear that the separation bubble is shorter in length and height in the case of the tripped boundary layer.

The wire produces a distortion of the flow at the position where it is located. This distortion affects locally the mean velocity profiles. In this case, the trip wire Reynolds number at 60%S_0 is 218. The wire should not produce transition at the wire location (Gibbins [5]). Hence, behind the wire the velocity profile starts to recover the shape that it would have without the presence of the wire. However, according to Klebanoff and Tidstrom [6], the signature of the wire remains within the flow, i.e., disturbances within the flow have been amplified to some degree. If the velocity profile recovers the same shape as it has without the trip, the point of steady separation does not change due to the presence of the wire. Separation is accompanied by an inflectional profile and, consequently, there is a more favorable environment for the instabilities to grow producing an earlier transition.
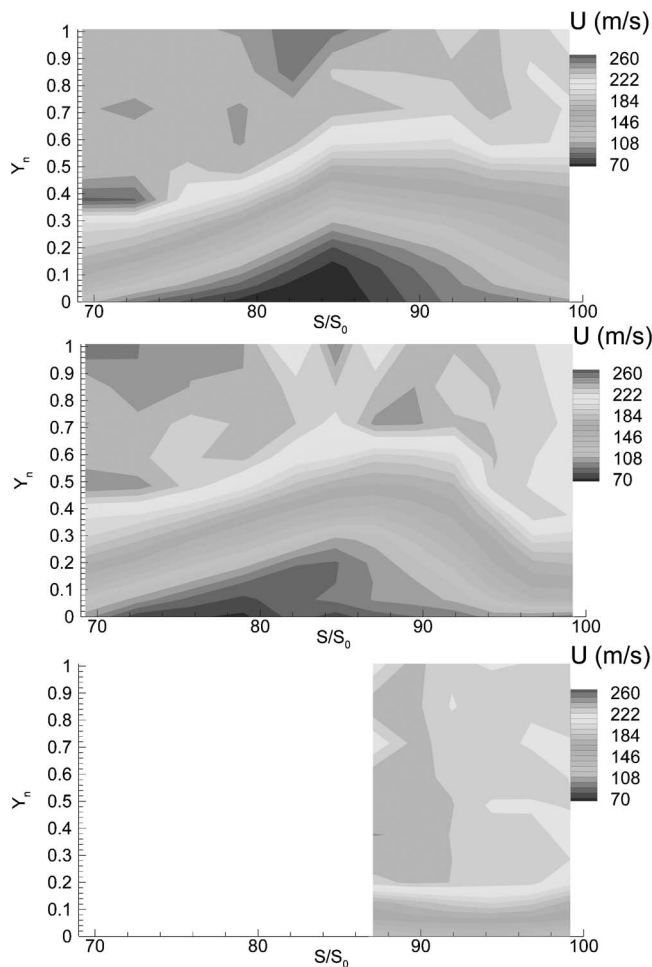
In Fig. 7 the shape factor for the case of $M_3=0.61$, $Re_3=1.3 \times 10^5$ is presented. Focusing for now on the case of the steady inflow conditions and smooth surface, it is seen that up to 85%S_0, the shape factor increases due to the separation of the flow from the blade surface. This is because when separation occurs, the displacement thickness increases steeply whereas the momentum thickness remains approximately constant.

In addition, it is seen that the shape factor for the cases of smooth surface and when the trip is at 60%S_0 present similar values up to 75%S. Downstream of this location the differences between both cases are larger because of the different geometry of the bubble. This shows that the trip does not affect the location of separation (the flow separates around 70–72%S_0). The differences occur because transition starts earlier for the case of the tripped surface. For the case of smooth surface, transition within the separated shear layer occurs around 85%S_0, promoting the entrainment of fluid into the separated flow region and assisting the reattachment of the flow back to the blade surface. Therefore, the shape factor decreases downstream of 85%S_0.

Figure 8 shows the time-mean velocity contours for the case of $Re_3=1.3 \times 10^5$ and $M_3=0.74$. Results are presented for the cases of smooth surface (top), with the wire at 66%S_0 (center), and with the wire at 60%S_0 (bottom). Even though only the rear portion of the blade was surveyed for the case of the trip at 60%S_0 it is seen that the separation bubble is more effectively suppressed for this latter case than when the wire is at 66%S_0, where just a small reduction in the size of the bubble is noticeable.

For both exit conditions ($M_3=0.74$ and $M_3=0.61$), the wire at 60%S_0 is located between the suction peak and the point of steady separation. By comparing Figs. 6 and 7 for the case of trip at 60%S_0, it is seen that the bubble has not been suppressed for the case of $M_3=0.61$ as much as for the case of $M_3=0.74$, which indicates that a bigger wire would have been needed for the case of the lower Mach number.

Unsteady Inflow Conditions. The time mean measurements showed that the use of roughness together with the unsteadiness could not be seen as the superposition of two individual effects. In this situation, if either the roughness or the unsteadiness is enough to effectively reduce the size of the separation bubble, the combination of both will probably increase the losses.
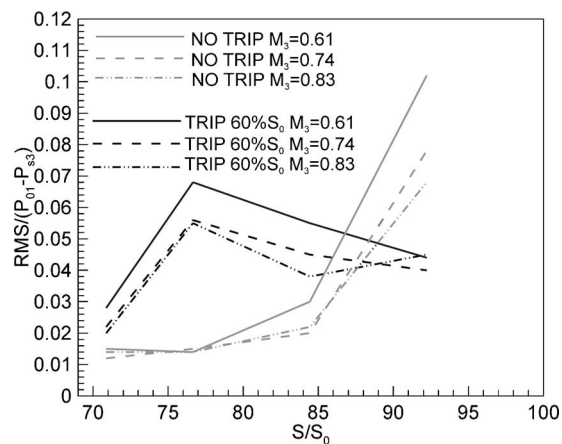
Fig. 9 rms of the unsteady pressure measurements as fractions of the exit dynamic pressure. $Re_3 = 1.3 \times 10^5$. Steady inflow.

Fig. 8 Contours of time mean velocity on smooth surface (top) and with the trip at $66\%S_0$ (center) and with the trip at $60\%S_0$ (bottom). Steady inflow. $M_3 = 0.74$, $Re_3 = 1.3 \times 10^5$.

Figure 7 shows different snapshots[1] of the shape factor for the cases of a smooth surface and when the trip is at $60\%S_0$ for the exit conditions $Re_3 = 1.3 \times 10^5$ and $M_3 = 0.61$. For clarity, the results are divided between two figures. At $t/\tau_0 = 0.04$, the wake is around $76\%S_0$, and the cases of smooth surface and when the trip is at $60\%S_0$ present similar values of shape factor upstream of $80\%S_0$ showing that the wake is having approximately the same influence for the smooth and the tripped surface along the fore part of the bubble. Downstream of $80\%S_0$, the differences between the cases of rough and tripped surface persist because this part of the bubble has not been affected by the wake yet. At $t/\tau_0 = 0.16$ the height of the bubble reaches its minimum during the wake passing period for the case of the smooth surface.

At $t/\tau_0 = 0.76$, the separation bubble for the case of the trip is almost re-established after the passing of the wake whereas the larger separation bubble for the case of a smooth surface is still re-establishing. At $t/\tau_0 = 0.96$, this re-establishing separation bubble reaches its maximum size during the wake passing period. This maximum size is smaller than for the case of steady inflow which is shown in the upper figure. This latter point and the fact that the sizes of the separation bubbles under unsteady inflow for the cases of a smooth surface and for the case of the trip at $60\%S_0$ are of more similar size during longer fraction of the wake passing period produces the similarity of losses when the wakes are

---

[1]For simplicity, it is considered that $t/\tau_0 = 0$ is when the center of the wake is at $70\%S_0$.

present.

The case of $Re_3 = 1.3 \times 10^5$ and $M_3 = 0.74$ is not shown for the sake of brevity. In this case also, even though the reduced frequency is lower, the separation bubble does not recover the size that it had under steady inflow. The lower reduced frequency contributes to the smaller differences between the cases of a smooth surface and with a tripped surface. In addition, the case of the trip at $60\%S_0$ was identified as the optimum in terms of losses for the case of steady inflow conditions. In the presence of wakes, the benefit of this case (trip at 60%) in comparison with the case of unsteady inflow and smooth surface is only a 5% reduction in loss. This benefit is probably due to the reduction of the size of the separation bubble between the wakes. At Mach 0.83, the effects of both roughness and unsteadiness contribute to a further reduction of the losses in comparison to either effect alone. This confirms that for the case of steady conditions and tripped surface, the increase of losses after the minimum at $M_3 = 0.76$ when the Mach number increases was because the size of the bubble was not reduced enough and there was still room for improvement in terms of the losses.

Time Resolved Measurements: Unsteady Pressures.

Steady Inflow Conditions. According to Johnson [14] the unsteady pressure field results in the velocity fluctuations near the wall that at the end control the onset and evolution of transition. Therefore, the root-mean-square (rms) of the unsteady pressure traces could be indicative of the state of the boundary layer. In Fig. 9, the rms of the unsteady pressure is shown for different streamwise locations. This value is presented as a fraction of the exit dynamic pressure. The point of maximum fluctuations is approximately coincident with the point of midtransition. When the wire is at $60\%S_0$, the maximum of rms moves upstream in comparison with the cases of smooth surface.

The cases of smooth surface and wire at $60\%S_0$ present the same tendencies and the same level of rms for the three exit Mach numbers shown in Fig. 9. Nevertheless, the case of trip at $60\%S_0$ presents a reduction in loss of up to 21% at $M_3 = 0.74$ in comparison to the case of smooth surface, whereas at $M_3 = 0.61$ the reduction of losses is only about 5%. These values indicate that in the case of steady inflow, the contribution of the transitional state of the boundary layer to the loss is of the same order for the three different Mach numbers. Therefore, the differences of losses seen in Fig. 3 are mainly due to the effect of the reduction of the separation bubble being more beneficial at higher Mach numbers.

Unsteady Inflow Conditions. Stieger [15] measured the pressure fluctuations underneath a laminar separated boundary layer dis-
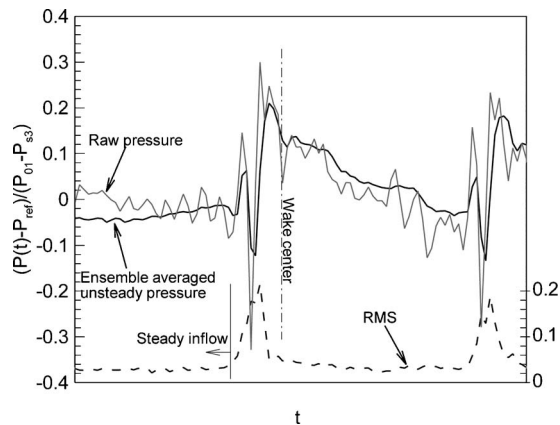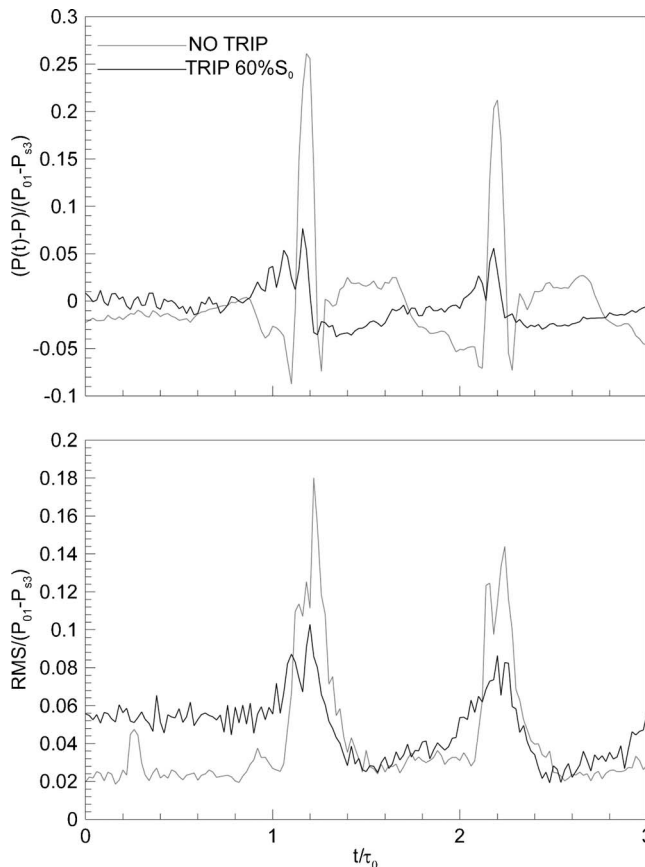
Fig. 10 Ensemble averaged unsteady pressure, raw pressure and rms as fractions of the exit dynamic pressure. $M_3=0.61$, $Re_3=1.3\times10^5$. Streamwise location 85% S_0. Unsteady inflow, $f_r=0.48$.

Fig. 11 Unsteady ensemble averaged pressure (top) and rms as a fraction of exit dynamic pressure (bottom) for the case of smooth surface and trip at 60% S_0. $M_3=0.74$, $Re_3=1.3\times10^5$. Streamwise location 85% S_0. Unsteady inflow, $f_r=0.40$.

turbed by wakes. The measurements showed large-coherent pressure fluctuations underneath the wake path. He argued that the coherent structures responsible for the large amplitude pressure fluctuations were rollup vortices created as a consequence of the wake passing over an inflexional profile. This rolling up of the separated shear layer occurred by the Kelvin–Helmholtz mechanism. It needs to be determined whether these structures are also present in high speed flows.

Figure 10 shows the ensemble averaged unsteady pressure and the raw data as a fraction of the exit dynamic pressure at 85% S_0 for the case of $M_3=0.61$ and $Re_3=1.3\times10^5$. In this particular experiment some of the bars were removed (keeping the same bar pitch) so that the steady and unsteady flows could be studied in the same experiment. At this location, the flow is separated under steady inflow conditions (see Fig. 4). The position of the wake is indicated in the figure. Large-coherent pressure fluctuations are present at the current exit Mach number. These are believed to be due to the Kelvin–Helmholtz rollup vortices observed by Stieger [15]. The associated rms as a fraction of the exit dynamic pressure is also presented at the bottom of the figure. The maximum rms occurs underneath the rollup vortices and starts to decay after the passing of the wake. According to Stieger (private communication), the size and position of the vortices varied. This point explains the maximum of rms being underneath the pressure fluctuations. It is worth mentioning that in the raw data presented in Fig. 10, the pressure fluctuations were always larger than the ensemble averaged. This could indicate that what produces the reduction of the peak-to-peak amplitude of the ensemble averaged data in comparison with the raw data is the shifting in time. Thus the real fluctuations are larger than indicated by the ensemble averaged pressures. Stieger [15] showed that the formation and decay of the rollup vortices produced the high levels of turbulent kinetic energy production. In fact, Fig. 10 presents the arrival of the wakes after a period of steadiness. The interaction of the first wake with the bubble existing under steady inflow is stronger than the interaction with a re-establishing bubble. This is because the former bubble is thicker. It is worth mentioning that for the first wake arriving, the raw data shows a peak-to-peak pressure fluctuation of 63% of the dynamic pressure. For subsequent wakes, this value is about 50% of the dynamic pressure.

Figure 10 represents a streamwise location where the flow is separated under steady inflow conditions. As the separation bubble re-establishes, the pressure will tend to decrease owing to the increasing blockage of the bubble. Figure 10 shows that once the effect of the wake has passed, the pressure decreases until the next wake arrives.

Zhang and Hodson [16] have shown that for the roughness

configuration which produces an optimum in terms of the loss, fewer, if any, rollup vortices are produced by each wake passing in comparison with the case of a smooth surface. This leads to a loss reduction. In the current case the amplitude of the rollup vortices is also reduced when using the trip at 60% S_0.

Figure 11 shows the ensemble averaged pressures and rms at the streamwise location of 85% S_0 for the cases of a smooth surface and roughness at 60% S_0. The conditions are $Re_3=1.3\times10^5$ and $M_3=0.74$. It is seen that the pressure fluctuations are reduced and consequently so is the rms underneath them. On the other hand, the rms between the wakes increases. This could indicate that transition is moved further upstream between the wakes due to the effect of the roughness. Therefore, the benefit of decreasing the amplitude of the pressure fluctuations seems to be balanced by the effect of covering more surface with turbulent flow between the wakes. The tradeoff between these two factors determines the final losses. For higher Mach numbers, $M_3=0.83$, a further benefit in terms of losses is possible when considering unsteadiness and roughness together.

Conclusions

The effect of a wire tripping the suction side boundary layer of the CLT2 profile has been presented in comparison with the case of a smooth surface. At low Reynolds numbers ($Re_3\sim1.3\times10^5$) and under steady inflow, the suppression of the separation bubble and, consequently, the reduction of the blockage seem to be the dominant factors in terms of losses. In contrast, under unsteady inflow the difference in the size of the separation bubble present

with and without trip is not as big as the difference existing under steady inflow. This is because underneath the wake, the size of the separation bubble is reduced and after the passing of the wake, the separation bubble does not recover the size it would have under steady inflow. Under these circumstances, the turbulent wetted area becomes the dominant factor in terms of the losses.

For the case of $Re_3 = 1.3 \times 10^5$, an optimum in terms of losses was found at about $M_3 = 0.75$ for steady inflow conditions. As was seen in the Mach number distribution for the case of the optimum conditions, the flow still separated from the blade surface. Therefore, the losses represent a balance of the positive effect of suppressing the blockage and the negative effect of the increased turbulent wetted area. For higher Mach numbers, a larger roughness element would have been more beneficial in terms of losses. In addition to the above, the presence of the rollup vortices for typical LPT engine conditions has been confirmed. Peak to peak variations in surface pressure of up to 63% of the exit dynamic pressure have been recorded.

The results presented in this paper in addition to the work from Ramesh et al. [1] and Zhang and Hodson [16] in low speed flows have demonstrated the benefits of controlling the suction side boundary layer by means of a selective roughening of the surface. These results suggest that the optimum surface finish of LPT blades might not be aerodynamically smooth.

Acknowledgment

Nomenclature

$$
\begin{aligned}
C &= \text{chord} \\
E &= \text{voltage} \\
f &= \text{bar passing frequency} \\
f_r &= \text{reduced frequency} = f(CV_2) \\
H_{12} &= \text{shape factor} \\
\text{KSI} &= \text{energy loss coefficient} = T_{s3}T_{3,is}/T_{01}T_{s3} \\
M &= \text{Mach number} \\
P &= \text{pressure} \\
\text{psid} &= \text{differential psi} \\
\text{Re} &= \text{Reynolds number (based on chord)} \\
S_0 &= \text{suction surface length} \\
t &= \text{time} \\
T &= \text{temperature} \\
U, V &= \text{velocity} \\
Y_n &= \text{coordinate normal to the wall, mm} \\
d^* &= \text{displacement thickness} \\
\theta &= \text{momentum thickness} \\
\rho &= \text{density} \\
\tau_0 &= \text{wake passing period}
\end{aligned}
$$

Subscripts

$$
\begin{aligned}
0 &= \text{stagnation} \\
1 &= \text{inlet conditions to the cascade} \\
2 &= \text{exit conditions from the cascade} \\
3 &= \text{mixed-out conditions} \\
\text{ax} &= \text{related to the axial direction} \\
e &= \text{related to the freestream} \\
\text{is} &= \text{isentropic} \\
\text{ND} &= \text{nondimensional} \\
s &= \text{static} \\
w &= \text{related to the hot wire} \\
\diamond &= \text{ensemble averaged}
\end{aligned}
$$

References

[1] Ramesh, O. N., Hodson, H. P., and Harvey, N. W., 2001, "Separation Control in Ultra-High Lift Airfoils by Unsteadiness and Surface Roughness," 15th International Symposium on Air Breathing Engines, Bangalore, India, Sept.

[2] Roman, K. M., 2002, "The Effect of Selective Roughness and Wake Unsteadiness on the Performance of Low Pressure Turbine Blades," M.Phil. thesis, Cambridge University.

[3] Zhang, X. F., and Hodson, H. P., 2003, "Parametric Study of Surface Roughness and Wake Unsteadiness on a Flat Plate with Large Pressure Gradient," 10th ISUAAAT Durham NC, Sep 7–11.

[4] Brinich, P. F., 1954, "Boundary Layer Transition at Mach 3.12 with and without Single Roughness Element," NACA TN 3267.

[5] Gibbings, J. C., 1959, "On Boundary-Layer Transition Wires," C.P.No. 462, A.R.C. Technical Report, Department of Fluid Mechanics, University of Liverpool.

[6] Klebanoff, P. S., and Tidstrom, K. D., 1972, "Mechanism by Which a Two-Dimensional Roughness Element Induces Boundary-Layer Transition," Phys. Fluids, **15**(7), pp. 1173–1188.

[7] Mack, 1969, "Boundary Layer Stability Theory," Document 900-277, Rev. A, Jet Propulsion Lab., Pasadena, California.

[8] Doorly, D. J., 1984, "A Study of the Effect of Wake Passing on Turbine Blades," Ph.D. thesis, Oxford University.

[9] Vera, M., Hodson, H. P., and Vazquez, R., 2003, "The Effect of Mach Number on LP Turbine Wake-Blade Interaction," 10th ISUAAAT Durham NC, Sep 7–11.

[10] Sieverding, C., and Maretto, L., 1974, "Design and Calibration of Four Probes for Using in the Transonic Cascade Testing," von Karman Institute, Tech. Note 100.

[11] Vera Morales, M., 2004, "The Effect of Compressibility on Unsteady Boundary Layers in High Lift Low Pressure Turbines," Ph.D. thesis, Cambridge University.

[12] Hodson, H. P., 1984, "Measurements of Wake-Generated Unsteadiness in the Rotor Passages of Axial Flow Turbines," ASME Paper 84-GT-189.

[13] Cox, R. N., 1957, "Wall Neighborhood Measurements in Turbulent Boundary Layers Using Hot-Wire Anemometer," A.R.C. Report 19101, February.

[14] Johnson, M. W., 1993, "A Bypass Transition Model for Boundary Layers," ASME Paper 93-GT-90.

[15] Stieger, R. D., 2002, "The Effects of Wakes on Separating Boundary Layers in Low Pressure Turbines," Ph.D. thesis, Cambridge University.

[16] Zhang, X. F., and Hodson, H. P., 2004, "The Combined Effects of Surface Trips and Unsteady Wakes on the Boundary Layer Development of an Ultra-High-Lift LP Turbine Blade," ASME Paper GT2004-53081.

Pump Performance Improvement by Restraining Back Flow in Screw-Type Centrifugal Pump

Yasushi Tatebayashi
e-mail: tate@mse.kyutech.ac.jp

Kazuhiro Tanaka
e-mail: kazuhiro@mse.kyutech.ac.jp
Department of Mechanical Information, Science
and Technology,
Kyushu Institute of Technology,
680-4 Kawazu, Iizuka-City,
Fukuoka 820-8502, Japan

Toshio Kobayashi
e-mail: kobaya@jari.or.jp
Japan Automobile Research Institute,
1-1-30 Shibadaimon Minato-ku,
Tokyo 105-0012, Japan

The authors have been investigating the various characteristics of screw-type centrifugal pumps, such as pressure fluctuations in impellers, flow patterns in volute casings, and pump performance in air-water two-phase flow conditions. During these investigations, numerical results of our investigations made it clear that three back flow regions existed in this type of pump. Among these, the back flow from the volute casing toward the impeller outlet was the most influential on the pump performance. Thus the most important factor to achieve higher pump performance was to reduce the influence of this back flow. One simple method was proposed to obtain the restraint of back flow and so as to improve the pump performance. This method was to set up a ringlike wall at the suction cover casing between the impeller outlet and the volute casing. Its effects on the flow pattern and the pump performance have been discussed and clarified to compare the calculated results with experimental results done under two conditions, namely, one with and one without this ring-type wall. The influence of wall's height on the pump head was investigated by numerical simulations. In addition, the difference due to the wall's effect was clarified to compare its effects on two kinds of volute casing. From the results obtained it can be said that restraining the back flow of such pumps was very important to achieve higher pump performance. Furthermore, another method was suggested to restrain back flow effectively. This method was to attach a wall at the trailing edge of impeller. This method was very useful for avoiding the congestion of solids because this wall was smaller than that used in the first method. The influence of these factors on the pump performance was also discussed by comparing simulated calculations with actual experiments. [DOI: 10.1115/1.2019217]

Introduction

Phenomena such as back flow and secondary flow in turbomachinery are main factors determining pump performance and rate of deterioration. Various trials have been investigated and done in order to improve unstable performance due to positive slope and undesirable flow pattern such as the back flow at the inlet of back shrouds in blowers. Ishida et al. [1] protected the back flow at a blower inlet from the circulation flow coming from impeller outlets at front shroud. On the other hand, the mixed flow pumps generally have a positive slope at low flow rates in H-Q performance. Kurokawa et al. [2,3] ascertained that this phenomenon was derived from a swirl at the impeller inlet. A groove, called a "J-GROOVE," was attached at the pump casing near the shroud, so as to improve the characteristics of this positive slope. However, as for the screw-type centrifugal pump, improvements have not yet been carried out in the pump performance or in its flow patterns.

A screw-type centrifugal pump (shown in Fig. 1) has superior performance that works against the blockage of solids because it has one three-dimensional spiral blade added to a conical hub cone and has a wide flow passage. This type of pump has been used widely, for instance in such purposes as the drainage of rainwater, slurry and mud in sewage control systems. As the impeller's profile is very complex, the most effective design method has not yet been established in this pump.

The authors have been investigating the characteristics of the screw-type centrifugal pump by means of numerical simulations [4] and experiments. When comparing the numerical results with

the experimental results, not only calculations for the flow pattern in the volute casing [5] but also those for the pressure fluctuation occurring in the impeller [6] agreed well. Moreover, numerical simulations done to take into consideration both disk friction and the mechanical loss could predict the pump performance precisely [7], and were compared with the experimental results. Detailed numerical investigations on flow patterns clarified that the screw-type impeller has the three back flow regions [6]. The first exists at the impeller inlet and it is generated by the relative difference between the impeller inlet angle and inflow velocity. The second exists inside the impeller flow passage because of Coriolis force. The last is the back flow from the volute casing toward the impeller outlet, which is the most influential on the amount of pump performance deterioration. As for this back flow, Kim et al. [8] reported that the bubble belt was generated at between the volute casing and the impeller outlet under the air-water two-phase flow situation and that pressure in the volute casing arose due to this belt. From these findings it was concluded that this back flow region was very influential on the pump performance. However, the details of its effect have not yet been clarified. Besides, an alternative method has actually been necessary, because controlling this back flow by this air belt is very difficult from the viewpoint of the positive suppression methods.

In this paper a method of restraining this back flow and its effect were investigated. In order to restrain this third type of back flow from the volute casing toward the impeller outlet, one simple method was proposed. This method involved placing a wall-like ring at the inlet the volute casing. First, its effects on flow patterns and the pump performance were examined by means of numerical simulations. The influence of the wall's height on the pump head was also investigated by numerical simulations. Furthermore, the matching of the wall with an optimum volute casing configuration was investigated by using two kinds of volute casing. Second, another method was proposed which considered how to avoid the
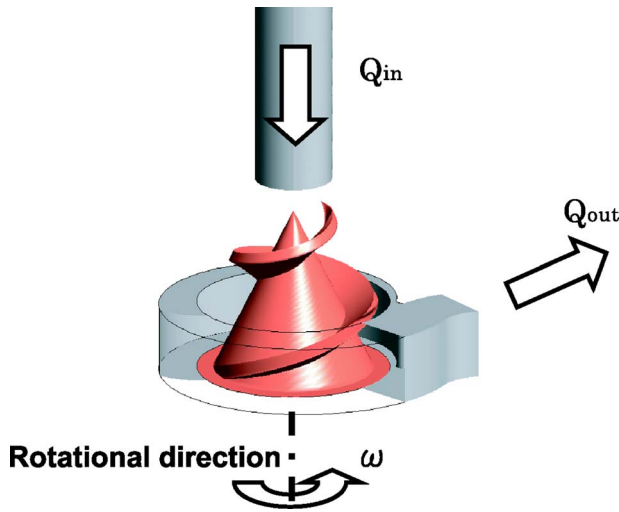
Fig. 1 Schematic configuration of a screw-type centrifugal pump

blockage of solids, because a ring-type wall has this problem with solids building up and blocking the pump mechanism. The second method involved setting up a wall at the trailing edge of the impeller blade. Its effect was also examined by numerical simulations. Finally the validity of numerical results and the effects of these two different types of walls were verified by the experiments.

Basic Equations

For three-dimensional incompressible and unsteady flow, the continuity and the momentum (Navier-Stokes) equations in the rotating coordinate systems can be written as follows:

$$\frac{\partial \rho}{\partial t} + \frac{\partial u_j}{\partial x_j} = 0, \tag{1}$$

$$\frac{\partial}{\partial t}(\rho u_i) + \frac{\partial}{\partial x_j}(\rho u_j u_i) = -\frac{\partial P}{\partial x_i} + \frac{\partial}{\partial x_j}\left\{\mu_{\text{eff}}\left(\frac{\partial u_i}{\partial x_j} + \frac{\partial u_j}{\partial x_i}\right)\right\} + S_{ui}. \tag{2}$$

In the rotating coordinate system, S_u is defined as

$$S_u = -2\boldsymbol{\omega} \times \boldsymbol{U} - \boldsymbol{\omega} \times (\boldsymbol{\omega} \times \boldsymbol{r}). \tag{3}$$

The first term on the right-hand side of Eq. (3) means the Coriolis force and the second means the centrifugal force. Because these terms exist due to the effects of a rotating impeller, they should be ignored when Eq. (2) is used in a stationary volute casing.

For closing the stated equations, the standard k-ε turbulence model is used while introducing an effective viscosity where the turbulent viscosity μ_t,

$$\mu_{\text{eff}} = \mu + \mu_t \tag{4}$$

is directly related to "k" and "ε," as shown in Eq. (5),

$$\mu_t = C_\mu \rho k^2/\varepsilon. \tag{5}$$

The transport equations for "k" and "ε" are described as follows:

$$\rho U_j \frac{\partial k}{\partial x_j} = \frac{\partial}{\partial x_j}\left(\frac{\mu_t}{\sigma_k}\frac{\partial k}{\partial x_j}\right) + P_k - \rho\varepsilon, \tag{6}$$

$$\rho U_j \frac{\partial \varepsilon}{\partial x_j} = \frac{\partial}{\partial x_j}\left(\frac{\mu_t}{\sigma_\varepsilon}\frac{\partial \varepsilon}{\partial x_j}\right) + C_1 \frac{\varepsilon}{k}P_k - C_2\rho\frac{\varepsilon^2}{k}, \tag{7}$$

where σ_k, σ_ε, C_1, and C_2 are model constants, and P_k is the source term of k.

Table 1 Specifications of a screw centrifugal pump

Impeller	Angle of the location of R_2	400	deg
	Blade width	17.3	mm
	Hub cone angle	60	deg
	Maximum radius R_2	44	mm
	Total angle along blade	540	deg
Rotating condition	Flow rate (at BEP)	0.172	m³/min
	Rotational speed	3000	rpm

Impeller Configuration and Calculation Conditions

The main geometric data of this screw-type centrifugal pump and the operating conditions are summarized in Table 1. The tip clearance is kept at 0.2 mm in these calculations, regardless of the cross section configuration of the volute casing. On the other hand, the tip clearance is kept at an average of 0.5 mm in the experiment because a wide tip clearance is easy to set up experimentally. In a previous research, changes in pump performance due to the magnitude of tip clearance was investigated. The pump performance decreases in proportion to the magnitude of its tip clearance. The effectiveness of restraining the back flow can be examined by making respective comparisons between numerical and experimental results of wall's effects with different tip clearances. Numerical simulations have been performed under these conditions: at 80%, 90%, 100%, 110%, and 120% of flow rate delivery at the best efficiency point (BEP). The working fluid assumed is water.

Figure 2 shows the computational grids in this simulation. The computational domain consists of (a) the impeller, (b) disk clearance, (c) the volute casing, (d) the suction pipe, and (e) the discharge pipe. Figure 2(a) shows grids of the impeller with a tip clearance whose size is $65 \times 32 \times 49$. The grid number of the volute casing is $11 \times 11 \times 141$. The grid number of the suction pipe is $11 \times 49 \times 31$, and that of the discharge pipe is $11 \times 11 \times 21$. Disk friction at the back shroud is considered in calculation like the close-up in Fig. 2(b). The grid number of the disk clearance is $30 \times 49 \times 75$.

Boundary Conditions

Inlet. At the entrance of the suction pipe, the constant flow velocity based on the volume flow rate is given as follows:

$$w = Q/(\pi R_{\text{suc}}^2). \tag{8}$$

Outlet. At the exit of the discharge pipe, the pressure is given as 0 Pa.

Surface of Walls. The wall function is applied (see Table 1).

Interaction Between Impeller and Volute Casing. Between the rotating impeller and the stationary volute casing, data exchange is necessary to analyze their interaction. Transient sliding interface is used in this study, in which the calculated data are exchanged at every time step under the condition that the mass and the momentum of flow are conserved.

Pump Torque Prediction

In order to predict the pump efficiency, its torque is calculated by integrating pressure and wall sheer stress over the wet wall of the impeller. The influence of disk friction loss at the main plate (which is located at the back of an impeller) is included in numerical results. The reason for the considering disk friction is that it is very influential in the pump efficiency prediction due to the small test impeller in this simulation case. Figure 3 shows the schematic cross section of the pump. In Fig. 3, the configuration of disk at the back shroud is illustrated and its scale is indicated.
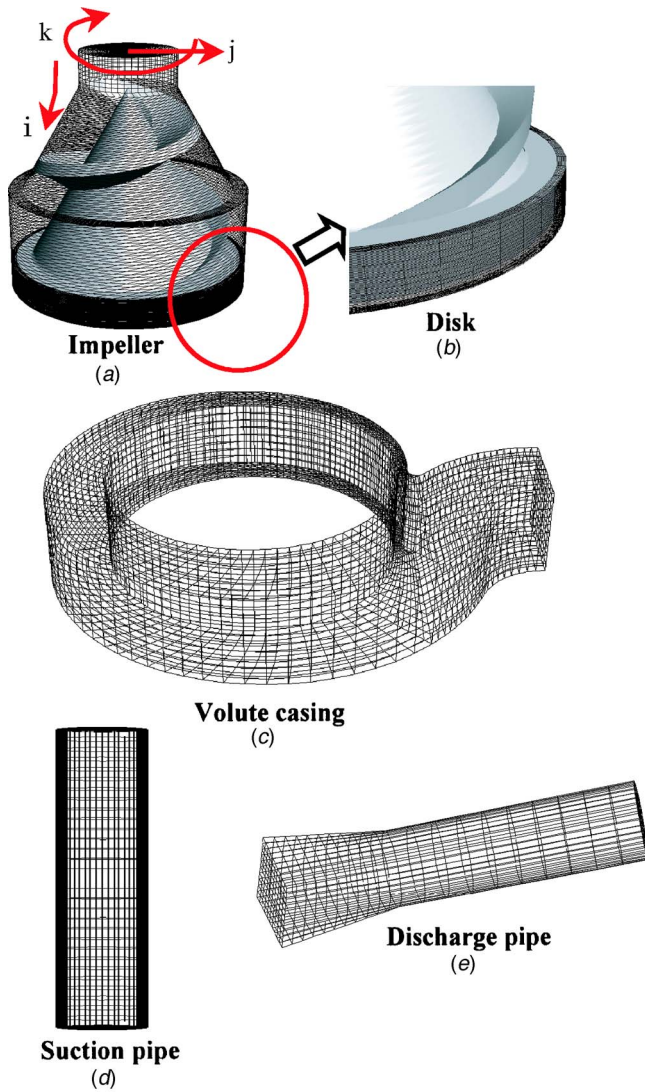
Fig. 2 Computational grid systems: (*a*) Impeller; (*b*) Disk; (*c*) Volute casing; (*d*) Suction pipe; (*e*) Discharge pipe

Comparing the calculated disk torque with the results of Dairy and Nece [9], the torque due to the disk friction was predicted accurately.

Furthermore, the pump torque in the experiment includes the torque by a mechanical seal and so on. However, the torque in the calculation excludes the frictional torque due to the mechanical loss. Therefore, the consideration of mechanical loss is necessary in order to predict the pump efficiency precisely. The motor power is defined as the mechanical loss component when the experimental pump system is operated without the impeller. And the pump torque is accurately and rationally calculated by adding this motor power to the amount of calculated torque.

Influence of Volute Casing Configuration

The back flow between the impeller outlet and the volute casing needed to be restrained in this research. Consequently, the wall's effect on the pump performance may change due to differences in the cross section configuration of the volute casing since the back flow region may be reduced or disappeared by changing its configuration. Therefore, the numerical simulations were carried out on two kinds of volute casing in order to examine the effectiveness of restraining the back flow by different volute casing configurations. Figure 4 shows two kinds of volute casing. One of
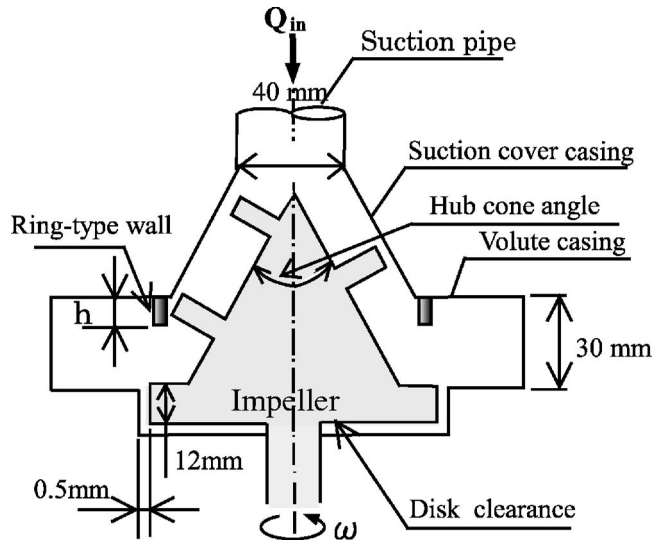
**Fig. 3 Cross section of a screw-type centrifugal pump**

them has a rectangular cross section (R-type), shown in Fig. 4(*a*). Another has a circular cross section (C-type), shown in Fig. 4(*b*). However, the volute casing with a rectangular cross section is only used to compare numerical results with experimental results and in order to verify the validity of numerical simulations.
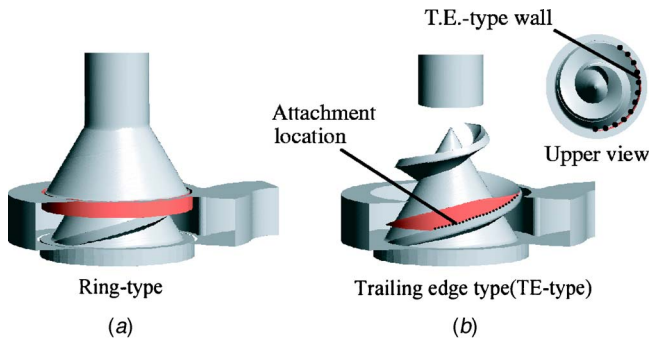
Ring-Type Wall

The schematic cross section of the screw-type centrifugal pump in R-type volute casing is shown in Fig. 3. In order to restrain the back flow from the volute casing toward the impeller outlet, a wall-like ring is set at the inlet of the volute casing. The location of this wall attachment is the same in both R-type and C-type volute casing. The wall is circular and its height is constant along the direction of the circumference. The cross section of this wall is rectangular. In particular, the third back flow region includes the back flow from the pressure surface of blade toward its suction surface. So the distance between the wall and the impeller is kept the same as the tip clearance so as to reduce the influence of the back flow from the pressure surface of blade toward its suction surface. The height of wall *h*, which is shown in Fig. 3, is kept at 7, 10, 15, and 20 mm in calculations. On the other hand, two kinds of walls are used in the experiment, whose heights are 5 and 10 mm. From numerical results, the influences of the wall on the pump performance and on the flow pattern due to the wall's height are discussed. The validity of numerical simulations and the actual effects of the wall are examined by comparing numerical and experimental results.

TE-Type Wall

In case of the ring-type wall proposed in the previous paragraph, shown in Fig. 5(*a*), it seems that a reduction in the flow
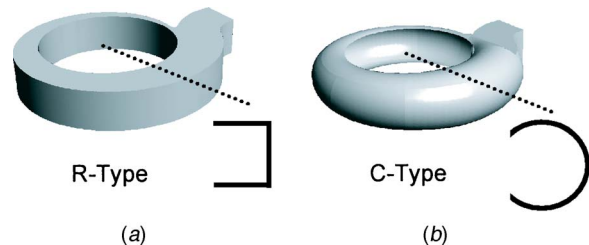
Fig. 4 Configurations of volute casing and cross section: (*a*) R-type; (*b*) C-type

Fig. 5 Configurations of restraint walls: (a) ring-type; (b) Trailing edge type (TE-type)

passage may occur even though this method is very simple. It is desirable that the size of the restraint wall be kept small, so as not to reduce this flow passage. Another method is proposed to improve the passage of solids. In this method, a wall is set up only at the location where the influence of the back flow is large, as shown in Fig. 5(b). This location is the trailing edge of an impeller. Here exist two kinds of back flow—one from the volute casing to the impeller outlet and another back flow rolling up from the blade pressure surface to the blade suction surface exist. As shown in Figs. 3 and 5, a ring-type wall is installed at the volute casing wall and a TE-type wall at the trailing edge of the impeller. Therefore, the large difference in these two methods is that a ring-type wall is a stator and a TE-type wall a rotor. It is expected that the pump performance can be improved when these back flows are suppressed by these walls. This effect is clarified from our numerical analysis by comparing the effects of a ring-type wall, which is confirmed by the experiment.

Results and Discussions

Flow Pattern Without a Ring-Type Wall. Figure 6 shows velocity vectors and total pressure contours near the impeller outlet and the volute casing at the three cross sections. The type of volute casing is R-type. The location of the cross sections is shown on the upper right side of Fig. 6(a). The impeller phase θ_{imp} is defined as a counterclockwise rotation angle measured from the location where the front of the impeller is right vertically above the pump shaft. The impeller phase is 0 deg in Fig. 6.

Figure 6(a) shows the back flow from the pressure surface of the blade toward its suction surface and the back flow from the volute casing toward the impeller outlet existing without a ring-

type wall. Because of these back flows, the direction of the main flow is distorted. This back flow at the cross section II shown in Fig. 6(b) (located on the opposite side of the cross section shown in Fig. 6(a)) has less influence on the main flow than the back flow at the cross section I. On the other hand, this back flow at the cross section III shown in Fig. 6(c) is more influential than that at the cross section I because this back flow distorts the main flow greatly, and the area influenced reaches even to the inside of the impeller outlet. L1 and L2 in Figs. 6(b) and 6(c) indicate the distance from the blade pressure surface to the maximum radius of the pump cover casing at each cross section. The blade pressure surface at the cross section II is located more closer to the confluence surface of both the main flow and the back flow because L1 is shorter than L2. This screw-type centrifugal pump has a displacement pump effect such that the working fluid is pushed toward the downstream of flow passage by the blade. For this reason, the main flow becomes stronger and pushes the back flow toward the volute casing when the blade pressure surface comes closer to the confluence surface. Therefore, the back flow from the volute casing toward the impeller outlet in Fig. 6(c) seems to have much more influence on the upstream flow in the impeller because the main flow at section II (shown in Fig. 6(b)) is stronger than that at section I (shown in Fig. 6(c)). However, a low-pressure area exists at the confluence surface of the main flow and the back flow at each cross section because the mixing generates loss. Although the degree of influence is different along the cross section locations, it was discovered that this back flow has much influence on the internal flow.

Flow Pattern With a Ring-Type Wall. Figure 7 shows the velocity vectors and total pressure contours improved by a ring-type wall. The nondimensional height of the wall h/B is 0.333. These results in Fig. 7 were obtained under the same conditions as those in Fig. 6. Figure 7(a) shows that a ring-type wall restrains the back flow from the volute casing toward the impeller outlet. However, another back flow exists, as shown by the arrow ① (shown moving from the blade pressure surface to the blade suction surface) in Fig. 7(a). This is the reason why the back flow rolls up from the blade pressure surface to the suction surface. This back flow can be observed at the corner between the wall and the cover casing regardless of impeller phase in Figs. 7(b) and 7(c). However, this back flow is very small so its influence is also small.

Similarly, a ring-type wall restrains the back flow at each cross section in Figs. 7(b) and 7(c). Comparing velocity vectors in Figs. 6(c) and 7(c), flow distortion is greatly improved at the cross section III in Fig. 7(c), while distortion of the main flow is caused
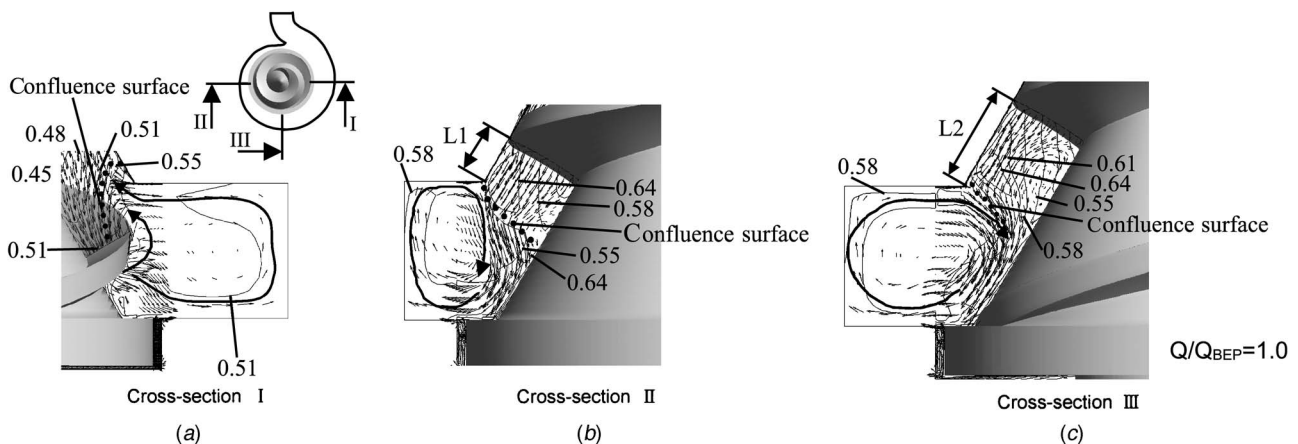
Fig. 6 Velocity vectors and total pressure distributions at each cross-section without a ring-type wall: (a) Cross-section I; (b) Cross-section II; (c) Cross-section III
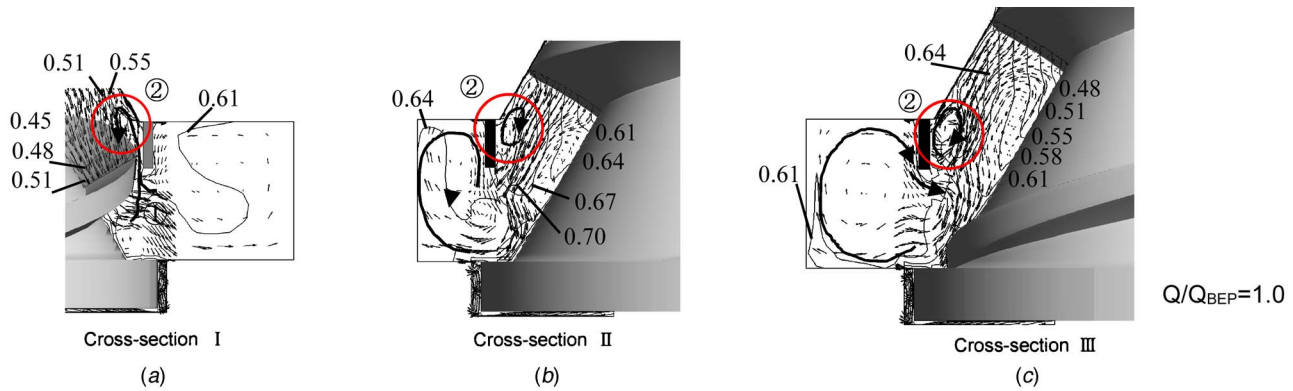
Fig. 7 Velocity vectors and total pressure distributions at each cross section with a ring-type wall: (*a*) **Cross-section I;** (*b*) **Cross-section II;** (*c*) **Cross-section III**

by the back flow at the cross section III shown in Fig. 6(*c*).

The influence of the wall's height is discussed in the following paragraphs.

Pressure Distribution in Pumps by Ring-Type Walls. Figure 8(*a*) shows pressure distributions from the impeller inlet to the outlet at the BEP in two kinds of volute casing. Calculated pressure at each flow passage section is initialized by pressure at the pump suction pipe and is mass-averaged during two revolutions of the impeller. The abscissa indicates the location number in the cross section which is vertical to the meridian stream line. The ordinate indicates the pressure coefficient. On the right figure of Fig. 8(*a*), location 1 indicates the pump inlet at the suction pipe, location 10 shows the impeller inlet (surface on L. E. of blade). Location 50 shows the impeller outlet (surface on T. E. of blade) and location 65 the inlet of the volute casing. A ring-type wall exists at a position between location 52 and location 57.

The pressure becomes different since location 30 when compar-

ing pumps with and without a ring-type wall. The area influenced by the back flow reaches the upstream region of impeller outlet, as shown in Fig. 6. The pump pressure recovers at the upstream region of impeller outlet because a ring-type wall restrains the back flow. Pressure also recovers because when one compares pumps with and without a wall, the pressure is mostly constant after the maximum blade radius part of the pump (location 50). Thus it is thought that pressure was improved only by decreasing the back flow. The effect of restraining the back flow can be recognized regardless of the configuration of the volute casing.

Figure 8(*b*) shows the mass-averaged pressure distributions during two revolutions of the impeller at each section of the volute casing. Twelve locations at each section are indicated in the smaller inserted figure on the right of Fig. 8(*b*). Regardless of the configuration of the volute casing, the general tendency is that pressure recovers gradually when the cross section comes closer to the tongue, as shown in Fig. 8(*b*).

In both volute casings, the pressure at every cross section rises by a constant quantity, when comparing the pressure of pumps with and without ring-type walls. The effect of a wall is clear from these facts. The pressure distribution without a wall is similar to that with a wall at each volute casing. The amount of pressure loss does not change by the attachment of a wall. Therefore, a ring-type wall can improve the loss of impeller performance due to this back flow, and will not have a bad influence on the volute performance.

Influence of Ring-Type Walls on Pump Performance. Figure 9 shows the pump performance in calculations which investigate the influence of a ring-type wall on it. The wall's height is h/B $=0.333$, which is the same as that in Fig. 7. Comparing the pump performance having an R-type volute casing with that of a pump in C-type volute casing, the difference of pump head and best efficiency is within 1%. This relation between two kinds of volute casing without ring-type walls is the same as that for pumps with ring-type walls. Therefore the influence of the volute casing on pump performance seems to be very small. However, the pump performance in R-type volute casing is slightly better than that in C-type volute casing. This reason may be that the size of the tongue in both volute casings is a little different and its influence on pump performance is large. Regardless of volute casing configuration, the best efficiency is improved by 4% by the attachment of a ring-type wall. In addition, the pump head can be improved by a constant amount at any flow rate. At the BEP, the pump head rises by 10%. The power coefficient rises by attaching a ring-type wall, since the blade loading becomes larger due to high pressure in the impeller, as shown in Fig. 8(*a*). However, the best efficiency is improved because the rise of the pump head is
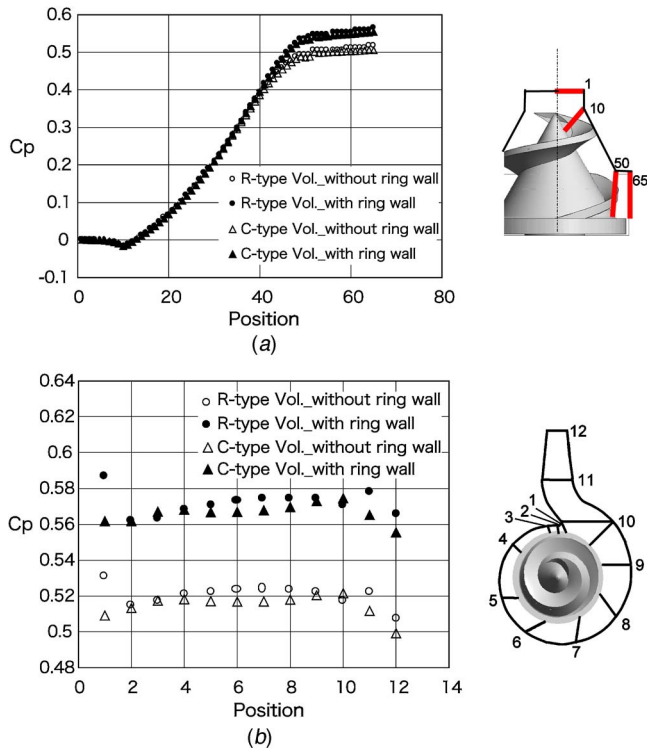

Fig. 8 Pressure distributions in pumps with or without ring-type walls: (*a*) **In impeller;** (*b*) **In volute casing**
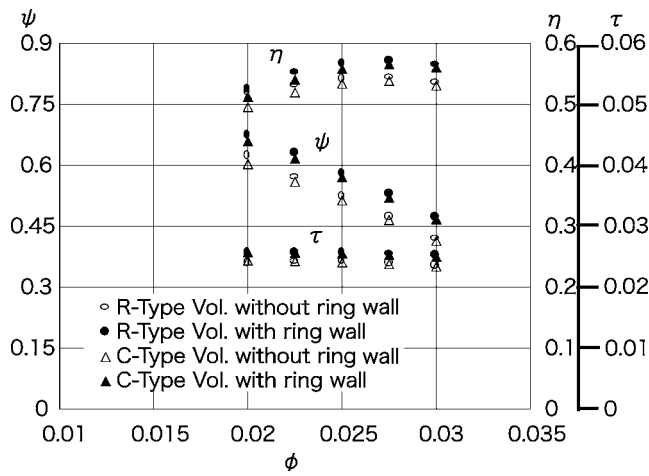
Fig. 9 Improvement of pump performance with a ring-type wall in Cal.

larger than that of the power coefficient. Thus it was found from numerical calculations that a ring-type wall makes an improvement in pump performance.

Optimum Height of Ring-Type Wall. Figure 10 shows the relationship between the wall's height and the pump discharge
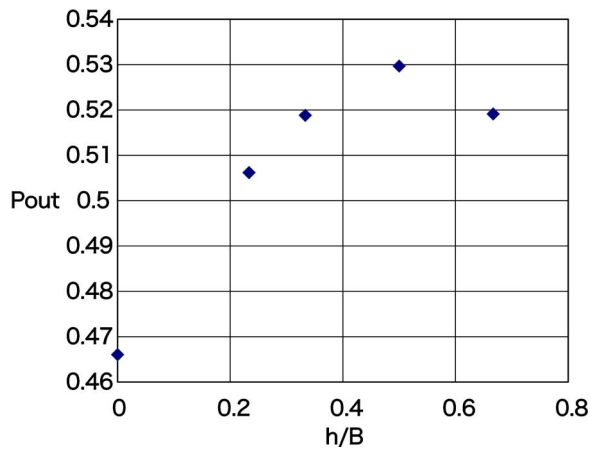
Fig. 10 Best height of ring-type wall
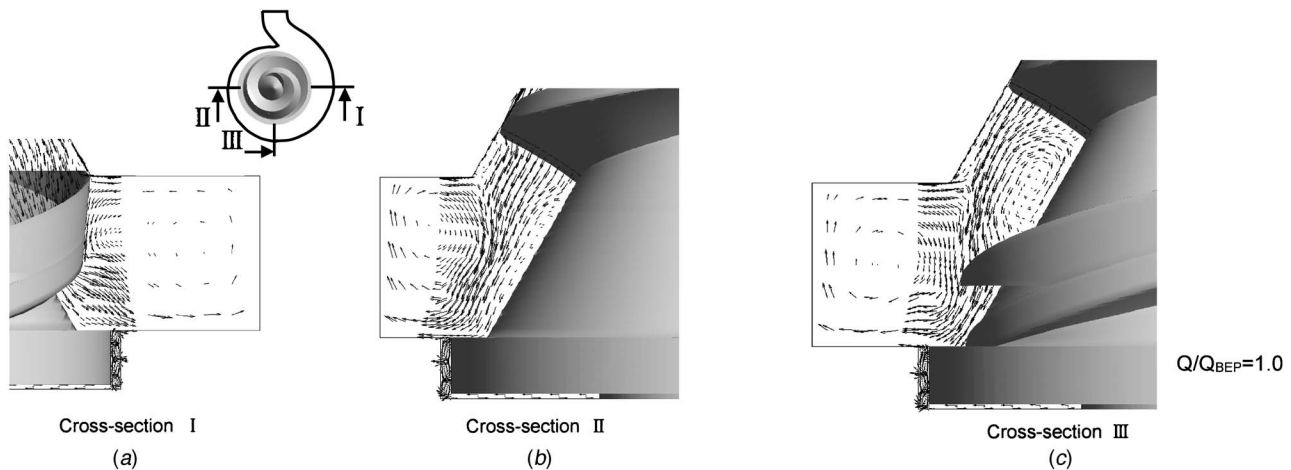
pressure. The abscissa indicates the nondimensional wall's height and the ordinate shows the pump discharge pressure. As the wall's height becomes higher, the pump discharge pressure also becomes higher gradually. However, over a wall's height $h/B=0.5$ the pump discharge pressure becomes smaller in contrast. The reason for this is considered to be the magnitude of the back flow and the loss encountered by the attachment of a ring-type wall. As shown in Fig. 6, secondary flow in the volute casing causes a back flow from the volute casing toward the impeller outlet. The center of this secondary flow is located at half the height of the volute casing's width. Therefore, the pump discharge pressure—when the wall is lower than half the height of the volute width—does not become high because the back flow from volute casing toward the impeller outlet cannot be restrained enough. A ring-type wall at half the height of the volute casing's width can suppress the back flow completely. Therefore, the discharge pressure rises in proportion to the wall's height until the height becomes half that of the volute casing's width.

The effect of restraining the back flow over $h/B=0.5$ is almost the same as that at $h/B=0.5$. However, the flow passage is squeezed extremely when a ring-type wall is over $h/B=0.5$. The squeezing loss has increased, though control of the back flow is performed well enough when the wall's height is over the half height of the volute casing's width. Therefore, when the wall's height (h/B) goes over 0.5, the discharge pressure at the suction pipe becomes low.

TE Type Wall Effect. Figure 11 shows velocity vectors near the impeller outlet and the volute casing at the cross sections I-III in pumps with TE-type walls. The locations of the cross sections are shown on the upper right side of Fig. 11(a). The impeller phase is 0 deg. In Fig. 11(a), this TE-type wall can suppress the back flow from the volute casing to the impeller outlet. Besides, the back flow, which rolls up from the pressure surface to the suction surface as shown in Fig. 7(a), has disappeared. In Fig. 11(b) the flow pattern does not change, compared with that in Fig. 6(b). Moreover, in Fig. 11(c) the influenced region of this back flow becomes small, while this back flow has much influence on the region inside of the impeller outlet in Fig. 6(c). The influence of this restraint wall is the largest at the cross section where the wall exists. The influence has an effective influence even at the section where the wall has just passed. An impeller phase brings different effects to each section. Because a TE-type wall never becomes extremely narrow, the flow passage in the impeller compared to pumps with ring-type walls clearly is seen to enhance the pump performance.
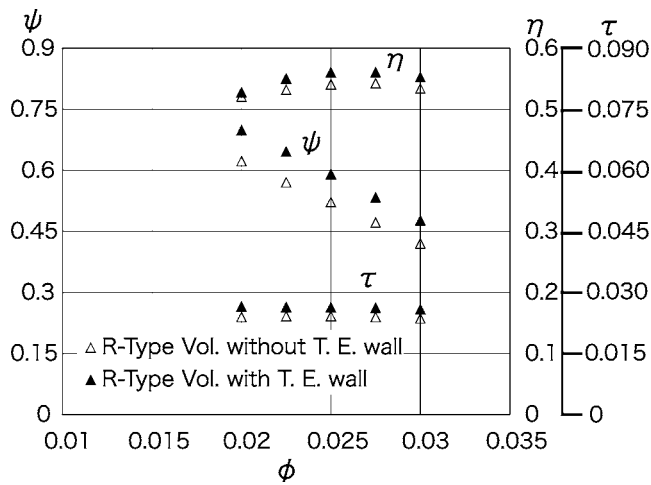
Figure 12 shows the pump performance with and without TE-

Cross-section I
(a)

Cross-section II
(b)

Cross-section III
(c)

$Q/Q_{BEP}=1.0$

Fig. 11 Velocity vectors distributions at each cross-section with a TE-type wall: (a) Cross-section I; (b) Cross-section II; (c) Cross-section III

Fig. 12   Improvement of pump performance using a TE-type wall

type walls. Pump head is improved by 10% at the BEP and the best efficiency is improved by 3%. The flow rate at the BEP is the same regardless of the existence of a wall. The power coefficient with a TE-type wall increases because the blade loading becomes large, as well as that with the ring-type wall, compared to the shaft power without the TE-type wall.

Verification by Experiment. From the numerical results referred to in previous paragraphs, the back flow can be restrained and the pump performance can be improved by the two kinds of walls. In order to verify these numerical results, the influence of two kinds of walls on the pump performance was clarified by experiments.

Figure 13 shows the pump performance with a ring-type wall ($h/B=0.0$, 0.167, and 0.333) in R-type volute casing. Due to the attachment of a wall, the pump head becomes higher by a constant quantity, regardless of the flow rate. Furthermore, the best efficiency rises though the power coefficient increases. These numerical and experimental results and tendencies coincide and support each other. The improvement in pump performance with a wall of $h/B=0.167$ is less than that with a wall of $h/B=0.333$. This tendency in the calculation agrees well with that of the experiment as well. As a result, the validity of numerical results and the improvement in the pump performance due to addition of a ring-type wall are clarified.

Next, the pump performance is shown in Fig. 14, when a TE-type wall is installed. The best efficiency is improved by 3% and
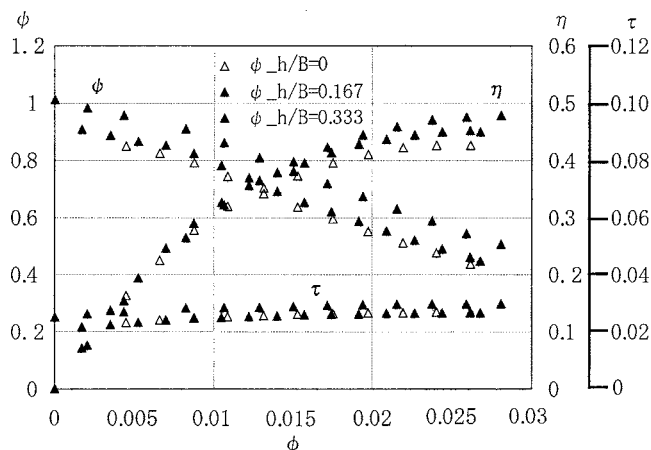

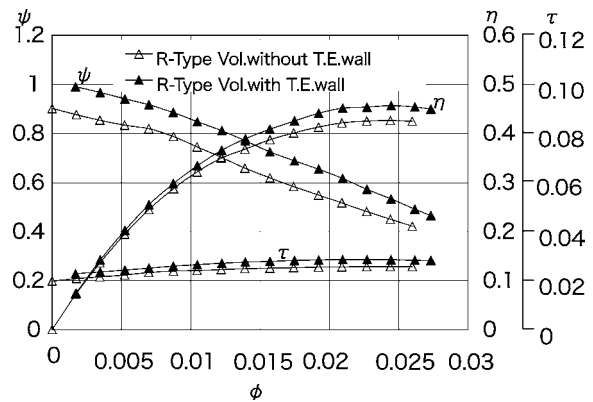**Fig. 13   Pump performance in Exp. with a ring-type wall**

the pump head at the BEP is improved by 10%, just as it was with a ring-type wall ($h/B=0.333$). Moreover, the flow rate at the BEP does not change, regardless of the attachment of a TE-type wall. The improvement in pump performance with a TE-type wall is the same with that of pumps with a ring-type wall, though the region where can be suppressed by a TE-type wall is smaller. In addition, the flow passage of solids can be secured because a TE-type wall is small. Therefore, a TE-type wall has better performance for the congestion of solids.

Conclusions

Pump performance improvement by two kinds of walls (ring-type walls and TE-type walls), which restrain the back flow from the volute casing to the impeller outlet, was investigated mainly by numerical simulations. Experimental study was also carried out in order to verify numerical results. The followings were obtained:

(1) The back flow from the volute casing to the impeller outlet could be restrained by use of a ring-type wall regardless of the configuration of the volute casing.

(2) When a ring-type wall at a height of $h/B=1/3$ is attached, the head performance is improved by a constant amount (it is 10% at BEP) regardless of the flow rate. Furthermore, the best efficiency is improved by 4%. This tendency corresponded to the experimental findings.

(3) The head performance in pumps is improved more as the height of a ring-type wall becomes large. The optimum height of a ring-type wall is $h/B=1/2$, and the discharge pressure becomes lower as the wall's height goes over this optimum height.

(4) The back flow was restrained by use of a TE-type wall, though its effect was different along cross sections of the volute casing in numerical simulations. However, a TE-type wall especially suppressed the back flow from the pressure surface to the suction surface especially. Its influence on the pump performance is the same as that of a ring-type wall at a height of $h/B=1/3$. This wall gives a pump better performance for the congestion of solids, because it never narrow the flow passage.

Nomenclature

A_2 = area at impeller outlet
B = width at volute casing inlet
C_p = pressure coefficient ($=P/(u_2^2/2g)$)
H = pump head
h = height of ring-type wall
L = shaft power
P = pressure
Q = flow rate
R_2 = maximum radius of the impeller

U_2 = circumferential velocity at R_2

u,v,w = velocity components in the Cartesian coordinate

Greek Symbols

ϕ = discharge coefficient ($=Q/(2\pi R_2 B u_2)$)

η = pump efficiency ($=\phi\psi/\tau$)

μ = coefficient of viscosity

ρ = fluid density

τ = power coefficient ($=L/(\rho A_2 u_2^3/2)$)

ω = angular speed

ψ = head coefficient ($=H/(u_2^2/2g)$)

Subscript

BEP = best efficiency point

2 = location of the maximum radius part of the impeller

References

[1] Zixiang, S., and Ishida, M., 2000, "A Computational Study on Optimum Inducer Leading Geometry For Stall Suppression in a Centrifugal Blower," in Proceedings of ASME Fluids Engineering Summer Meeting, FEDSM00-11059, USA.

[2] Kurokawa, J., Saha, S. L., Matsui, J., and Imamura, H., 2000, "An Innovative Device to Suppression of Performance Curve Instability of Mixed Flow Pump by Use of J-Groove," Trans. JSME, **66**, No. 642 (B), pp. 460–467 (in Japanese).

[3] Kurokawa, J., Saha, S. L., Matsui, J., and Imamura, H., 2000, "Suppression of Performance Curve Instability of Mixed Flow Pump by Use of J-Groove," ASME J. Fluids Eng., **122**, pp. 592–597.

[4] Han, H., Tanaka, K., and Kobayashi, T., 2000, "Internal Flow Simulation in Screw-Type Centrifugal Pump," J. Turbomach., **28-3**, pp. 183–190 (in Japanese).

[5] Tatebayashi, Y., Tanaka, K., Han, H., and Kobayashi, T., 2000, "A 3-D Simulation of Flow in Screw-Type Centrifugal Pump with Tip Clearance," The 2nd International Symposium on Fluid Machinery and Fluid Engineering, China.

[6] Tatebayashi, Y., and Tanaka, K., 2002, "Meridian Shape Influence on Screw-Type Centrifugal Pump Performance," in Proceedings of the ASME Fluids Engineering Summer Meeting, FEDSM02-31183, Canada.

[7] Tatebayashi, Y., Tanaka, K., and Kobayashi, T., 2003, "Pump Performance Prediction in Screw-Type Centrifugal Pump," J. Turbomach., **31-10**, pp. 582–589, (in Japanese).

[8] Kim, Y. T., Tanaka, K., Yamada, I., and Matsumoto, Y., 2000, "Pressure Fluctuation Due to Air Entrainment in Screw-Type Centrifugal Pump," Trans. JSME, **66**, No. 644 (B), pp. 1126–1131 (in Japanese).

[9] Daily, J. W., and Nece, R. E., March 1960, "Chamber Dimension Effects on Induced Flow and Frictional Residence of Enclosed Rotating Disks," ASME J. Basic Eng., **82**, pp. 217–231.

The Impact of Blade-to-Blade Flow Variability on Turbine Blade Cooling Performance

Vince Sidwell

Manager
Multidisciplinary Design and Optimization
Group,
Pratt & Whitney,
400 Main Street, M/S 165-16,
East Hartford, CT 06109

David Darmofal

Associate Professor
Aeronautics and Astronautics,
Massachusetts Institute of Technology,
77 Massachusetts Avenue, Room 37-401,
Cambridge, MA 02139

The focus of this paper is the impact of manufacturing variability on turbine blade cooling flow and, subsequently, its impact on oxidation life. A simplified flow network model of the cooling air supply system and a row of blades is proposed. Using this simplified model, the controlling parameters which affect the distribution of cooling flow in a blade row are identified. Small changes in the blade flow tolerances (prior to assembly of the blades into a row) are shown to have a significant impact on the minimum flow observed in a row of blades resulting in substantial increases in the life of a blade row. A selective assembly method is described in which blades are classified into a low-flow and a high-flow group based on passage flow capability (effective areas) in life-limiting regions and assembled into rows from within the groups. Since assembling rows from only high-flow blades is equivalent to raising the low-flow tolerance limit, high-flow blade rows will have the same improvements in minimum flow and life that would result from more stringent tolerances. Furthermore, low-flow blade rows are shown to have minimum blade flows which are the same or somewhat better than a low-flow blade that is isolated in a row of otherwise higher-flowing blades. As a result, low-flow blade rows are shown to have lives that are no worse than random assembly from the full population. Using a higher fidelity model for the auxiliary air system of an existing jet engine, the impact of selective assembly on minimum blade flow and life of a row is estimated and shown to be in qualitative and quantitative agreement with the simplified model analysis. [DOI: 10.1115/1.2019247]

1 Introduction

Temperature-related damage to turbine blades is a leading cause of unscheduled engine removals for gas turbine engines and is one of the largest contributors to engine maintenance costs [1–3]. In particular, variability in turbine oxidation life has been observed in the field resulting in engine-related service disruptions [4]. When turbine blades fail unexpectedly, an in-service engine must be removed from the aircraft for repair, often resulting in flight delays, cancellations, and thus lost airline revenue.

Recent analysis of a commercial jet engine has shown that manufacturing variability in the effective flow area of blade internal cooling passages is a leading contributor to oxidation-related turbine failures [5,6]. The importance of cooling flow variability on the life of a blade is a result of the strong dependence of life on blade metal temperature, and blade metal temperature on cooling flow rate. For example, the life of a turbine blade due to typical wear-out failure mechanisms (oxidation and creep, for example) often has an exponential dependence on the blade metal temperature, that is,

$$t_f \approx A e^{B/T_{\text{metal}}}, \tag{1}$$

where t_f is the time to failure and A and B are constants depending on the alloy and the failure mechanism [7]. For oxidation, the strength of this temperature dependence is such that changes of $\pm 70\,^{\circ}\text{F}$ can result in a doubling (or halving) of life capability [1]. Other failure mechanisms such as creep can be even more sensitive to temperature changes [8]. The dependence of blade metal temperature on cooling flow rate can be estimated using a cooling effectiveness parameter, η [9],

$$\eta \equiv \frac{T_{\text{gas}} - T_{\text{metal}}}{T_{\text{metal}} - T_{\text{cool}}} \Rightarrow T_{\text{metal}} = \frac{T_{\text{gas}} + \eta T_{\text{cool}}}{\eta + 1}. \tag{2}$$

Given nominal (reference) values for airfoil internal mass flow ($\dot{m}_{\text{nom}}$) and cooling effectiveness (η_{nom}), the cooling effectiveness at the actual mass flow ($\dot{m}$) is approximated as,

$$\eta \approx \eta_{\text{nom}} \left(\frac{\dot{m}}{\dot{m}_{\text{nom}}} \right)^\alpha \tag{3}$$

where α is an experience-based scaling parameter close to 1. Linearizing about the reference conditions gives the following relationship:

$$\Delta T_{\text{metal}} \approx -\alpha \frac{\eta_{\text{nom}}}{(\eta_{\text{nom}} + 1)^2} (T_{\text{gas}} - T_{\text{cool}}) \frac{\Delta \dot{m}}{\dot{m}_{\text{nom}}}. \tag{4}$$

Since passage flow variability due to manufacturing can be as much as $\pm 10\%$ and $T_{\text{gas}} - T_{\text{cool}}$ is often $1500\,^{\circ}\text{F}$ or more (depending on the engine design), blade metal tempatures can vary by $\pm 30\,^{\circ}\text{F}$ or more (assuming $\alpha \approx 1$ and $\eta_{\text{nom}} \approx 1$). As a result, turbine blades can exhibit a large variability in life due solely to manufacturing-induced blade flow variability.

For a row of turbine blades, maintenance is required when even a few blades begin to fail, thus, the time-between-overhaul for a row of turbine blades is determined by the few lowest-life blades in the row. Since turbine rows have a large number of individual blades, the probability of a row containing a blade from the low-flow tail of the population of all manufactured blades is high. Specifically, if the probability of manufacturing a blade with a low flow capability is p, then for a row of n turbine blades, the probability of having at least one low flow blade is, $1 - (1-p)^n$. For example, if a low flowing blade is manufactured at a rate of 1%, then the probability of observing at least one low flow blade in a row of 80 blades is approximately 55%. As a result of this effect and the strong dependence of blade life on cooling flow, changes in the manufacturing and assembly process that impact the lower-

flowing portion of the distribution of blade cooling flow capability can make substantial differences in the life of most blade rows.

Unfortunately, due to the expense of manufacturing these blades, large variations in passage flow capability are generally accepted. However, since the life of a blade row is sensitive to changes in the distribution of the lowest-flowing blades, economic benefits may exist for rejecting more blades by raising the low-flow tolerance (i.e., trading the cost of scrapping more blades prior to assembly versus the cost of more frequent, possibly unscheduled, maintenance during operation). In this paper, we do not attempt to quantify the economic impact of changing tolerances, but rather estimate the effect of changing tolerances on the distribution of the minimum passage flow in each row, and subsequently on oxidation life.

As an alternative to tightening tolerances, we also investigate a selective assembly method in which blades are assembled into rows according to their effective flow areas [10,11]. In this paper, we consider a two-class selective assembly method in which the blades are grouped into low-flowing and high-flowing classes and rows are assembled exclusively from within these classes. For the high-flow rows, the benefits in life can be substantial as the life-limiting lowest-flowing manufactured blades have been eliminated from these rows. Furthermore, we will show that the life of low-flow rows will tend to be the same as (or even slightly better than) the life of rows assembled randomly from all manufactured blades. With a selective assembly strategy, the cost of handling more than one class of turbine blades must be weighed against the potential benefits in life for the majority of the blade rows.

The paper begins with a description of a simplified network-flow model for a cooling air supply system and a row of cooled turbine blades. Using this model, we qualitatively and quantitatively describe the impact of blade flow manufacturing tolerances and selective assembly on the row-to-row distribution of blade flow. Finally, we quantify the impact of blade effective area variability on oxidation life using a higher-fidelity flow model for an existing commercial jet engine and show that the simplified model is in good agreement with these higher-fidelity results.

## 2 Simplified Model of a Flow System With Single-Passage Blades

This section describes a simplified flow network model of a cooling air supply system. Figure 1 shows a cross section of a typical first-stage of a high-pressure turbine and the aft portion of the combustor, including the schematic representation of the turbine cooling air delivery portion of a higher-fidelity auxiliary air system flow network model. Note, the specific auxiliary air system and the corresponding flow network shown in the figure are analyzed in detail in Sec. 4. This figure highlights three plenums that are used in the simplified model and divide the cooling air supply system into two portions: the supply system and the turbine blades. Figure 2 shows a schematic of the simplified model of the cooling air supply system, where the plenums (P_s, P_p, and P_g) correspond to the plenums highlighted in Fig. 1. In this simplified model of a turbine row with cooled blades, the cooling air delivery subsystem is represented by the effective area, A_s, and a mass flow-pressure relationship, $f_s(P_s, P_p)$. Each of the n single-passage cooled blades is represented by an individual effective area, A_i, and a mass flow-pressure relationship, $f_b(P_p, P_g)$. The governing equations for the system can be written as

$$\dot{m}_s = A_s f_s(P_s, P_p) \tag{5}$$

$$\dot{m}_i = A_i f_b(P_p, P_g) \quad i = 1, 2, \ldots, n \tag{6}$$

$$\dot{m}_s = \sum_{i=1}^{n} \dot{m}_i. \tag{7}$$

Note that for simplicity, we have not included a temperature dependence in the mass flow relationships though this dependence is
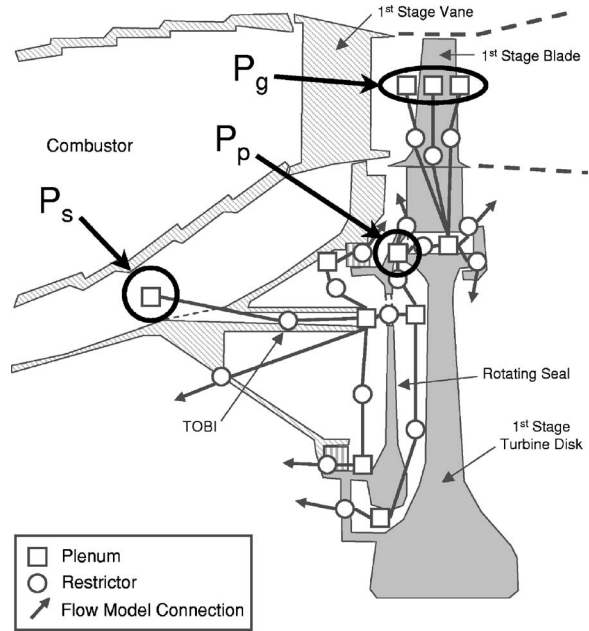
Fig. 1 Cross section of the first-stage of an existing high-pressure turbine and the aft portion of the combustor, including the schematic representation of the turbine cooling air delivery portion of a higher-fidelity auxiliary air system model. Three plenums are highlighted that correspond to plenums in the simplified model.

included in the flow network model analyzed in Sec. 4. As will be demonstrated, this simple model without temperature dependence is quite representative of the more complex model that includes temperature effects.

For the situation in which all blades are at their nominal effective areas ($A_i = A_{nom}$ for all i, where A_{nom} is the nominal effective area), define the nominal blade mass flow as $\dot{m}_{nom}$. Then, variability in blade mass flow capability is introduced through independent perturbations, $\tilde{A}_i$, to the individual blade areas

$$A_i = A_{nom} + \tilde{A}_i. \tag{8}$$

Solution of the linearized equations gives the plenum pressure and total system mass flow perturbations (rearranged into nondimensional form) as

$$\tilde{P}_p \left(\frac{A_{nom} \dfrac{\partial f_b}{\partial P_p}}{\dot{m}_{nom}} \right) = -\frac{1}{1+\beta} \left(\frac{1}{n} \sum_{i=1}^{n} \frac{\tilde{A}_i}{A_{nom}} \right) \tag{9}$$
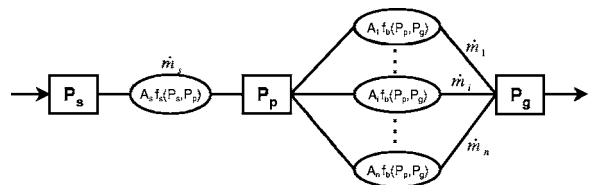
Fig. 2 Simplified model of a turbine cooling air supply system and a row of n single-passage cooled turbine blades. $A_s f_s(P_s, P_p)$ represents the flow through the cooling air supply system and $A_i f_b(P_p, P_g)$ represents the flow through each cooled blade.

$$\frac{\widetilde{\dot{m}}_s}{n\dot{m}_{\text{nom}}} = \frac{\beta}{1+\beta}\left(\frac{1}{n}\sum_{i=1}^{n}\frac{\widetilde{A}_i}{A_{\text{nom}}}\right) \qquad (10)$$

In Eqs. (9) and (10), the nondimensional parameter β has been introduced:

$$\beta \equiv -\frac{A_s\dfrac{\partial f_s}{\partial P_p}}{nA_{\text{nom}}\dfrac{\partial f_b}{\partial P_p}}. \qquad (11)$$

The parameter β represents the relative sensitivity of the flow rates of the delivery system and the blade row to changes in the plenum pressure, P_p. In general, $\partial f_s/\partial P_p \leqslant 0$ and $\partial f_b/\partial P_p \geqslant 0$, thus $\beta \geqslant 0$. Equations (9) and (10) show that the plenum pressure and total mass flow perturbations are governed by β and the row-average effective area perturbation,

$$\text{Row-Average Effective Area Perturbation} = \frac{1}{n}\sum_{i=1}^{n}\frac{\widetilde{A}_i}{A_{\text{nom}}}. \qquad (12)$$

For a manufacturing process that is centered about the design intent blade flow (such that the expected value of the row-average effective area perturbation is zero), the plenum pressure and the total mass flow are their nominal values. However, if a row is assembled from blades that are on average low-flow blades (in this case the average effective area perturbation is negative), the plenum pressure will increase. While the total mass flow does decrease for a low-flow set of blades, the amount of decrease depends on β. In the particular limit of $\beta \to 0$, the total system mass flow tends to the nominal mass flow regardless of the row-average effective area perturbation. This effect occurs because the system is choked by the delivery system's lack of sensitivity to P_p changes. Thus, P_p will increase to pass the delivered amount of flow through the blades.

The mass flow perturbation in an individual blade (blade j, for example) is given by,

$$\frac{\widetilde{\dot{m}}_j}{\dot{m}_{\text{nom}}} = \frac{\widetilde{A}_j}{A_{\text{nom}}} - \frac{1}{1+\beta}\left(\frac{1}{n}\sum_{i=1}^{n}\frac{\widetilde{A}_i}{A_{\text{nom}}}\right). \qquad (13)$$

Thus, the flow through an individual blade is controlled by not only the effective area perturbation for the specific blade $\widetilde{A}_j/A_{\text{nom}}$ but also the row-average effective area perturbation. For a row assembled from a population of blades with effective areas centered on the nominal, the row-average effective area is zero; therefore, the flow through an individual low-flow blade will be given solely by the individual blade's area perturbation, $\widetilde{A}_j/A_{\text{nom}}$. However, for a row assembled from a set of low-flow blades, the row-averaged effective area will be negative providing a compensating effect which increases the flow to the row. As described previously, this compensation occurs because the plenum pressure increases for a low-flow class of blades. Thus, an individual low-flow blade in a low-flow row will have a higher pressure ratio and greater coolant flow than if it were in a nominally-centered set of blades.

While the model described above helps provide a qualitative sense of the behavior of a set of cooled turbine blades, it includes the assumption that each blade consists of a single cooling passage. In practice, turbine blades have more than one passage, often two or three. Figure 3 shows a schematic of a simplified model where each blade consists of three cooling passages. For simplicity, the blade passages are assumed to have the same dependence of flow on pressure, $f_b(P_p, P_g)$. The perturbation in flow through passage a of blade j is given by,
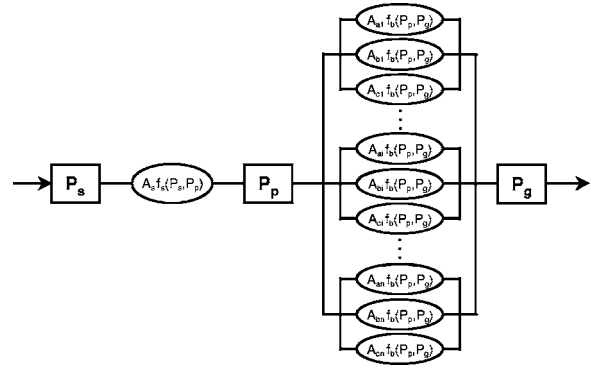
Fig. 3 Schematic of a simplified turbine cooling air supply system where each blade consists of three passages (*a*, *b*, and *c*)

$$\frac{\widetilde{\dot{m}}_{aj}}{\dot{m}_a} = \frac{\widetilde{A}_{aj}}{A_a} - \frac{1}{1+\beta}\frac{1}{n}\sum_{i=1}^{n}\frac{\widetilde{A}_{ai}+\widetilde{A}_{bi}+\widetilde{A}_{ci}}{A_a+A_b+A_c}, \qquad (14)$$

where A_a and $\dot{m}_a$ are the nominal area and flow for passage a. Analogous results hold for the other passages. For the three-passage blade, β is defined as,

$$\beta \equiv -\frac{A_s\dfrac{\partial f_s}{\partial P_p}}{n(A_a+A_b+A_c)\dfrac{\partial f_b}{\partial P_p}}. \qquad (15)$$

A detailed discussion of the multiple-passage blade case can be found in Sidwell [5]. In particular, we note that statistical correlation between the passage effective areas in a multiple-passage blade must be accounted for when determining the distribution of passage flows in a row [5].

3 Impact of Flow Tolerances and Selective Assembly

As described previously, manufacturing processes create blade-to-blade variability in the flow effective areas of cooling passages. With respect to a row of blades, this blade-to-blade distribution of effective areas leads to blade flows (and therefore life) which are different from row-to-row. In this section, the impact of blade flow tolerances and selective assembly on the row-to-row distribution of cooling flow is quantified using the simplified model described in Sec. 2 for a representative cooling system, turbine blade, and manufacturing variability. Specifically, for most of this section, we assume:

(a) the turbine row is composed of $n=80$, three-passage blades;
(b) nominal effective areas for the three passages are the same, i.e., $A_a=A_b=A_c$;
(c) $\beta=1.0$;
(d) normally distributed blade passage areas (due to manufacture), centered at the nominal effective areas with 3% variability (i.e., σ is 3% of the nominal passage area), and truncated at $\widetilde{A}_{\text{low}}/A_{\text{nom}}=-3\sigma/\mu=-9\%$ and $\widetilde{A}_{\text{high}}/A_{\text{nom}}=3\sigma/\mu=9\%$;
(e) variability of each passage is uncorrelated with the other passages.

These assumptions are representative of the cooling flow system, turbine blades, and manufacturing variability of the existing jet engine analyzed in Sec. 4.
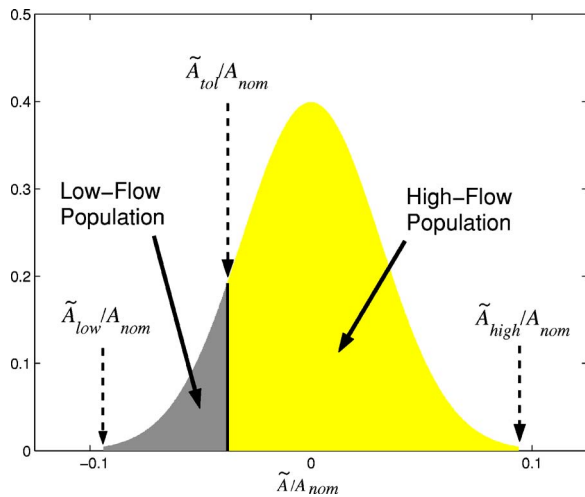
Fig. 4 Probability density function representing the passage *a* cooling flow effective area and defining *low-flow* and *high-flow* populations. Note: for the example given, blades are classified only according to their passage *a* flows.

We will assume that the highest temperatures and lowest life occur near passage *a* and define three populations of blade rows based on the passage *a* effective area (see Fig. 4) and the tolerance parameter $(\widetilde{A}_{tol})_a$. The first population of rows (referred to as the *full* population) are randomly assembled from blades whose passage *a* flow spans the entire manufacturing range, i.e., between $(\widetilde{A}_{low})_a < \widetilde{A}_a < (\widetilde{A}_{high})_a$. Given the above assumptions on the effective area variability, this full population is representative of current assembly practices with passage flow tolerances set at ±9%. The second population (referred to as the *high-flow* population) is randomly assembled from blades whose passage *a* flow is between $(\widetilde{A}_{tol})_a < \widetilde{A}_a < (\widetilde{A}_{high})_a$, and is compared with the *full* population to determine the impact of raising the low-flow tolerance limit for the life-limiting passage. The third population (referred to as the *low-flow* population) is randomly assembled from blades whose passage *a* flow is between $(\widetilde{A}_{low})_a < \widetilde{A}_a < (\widetilde{A}_{tol})_a$, and is compared to the *full* population to illustrate the behavior of low-flow rows if selective assembly were used. Note, in all three populations, passage *b* and *c* effective areas have been assumed to be

uncorrelated with passage *a* effective area, thus these passage areas range from their respective $\widetilde{A}_{low}$ to $\widetilde{A}_{high}$.

Given a specific value for $(\widetilde{A}_{tol})_a$, Monte Carlo analysis is used to propagate the variability through the linearized, three-passage simplified model [i.e., Eq. (14)] for a large population of rows.

Before studying the parametric dependence of the flows on a range of $(\widetilde{A}_{tol})_a$ values, we consider in detail the specific (though arbitrary) case of $(\widetilde{A}_{tol})_a/A_{nom}=-1\sigma/\mu=-3\%$. At this tolerance level, approximately 16% of the manufactured blades would be classified as low-flowing. The top row of Fig. 5 shows histograms of passage *a* flow for all the blades in each row for the full, low-flow, and high-flow populations. The distribution of passage *a* flows for all blades is essentially the same as the distribution of passage *a* effective areas [i.e., $(\widetilde{A}/A_{nom})_a$] that define the three populations. Thus, the full population flows are normally-distributed between ±9%, while the low-flow and high-flow populations truncate at approximately $(\widetilde{A}_{tol})_a/A_{nom}=-3\%$.

As the life of a blade row is controlled by the lowest-life blades in the row, a good indicator of the life of the row is the minimum passage *a* flow in the row,

$$\widetilde{\dot{m}}_{a\ min} \equiv \min_{j \in [1,n]} \widetilde{\dot{m}}_{aj}. \qquad (16)$$

The row-to-row distribution of $\dot{m}_{a\ min}$ for the $(\widetilde{A}_{tol})_a=-1\sigma$ case is shown in the lower half of Fig. 5. Comparing these minimum flow distributions to the all blade flow distributions above them, minimum flow blades are clearly drawn from the left of the all blade flow distributions. The minimum flow distribution for the full population has the largest variability driven by the selection of blades from the entire range of passage *a* flows. In contrast, the low-flow population has about half the variability. Of particular interest, the high-flow population has significantly lower variability than either the full or low-flow population. This decreased variability is due to the significantly larger probability of selecting a blade with effective area around $(\widetilde{A}_{tol})_a$ for the high-flow population than selecting a blade with effective area around $(\widetilde{A}_{low})_a$ for either full or low-flow populations. Thus, the minimum flowing passages in high-flow rows will tightly clustered around $(\widetilde{A}_{tol})_a$.

Plots of the row-to-row distributions of $\dot{m}_{a\ min}$ are also shown in Fig. 6. This figure shows the same data as the lower half of Fig. 5 but normalized by the mean value of $\dot{m}_{a\ min}$ for the full population
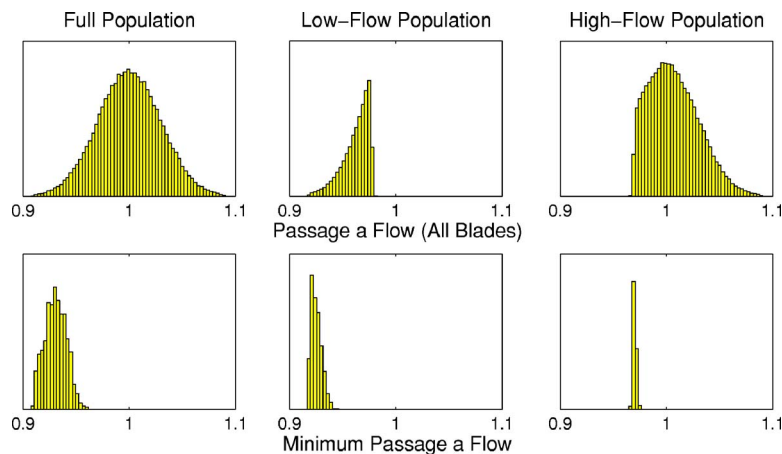
Fig. 5 Histograms showing passage *a* cooling flow for all blades in each row (top) and minimum passage *a* cooling flow in each row (bottom) for blade rows assembled from the full population, the low-flow population, and the high-flow population. Values are normalized by the mean passage *a* flow of all blades in the full population.
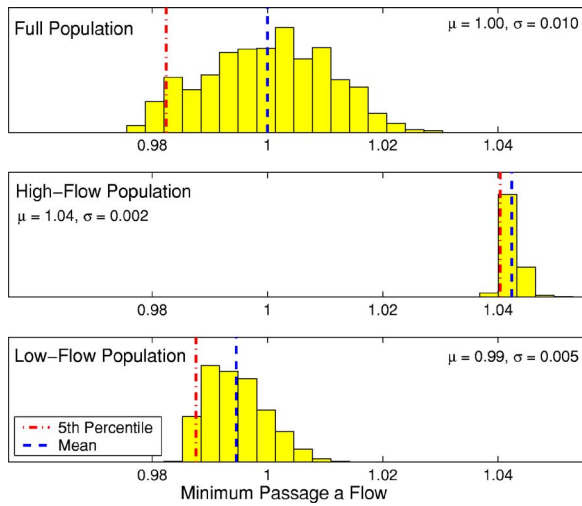
Fig. 6 Histograms showing the minimum passage *a* cooling flow in each row for rows assembled from the full, high-flow, and low-flow populations. Values are normalized to the mean value of the minimum passage *a* flow through the full population. Note: the data here is the same shown in the lower half of Fig. 5 though scaled differently to increase clarity.
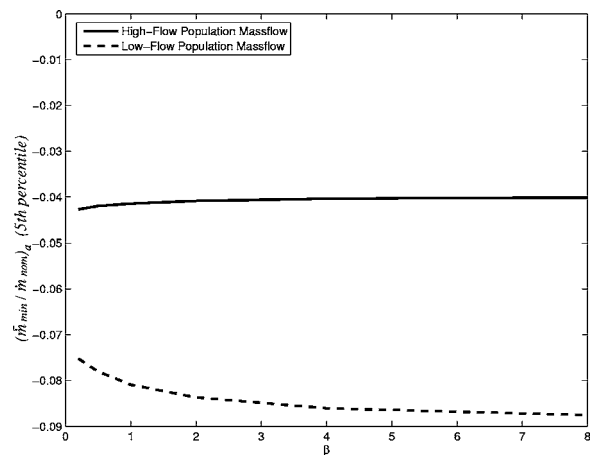

Fig. 7 Fifth percentile $\tilde{\dot{m}}_{a\,\mathrm{min}}$ for both the low-flow and high-flow classes of blades as a function of the tolerance value $[(\tilde{A}_{\mathrm{tol}}/A_{\mathrm{nom}})_a]$. Also included is the corresponding percent of low-flow blades.

and increased in scale to improve clarity. Lines are included in the plots indicating both the mean and fifth-percentile values, and the numerical values of the mean and standard deviation are also given. When considering the distribution of the life of a turbine row (or other part), the fifth-percentile life is a common measure of reliability quantifying the time at which 5% of the rows would be expected to have at least one blade fail. In this section, since the life of a blade is strongly impacted by the cooling flow, we use the fifth percentile of the minimum passage flow as a surrogate measure for the fifth percentile of row life. With respect to the fifth percentile of $\dot{m}_{a\,\mathrm{min}}$, the high-flow population shows a 6% increase compared to the full population. Recall from Sec. 1 that an increase of 6% in flow is roughly equivalent to 18 °F in metal temperature, or about 32% increase in life. The mean $\tilde{\dot{m}}_{a\,\mathrm{min}}$ for the high-flow population is also higher, in this case by 4%, compared to the full population. Finally, comparing the low-flow and full populations shows that the distributions are similar with a 0.5% decrease in the mean minimum flow but a 0.5% increase in the fifth percentile minimum flow.

Next, a range of $(\tilde{A}_{\mathrm{tol}})_a$ values are considered to quantify how the low-flow and high-flow populations behave as a function of different tolerance levels. Figure 7 shows the fifth percentile $\dot{m}_{a\,\mathrm{min}}$ as a function of $(\tilde{A}_{\mathrm{tol}})_a$. The fifth percentile $\dot{m}_{a\,\mathrm{min}}$ for the high-flow rows is clearly an increasing linear function of $(\tilde{A}_{\mathrm{tol}})_a$. By contrast, the fifth percentile $\dot{m}_{a\,\mathrm{min}}$ for the low-flow rows, while a decreasing linear function of $(\tilde{A}_{\mathrm{tol}})_a$, is nearly constant. The different behaviors for the high-flow and low-flow rows is a consequence of the minimum flowing blades for high-flow rows being dominated by blades with passage *a* effective areas around $(\tilde{A}_{\mathrm{tol}})_a$, while the low-flow rows minimum flowing blades will occur around the fixed-value of $(\tilde{A}_{\mathrm{low}})_a$. The result that the minimum flowing blades for the low-flow rows have higher mass flows for $(\tilde{A}_{\mathrm{tol}})_a \rightarrow (\tilde{A}_{\mathrm{low}})_a$ is consistent with the previous discussion of Eq. (13). Specifically, low-flow blades have higher mass flows when assembled together in a blade row rather than occurring within a row assembled from all blades.

Figure 7 also shows the relationship between the tolerance location $[(\tilde{A}_{\mathrm{tol}}/A_{\mathrm{nom}})_a]$ and the quantity of low-flow blades. Since
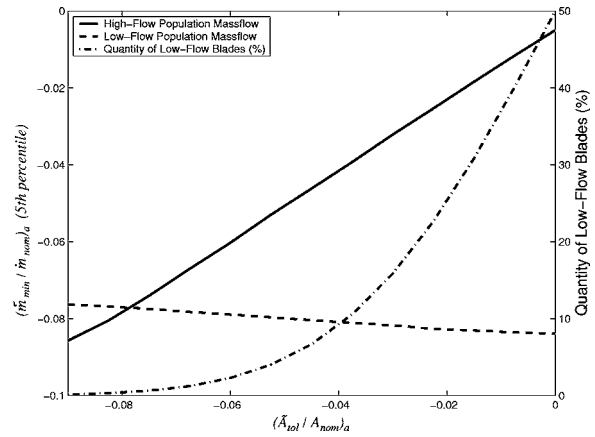
the blades classified as low-flowing occur in the tail of the effective area distribution, the percentage of low-flowing blades increases slowly as $(\tilde{A}_{\mathrm{tol}})_a$ is initially raised above $(\tilde{A}_{\mathrm{low}})_a$. Thus, for relatively small increases in the percentage of blades classified as low-flowing, significant increases would be observed for the minimum blade flows in the high-flowing rows.

While $\beta = 1$ was assumed in the previous results, the value of β may not be near unity in general. To quantify the dependence of the minimum flow rates on β, a set of calculations were performed in which β was varied from 0.25 to 8. For these calculations, $(\tilde{A}_{\mathrm{tol}}/A_{\mathrm{nom}})_a = -0.04$ which corresponds to approximately 10% of the blades being classified as low flow. As the results in Fig. 8 show, the dependence of the fifth percentile $\dot{m}_{a\,\mathrm{min}}$ on β is quite weak especially for $\beta > 1$. Thus, the estimated impact of selective assembly on the minimum flow in a row is likely to be similar for a wide range of β.

4 Application to a Commercial Turbofan

In this section, we consider the cooling performance of a low-flow and high-flow population for the first turbine rotor of an existing, large commercial turbofan. In particular, we perform probabilistic simulations of the auxiliary air system of this turbo-

Fig. 8 Fifth percentile $\tilde{\dot{m}}_{a\,\mathrm{min}}$ for both the low-flow and high-flow classes of blades as a function of β for $(\tilde{A}_{\mathrm{tol}}/A_{\mathrm{nom}})_a = -0.04$
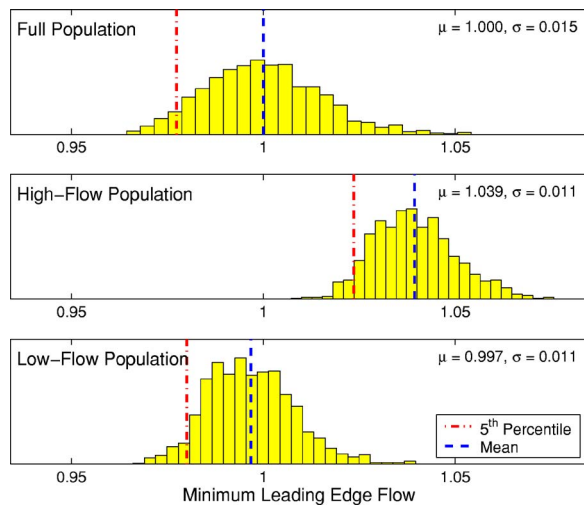
Fig. 9 Histograms showing the minimum leading-edge passage flow for rows assembled from the full, high-flow, and low-flow populations for an existing commercial jet engine. Values are normalized to the mean value of the minimum leading-edge passage flow through the full population blade rows.
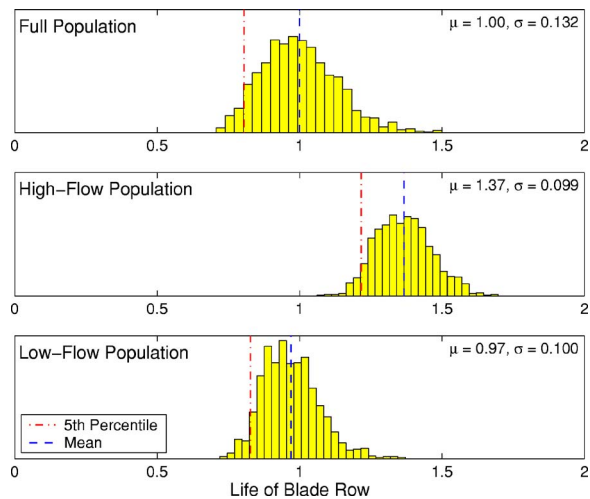

Fig. 10 Histograms showing the blade row oxidation life for rows assembled from the full, high-flow, and low-flow populations for an existing commercial jet engine. Values are normalized to the mean value of the row life for the full population rows.

fan to quantify the benefits of the selective assembly process on minimum blade flow and life due to oxidation damage. We also compare these high-fidelity results with the previous simplified model.

The entire auxiliary air system is modeled using a high-fidelity flow network in which all of the blades in the first-stage rotor are included as separate elements. The portion of the auxiliary air system responsible for delivering the cooling air to the first-stage rotor blades is shown in Fig. 1 along with an overlay of the corresponding section of the high-fidelity flow network. Using this high-fidelity model, the blade metal temperature and oxidation life are estimated at a variety of points on the surface of each airfoil in the row using a flow-scaling analysis similar, though somewhat more complex, to that described in the Introduction [Eqs. (1)–(3)]. An in-depth description of the model and a comparison to field failure data is included in Sidwell [5] and Sidwell and Darmofal [6].

The first turbine rotor blades for this turbofan consist of three passages: a leading-edge passage, a mid-body passage, and a trailing-edge passage, where the total blade flow allocation is 30%, 30%, and 40%, respectively. Manufacturing data from flow tolerance measurements were used to determine the distribution of the flow effective areas in each passage. The coefficients of variation for the leading-edge, mid-body, and trailing-edge passages were 3%, 4%, and 4%, respectively, and all were found to be well fit by a normal distribution (truncated at $\pm 3\sigma/\mu$). Although the correlations between passage areas were weak (with correlation coefficients less than 0.25) the correlations were included in the probabilistic simulations.

In addition to individual blade flow variability, the probabilistic simulations include other relevant sources of variability within the engine. These include engine-to-engine variability in gas path conditions (temperatures, pressures, rotational speeds), geometric variability within the cooling air delivery system (hole diameters, radii from engine centerline, rotating seal clearances, effective areas of flow components), and engine deterioration effects. A complete description of the included variabilities is available in Sidwell [5] and Sidwell and Darmofal [6].

For this blade, the classification for life is based on the leading-edge effective flow area since the hottest metal temperatures and the life-limiting area occurs in this region. In the analysis presented here, the tolerance is set at -1σ. Figure 9 shows histograms of the minimum leading-edge passage flow for rows assembled
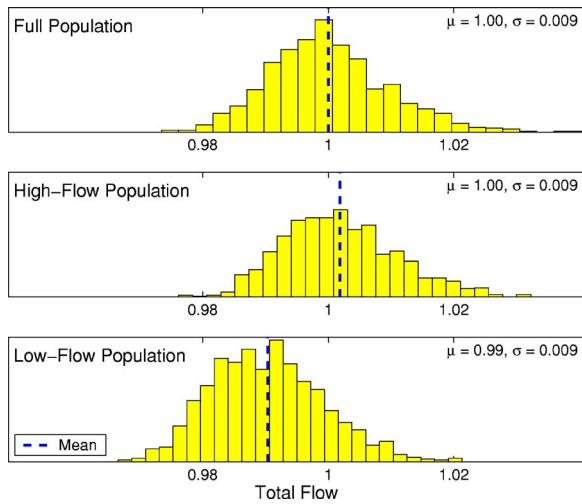
from the full, high-flow, and low-flow populations. Like the simplified model results of Sec. 3, the high-flow population has a mean minimum passage flow that is 4% higher than the full population, and the low-flow population has nearly the same mean minimum leading-edge flow as the full population. The fifth percentile minimum flow increases 4.7% for the high-flow population and 0.3% for the low-flow population. Unlike the simplified model results, the variability in the high-flow and low-flow populations is not as dramatically reduced. This is due to the correlation between the different blade flow passages as well as the inclusion of many noise parameters in the high-fidelity probabilistic analysis beyond the passage effective areas.

Figure 10 shows histograms of row oxidation life (as determined by the minimum-life blade in the row). These histograms show that the high-flow population has a mean row life that is 37% higher than that of the full population. The fifth percentile life has an even larger 51% increase relative to the full population. Furthermore, the low-flow rows have a distribution of life that is similar to the full population.

While the life of a blade can be increased by raising the flow through all of the blades, this approach has a detrimental effect on engine performance. However, the improvements in life observed in the high-flow population are largely due to the segregation of the lowest-flowing manufactured blades into the same rows, with a much smaller impact on the actual flow delivered to any individual blade. Thus, the overall impact on the total flow to a blade row will be small. Figure 11 shows histograms of total flow delivered to the row of first-stage turbine blades for the full, high-flow, and low-flow populations. The full population and the high-flow populations exhibit the same mean flow and the same standard deviation in flow, while the low-flow population passes approximately 1% less total flow than the full population. Note that since the classification into low and high-flow blades occurred at -1σ, the low-flow/high-flow rows account for approximately 16%/84% of the total number of assembled rows.

Finally, we compare the results of this higher-fidelity auxiliary air system model to the simplified model described in Sec. 2. For this air system, the value of $\beta \approx 1.4$. β was estimated by first solving for the flow through the system under nominal conditions. Then, the plenum pressure (P_p as shown in Fig. 1) was perturbed by 1% and the value of β was estimated from a finite difference of the different mass flows. Using this value of β and the flow effective area variabilities (including correlation), a Monte Carlo

Fig. 11 Histograms showing the total cooling flow (for all passages) delivered to rows assembled from the full, high-flow, and low-flow populations for an existing commercial jet engine. Values are normalized to the mean value of the total flow for the full population blade rows.

simulation was performed on Eq. (14). Table 1 shows the change (relative to the full population) in the mean and fifth percentile minimum passage a flows for the low-flow and high-flow populations computed using the simplified and higher-fidelity models. In each case, the simplified model results are similar to the higher-fidelity model results.

5 Conclusion

In this paper, we considered the impact of blade-to-blade variability in cooling flow capability on the life of a row of cooled turbine blades. As a result of the strong dependence of life on temperature, and temperature on cooling flow, small changes in tolerances that affect the lowest-flowing blades assembled into a row were shown to make a significant impact on the life of a row. Through a simplified flow network model, we demonstrated that the flow through an individual blade is a function of both its individual flow area and the average-flow area of all blades assembled in the row. In particular, the blade plenum pressure tends to increase with decreased average-blade flow area. As a result, the individual blade flow for a row assembled entirely from low-flow blades will tend to be closer to the design intent than for a single low-flow blade in a randomly-assembled row. Specifically, we show that rows selectively assembled from low-flowing blades have a minimum flow and life which are the same or better than rows assembled at random from all manufactured blades. Furthermore, using a higher-fidelity model of the flow through the auxiliary air system of an existing jet engine, the impact of selective assembly as estimated by the simplified model was shown to be qualitatively and quantitatively accurate.

Table 1 Comparison of the simplified and high-fidelity model estimates of the change (relative to the full population) in the mean and fifth percentile leading-edge passage flow for an existing commerical jet engine for low-flow and high-flow populations

	Mean		Fifth	percentile
	Simplified	High-fidelity	Simplified	High-fidelity
Low-flow	−0.35%	−0.33%	+0.59%	+0.28%
High-flow	+4.0%	+3.9%	+5.5%	+4.7%

While this paper shows the potential for significant benefits due to more stringent flow tolerances and/or selective assembly, a variety of other issues could be explored. Specifically,

(1) Although beyond the scope of the current work, a clear next step would be to estimate the economic impact of more stringent tolerances or selective assembly. This analysis would require financial and manufacturing models to properly account for the impact of improved life, increased scrap, management of multiple blade classes including part availability, etc.

(2) While the blades considered in this paper exhibited a dominant failure location, blades exist which have multiple critical failure locations. In this case, the selective assembly approach would need to be generalized by defining a low-life class of blades which are likely to fail at any of the critical locations. The feasibility and the potential benefits of such an approach are not known.

(3) As described in this paper, more stringent tolerances and/or selective assembly can be used to improve the life for the majority of blade rows; however, an alternative use would be to increase the performance of an engine by raising the gas turbine operating temperature while maintaining the maximum blade metal temperature for the higher-flowing blade rows. A preliminary study of this possibility has already been performed that indicates the benefits to turbine inlet temperature could be significant [5,10]. However, this analysis did not include constraints on turbine inlet temperature due to the life of other hot-section components.

Acknowledgment

Nomenclature

t_f = time to failure of blade
P_p = blade plenum pressure
P_s = source pressure for air delivery system
P_g = gas path dump pressure for blade flow
$\dot{m}_s$ = total cooling flow
$\dot{m}_i$ = individual blade cooling flow
$\dot{m}_{nom}$ = nominal individual blade cooling flow
A_s = effective flow area of upstream air delivery system
$f_s(P_s, P_p)$ = mass flow-pressure relation for upstream air delivery system
A_i = effective flow area for blade i
A_{nom} = nominal effective flow area for blades
$\tilde{A}_{low}$ = largest decrease in effective flow area from A_{nom} due to manufacturing
$\tilde{A}_{high}$ = largest increase in effective flow area from A_{nom} due to manufacturing
$\tilde{A}_{tol}$ = value of $\tilde{A}$ used to classify blades
$f_b(P_p, P_g)$ = mass flow-pressure relation for blades
n = number of blades in row
α = power used in empirical correlation between $\dot{m}$ and η
β = nondimensional parameter relating upstream and downstream flow sensitivity to P_s
μ, σ = mean and standard deviation
T_{gas} = turbine inlet gas path temperature
T_{metal} = blade metal temperature
T_{cool} = temperature of internal blade cooling flow

η = blade cooling effectiveness
$\tilde{(\ )}$ = perturbation
$(\ )_{nom}$ = nominal value
$(\ )_{min}$ = minimum value observed over all blades in a row
$(\ )_{a,b,c}$ = denotes specific passage for three passage blades

References

[1] Cyrus, J. D., 1986, "Engine Component Life Prediction Methodology for Conceptual Design Investigations," ASME Paper 86-GT-24.
[2] Tumer, I. Y., and Bajwa, A., 1999, "Learning About How Aircraft Engines Work and Fail," AIAA Paper No. AIAA-99-2850.
[3] Wood, M. I., 2000, "Gas Turbine Hot Section Components: The Challenge of 'Residual Life' Assessment," in *Proceedings of the I MECH E: Journal of Power and Energy*, Proc. Inst. Mech. Eng., IMechE Conf., **214**(3), pp. 193–201.
[4] Holland, M. J., and Thake, T. F., 1980, "Rotor Blade Cooling in High Pressure Turbines," J. Aircr., **17**(6), pp. 412–418.
[5] Sidwell, C. V., 2004, "On the Impact of Variability and Assembly on Turbine Blade Cooling Flow and Oxidation Life," PhD thesis, Massachusetts Institute of Technology.
[6] Sidwell, V., and Darmofal, D. L., 2003, "Probabilistic Analysis of a Turbine Cooling Air Supply System: The Effect on Airfoil Oxidation Life," ASME Paper No. GT2003-38119.
[7] Swaminathan, V. P., Allen, J. M., and Touchton, G. L., 1986, "Temperature Estimation and Life Prediction of Turbine Blades Using Post Service Oxidation Measurements," ASME Paper No. 96-GT-528.
[8] Liu, Z., Volovoi, V., and Mavris, D. N., 2002, "Probabilistic Remaining Creep Life Assessment for Gas Turbine Components Under Varying Operating Conditions," AIAA Paper No. AIAA-2002-1277.
[9] Suo, M., 1978, *The Aerothermodynamics of Aircraft Gas Turbine Engines*, Chapter on Turbine Cooling, G. Oates, ed., Air Force Wright Aeronautical Laboratories, Wright-Patterson AFB, OH, Report No. AFAPL-TR-78-52.
[10] Sidwell, V., and Darmofal, D. L., 2004, "A Selective Assembly Method to Reduce the Impact of Blade Flow Variability on Turbine Life," ASME Paper No. GT2004-53930.
[11] Sidwell, V., and Darmofal, D. L., 2003, "Method for Assembling Gas Turbine Engine Components," U.S. Patent Application, Nov. 2003, Serial Number 10/717408.

Erratum: "The Transient Liquid Crystal Technique: Influence of Surface Curvature and Finite Wall Thickness" [Journal of Turbomachinery, 2005, 127(1), pp. 175–182]

G. Wagner, M. Kottula, P. Ott, B. Weigand, and J. von Wolfersdorf

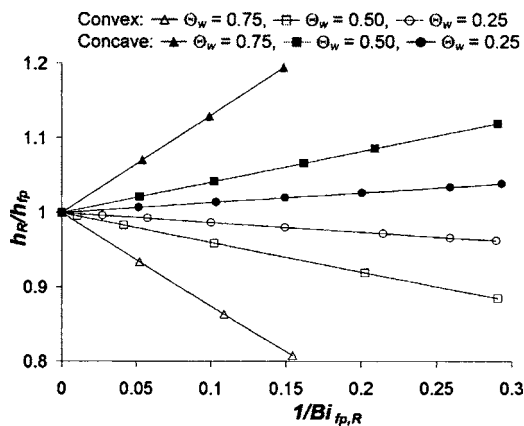The definitions of the symbols of Figs. 4–10 were missing:

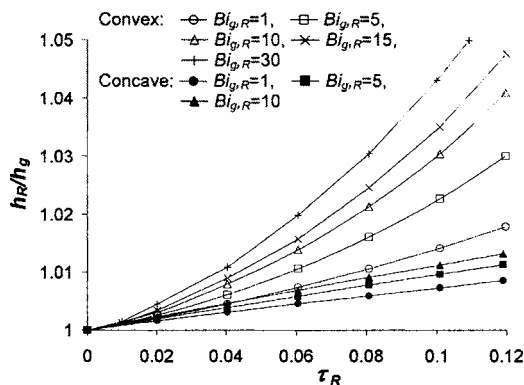**Fig. 4 Effect of surface curvature using comparison between Eqs. (1) and (21)**

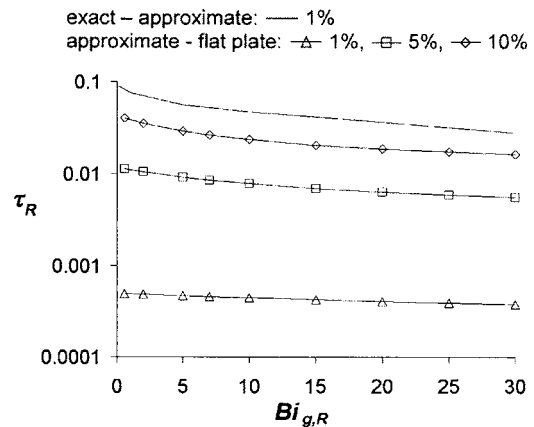**Fig. 5 Deviation of the approximate solution Eq. (21) from the exact solution Eq. (20)**

Fig. 6 Regions of validity for approximate (Eq. (21)) and flat plate (Eq. (1)) solutions depending on allowable error
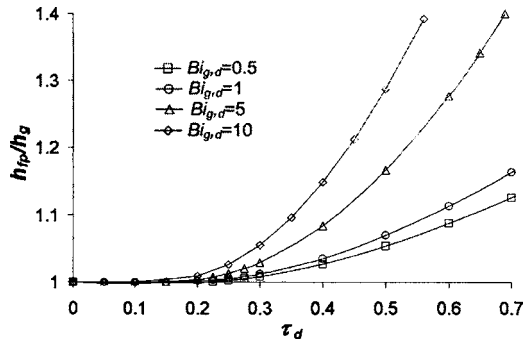
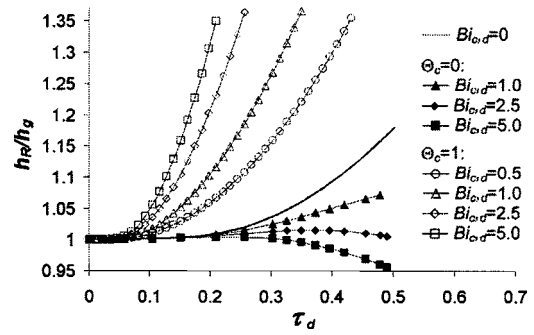**Fig. 7 Effect of finite wall thickness for flat plate**

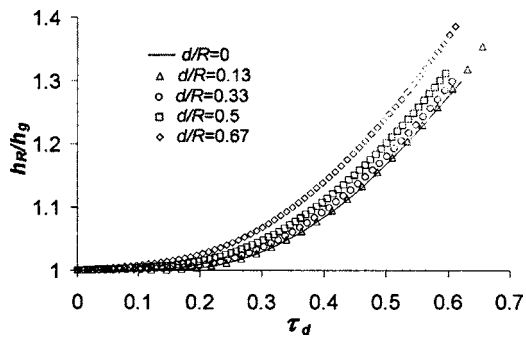**Fig. 9 Effect of backside convection for $Bi_{g,d}=5$**

Fig. 8 Effect of finite wall thickness for convex cylinder wall for $Bi_{g,d}=5$
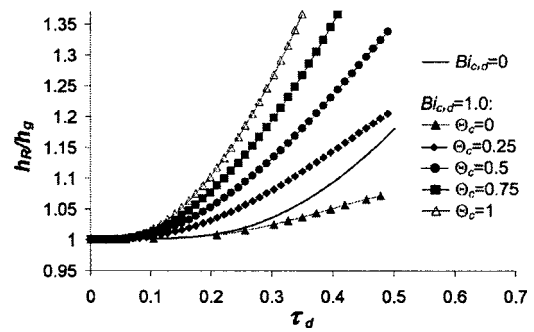

Fig. 10 Effect of backside temperature condition for $Bi_{g,d}=5$